THEORETICAL STUDIES OF THE MID-LATITUDE IONOSPHERE

ALI ABDULAZIZ AL-NAGHMOOSH

Thesis submitted for the degree
of Doctor of Philosophy

Department of Mathematics
University of Aston
in Birmingham
November 1981

THEORETICAL STUDIES OF THE MID-LATITUDE IONOSPHERE

ALI ABDULAZIZ AL-NAGHMOOSH

Ph.D., 1981

SUMMARY

In this thesis we give a brief description of the atmospheric and ionospheric regions. This is done in Chapter I. In Chapter II we describe how the O^+, H^+, He^+ and O^{++} equations are derived using two different formulations. In Chapter III we investigate the downward flow of protons in a collapsing post-sunset ionosphere. The time dependent behaviour of He^+ under sunspot minimum conditions is investigated in Chapter IV. This is achieved by numerical solution of the O^+, H^+ and He^+ continuity and momentum equations, treating He^+ as a minor ion with O^+ and H^+ as major ions. Then we move on to investigate the behaviour of O^{++} using sunspot maximum parameters. In Chapter V, O^{++} is treated theoretically as a minor ion with O^+ and H^+ as the major ions. In Chapter VI we extend the work of Chapter IV, presenting a comparative study of H^+ and He^+ at sunspot minimum and sunspot maximum. In this last chapter all three ions, O^+, H^+ and He^+, are treated theoretically as major ions and we concentrate mainly on light ion contents and fluxes.

Tables and figures for each chapter are given at the end of the corresponding chapter.

Modelling

Terrestrial Ionosphere

Mid-latitudes

O^+, H^+, He^+, O^{++}

ABSTRACT

Following a brief description of the atmosphere and ionosphere in Chapter I we describe how the equations of continuity and momentum for O^+, H^+, He^+, O^{++} are derived from the formulations of St-Maurice and Schunk(1977) and Quegan et al.(1981) in Chapter II

In Chapter III we investigate the nature of the downward flow of protons in a collapsing post-sunset ionosphere. We derive an analytical form for the limiting temperature, we also note the importance of the polarization field term and concluded that the flow will remain subsonic for realistic conditions.

The time-dependent behaviour of He^+ under sunspot minimum conditions is investigated in Chapter IV. This is achieved by numerical solution of the O^+, H^+ and He^+ continuity and momentum equations ,treating He^+ as a minor ion with O^+ , H^+ as major ions. We found that He^+ flows upwards during the day-time and downwards during the nighttime. He^+ flux tube content reached a maximum on the 8th day of the integration period and started to decreasing . This is due to the large amount of H^+ present at the late stages of the integration period which makes He^+ unable to diffuse through the H^+ layer away from the loss region.

In Chapter V we investigate the behaviour of O^{++} using sunspot maximum parameters. Although our results support the findings of Geis and Young(1981) that the large amounts of O^{++} at the equator are caused mainly by thermal diffusion, the model used by Geis and Young overemphesizes the effect of thermal diffusion. The importance of O^{++}- O^+ collision frequency is also noted .

In Chapter VI we extend the work of Chapter IV, presenting acomparative study of H and He at sunspot minimum and sunspot maximum.In this last Chapter all three ions, O^+ ,H^+ and He^+ , are treated theoretically as major ions and we concentrate mainly on light ion contents and fluxes. The results of this Chapter indicate that by assuming He^+ as a minor ion we under-estimate He^+ and over-estimate H^+ . Some interesting features concerning the day to day behaviour of the light ion fluxes arise. In particular the day-time H^+ fluxes decrease from day to day in contrast to the work of Murphy et al.(1976).

In appendix A we derive some analytical forms for the optical depth so that the models can include a realistic description of photoionization .

ACKNOWLEDGEMENT

The author would like to express his deep appreciation and gratitude to Dr J A Murphy for his friendly supervision and very helpful advice and encouragement throughout the course of this work.

The author's sincere thanks go to Dr R J Moffett for some useful comments and helpful discussions relating to some parts of this work.

The author wishes to express his deep gratitude to the University of Riyadh, Saudi Arabia, for their financial support throughout the course of this research.

The author would like to thank his mother, father, wife, brothers, sisters, relatives and friends, and all those without whose encouragement this work would not have been possible.

Finally the author wishes to thanks Mrs B J Tennant for her careful and excellent typing of this manuscript.

CONTENTS

Chapter I INTRODUCTION 1

Chapter II EQUATIONS

Chapter III DOWNWARD PROTON FLOW IN THE TOPSIDE IONOSPHERE

Chapter IV BEHAVIOUR OF HE^+ IN THE MID LATITUDE PLASMASPHERE UNDER SUNSPOT MINIMUM CONDITIONS.

Chapter V A THEORETICAL STUDY OF DOUBLY CHARGED ATOMIC OXYGEN IN THE MID-LATITUDE PLASMASPHERE.

Chapter VI A COMPARATIVE STUDY OF H^+ AND HE^+ AT SUNSPOT MINIMUM AND SUNSPOT MAXIMUM IN THE MID-LATITUDE PLASMASPHERE.

LIST OF TABLES AND FIGURES

FIGURES FOR CHAPTER I

FIGURES FOR CHAPTER III

TABLES AND FIGURES FOR CHAPTER IV

TABLES AND FIGURES FOR CHAPTER IV (continued)

TABLES AND FIGURES FOR CHAPTER V

FIGURES FOR CHAPTER VI

FIGURES FOR APPENDIX A

I INTRODUCTION

1.1 The neutral atmosphere; Structure and Composition.

The Earth's upper atmosphere is a complex medium. As generally happens in the study of a complex natural system nomenclature has been developed to describe the different parts of the atmosphere (Chapman, 1950). The description may be based on chemical composition or on temperature or on the dominant physical processes.

The troposphere is the lowest atmospheric region and begins at the Earth's surface. This region is characterised by its negative vertical temperature gradient which leads to temperatures between 190°K (equator) and 220°K (high latitudes). The relative composition of the air in the troposphere is constant as far as the principal constituents are concerned.

The stratosphere lies above the troposphere and is a region of increasing temperature up to a maximum of about 270°K near 50 km. It was widely thought after the discovery of the change in temperature gradient that the stratosphere was a calm region and subject to molecular diffusion. It is now known that turbulence exists and atmospheric mixing to the extent of a constant relative composition for the principal constituents has been verified by various observations. Although atmospheric mixing is present in the stratosphere, aeronomic reactions affecting minor constituents result in variations in concentrations of these gases which differ from the mixing distributions. Ozone is particularly important in this regard since it absorbs ultraviolet radiation harmful to life at the Earth's surface.

The mesosphere is a region of decreasing temperature between the stratopause and the mesopause, with a minimum of temperature found at 85±5 km. The atmospheric conditions at the mesopause are similar to those at the tropopause.

Because of oxidation processes and penetration of ultraviolet radiation which dissociate polyatomic molecules, the mesosphere is a more complex region than the stratosphere or troposphere. In the three lowest regions of the terrestrial atmosphere turbulence prevails and the rate of mixing of the atmospheric gases is sufficiently rapid to produce a uniform relative composition for the major constituents (N_2, O_2, Ar, Co_2). This region of uniform relative composition is called the homosphere and its upper boundary, which lies at altitude of approximately 100 km, is called the turbopause. Within the homosphere the mean molecular mass does not change significantly. Differences do exist, however, since the heat source and losses are different in the three regions. Thus, while the Earth's surface is the principal source of heat for the troposphere, the heat budget in the stratosphere is related to the absorption of solar ultraviolet radiation by ozone and to atmospheric infrared emission.

The region above the mesopause is called the thermosphere. The behaviour of the atmosphere in this region changes dramatically. Atomic oxygen becomes a permanent constituent of the atmosphere and there is a positive temperature gradient leading to temperatures greater than 1000°K. The large temperature gradient results from the absorption of solar ultraviolet energy and the lack of any effective means of thermal emission. The region of the upper atmosphere, where mixing of the constituents by wind and dissipative turbulence does not greatly affect the vertical distribution of individual gases, is called heterosphere. Figures 1 and 2 show the regions of the atmosphere and an approximate distribution of neutral constituents in the upper atmosphere. The rate at which the concentration of a gas decreases with height may be described by means of its scale height. The general definition of the scale height is the distance in which the concentration of the gas will change by a factor of e. To obtain the alternative definition of scale height we first note that a neutral atmospheric gas may be assumed to obey the perfect gas law

$$P = nkT \tag{1.1}$$

and when gravitational separation exists the hydrostatic equation

$$\frac{dP}{dz} = -nmg \tag{1.2}$$

may be assumed to hold, where

P = partial pressure of the gas

n = number density

k = Boltzmann's constant = 1.38×10^{-16} ergs/deg

T = neutral temperature

m = molecular mass

g = gravitational acceleration

z = height.

Combining equations (1.1) and (1.2) gives

$$-\frac{1}{P}\frac{dP}{dz} = \frac{mg}{kT} \tag{1.3}$$

This equation leads to the alternative definition of the scale height of a gas, H, namely

$$H = \frac{kT}{mg} \tag{1.4}$$

so that

$$\frac{1}{P}\frac{dP}{dz} = -\frac{1}{H} \tag{1.5}$$

For a completely mixed atmosphere these equations may still be valid. However, n is then the total concentration and m represents the mean molecular mass. These two definitions are only equivalent for gases in diffusive equilibrium in isothermal regions. According to the definition (1.4) the scale height of a gas is inversely proportional to its molecular mass, so that the lighter gases, such as atomic hydrogen, have larger scale heights and decay less rapidly than the heavier gases.

For each gas there is a height at which turbulence ceases or becomes less important and is overtaken by molecular diffusion. This height is approximately the same for each gas and is the turbopause. Below the turbopause (i.e. in the homosphere) each gas decays as if its mass was equal to the mean mass in that region,

i.e.

$$H = \frac{kT}{\overline{m}g} ,$$

where $\overline{m}$ = mean mass of atmosphere.

Above the turbopause, each neutral gas approaches a distribution depending on its molecular mass. Therefore in this region the heavier gases dominate at lower height and decay more rapidly than the lighter gases which dominate at greater heights. This separation process of the constituent gases according to their own molecular mass is called diffusive separation. It is sometimes referred to more descriptively by gravitational separation, and the gases are said to be in diffusive equilibrium.

1.2 Ionosphere

The Earth's ionosphere results from the passage of the sun's radiation through the atmosphere. If the radiation has sufficient energy it may dislodge an electron from a neutral particle lying in its path, resulting in a positively charged ion and an electron. This process of production of charged particles by solar radiation is called photoionization and is discussed in section 1.3. At the top of the atmosphere relatively few ions and electrons are produced by the sun's radiation because of the small number of neutral particles available for photoionization.

As the radiation passes to denser regions more charged particles are produced because of the increased neutral density. However, simultaneously the radiation intensity is decaying exponentially along the radiation path due to absorption, and there must come a point where the photo-ionization production rate starts to decrease. In this way the opposing effect of exponential decrease of radiation and exponential increase of neutral particles results in an ionized layer. Layers formed in this way are called Chapman Layers. The ionosphere is divided into layers or ledges of ionization which are referred to as the D-, E-, F_1- and F_2- regions, as shown in Fig. 3.

The D-and E- regions are only mentioned briefly here since this work relates to the region of the atmosphere above 200 km. These are regions of complex chemistry with negative ions as well as positive ions in existence, particularly in the D- region. The main ions of the E-region are O_2^+, N_2^+ and NO^+. The molecular ions of the D- and E- regions recombine rapidly with electrons at night.

The F-region is subdivided into lower and upper regions known as the F1-region and F2-region respectively. The transition from molecular ions to atomic ions occurs in the F1-region. The F1-region is only a hesitation or inflexion in the electron density profile. The lower boundary of the F1-region is round about 150 km. The F2-region is a region of atomic ions whereas molecular ions occupy the lower layers. Rocket and satellite observations show that the predominant ionic constituent near the F2-peak is O^+, and it is found that there is finally a change with increasing altitude from O^+ to He^+ and H^+ in the top-side region. The region in which H^+ dominates is called the protonosphere.

The behaviour of the F2-region is very complicated. Some of the parameters that affect the behaviour of the F-region are solar ultraviolet radiation, the Earth's magnetic field, composition and motion of the neutral atmosphere and interaction with the thermal plasma above the F-region. In fact the splitting of the F-region into F1- and F2-regions is attributed to the ion-atom interchange reactions

$$O^+ + N_2 \rightarrow NO^+ + N$$

$$O^+ + O_2 \rightarrow O_2^+ + O$$

followed by the dissociative recombination reactions

$$NO^+ + e \rightarrow N + O$$

$$O_2^+ + e \rightarrow O + O \quad .$$

These reactions provide an overall recombination process between atomic oxygen ions and electrons. In the absence of photochemical reactions, consideration of the sun's radiation spectrum and different atomospheric constituents would suggest two peaks in the photoionization production rate, giving two Chapman layers, one at the level of the

E-layer and the other at the F1-ledge. The increasing electron density in and above the F1-ledge can be explained in terms of photoionization production and photochemical loss determined by the above reactions. Although the photoionization rate decreases above the F1-region the loss rate decreases even more rapidly,with the result that the electron concentration increases. The decreasing loss rate is a consequence of the rapid exponential decrease of molecular oxygen and nitrogen with height. The increasing electron concentration above the F2-region is halted by diffusion and the F2 peak is formed around 300 km. The diffusive separation that is often assumed to exist above the F2 peak is not as simple as diffusive separation of neutral constituents. Although electrons and positively charged ions exist in this region they are held together by electric forces. The ion-electron pairs then diffuse through the neutral gas and settle out with a distribution corresponding to an atomic mass equal to one half that of an atomic oxygen ion. This is simply the average of the masses of O^+ and an electron, since an electron has negligible mass. This type of diffusion is called ambipolar diffusion.

In the lower F-region transport processes have little importance and the O^+ densities can be obtained by assuming a balance between photoionization and recombination, and photochemical equilibrium is said to exist. Above about 2000 km O^+ is in diffusive equilibrium, i.e. the O^+ flow is negligible. In addition, at great altitudes the H^+

profile often resembles a diffusive equilibrium profile. However, the H^+ flow is not negligible. The pseudo-diffusive equilibrium profile results from very few collisions occurring at great altitude. The O^+ and H^+ layers are coupled chemically by the charge exchange reaction.

$$O + H^+ \rightarrow O^+ + H \tag{1.6}$$

and its reverse

$$O^+ + H \rightarrow O + H^+ \tag{1.7}$$

These reactions provide production and loss processes for both ionic constituents. The processes associated with O^+ and H^+ behaviour are summarised in Fig. 4.

A downward flux of H^+ ions from the protonosphere is thought to assist the maintenance of the night-time F-layer via the above reaction (1.6). It has been suggested that the collapse of temperature in the post-sunset ionosphere induces this downward flux of protons with the possibility of supersonic flow (Fontheim and Banks, 1972). This possibility will be discussed in Chapter III.

In and above the F-region the Earth's magnetic field is sufficiently strong to ensure that the ambipolar diffusion described above takes place parallel to the Earth's magnetic field. This situation is modified when magnetic disturbances occur. This is discussed in section 1.4. The region in which the Earth's magnetic field controls the dynamics of the atmosphere is called the magnetosphere. It is difficult to define a lower limit, since the movement of ionization is geomagnetically controlled at all heights above about 150 km (or even less); but the magnetosphere certainly includes the whole atmosphere above the level at which ionized constituents become predominant over neutral constituents. The boundary of the geomagnetic field lies at about ten earth radii on the day side of the Earth and at greater distance on the night side. The simplest magnetic field which corresponds most closely to the observed magnetic field of the Earth is that of a central dipole. A better approximation to the field is obtained if the dipole is inclined at an angle of about 11.5° to the geographic axis. Fig. 5 shows the Earth's magnetic field lines for the centred dipole approximation. With this approximation for the magnetic field, the lines of force, arc length along a field line and the sine and cosine of the dip angle are given in Appendix B.

1.3 Theory of Photoionisation

The process in which a photon dislodges an electron from a neutral particle is called photoionization. Since this work examines the behaviour of O^+, H^+ and He^+ in the upper atmosphere, production of these ions by photoionization must be included in the mathematical models. Thus here the basic theory of photoionization is discussed and this leads to the photoionization production functions.

The basic theory of photoionization was developed by

Chapman (1931a,b). The theory considers the attenuation of solar radiation as it passes downwards through the atmosphere, and derives a general formula for the rate of production of ionization, q, as a function of height h and the sun's zenith angle χ, assuming

(i) the radiation is monochromatic with photon flux I(h) at height h,

(ii) the atmosphere consists of only one absorbing gas with concentration n(h).

Let σ = the cross section for absorption of radiation

η = ionizing efficiency, the number of electrons produced per photon absorbed. Thus for a single neutral particle illuminated by monochromatic radiation, the probability per unit time that a given molecule absorbs a photon is $I\sigma$ and the probability of producing an ion/electron pair is $I\sigma\eta$. This is sometimes called the ionizing rate coefficient. Hence the rate of production of ionization per unit volume is

$$q = I\sigma\eta\, n \qquad (1.8)$$

An elemental volume along the radiation path is $\sigma\delta s$ where s is a coordinate measuring length along the radiation path. The number of molecules in this volume is $n\sigma\delta s$ and thus the amount of radiation flux absorbed in this volume is

$$\delta I = -I(n\sigma\delta s) \qquad (1.9)$$

In the limit

$$\frac{d}{ds}(\log I) = -n\sigma \qquad (1.10)$$

If s is measured such that it increases moving away from the sun, then taking the sun to be an infinite distance away

$$\Big[\log I\Big]_{-\infty}^{s_p} = -\int_{-\infty}^{s_p} \sigma n ds \quad ,$$

where s_p is the value of s at the point P (Figure 6).
Hence

$$\log\left({}^{I_p}/I_\infty\right) = -\int_{-\infty}^{s_p} \sigma n ds \quad , \qquad (1.11)$$

where I_∞ is the unattenuated photon flux leaving the sun (1.9) can be written

$$I_p = I_\infty \exp\left[-\int_{-\infty}^{s_p} \sigma n ds\right] \qquad (1.12)$$

A quantity called the optical depth and denoted by τ is often introduced as a measure of the attenuation of the radiation. The optical depth is defined by

$$\tau = \log\left(\frac{I_\infty}{I_p}\right) \qquad (1.13)$$

so that

$$I_p = I_\infty \exp(-\tau) \qquad (1.14)$$

It is clear from (1.10) that

$$\tau = \int_{-\infty}^{s_p} \sigma n ds \qquad (1.15)$$

One would expect the optical depth to have dimensions of length. However, it is clear from (1.13) that it is a dimensionless parameter. From equation (1.15) it can be seen that τ gives the number of molecules along the radiation path that absorbs photons, i.e. τ is the column content of molecules from P to the sun.

Thus the problem of evaluating I in equation (1.14) and consequently q in equation (1.8) has been reduced to one of evaluating τ in equation (1.15), which is the number of molecules lying in the radiation path between P and the sun.

In the actual atmosphere, the production $q(x,\chi)$ is more complicated and is given by

$$q(x,\chi) = I_{\infty}e^{-\tau} \sum_{i} \eta_i \sigma_i n_i(h) \qquad (1.16)$$

Also σn in equation (1.15) can be replaced by $\sum_{i} \sigma_i n_i$.

The form of the optical depth τ is derived in Appendix A.

1.4 The dynamic state of the plasmasphere

At low geomagnetic latitudes the plasmasphere represents a region of relatively high ion density contained along the closed lines of geomagnetic force. The topside ionosphere in these regions is relatively quiet and corotates with the Earth. Within the plasmasphere H^+ and He^+ are the principal ionic components above about 1500 km and undergo diurnal flows along the magnetic field lines as a result of changes in the F2 region (0^+) density and temperature.

The termination of the plasmasphere occurs at the plasmasphere where there is a sharp latitudinal drop in plasma density. Carpenter (1963) called the region where the density dropped from a relatively normal density to a substantially depressed one the whistler knee. Carpenter suggested that the knee moved inwards with increasing magnetic activity. The plasmapause location shows a general decrease in radius with increasing magnetic activity (Chappell et al, 1970). The plasmapause is usually situated between L=3.5 and L=6 (Carpenter,1966).

The behaviour of the topside ionosphere outside the plasmapause is very complex as a result of magnetospheric convection. Due to the interaction of the solar wind with the geomagnetic field, a large scale electric field is established within the magnetosphere. This electric field drives thermal plasma at altitudes above 150 km towards the front of the magnetosphere in regions where the field lines are closed, and towards the tail of the magnetosphere in regions where field lines are open. When the solar wind is sufficiently variable the Earth's magnetosphere is disturbed. If the disturbance is sufficiently intense it is called a magnetic storm. When a magnetic storm occurs the magnetosphere is compressed. This compression may cause explosive processes within the magnetosphere. An individual explosive process lasts typically for one to three hours, which is much shorter than the duration of a typical magnetic storm. These explosive processes are called magnetic substorms. Thus a magnetic storm is usually followed by several substorms.

Following the ideas of the theory of magnetospheric convection, it is possible to understand the behaviour of the thermal plasma in terms of motions of the magnetic field lines themselves. Thus in the initial step of the convection cycle, the dipole-like field lines from the Earth become connected to the interplanetary magnetic field, at the front of the magnetosphere. These field lines are then swept back over the polar cap into the tail of the magnetosphere where they eventually reconnect in the vicinity of the neutral sheet. During their traversal over the polar cap the field lines are open to the interplanetary medium and solar wind. Following reconnection in the tail of the magnetosphere, the field tubes migrate around the Earth at relatively low geomagnetic latitudes. As the field tubes approach the front of the magnetosphere they begin to move towards higher geomagnetic latitudes and eventually disconnect to begin the convection cycle. The behaviour of the topside ionosphere is strongly affected by the convection cycle. In the region of open field lines, H^+ and He^+ may be accelerated along the field tubes to high speeds (Banks et al., 1974, Raitt et al., 1975) resulting in a net loss of plasma from the Earth. The low H^+ and He^+ densities and dominance of O^+ to altitudes of 3000 - 5000 km at high latitudes may result from this high speed outflow of lighter ions, called the polar wind.

The magnetic and electric fields of the magnetosphere satisfy the 'freezing in' equation

$$\underline{E} + \underline{V} X \underline{B} = \underline{0}$$

or

$$\underline{V} = \frac{\underline{EXB}}{B^2}$$, since V is perpendicular to $\underline{B}$

where $\underline{V}$ is the velocity for the convective motion of the field lines. Charged particles are then thought of as being convected by the moving magnetic field.

When a magnetic storm occurs the plasmapause and magnetospheric convection region move to lower L-values, so that the mid-latitude field lines are also convected into the tail of the magnetosphere. After the storm the convection region moves to higher L-values, leaving closed field tubes with extremely low light ion concentrations which the ionosphere then attempts to refill. It has been suggested that another magnetic storm occurs before replenishment of the depleted field tubes is completed, so that the ionosphere and magnetosphere, which are usually within the closed corotating field tube region, are in a continual dynamic state.

The replenishment of H^+ ions was examined by Murphy et al. (1976). Their results suggest that it is extremely unlikely that the protonosphere is replenished before the occurrence of another magnetic storm. They found that the time required for total replenishment is well in excess of the average time between magnetic storms or substorms, and this is in agreement with the idea that the mid-latitude plasmasphere is in a continual dynamic state.

In this work we examine the time-dependent behaviour of He^+ and O^{++} in the mid-latitude plasmasphere treating He^+ and O^{++} as minor ions with O^+ and H^+ as major ions. We also examine the behaviour of O^+, H^+ and He^+ when all three ions are treated theoretically as major ions.

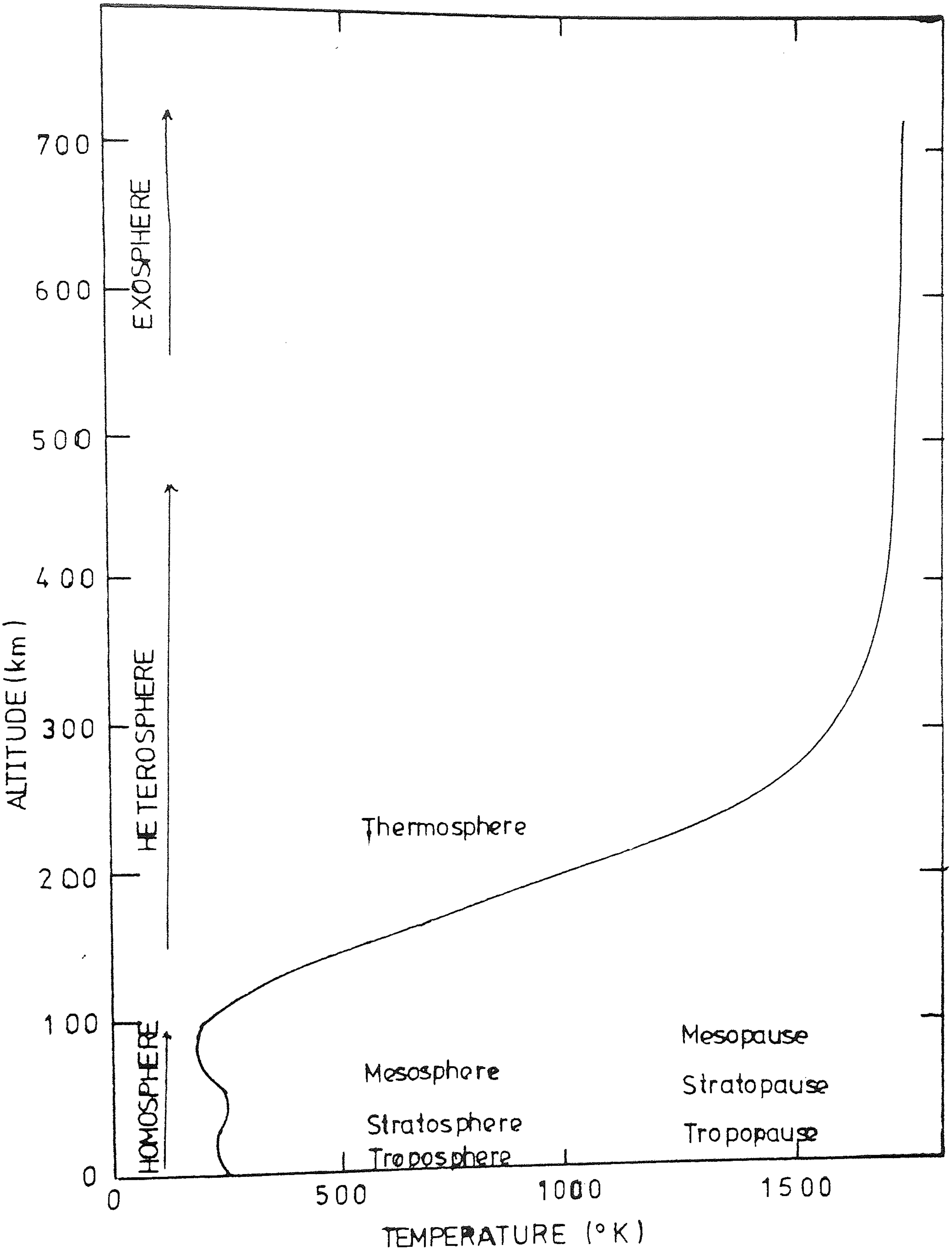

Figure 1. The regions of the neutral atmosphere with the vertical distribution of temperature in these regions.

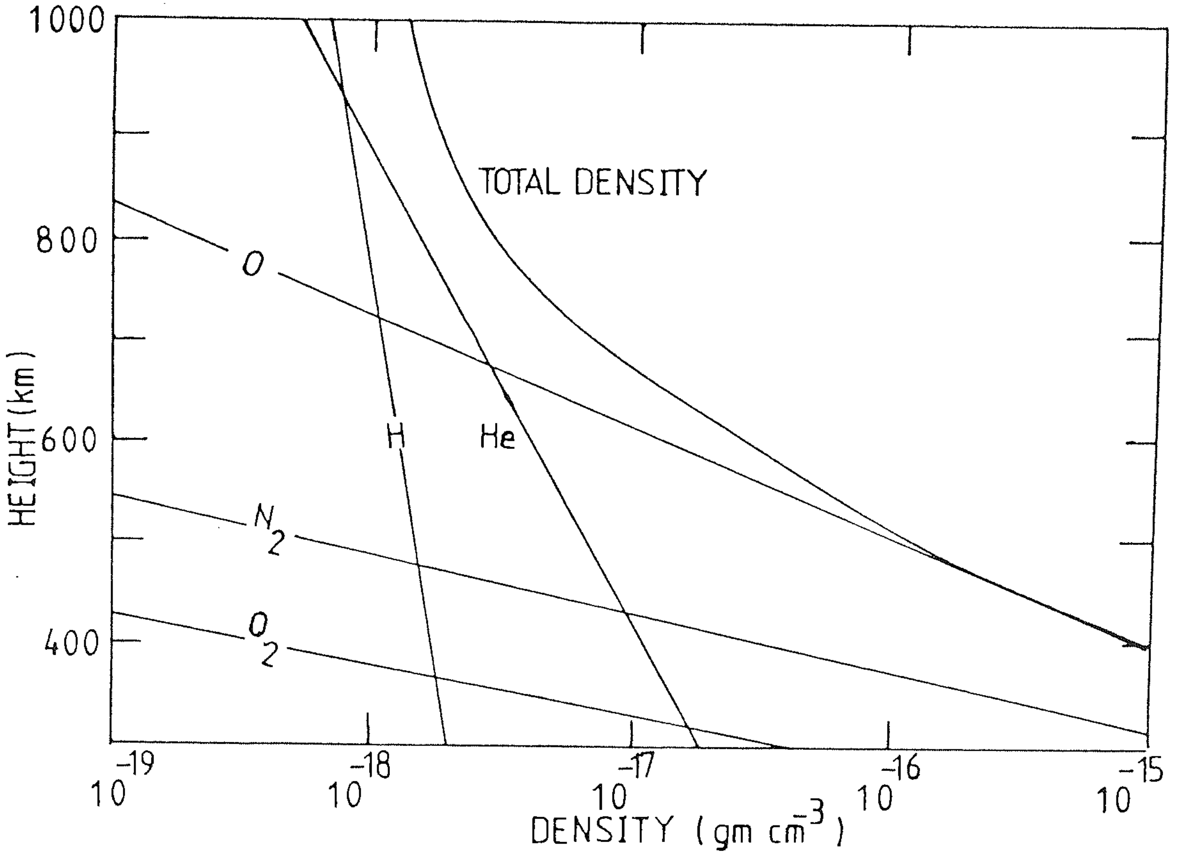

Figure 2. Approximate distribution of neutral constituents in the upper atmosphere. The symbols O, O_2, H, He and N_2 denote atomic oxygen, molecular oxygen, hydrogen, helium and nitrogen.

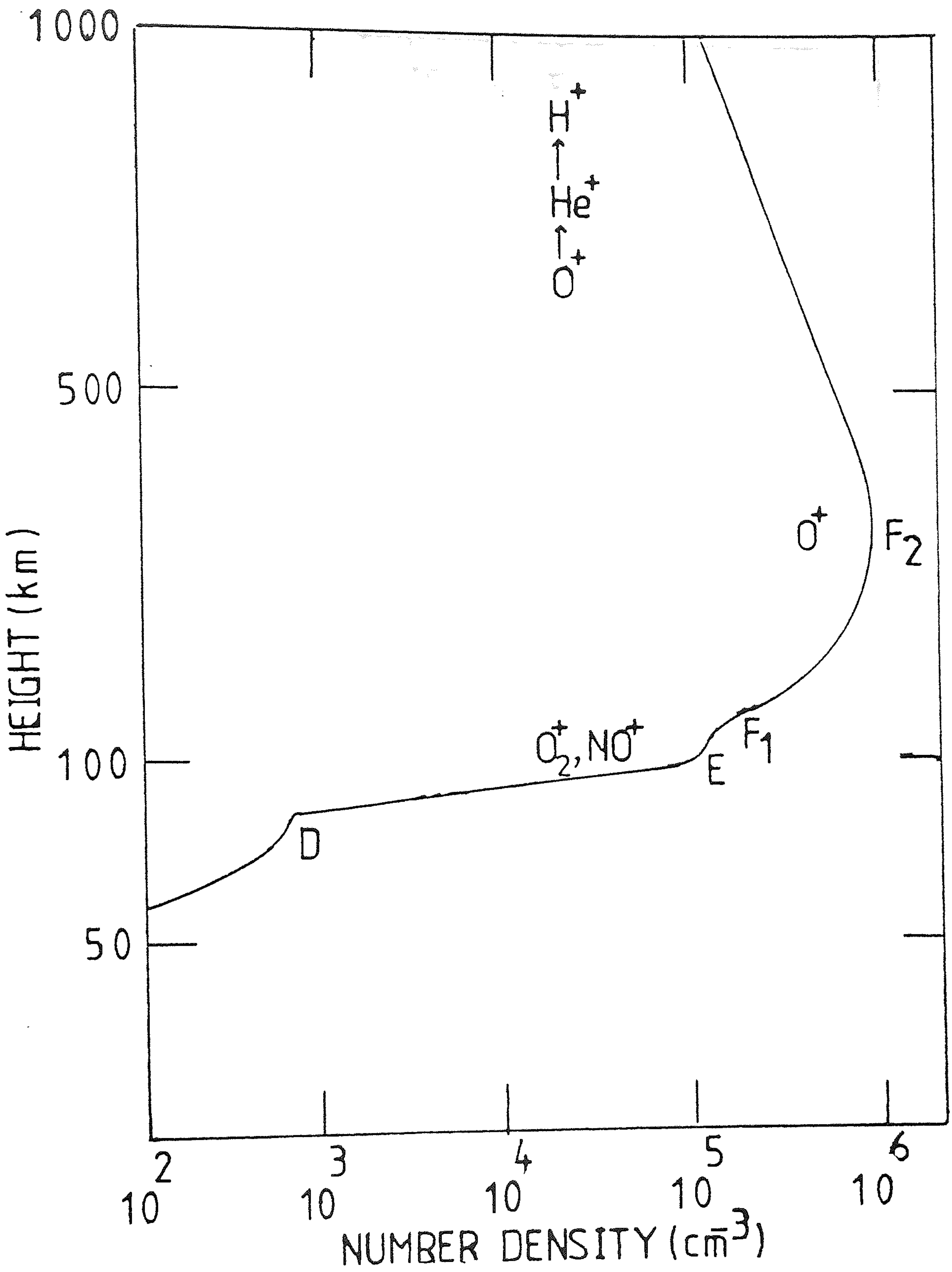

Figure 3. The regions of the ionosphere with some of the major ions indicated. The '+' superfix indicates a positively charged ion, i.e. atom or molecule less an electron. The symbol No^+ denotes a nitric oxide ion.

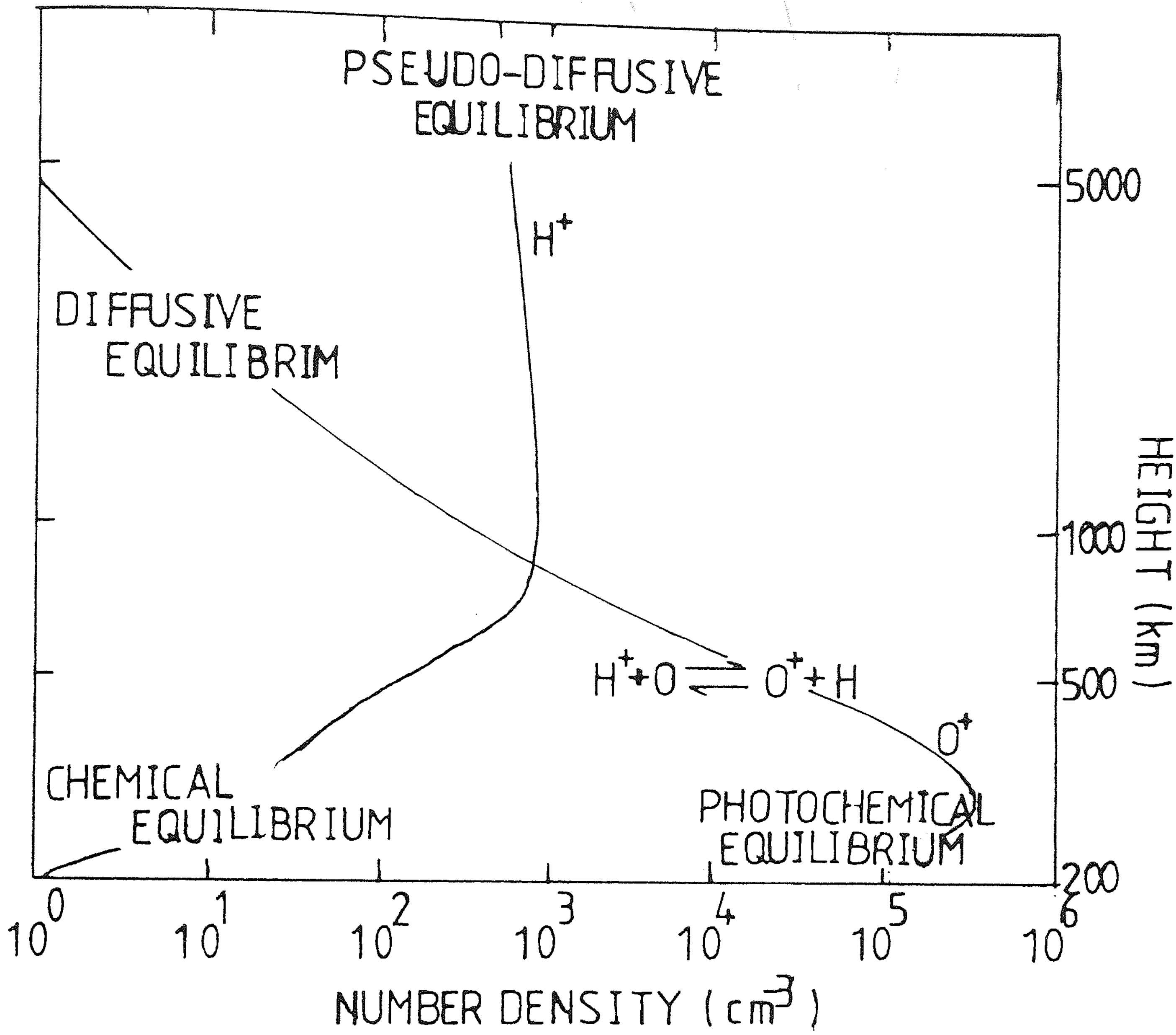

Figure 4. Typical O^+ and H^+ profiles and some of the features of O^+/H^+ behaviour.

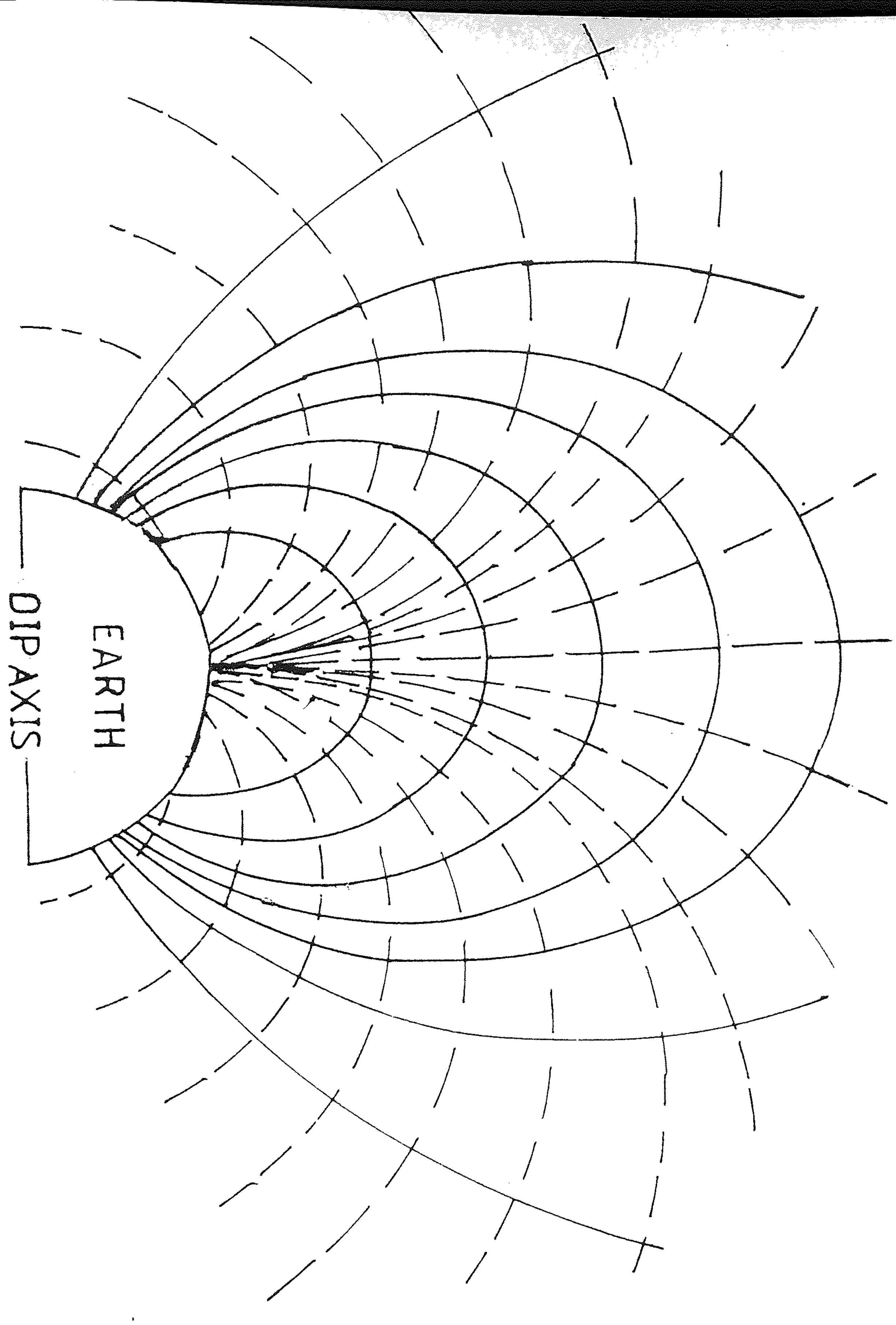

Figure 5. The dipole approximation to the Earth's magnetic field. The diagram is in a meridian plane and the full lines represent magnetic lines of force. The broken lines indicate the direction of plasma motion caused by an electro-magnetic field.

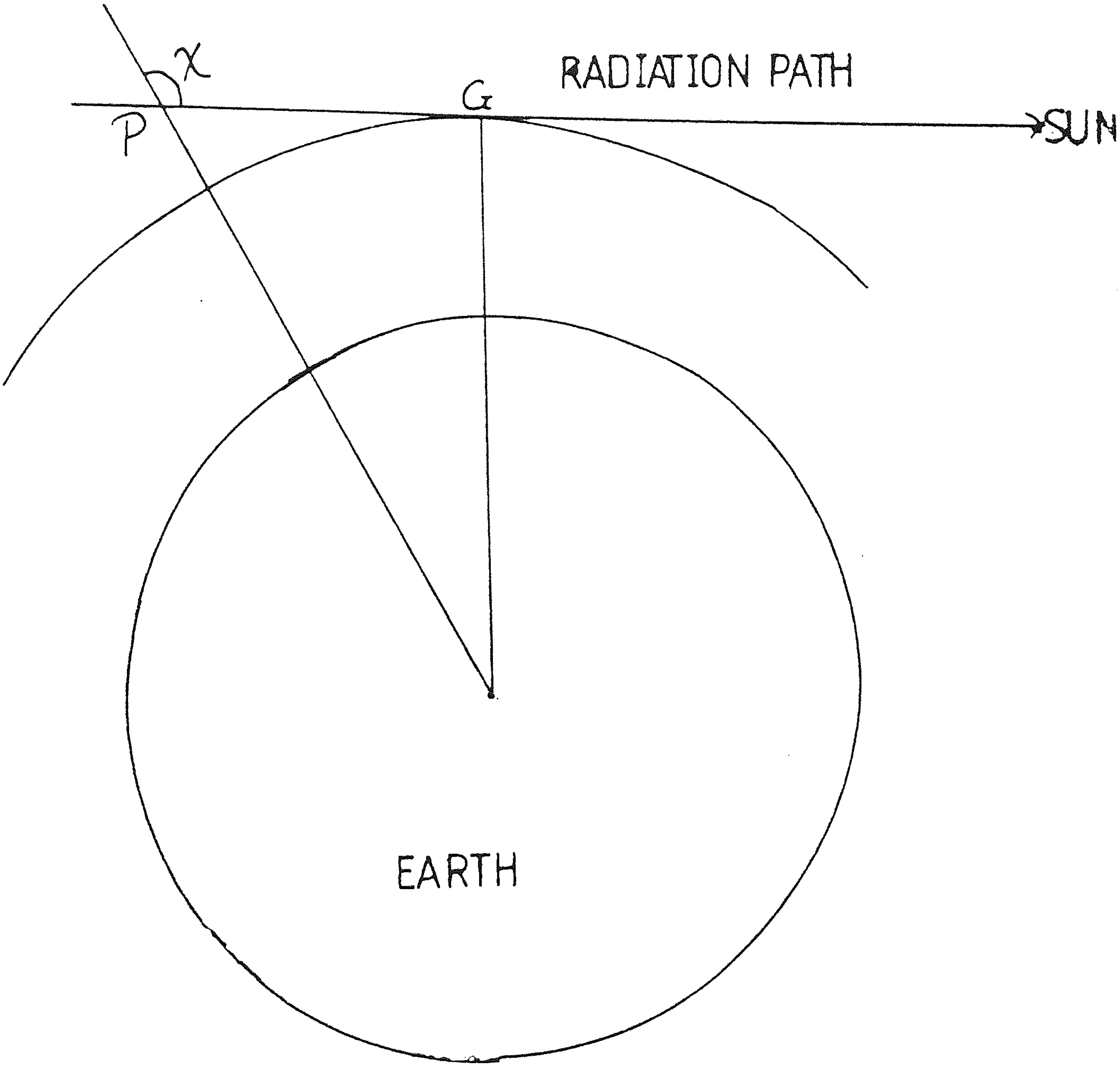

Figure 6. The radiation path (extended) from the sun to a point P is shown. s_p is the value of s at p where s is the distance along a radiation path, increasing from the sun to the point P.

II EQUATIONS

2.1 INTRODUCTION

Early studies of the topside ionosphere by Johnson (1960), Mange (1960), Kockarts and Nicolet (1963), Bauer (1966) and others, restricted attention to static nonflow models where the principal topside ions (O^+, H^+ and He^+) arranged themselves in stratified layers according to ion mass. These models of the mid-latitude topside ionosphere were extended by Walker (1967), and Schunk and Walker (1969), to include thermal diffusion effects.

With the increasing evidence of a significant ionization flow between the ionosphere and the protonosphere (Vassear and Waldteufel, 1968; Evans, 1969; Evans et al., 1970; Behnke, 1970; Evans, 1971a, 1971b; Hagen, 1972),more dynamic models were considered. These dynamic models took account of the relative flow between the interacting species (Banks et al., 1971; Mayr et al., 1972; Nagy and Banks, 1972; Moffett and Murphy, 1973; Massa et al., 1974; Murphy et al., 1976). These studies showed that ionization flow between the ionosphere and protonosphere is strong enough to affect the F-region and topside ionosphere. In all of these studies except Murphy et al.(1976), thermal diffusion effects are neglected. Later Schunk (1975) presented an alternative approach to derive a general system of transport equations for the Earth's upper atmosphere and ionosphere. This approach is based on the work of Grad (1949,1958) and

Burgers (1969). Schunk's system contains a continuity, momentum, internal energy, pressure tensor and heat flow equation for each species in a multi-constituent gas mixture. These equations are obtained via methods of statistical mechanics and are based on the assumption that macroscopically observed variables of a gas correspond to those dynamical states that are most probable. The velocity distribution function of a single particle is the density of points in a six dimensional space, called phase space, with coordinates made up of the space and velocity coordinates. Boltzmann's equation includes a term resulting from collisions. If the Boltzmann's equation is multiplied by 1, $m_s\underline{c}_s$, $\frac{1}{2}m_s c_s^2$, $m_s\underline{c}_s\underline{c}_s$ and $m_s c_s^2\underline{c}_s$ (m_s = mass and $\underline{c}_s = \underline{v}_s - \underline{u}_s$, where $\underline{v}_s$ is the velocity and $\underline{u}_s$ is the average velocity) and integrated over the velocity space, we obtain, respectively, the continuity, momentum, internal energy, pressure tensor, and heat flow equations for each species s in a gas mixture. Therefore Schunk's system provides a better description of transport for situations where the species of a gas mixture have separate flow velocities and temperatures. Also this system takes account of ordinary and thermal diffusion.

Using Schunk's general system of equations, St.-Maurice and Schunk (1977) derived diffusion and heat flow equations for the mid-latitude topside ionosphere where temperature differences are often small. Their theoretical formulation assumed that the gas mixture was composed of two major ions, electrons and a number of minor ions. In the work presented here, the behaviour of He^+ is investigated at mid-latitudes. In Chapter IV the formulation of St. Maurice and Schunk is used, and we assume that He^+ is a minor ion, with O^+ and H^+ treated as major ions. Their formulation is also used here to investigate the behaviour of O^{++} at mid-latitudes - again taking O^+ and H^+ as major ions and O^{++} as the minor ion. The equations of continuity and momentum, based on the formulation of St.-Maurice and Schunk, are presented in section 2.2.

More recently Quegan et al. (1981) have derived a system of diffusion and heat flow equations allowing for three major ions. Their formulation allows a more detailed study of the mid-latitude ionosphere in which O^+, H^+ and He^+ can all be treated as major ions. The results of this study are presented in Chapter VI. The study is carried out not only with the purpose of looking for new features in the He^+ behaviour (compared to the model treating He^+ as a minor ion) but also to re-examine H^+ behaviour with the additional influence of He^+. In the previous studies of Murphy et al. (1976), Bailey et al.(1978), Bailey et al. (1979), He^+ was not included in the calculations. The continuity and momentum equations based on the formulation of Quegan et al. are presented in section 2.3.

The numerical procedure used to solve the system of equations is described in section 2.4.

2.2 EQUATIONS - Two major ions formulation.

When St.-Maurice and Schunk (1977) applied Schunk's general system to the mid-latitude topside ionosphere, they made some simplifying assumptions. As mentioned before, they assumed a fully ionised plasma composed of two major ions, electrons and a number of minor ions, and that the species temperature and flow velocity differences are small. Those assumptions are often realistic for the mid-latitude topside ionosphere. They also neglected density and temperature gradients perpendicular to the geomagnetic field lines.

With these simplifying assumptions, the momentum equation derived in the above manner can be written as

$$\underline{\nabla} P_s - n_s m_s \underline{G} - n_s e_s \underline{E} = - n_s m_s \sum_t \nu_{st} (\underline{u}_s - \underline{u}_t) + \\ + \frac{3}{5} \sum_t \nu_{st} \frac{\mu_{st}}{kT_{st}} \left(\underline{q}_s - \frac{\rho_s}{\rho_t} \underline{q}_t \right) \tag{2.1}$$

and the heat flow equation can be written as

$$- \frac{5}{2} \frac{kP_s}{m_s} \underline{\nabla} T_s = \underline{q}_s \left[\frac{4}{5} \nu_{ss} + \sum_{t \neq s} \nu_{st} \left(D_{st}^{(1)} + \frac{3}{2} \frac{\mu_{st}}{m_s} \frac{T_s}{T_{st}} \right) \right] - \\ - \sum_{t \neq s} \nu_{st} \left(D_{st}^{(4)} + \frac{3}{2} \frac{\mu_{st}}{m_s} \cdot \frac{T_s}{T_{st}} \right) \frac{\rho_s}{\rho_t} \underline{q}_t - \\ - \frac{3}{2} P_s \sum_{t \neq s} \frac{m_t \nu_{st}}{m_s + m_t} (\underline{u}_s - \underline{u}_t) \tag{2.2}$$

The continuity equation is given by

$$\frac{\partial n_s}{\partial t} + \underline{\nabla}.(n_s \underline{u}_s) = P_s - L_s \qquad (2.3)$$

where

$$\nu_{st} = \frac{16\sqrt{\pi}}{3} \cdot \frac{m_t n_t}{m_s + m_t} \cdot \left(\frac{\mu_{st}}{2kT_{st}} \right)^{3/2} \cdot \frac{z_s^2 z_t^2}{\mu_{st}} \ln\Lambda \quad , \qquad (2.4)$$

$$D_{st}^{(1)} = (3m_s^2 + \frac{1}{10} m_s m_t - \frac{1}{5} m_t^2)/(m_s + m_t)^2 \quad , \qquad (2.5)$$

$$D_{st}^{(4)} = (\frac{6}{5} m_t^2 - \frac{3}{2} m_s m_t)/(m_s + m_t)^2 \quad , \qquad (2.6)$$

$$\mu_{st} = \frac{m_s m_t}{m_s + m_t} \quad , \qquad (2.7)$$

$$T_{st} = \frac{m_s T_s + m_t T_t}{m_s + m_t} \quad , \qquad (2.8)$$

$$\rho_s = m_s n_s \quad , \qquad (2.9)$$

$\ln\Lambda$ is the Coulomb logarithm (Burger,1969; Schunk,1975),

n_s is the number density,

m_s is the mass ,

z_s is the species charge ,

$\underline{E}$ is the electric field ,

$\underline{G}$ is the acceleration due to gravity ,

$\underline{u}_s$ is the flow velocity ,

T_s is the species temperature ,

$p_s = n_s k T_s$, is the partial pressure ,

$\underline{q}_s$ is the heat flow vector ,

P_s is the production of species s ,

L_s is the loss of species s ,

t is the time ,

k is the Boltzmann's constant ,

and the suffices s and t take the values 1,2,3 and e, which correspond to O^+, H^+, He^+ and electrons respectively.

The ion and electron densities and flow velocities are not independent, but are coupled through the requirements of charge neutrality and charge conservation. In the steady state, these requirements become

$$\sum n_s z_s = 0 \tag{2.10}$$

and

$$\sum n_s z_s \underline{u}_s = 0 \qquad (2.11)$$

provided no current flows parallel to the geomagnetic field.

In section 2.2.1 we use the St.-Maurice and Schunk (1977) formulation to derive the momentum and continuity equations with O^+ and H^+ as major ions, and in section 2.2.2 we also use their formulation to derive the momentum and continuity equations for He^+ as a minor ion. Based on the same formulation we derive the O^{++} momentum and continuity equations in section 2.2.3, treating O^{++} as a minor ion.

2.2.1 O^+ and H^+ Equations

Momentum equations.

We describe briefly how the O^+ and H^+ momentum equations are obtained in their classical form for situations where the He^+ densities are so small that He^+ does not influence the behaviour of O^+ and H^+. Further details are given by St.-Maurice and Schunk (1977). We also manipulate these equations and the continuity equations so that they are in a suitable form to be solved numerically.

Substituting s = 1,2,e respectively, in equation (2.2), we obtain three equations which can be solved to obtain explicit expressions for the heat flow vectors $\underline{q}_1$, $\underline{q}_2$ and

$\underline{q}_e$. Using these expressions for the heat flow vectors, it is possible to derive the diffusion equations in their classical form. Since electrons are more mobile than ions, the electrons establish the polarisation electrostatic field. Setting s = e in equation (2.1) and substituting for the heat flow vectors, we obtain

$$e\underline{E} = -\frac{1}{n_e}\nabla P_e - \frac{15}{8}\cdot\frac{\nu_{e1}+\nu_{e2}}{\nu'_e}\,k\nabla T_e - $$

$$- m_e\left[1 - \frac{9}{8}\,\frac{\nu_{e1}+\nu_{e2}}{\nu'_e}\right]\left[\nu_{e1}(\underline{u}_e - \underline{u}_1) + \nu_{e2}(\underline{u}_e - \underline{u}_2)\right], \tag{2.12}$$

where we have neglected $\frac{m_e}{m_1}$ and $\frac{m_e}{m_2}$ compared to terms of order one. When we substitute (2.12) in the ion momentum equations, the terms that contain relative flow will be neglected since they are of order $\left({}^{m_e}/_{m_1}\right)^{\frac{1}{2}}$ and $\left({}^{m_e}/_{m_2}\right)^{\frac{1}{2}}$ or smaller in comparison with other terms. Therefore, effectively, the polarisation electrostatic field becomes

$$e\underline{E} = -\frac{1}{n_e}\,\nabla P_e - \frac{15\sqrt{2}(n_1z_1^2+n_2z_2^2)}{8(n_1z_1+n_2z_2) + 13\sqrt{2}(n_1z_1^2+n_2z_2^2)}k\nabla T_e$$

where we have used the collision frequency expression (2.4) and the equation for charge neutrality (2.10). Using the fact that $z_1 = z_2 = 1$, where z is the ion charge number,

$$e\underline{E} = -\frac{1}{n_e}\nabla P_e - \frac{15\sqrt{2}}{8 + 13\sqrt{2}}\,k\nabla T_e \quad . \tag{2.13}$$

The second term on the right-hand side of (2.13) represents the influence of thermal diffusion.

The O^+ and H^+ diffusion equations are obtained by setting s = 1 and 2 respectively in equation (2.1), using equation (2.13) for the polarisation electrostatic field and substituting for the ion flow velocities. These diffusion equations are as follows.

The O^+ diffusion equation takes the form

$$\underline{u}_1 = \underline{u}_2 - D_1 \left[\frac{1}{n_1} \underline{\nabla} n_1 - \frac{m_1 \underline{G}}{kT_1} + \frac{1}{T_1} \underline{\nabla} T_1 + \frac{T_e/T_1}{n_e} \underline{\nabla} n_e + \frac{(1-\gamma_1)}{T_1} \underline{\nabla} T_e + \frac{n_2}{n_1+n_2} \left(\frac{\alpha_{12}}{T_1} \underline{\nabla} T_1 - \frac{\alpha^*_{12}}{T_1} \underline{\nabla} T_2 \right) \right] \quad (2.14)$$

and the H^+ diffusion equation takes the form

$$\underline{u}_2 = \underline{u}_1 - D_2 \left[\frac{1}{n_2} \underline{\nabla} n_2 - \frac{m_2 G}{kT_2} + \frac{1}{T_2} \underline{\nabla} T_2 + \frac{T_e/T_2}{n_e} \underline{\nabla} n_e + \frac{(1-\gamma_2)}{T_2} \underline{\nabla} T_e - \frac{n_1}{n_1+n_2} \left(\frac{\alpha_{12}}{T_2} \nabla T_1 - \frac{\alpha^*_{12}}{T_2} \underline{\nabla} T_2 \right) \right], \quad (2.15)$$

where D_1, D_2 are the ordinary diffusion coefficients and α_{12}, α^*_{12}, γ_1 and γ_2 are thermal diffusion coefficients. These coefficients are given by

$$D_1 = \frac{kT_1}{m_1 \nu_{12} (1-\Delta_{12})} , \quad (2.16)$$

$$D_2 = \frac{kT_2}{m_2 \nu_{21} (1-\Delta_{12})} , \tag{2.17}$$

$$\gamma_1 = \frac{15\left[\frac{n_e}{n_1} \nu_{e1} - (\nu_{e1}+\nu_{e2}) \right]}{13(\nu_{e1}+\nu_{e2}) + 8\nu_{ee}} , \tag{2.18}$$

$$\gamma_2 = \frac{-15\left[\frac{n_e}{n_2} - (\nu_{e1}+\nu_{e2}) \right]}{13(\nu_{e1}+\nu_{e2}) + 8\nu_{ee}} , \tag{2.19}$$

$$\alpha_{12} = \frac{15}{8} \cdot \frac{n_e}{n_2} \cdot \frac{\mu_{12}}{m_1} \cdot \frac{\nu_{12}\,(\nu'_2 - \nu'_{21})}{(\nu'_1 \nu'_2 - \nu'_{12}\,\nu'_{21})} , \tag{2.20}$$

$$\alpha^{\star}_{12} = \left(\frac{m_1}{m_2}\right)^2 \cdot \frac{(\nu'_1 - \nu'_{12})}{(\nu'_2 - \nu'_{21})}\,\alpha_{12} , \tag{2.21}$$

where

$$\Delta_{12} = \frac{3}{5} \cdot \frac{n_2}{n_e} \cdot \frac{\mu_{12}}{m_1} \cdot \left[\alpha_{12} + \frac{\rho_1}{\rho_2}\,\alpha^{\star}_{12} \right] , \tag{2.22}$$

$n_e = n_1 + n_2$, is the electron density

and the collision frequencies ν_{ee}, ν_{e1}, ν_{e2}, ν_{12} , ν_{21}

and the effective collisions frequencies ν'_e, ν'_1, ν'_2, ν'_{12} and ν'_{21} are given in Appendix C.

The coefficients γ_1 and γ_2 can be expressed in terms of the ion and electron parameters by using the electron collision frequencies, and the results are

$$\gamma_1 = \frac{15\sqrt{2}}{8} \cdot \frac{n_1 z_1 z_2 (z_1 - z_2)}{\frac{13\sqrt{2}}{8}(n_1 z_1^2 + n_2 z_2^2) + n_1 z_1 + n_2 z_2} , \tag{2.23}$$

and

$$\gamma_2 = \frac{-15\sqrt{2}}{8} \cdot \frac{n_2 z_1 z_2 (z_1 - z_2)}{\frac{13\sqrt{2}}{8}(n_1 z_1^2 + n_2 z_2^2) + n_1 z_1 + n_2 z_2} , \tag{2.24}$$

For 0^+ and H^+ ions $z_1 = z_2 = 1$ and therefore

$$\gamma_1 = \gamma_2 = 0 \quad .$$

In our model, we assume that the ions have a common temperature, i.e. $T_1 = T_2 = T_i$.

This leads to

$$\alpha = \alpha_{12} - \alpha_{12}^{*}$$

$$= \frac{-3}{2} \cdot \frac{(n_{12}+1)}{(m_{12}+1)} \cdot \frac{m_{12}\left(\frac{B_3}{n_{12}} - B_1\right) + \left(\frac{B_1}{n_{12}} - B_2\right)}{(B_1^2 - B_2 \times B_3)} \tag{2.25}$$

where

$$B_1 = 0.149481 \quad ,$$

$$B_2 = 1.25052 + 0.5831/n_{12} \quad , \quad B_3 = 2.7505 + 2.3324n_{12}$$

$$m_{12} = \frac{m_1}{m_2} \quad , \quad n_{12} = \frac{n_1}{n_2} \quad .$$

This agrees with the thermal diffusion coefficient given by Schunk and Walker (1969).

Taking the component of equations (2.14) and (2.15) along the field line we get

$$u_1 = u_2 - D_1\left[\frac{1}{n_1}\frac{\partial n_1}{\partial s} + \frac{m_1}{kT_i} g \sin I + \frac{1}{T_i}\frac{\partial}{\partial s}(T_i+T_e) + \frac{T_e/T_i}{n_e}\frac{\partial}{\partial s}(n_1+n_2) + \frac{n_2}{n_1+n_2}\alpha\frac{\partial T_i}{\partial s}\right] + \nu_{10}\, u \cos I \qquad (2.26)$$

and

$$u_2 = u_1 - D_2\left[\frac{1}{n_2}\frac{\partial n_2}{\partial s} + \frac{m_2}{kT_i} g \sin I + \frac{1}{T_i}\frac{\partial}{\partial s}(T_i+T_e) + \frac{T_e/T_i}{n_e}\frac{\partial}{\partial s}(n_1+n_2) - \frac{n_1}{n_1+n_2}\alpha\frac{\partial T_i}{\partial s}\right] + \nu_{20}\, u \cos I \qquad (2.27)$$

where s is a coordinate along the field line, I is the magnetic dip angle. The last term on the right-hand side of equations (2.26) and (2.27) is due to neutral collisions and u is the neutral wind speed. We have used the relations

$$P_1 = n_1 kT_i \;, \qquad P_2 = n_2 kT_i \quad \text{and } P_e = n_e kT_e$$

to obtain equations (2.26) and (2.27).

It easily follows from the definition of collision frequency that

$$n_1 m_1 \nu_{12} = n_2 m_2 \nu_{21} \quad .$$

Noting also that

$$\phi_1 = n_1 u_1 \quad \text{and} \quad \phi_2 = n_2 u_2$$

the O^+ momentum equation can be put in the form

$$\begin{aligned}
\phi_1 (\nu_{12}(1-\Delta_{12}) + \nu_{10}) = & - \frac{k}{m_1}\left(T_i + \frac{n_1}{n_e} T_e \right) \frac{\partial n_1}{\partial s} \\
& - n_1 \left[\frac{k}{m_1} \left(\frac{\partial}{\partial s}(T_e + T_i) + \frac{T_e}{n_e} \frac{\partial n_2}{\partial s} \right.\right. \\
& \left. + \frac{n_2}{n_e} \alpha \frac{\partial T_i}{\partial s} \right) + g \sin I \\
& \left. - \nu_{10} u \cos I \right] \\
& + \frac{m_2}{m_1} \phi_2 \nu_{21} (1-\Delta_{12}) \qquad (2.28)
\end{aligned}$$

and the H^+ momentum equation becomes,

$$\begin{aligned}\frac{\partial}{\partial s}\log(n_2) = \Bigg\{ -\Bigg[g\sin I &+ \frac{k}{m_2}\left(\frac{\partial}{\partial s}(T_i + T_e) + \frac{T_e}{n_e}\frac{\partial n_1}{\partial s}\right. \\ &\left. - \frac{n_1}{n_e}\,\alpha\,\frac{\partial T_i}{\partial s}\right) - \nu_{20}\, u\cos I \Bigg] \\ &- \frac{\phi_2}{n_2}\left(\nu_{20} + \nu_{21}\,(1-\Delta_{12}) + \frac{m_1}{m_2}\,\nu_{12}\,(1-\Delta_{12})\right) \\ &+ C\,\frac{m_1}{m_2}\,\frac{\nu_{12}\,(1-\Delta_{12})}{n_2}\Bigg\} \Bigg/ \left(\frac{k}{m_2}\left(T_i + \frac{n_2}{n_e}\,T_e\right)\right)\end{aligned} \tag{2.29}$$

where $C = \phi_1 + \phi_2$ (Mayr, 1968).

To take account of the Earth's rotation, we must include the centrifugal force. The centrifugal acceleration of a particle is $\underline{\Omega}X(\underline{\Omega}X\underline{R})$, where $\underline{\Omega}$ is the angular velocity of the Earth and $\underline{R}$ is the shortest distance of the particle from the geographic axis. Note that this assumes that the atmosphere is rotating with the same speed as the Earth. It can be shown that the component of the acceleration along a field line is

$$\Omega^2 r\sin\theta\cos(\theta - I)$$

where θ denotes colatitude and r is the distance from the centre of the Earth. To take account of the centrifugal force we must include

$$n_1 \Omega^2 r \sin\theta \cos(\theta - I)$$

and

$$\Omega^2 r \sin\theta \cos(\theta - I)$$

in equations (2.28) and (2.29) respectively.

The Continuity Equations:

The 0^+ continuity equation takes the form

$$\frac{\partial n_1}{\partial t} + \nabla.(n_1 \underline{u}_1) = P_1 - L_1 \quad , \qquad (2.30)$$

where P_1 ia 0^+ production and L_1 is 0^+ loss. As mentioned before, in the magnetosphere it is generally assumed that in the absence of external electric fields the charged particle flow is field-aligned. The field aligned velocity may be expressed in the form

$$\underline{u}_1 = \frac{\underline{B} u_1}{|B|}$$

where $B = |\underline{B}|$. It follows that

$$\mathrm{div}(n_1 \underline{u}_1) = \frac{n_1 u_1}{B} \mathrm{div}(\underline{B}) + \underline{B}.\underline{\nabla}\left(\frac{n_1 u_1}{B} \right) .$$

Further, since $\mathrm{div}(\underline{B}) = 0$, then

$$\mathrm{div}(n_1\underline{u}_1) = \underline{B}.\nabla\left(\frac{n_1 u_1}{B}\right)$$

$$= B\frac{\partial}{\partial s}\left(\frac{\phi_1}{B}\right) \qquad (2.31)$$

and the 0^+ continuity equation can be written as

$$\frac{\partial n_1}{\partial t} = P_1 - L_1 - B\frac{\partial}{\partial s}\left(\frac{\phi_1}{B}\right) . \qquad (2.32)$$

We now substitute equation (2.28) into equation (2.32), and split the term $P_1 - L_1$ into two parts, one of which is proportional to the 0^+ number density, n_1, and one which is not proportional to n_1. The functions α_1 and α_2 are thus defined by

$$\alpha_1 n_1 + \alpha_2 = P_1 - L_1 \qquad (2.32')$$

The forms of α_1 and α_2 will be given later on, when we consider production and loss processes. The equation resulting from the substitution can be written as

$$\nu_1\frac{\partial n_1}{\partial t} = D_0\frac{\partial^2 n_1}{\partial s^2} + D_1\frac{\partial n_1}{\partial s} + D_2 n_1 + D_3 \qquad (2.33)$$

where

$$\nu_1 = \nu_{10} + \nu_{12}(1-\Delta_{12}) \quad , \tag{2.34a}$$

$$D_0 = A \quad , \tag{2.34b}$$

$$D_1 = \frac{\partial A}{\partial s} - A\frac{\partial}{\partial s}(\log \nu_1 B) + E + g\sin I \quad , \tag{2.34c}$$

$$D_2 = \frac{\partial E}{\partial s} + \frac{\partial}{\partial s}(g \sin I) - (E+g\sin I)\frac{\partial}{\partial s}(\log \nu_1 B) - \nu_1\alpha_1 \quad , \tag{2.34d}$$

$$D_3 = \nu_1\alpha_2 \tag{2.34e}$$

with

$$A = \frac{k}{m_1}\left(T_i + \frac{n_1}{n_e} T_e \right)$$

$$E = \frac{k}{m_1}\left(\frac{\partial}{\partial s}(T_e+T_i) + \frac{T_e}{n_e}\frac{\partial n_2}{\partial s} \right) - s_{12}\phi_2 - \nu_{10}\, u\cos I$$

and

$$s_{12} = \frac{\nu_{12}}{n_2}(1-\Delta_{12}) \quad .$$

The H^+ continuity equation can be written as

$$\frac{\partial n_2}{\partial t} + B\frac{\partial}{\partial s}\left(\frac{\phi_2}{B}\right) = P_2 - L_2 \tag{2.35}$$

where P_2 and L_2 are the H^+ production and loss respectively. By integrating equation (2.35), the following form is obtained

$$\left[\frac{\phi_2}{B}\right]_s^{s_E} = \int_s^{s_E} \frac{1}{B}\left(P_2 - L_2 - \frac{\partial n_2}{\partial t}\right) ds. \qquad (2.36)$$

In this equation the upper limit, s_E, denotes the equatorial value of the arc length, s, along a field line. Assuming a zero flux across the equator (i.e. $\phi_2(s_E) = 0$), gives

$$\phi_2(s,t) = -B(s)\int_s^{s_E} \frac{1}{B(s)}\left(P_2 - L_2 - \frac{\partial n_2}{\partial t}\right) ds \qquad (2.37)$$

Similarly, the O^+ continuity equation (2.32) can be integrated to give

$$\phi_1(s,t) = -B(s)\int_s^{s_E} \frac{1}{B(s)}\left(P_1 - L_1 - \frac{\partial n_1}{\partial t}\right) ds \qquad (2.38)$$

and the function C(s,t) is given by

$$C(s,t) = -B(s)\int_s^{s_E} \frac{1}{B(s)}\left(P_1 + P_2 - L_1 - L_2 - \frac{\partial n_1}{\partial t} - \frac{\partial n_2}{\partial t}\right) ds \qquad (2.38')$$

2.2.2 He^+ EQUATIONS

We consider a fully ionized plasma composed of two major ions, O^+ and H^+, electrons and a minor ion, namely He^+. Under these circumstances the He^+ momentum equation, derived by St.-Maurice and Schunk, can be expressed in the form

$$\underline{u}_3 = h_{31}\,\underline{u}_1 - h_{32}\,\underline{u}_2 - D_3\left[\frac{1}{n_3}\underline{\nabla} n_3 - \frac{m_3\underline{G}}{kT_3} + \frac{1}{T_3}\underline{\nabla} T_3 + \frac{T_e}{T_3 n_e}\underline{\nabla} n_e + \frac{(z_3-\gamma_3)}{T_3}\underline{\nabla} T_e - \frac{1}{T_3}\left(B_3\underline{\nabla} T_3 + \beta_1\underline{\nabla} T_1 + \beta_2\underline{\nabla} T_2\right)\right] \tag{2.39}$$

where the ordinary (D_3) and thermal ($\beta_1, \beta_2, \beta_3$ and γ_3) diffusion coefficients are given by

$$D_3 = \frac{kT_3/m_3}{\nu_{31}(1-\Delta_{31})+\nu_{32}(1-\Delta_{32})} , \tag{2.40}$$

$$\beta_s = \frac{15}{8}\cdot\frac{m_3/m_s}{1-\xi}\sum_{t=1,2}\frac{\mu_{3t}}{m_s}\cdot\cdot\frac{\nu_{3t}}{\nu'_s}\,\frac{T_s}{T_{st}}\,\gamma_{st} ,$$

$$(s = 1,2 \text{ and } 3) \tag{2.41}$$

$$\text{and } \gamma_3 = \frac{15\left[\frac{n_e}{n_3}\nu_{e3} - z_3(\nu_{e1}+\nu_{e2})\right]}{13(\nu_{e1}+\nu_{e2}) + 8\nu_{ee}} . \tag{2.42}$$

Also

$$\Delta_{31} = \frac{9}{8}\,\frac{\mu_{31}}{m_3}\left[\frac{\mu_{31}}{m_3}\cdot\frac{\nu_{31}}{\nu'_3}\,\frac{T_3}{T_{31}} + \frac{\mu_{32}}{m_3}\cdot\frac{\nu_{32}}{\nu'_3}\cdot\frac{T_3}{T_{32}}\right], \tag{2.43}$$

$$h_{31} = \frac{\nu_{31}(1-\Delta_{31}) - R_{12} + R_{21}}{\nu_{31}(1-\Delta_{31}) + \nu_{32}(1-\Delta_{32})} , \qquad (2.44)$$

$$R_{12} = \frac{9}{8} \frac{\mu_{12}}{m_1^2} \cdot \frac{\nu_{12}}{\nu_1'} \cdot \frac{1}{1-\xi} \left[\mu_{31} \nu_{31} Y_{11} + \mu_{32} \nu_{32} Y_{22} \right] , \qquad (2.45)$$

$$\xi = \frac{\nu_{12}' \nu_{21}'}{\nu_1' \nu_2'} \qquad (2.46)$$

The quantities h_{32}, Δ_{32} and R_{21} can be obtained from the last equations by interchanging the subscripts 1 and 2. Also

$$Y_{11} = 1 - \frac{\nu_{31}'}{\nu_3'} - \frac{\nu_{21}'}{\nu_2'} \cdot \frac{\nu_{32}'}{\nu_3'} , \qquad (2.47)$$

$$Y_{12} = Y_{11} - 1 + \frac{\nu_{21}'}{\nu_2'} , \qquad (2.48)$$

$$Y_{31} = Y_{32} = -(1-\xi) , \qquad (2.49)$$

Y_{22} and Y_{21} can be obtained by interchanging the subscripts 1 and 2.

Equation (2.39) has been derived from the momentum and heat flow equations (2.1) and (2.2) with $s = 3$ to correspond to He^+. Terms of order $(m_e/m_t)^{\frac{1}{2}}$ $(t=1,2,3)$ are neglected and it is assumed that

$$\frac{n_3}{n_e} << 1$$

since He^+ is being treated as a minor ion. Small ion temperature differences are also assumed in deriving equation (2.39). In fact, in our model we assume that the ions have a common temperature (i.e. $T_1=T_2=T_3=T_i$) and equation (2.39) simplifies further.

Electron-ion and electron-electron interactions influence the thermal diffusion coefficient γ_3. The coefficient γ_3 can be expressed in terms of the ion and electron parameters by using the electron collision frequencies and the result is

$$\gamma_3 = \frac{15\sqrt{2}}{8} \quad \frac{z_3^2(n_1z_1+n_2z_2)-z_3(n_1z_1^2+n_2z_2^2)}{\frac{13\sqrt{2}}{8}(n_1z_1^2+n_2z_2^2)+n_1z_1+n_2z_2} \tag{2.50}$$

and since all the three ions have the same charge ($z_1=z_2=z_3=1$), then

$$\gamma_3 = 0.$$

When the ions have a common temperature, T_i, the thermal diffusion term in equation (2.39) becomes

$$-\frac{1}{T_i}(\beta_1+\beta_2+\beta_3)\nabla T_i$$

Furthermore, $\beta_1+\beta_2+\beta_3$ reduces to the thermal diffusion coefficient β given by Schunk and Walker (1969) and is given by

$$\beta = \frac{3}{2}\left[-1. + 2.7\left(\frac{m_{13}}{1+m_{13}}\,Q_1 + \frac{m_{23}}{1+m_{23}}\,Q_2\right)\right]\left[\frac{m_{13}\,Y+m_{23}}{R_{13}\,Y+R_{23}}\right] - \frac{3}{2}(Q_1+Q_2) \qquad (2.51)$$

where

$$Q_1 = \frac{(1+m_{12})^{\frac{1}{2}}}{(1+m_{13})^{\frac{1}{2}}} \cdot \frac{(n_{12}\,B_2 - B_1)}{(B_1^2 - B_2\,B_3)} \quad , \qquad (2.52)$$

$$Q_2 = \left(\frac{1+m_{12}}{m_{12}}\right)^{\frac{1}{2}} \cdot \frac{1}{(1+m_{23})^{3/2}} \cdot \frac{(B_3/n_{12} - B_1)}{(B_1^2 - B_2\,B_3)} \qquad (2.53)$$

$$Y = (m_{12})^{\frac{1}{2}} \cdot \left(\frac{1+m_{23}}{1+m_{13}}\right)^{3/2} n_{12} \quad , \qquad (2.54)$$

$$R_{13} = \frac{13m_{13}^2 + 16m_{13} + 30}{10(1+m_{13})} \quad , \qquad (2.55)$$

$$R_{23} = \frac{13m_{23}^2 + 16m_{23} + 30}{10(1+m_{23})} \quad , \qquad (2.56)$$

$$m_{st} = \frac{m_s}{m_t} \quad (s \text{ and } t = 1,2,3) \quad , \tag{2.57}$$

$$n_{12} = \frac{n_1}{n_2} \quad , \tag{2.58}$$

and the other variables are as defined before.

Now take the component of equation (2.39) along the field line and use the definition $\phi_3 = n_3 u_3$ and after rearranging the result, the He^+ momentum equation takes the form

$$\begin{aligned} \frac{\partial}{\partial s} \log(n_3) = \Bigg\{ - \Bigg[g \sin I + \frac{k}{m_3} \Bigg(& \frac{\partial}{\partial s}(T_i + T_e) + \frac{T_e}{n_e} \frac{\partial}{\partial s}(n_1 + n_2) \\ & - \beta \frac{\partial}{\partial s} T_i \Bigg) - \nu_{30} \, u \cos I + \\ & + \Big(\nu_{30} + \eta_{31} + \eta_{32} \Big) \frac{\phi_3}{n_3} \Bigg] + \\ & + \frac{\eta_{31}}{n_1} \phi_1 + \frac{\eta_{32}}{n_2} \phi_2 \Bigg\} \Bigg/ \left(\frac{kT_i}{m_3} \right) \end{aligned} \tag{2.59}$$

where

$$\eta_{31} = \nu_{31}(1 - \Delta_{31}) - R_{12} + R_{21} \quad , \tag{2.60}$$

$$\eta_{32} = \nu_{32}(1-\Delta_{32}) - R_{21} + R_{12} \quad . \tag{2.61}$$

The He^+ continuity equation can be written in the form

$$\frac{\partial n_3}{\partial t} + B\frac{\partial}{\partial s}\left(\frac{\phi_3}{B}\right) = P_3 - L_3 \quad , \tag{2.62}$$

where

P_3 = He^+ production ,

L_3 = He^+ loss .

Integrating equation (2.62) and assuming a zero flux across the equator (i.e. $\phi_3(s_E) = 0$) we get,

$$\phi_3(s) = -B(s)\int_s^{s_E} \frac{1}{B(s)}\left(P_3 - L_3 - \frac{\partial n_3}{\partial t}\right) ds \quad , \tag{2.63}$$

where we have used the assumption that the He^+ ions flow parallel to the field line to put the He^+ continuity equation in the form (2.62).

2.2.3 O^{++} EQUATIONS

In this section we consider a fully-ionized plasma composed of two major ions O^+ and H^+, electrons and a minor ion, namely O^{++}. Assuming that the species temperature and flow velocity differences are small and neglecting density and temperature gradients perpendicular to geomagnetic field lines, the O^{++} momentum equation can be derived in the same way as we derived the He^+ momentum equation. The resulting equation can be put in the form

$$\begin{aligned}\frac{\partial}{\partial s}\log(n_4) = \Bigg\{ -\Bigg[g\sin I + \frac{k}{m_4}\Bigg(\frac{\partial T_4}{\partial s} + 0.392\,\frac{\partial T_e}{\partial s} + \frac{T_e}{n_e}\frac{\partial n_e}{\partial s} \; - \\ -\Bigg(\beta_4\frac{\partial T_4}{\partial s} + \beta_1\frac{\partial T_1}{\partial s} + \beta_2\frac{\partial T_2}{\partial s}\Bigg) + \Bigg[\nu_{41}(1-\Delta_{41}) \\ + \nu_{42}(1-\Delta_{42})\Bigg]\frac{\phi_4}{n_4}\Bigg] + s_{41}(1-\Delta_{41})\phi_1 \\ + s_{42}(1-\Delta_{42})\phi_2\Bigg\} \Bigg/ \Bigg(\frac{kT_4}{m_4}\Bigg) \quad \ldots\ldots \qquad (2.64)\end{aligned}$$

where the suffix 4 is attached to variables associated with the O^{++} ion. Also

$$s_{41} = \nu_{41}/n_1 \quad ,$$

$$s_{42} = \nu_{42}/n_2 \quad ,$$

$$n_e = n_1 + n_2 = \text{electron density} \; ,$$

the thermal diffusion coefficients β_1, β_2 and β_4 are given by equation (2.41) with s = 1,2 and 4, and the other variables are as defined before. The collision frequencies are given in Appendix C.

In our model we assume that the ions have a common temperature, T_i, this will enable us to simplify the last equation. The thermal diffusion coefficients β_1, β_2 and β_4 reduce to the thermal diffusion coefficient, β, given by Schunk and Walker (1969):

$$\beta = \frac{3}{2}\left[-1. + 2.7\left(\frac{m_{14}}{1+m_{14}}Q_1 + \frac{m_{24}}{1+m_{24}}Q_2\right)\right]\left[\frac{m_{14}Y + m_{24}}{R_{14}Y + R_{24}}\right] - $$

$$- \frac{3}{2}(Q_1 + Q_2) \quad ,$$

where

$$m_{14} = \frac{m_1}{m_4} \quad , \qquad m_{24} = \frac{m_2}{m_4} \quad ,$$

$$Q_1 = \frac{1}{z_{24}^2} \cdot \frac{(1+m_{12})^{\frac{1}{2}}}{(1+m_{14})^{3/2}} \cdot \left(\frac{n_{12}B_2 - B_1}{B_1^2 - B_2 B_3}\right)$$

$$= 5.83095\left(\frac{n_{12}B_2 - B_1}{B_1^2 - B_2 B_3}\right) \quad ,$$

$$Q_2 = \frac{1}{z_{14}^2}\frac{(1+m_{12})^{\frac{1}{2}}}{(1+m_{24})^{3/2}} \cdot \frac{1}{m_{12}^{\frac{1}{2}}} \cdot \left(\frac{B_3/n_{12} - B_1}{B_1^2 - B_2 B_3}\right)$$

$$= 3.76471\left(\frac{B_3/n_{12} - B_1}{B_1^2 - B_2 B_3}\right) \quad ,$$

B_1, B_2 and B_3 are as given before

with $$z_{12} = \frac{z_1}{z_2} \quad , \qquad z_{24} = \frac{z_2}{z_4} \quad ,$$

$$z_1 = z_2 = 1 \text{ and } z_4 = 2 \ ,$$

$$Y = n_{12} \, z_{12}^2 \sqrt{m}_{12} \left(\frac{1+m_{24}}{1+m_{14}} \right)^{3/2}$$

$$= 1.54885 \, n_{12} \quad ,$$

$$R_{14} = \frac{13m_{14}^2 + 16m_{14} + 30}{10(1+m_{14})}$$

$$= 2.9500 \quad ,$$

and

$$R_{24} = \frac{13m_{24}^2 + 16m_{24} + 30}{10(1+m_{24})}$$

$$= 2.92243.$$

The O^{++} continuity equation can be written in the same way as we have written the previous continuity equations, and it takes the form

$$\frac{\partial n_4}{\partial t} + B \frac{\partial}{\partial s} \left(\frac{\phi_4}{B} \right) = P_4 - L_4 \qquad (2.65)$$

where

P_4 is O^{++} production

L_4 is O^{++} loss.

By integrating this equation and assuming a zero flux across the equator, we get

$$\phi_4(s) = -B(s)\int_s^{s_E} \frac{1}{B(s)}\left(P_4 - L_4 - \frac{\partial n_4}{\partial t}\right)ds \qquad (2.65')$$

2.3 EQUATIONS - The Three Ions Forumlation

In the previous sections we represented our equations with the assumption that He^+ was a minor ion, which means its existence would not affect the two major ions, O^+ and H^+. In this section we will follow the work of Quegan et al. (1981), who extended the work of St.-Maurice and Schunk (1977) and Conrad and Schunk (1979) to allow for three major ions. The extended equations will be used in Chapter VI. to examine the effect of He^+ as a major ion on the other two major ions. With the new formulation, the diffusion equation for constituent i is given by:

$$\underline{u}_i = h_{ij}\underline{u}_j + h_{ik}\underline{u}_k - D_i\left[\frac{1}{n_i}\underline{\nabla} n_i + \frac{1}{T_i}\underline{\nabla} T_i - \frac{m_i\underline{g}}{kT_i} + \right.$$

$$\left. + \frac{z_i T_e}{T_i}\frac{\underline{\nabla} n_e}{n_e} + \frac{(z_i - \gamma_i)}{T_i}\underline{\nabla} T_e + \right.$$

$$+ \frac{\nabla T_i}{T_i} (\beta_i - \beta^*_{ij} - \beta^*_{ik}) \Bigg] \tag{2.66}$$

where the thermal diffusion coefficients, β_s and β^*_{st} are given by

$$\beta_s = \frac{-15}{8(1-\xi)} \cdot \frac{kT_s}{m_s \nu'_s} Y_{stu} \quad (Y_{stu} = Y_{sut}) , \tag{2.67}$$

$$\beta^*_{st} = \frac{-15}{8(1-\xi)} \cdot \frac{m_s}{m_t} \cdot \frac{kT_t}{m_t \nu'_t} z_{stu} , \tag{2.68}$$

the ordinary diffusion coefficient, D_s, is given by

$$D_s = \frac{kT_s}{m_s} \cdot \frac{1}{\nu_{st}(1-\Delta_{st}) + \nu_{su}(1-\Delta_{su})} , \tag{2.69}$$

and the drag coefficient, h_{st} is given by

$$h_{st} = \frac{\nu_{st}(1-\Delta_{st}) - R_{stu} + R_{sut}}{\nu_{st}(1-\Delta_{st}) + \nu_{su}(1-\Delta_{su})} \quad (h_{st} + h_{su} = 1). \tag{2.70}$$

with

$$\xi = \xi_{jk} + \xi_{ki} + \xi_{ij} + \frac{\nu'_{ik}\nu'_{ki}\nu'_{ij}}{\nu'_i \nu'_j \nu'_k} + \frac{\nu'_{kj}\nu'_{ji}\nu'_{ik}}{\nu'_i \nu'_j \nu'_k} ,$$

$$\xi_{st} = \frac{\nu'_{st}\nu'_{ts}}{\nu'_s \nu'_t} = \xi_{ts} ,$$

$$Y_{stu} = Q_{st}W_{stu} + Q_{su}W_{ust} = Y_{sut} \quad ,$$

$$Q_{st} = \frac{\nu_{st}\mu_{st}}{kT_i} \quad ,$$

$$W_{stu} = \nu_{stu} + \xi_{su} - 1 \quad ,$$

$$\nu_{stu} = \frac{\nu'_{st}}{\nu'_s} + \frac{\nu'_{su}\nu'_{ut}}{\nu'_s\nu'_u} \quad ,$$

$$z_{stu} = Q_{st}W_{stu} + Q_{su}X_{stu} \quad ,$$

$$X_{stu} = \nu_{stu} - \nu_{uts} = -X_{uts} \quad ,$$

$$\Delta_{st} = \frac{3}{5}\,\frac{\mu_{st}}{m_s}\left(\beta_s + \frac{\rho_s}{\rho_t}\,\beta^*_{st}\right) \quad ,$$

$$\rho_s = m_s n_s \quad ,$$

$$\mu_{st} = \frac{m_s m_t}{m_s + m_t} \quad ,$$

$$R_{stu} = \frac{3}{5} \cdot \frac{\mu_{tu}}{m_s} \cdot \nu_{tu}\beta^*_{st} \quad .$$

The thermal diffusion coefficient γ_i can be written, using charge neutrality, as

$$\gamma_s = \frac{15 z_s [n_t z_t (z_s - z_t) + n_u z_u (z_s - z_u)]}{13(n_s z_s^2 + n_t z_t^2 + n_u z_u^2) + \frac{8}{\sqrt{2}}(n_s z_s + n_t z_t + n_u z_u)} \quad . \quad (2.71)$$

For singly charged ions $z_i = 1$, and since O^+, H^+ and He^+ have the same charge, then $\gamma_s = 0$. In equation (2.66) we have assumed that ions have a common temperature.

Now we can write equation (2.66) in the form

$$(\eta_{ij} + \eta_{ik})\underline{u}_i = (\eta_{ij} - R_{ijk} + R_{ikj})\underline{u}_j + (\eta_{ik} - R_{ikj} + R_{ijk})\underline{u}_k + \frac{kT_i}{m_i}\underline{A} \qquad (2.72)$$

with

$$\eta_{st} = \nu_{st}(1 - \Delta_{st}) \quad ,$$

and

$$\underline{A} = \left(\frac{1}{n_i}\underline{\nabla} n_i + \frac{1}{T_i}\underline{\nabla} T_i - \frac{m_i \underline{G}}{kT_i} + \frac{T_e}{T_i}\frac{\underline{\nabla} n_e}{n_e} + \frac{\underline{\nabla} T_e}{T_i} + \frac{\underline{\nabla} T_i}{T_i}(\beta_i - \beta^*_{ij} - \beta^*_{ik}) \right) .$$

O^+ EQUATIONS

Putting i, j and k equal to 1, 2 and 3 respectively, the O^+ momentum equation can be written as

$$(\eta_{12} + \eta_{13})\underline{u}_1 = \eta_{12}\,\underline{u}_2 + \eta_{13}\,\underline{u}_3 + (R_{123} - R_{132})(\underline{u}_3 - \underline{u}_2)$$

$$- \frac{kT_i}{m_1}\left[\frac{1}{n_1}\underline{\nabla} n_1 + \frac{1}{T_i}\underline{\nabla} T_i - \frac{m_1}{kT_i}\underline{G} + \frac{T_e}{T_i}\frac{\underline{\nabla} n_e}{n_e}\right.$$

$$\left. + \frac{\underline{\nabla} T_e}{T_i} + \frac{\underline{\nabla} T_i}{T_i}(\beta_1 - \beta_{12}^* - \beta_{13}^*)\right] \qquad (2.73)$$

Taking the field aligned component of the last equation, we get

$$(\eta_{12} + \eta_{13})u_1 = \eta_{12}\,u_2 + \eta_{13}\,u_3 + (R_{123} - R_{132})(u_3 - u_2)$$

$$- g \sin I - \frac{k}{m_1}\left[\frac{T_i}{n_1}\frac{\partial n_1}{\partial s} + \frac{\partial}{\partial s}(T_i + T_e)\right.$$

$$\left. + \frac{T_e}{n_e}\frac{\partial n_e}{\partial s} + (\beta_1 - \beta_{12}^* - \beta_{13}^*)\frac{\partial T_i}{\partial s}\right] . \qquad (2.74)$$

This can be put in the form

$$(\eta_{12} + \eta_{13})\phi_1 = -\frac{k}{m_1}\left(T_i + \frac{n_1}{n_e} T_e\right) \frac{\partial n_1}{\partial s} + n_1 \Bigg[\eta_{12} u_2 + \eta_{13} u_3$$

$$+ (R_{123} - R_{132})(u_3 - u_2) - g \sin I$$

$$- \frac{k}{m_1} \left\{ \frac{\partial}{\partial s}(T_i + T_e) + (\beta_1 - \beta^*_{12} - \beta^*_{13}) \frac{\partial T_i}{\partial s} + \frac{T_e}{n_e} \frac{\partial}{\partial s}(n_2 + n_3) \right\} \Bigg] \tag{2.75}$$

and setting

$$\eta_1 = \eta_{12} + \eta_{13} + \nu_{10} = \nu_{12}(1 - \theta_{12}) + \nu_{13}(1 - \theta_{13}) + \nu_{10} \quad ,$$

$$A = \frac{k}{m_1}\left[T_i + \frac{n_1}{n_e} T_e \right] \quad ,$$

$$E = \frac{k}{m_1}\left\{ \frac{\partial}{\partial s}(T_i + T_e) + \frac{T_e}{n_e} \frac{\partial}{\partial s}(n_2 + n_3) + (\beta_1 - \beta^*_{12} - \beta^*_{13}) \frac{\partial T_i}{\partial s} \right\}$$

$$- \eta_{12} u_2 - \eta_{13} u_3 - (R_{123} - R_{132})(u_3 - u_2) - \nu_{10}\, u \cos I$$

gives

$$\eta_1 \phi_1 = -A \frac{\partial n_1}{\partial s} - (E + g \sin I) n_1 \ . \tag{2.76}$$

Substituting for ϕ_1 from (2.71), the O^+ continuity equation becomes

$$\eta_1 \frac{\partial n_1}{\partial t} = D_0 \frac{\partial^2 n_1}{\partial s^2} + D_1 \frac{\partial n_1}{\partial s} + D_2 n_1 + D_3 \tag{2.77}$$

where

$$D_0 = A$$

$$D_1 = \frac{\partial A}{\partial s} - A \frac{\partial}{\partial s} \log(n_1 B) + E + g \sin I$$

$$D_2 = \frac{\partial E}{\partial s} + \frac{\partial}{\partial s}(g \sin I) - (E+g \sin I) \frac{\partial}{\partial s} \log(n_1 B) - n_1 \alpha_1$$

$$D_3 = n_1 \alpha_2$$

where α_1 and α_2 are the same as in equation (2.32') and their forms will be given later on, when we consider the O^+ production and loss processes. The numerical procedure used to solve equation (2.77) is discussed in section 2.4.

H^+ EQUATIONS

By interchanging 1 and 2 in equation (2.74), the H^+ momentum equation takes the form

$$(n_{21} + n_{23}) u_2 = n_{21} u_1 + n_{23} u_3 + (R_{213} - R_{231})(u_3 - u_1)$$

$$- g \sin I - \frac{k}{m_2}\left[\frac{T_i}{n_2} \frac{\partial n_2}{\partial s} + \frac{\partial}{\partial s}(T_i + T_e) + \right.$$

$$+\frac{T_e}{n_e}\frac{\partial n_e}{\partial s} + (\beta_2 - \beta_{21}^{*} - \beta_{23}^{*})\frac{\partial T_i}{\partial s}\Bigg] \qquad (2.78)$$

This can be put in the form

$$\frac{k}{m_2}\left[T_i + \frac{n_2}{n_e}T_e\right]\frac{\partial}{\partial s}\log n_2 = -g\sin I - \frac{k}{m_2}\Bigg[\frac{\partial}{\partial s}(T_i + T_e) + (\beta_2 - \beta_{21} - \beta_{23})\frac{\partial T_i}{\partial s}$$

$$+\frac{T_e}{n_e}\frac{\partial}{\partial s}(n_1 + n_3)\Bigg] + \eta_{21}(u_1 - u_2)$$

$$+\eta_{23}(u_3 - u_2) + (R_{231} - R_{213})(u_1 - u_3)$$

$$+\nu_{20}u\cos I \qquad (2.74)$$

where

$$\eta_{21} = \nu_{21}(1 - \theta_{21}) \quad ,$$

$$\eta_{23} = \nu_{23}(1 - \theta_{23}) \quad .$$

The terms involving velocities can be written

$$-(\eta_{23} + \eta_{21})u_2 + \eta_{23}u_3 + \eta_{21}u_1 + R_2u_1 - R_2u_3$$

where $R_2 = R_{231} - R_{213}$; or

$$-(\eta_{23} + \eta_{21})\frac{\phi_2}{n_2} + (\eta_{23} - R_2)u_3 + \frac{(\eta_{21} + R_2)}{n_1}(C - \phi_2)$$

since $C = \phi_1 + \phi_2$. Continuing, these terms can be written

$$-\left[\left(\frac{\eta_{23}+\eta_{21}}{n_2}\right)+\left(\frac{\eta_{21}+R_2}{n_1}\right)\right]\phi_2+\left(\frac{\eta_{21}+R_2}{n_1}\right)C+(\eta_{23}-R_2)u_3$$

$$= -\left[\eta_{21}\frac{(n_1+n_2)}{n_1 n_2}+\frac{\eta_{23}}{n_2}+\frac{R_2}{n_1}\right]\phi_2+\left(\frac{\eta_{21}+R_2}{n_1}\right)C+(\eta_{23}-R_2)u_2$$

$$= -\left[\frac{\xi_{21}(n_1+n_2)+\eta_{23}}{n_2}\;\frac{R_2}{n_1}\right]\phi_2+\left(\eta_{21}+\frac{R_2}{n_1}\right)C+(\eta_{23}-R_2)u_2 ,$$

where $\xi_{21} = \dfrac{\eta_{21}}{n_1} = \dfrac{\nu_{21}(1-\theta_{21})}{n_1} = s_{21}(1-\theta_{21})$.

Hence the H^+ momentum equation takes the form

$$\frac{k}{m_2}\left[T_i+\frac{n_2}{n_e}T_e\right]\frac{\partial}{\partial s}(\log n_2) = -g\sin I-\frac{k}{m_2}\left[\frac{\partial}{\partial s}(T_e+T_i)\right.$$

$$\left.+\frac{T_e}{n_e}\frac{\partial}{\partial s}(n_1+n_3)+(\beta_2-\beta_{21}^{*}-\beta_{23}^{*})\frac{\partial T_i}{\partial s}\right]$$

$$-\left[\frac{\xi_{21}(n_1+n_2)+\eta_{23}}{n_2}+\frac{R_2}{n_1}\right]\phi_2$$

$$+\left(\xi_{21}+\frac{R_2}{n_1}\right)C+\left(\eta_{23}-R_2\right)u_2$$

$$+ \nu_{20} u \cos I \tag{2.80}$$

He$^+$ EQUATIONS

By interchanging 2 and 3 in equation (2.79) the He$^+$ momentum equation takes the form

$$\frac{k}{m_3}\left[T_i + \frac{n_3}{n_e} T_e\right] \frac{\partial}{\partial s}(\log n_3)$$

$$= - g \sin I - \frac{k}{m_3}\left[\frac{\partial}{\partial s}(T_i + T_e) + (\beta_3 - \beta_{31} - \beta_{32})\frac{\partial T_i}{\partial s} + \frac{T_e}{n_e}\frac{\partial}{\partial s}(n_1 + n_2)\right]$$

$$+ \eta_{31}(u_1 - u_3) + \eta_{32}(u_2 - u_3) + (R_{321} - R_{312})(u_1 - u_2)$$

$$+ \nu_{30} u \cos I \tag{2.81}$$

2.4 Numerical Procedure

The first stage of the numerical procedure is to determine the points of the selected field line at which the concentrations and fluxes of O$^+$, H$^+$, He$^+$ and O^{++} are to be calculated. These points will be placed Δs apart and will be referred to as the labelled points of the field line.

To determine these points we need to know the total length of the field line and this can be done using the arc length equation for a dipole field, namely

$$s(x) = \frac{r_e}{2\sqrt{3}}(x + \sinh(x)\cosh(x)) , \qquad (2.82)$$

where $\sinh x = \sqrt{3}\cos\theta$.

The arc length equation, (2.82) is derived in Appendix B. The total length of the field line is calculated by evaluating equation (2.82) for $\theta = {}^{\pi}/_{2}$. After knowing the total length of the field line we start stepping down the field line. The momentum equations for H^+, He^+ and O^{++} are solved for $\log(n_i)$ where n_i is the number density of H^+, He^+ or O^{++}. At great altitudes $\log(n_i)$ varies approximately linearly, so we can choose large step lengths and as we go down the field line we use smaller step lengths. This is necessary because the variables change more rapidly at lower altitudes. The same step lengths are used for O^+. It is assumed that O^+ is in diffusive equilibrium above 2000 km. All the calculations are carried out for L = 3. The selected step lengths for the field line at L = 3 are

$$\Delta s = 1000 \text{ km for } s(3000 \text{ km}) \leq s < s(\text{equator})$$

$$\Delta s = 100 \text{ km for } s(1500 \text{ km}) \leq s < s(3000 \text{ km})$$

$$\Delta s = 20 \text{ km for } s(1000 \text{ km}) \leq s < s(1500 \text{ km})$$

$$\Delta s = 10 \text{ km for } s(200 \text{ km}) \leq s < s(1000 \text{ km}),$$

where s(x km) is the nearest labelled point of the field line to the altitude x km. At each labelled point we calculate the height and colatitude, since several variables are functions of these variables.

After determining the labelled points and the height and colatitude at these points, we solve the equations for O^+, H^+, He^+ and O^{++}. The order of the calculation is as follows. We begin by calculating O^+ number densities and fluxes at each new time followed by the calculation of H^+ and then He^+ or O^{++}.

The O^+ Procedure.

The O^+ calculation is divided into two parts, below 2000 km and at and above 2000 km. If we denote the labelled point at about 2000 km by s_N and the labelled point at about 200 km by s_M, then between s_N and s_M the O^+ number density is calculated by numerical solution of equation (2.34). This is done using a fully implicit finite difference procedure (Laasonen, 1949). To do this we need to make the following approximations

$$\frac{\partial n}{\partial t} \doteq \frac{n(i,j+1)-n(i,j)}{\Delta t} \tag{2.83a}$$

$$\frac{\partial n}{\partial s} = \frac{\Delta s^2(i)n(i-1,j+1)+\Delta s(i-1)(\Delta s(i)-\Delta s(i-1)n(i,j+1)-\Delta s^2(i-1)n(i+1,j+1)}{\Delta s(i)\Delta s(i-1)(\Delta s(i-1)+\Delta s(i))} \tag{2.83b}$$

$$\frac{\partial^2 n}{\partial s^2} \doteq \frac{2(\Delta s(i)n(i-1,j+1)-(\Delta s(i)+\Delta s(i-1))n(i,j+1)+\Delta s(i)n(i+1,j+1))}{\Delta s(i)\Delta s(i-1)(\Delta s(i-1)+\Delta s(i))}\,, \tag{2.83c}$$

where Δt and Δs denotes the time step and the arc length step respectively and i and j are such that $t = t_0 + j\Delta t$ and $s(i) = s_{MAX} - \sum_i \Delta s(i)$. If we substitute these approximations in equation (2.33) and arrange the resulting equation so that all n's evaluated at $t+\Delta t$ are on the left-hand side of the equation, and all n's evaluated at time t are on the right-hand side of the equation, we get

$$P_i n_{i-1} + Q_i n_i + R_i n_{i+1} = S_i (i = N, M-1), \tag{2.84}$$

where the j suffices have been dropped. The coefficients are given by

$$P_i = - \frac{(2D_0 + D_1 \Delta s(i))}{\Delta s(i-1)(\Delta s(i) + \Delta s(i-1))} , \tag{2.85}$$

$$Q_i = \frac{\nu_1}{\Delta t} + \frac{2D_0 - D_1(\Delta s(i-1) - \Delta s(i))}{\Delta s(i)\Delta s(i-1)} - D_2 , \tag{2.86}$$

$$R_i = - \frac{(2D_0 - D_1 \Delta s(i-1))}{\Delta s(i)(\Delta s(i) + \Delta s(i-1)} , \tag{2.87}$$

and

$$S_i = D_3 + \frac{\nu_1}{\Delta t} n(i,j) \tag{2.88}$$

where ν_1, D_0, D_1, D_2 and D_3 are the same as in equation (2.33).

The system of linear equations (2.84) has two more unknowns than the number of the equations. We therefore need two more equations. These two equations are supplied by the boundary conditions. The lower boundary condition is applied at the labelled point s_n (at about 200 km). This gives

$$n_M = S_M \tag{2.89}$$

During the day-time this condition is photochemical equilibrium, i.e. $P_0 - \beta n = 0$ and S_M takes the form

$$S_M = \frac{P_0(M)}{\beta(M)} \tag{2.90}$$

where P_0 and β are the 0^+ production and loss coefficients respectively. They are given in later chapters when we discuss the 0^+ production and loss processes. At night-time we assume that the loss coefficient, β, determines the 0^+ number density gradient, i.e.

$$\frac{\partial}{\partial s}\log n = -\frac{\partial}{\partial s}\log\beta \quad , \tag{2.91}$$

or

$$\frac{\partial}{\partial s}\log(n\beta) = 0$$

i.e.

$$n\beta \simeq \text{constant} \tag{2.92}$$

and therefore the lower boundary condition during the night-time is given by

$$S_M = \frac{n(M-1)\beta(M-1)}{\beta(M)} \tag{2.93}$$

The upper boundary condition for O^+ is zero flux at s_N. Putting the O^+ flux equal to zero in equation (2.28) gives

$$\alpha_1 \frac{\partial n_1}{\partial s} = \alpha_2 n_1 \quad , \tag{2.94}$$

where

$$\alpha_1 = \frac{k}{m_1}\left(T_i + \frac{n_1}{n_e} T_e\right) \tag{2.95}$$

$$\alpha_2 = -\frac{k}{m_1}\left[\frac{\partial}{\partial s}(T_i + T_e) + \frac{T_e}{n_e}\frac{\partial n_2}{\partial s} + \frac{n_2}{n_e}\alpha\frac{\partial T_i}{\partial s}\right] -$$

$$- g \sin I + \nu_{10} u \cos I + \frac{m_2}{m_1} s_{21} \phi_2 \tag{2.96}$$

with

$$s_{21} = \frac{\nu_{21}(1-\Delta_{12})}{n} \tag{2.97}$$

and the other variables are as defined before. Application of these boundary conditions, the formulation of the tridiagonal system and the solution of the tridiagonal system is given in Appendix D.

After finding the O^+ number densities between s_N and s_M we then calculate the O^+ fluxes using equation (2.38) with the approximation (2.38a). The O^+ number densities above s_N(2000 km) are calculated by putting $\phi_1 = 0$ in equation (2.28) and arranging the equation to give an expression for $\frac{\partial}{\partial s} \log n_1$. This equation is similar to equation (2.29) with the flux terms omitted and the suffices 1 and 2 interchanged. The resulting equation has the form

$$\frac{dy}{dx} = f(x,y) \tag{2.98}$$

with $y = \log n_1$ and $x = s$

and this is integrated numerically using the modified Euler method. It involves prediction via the formula

$$y_{n+1} = y_n + h f(x_n, y_n) \tag{2.99}$$

and correction using the formula

$$y_{n+1} = y_n + \frac{h}{2}\left[f(x_n, y_n) + f(\ _{n+1}, y_{n+1})\right], \tag{2.100}$$

where h is the step length. Higher order methods are difficult to use because of the varying step lengths and are unnecessary in view of the fact that O^+ is in diffusive equilibrium and $\log n_1$ varies approximately linearly.

H^+, He^+ and O^{++} Procedure.

To solve the H^+, He^+ and O^{++} momentum equations we use the Adams-Moulton predictor corrector method (a fourth order method). This method can be applied to equations (and extended to systems of equations) that can be written in the form

$$\frac{dy}{dx} = f(x,y). \tag{2.101}$$

The method involves prediction using the Adams-Bashforth formula

$$y_{n+1} = y_n + \frac{h}{24}\left(55f_n - 59f_{n-1} + 37f_{n-2} - 9f_{n-3}\right), \quad (2.102)$$

where h is the step length and $f_n = f(x_n, y_n)$ and correction via the Adams-Moulton formula

$$y_{n+1} = y_n + \frac{h}{24}\left(9f_{n+1} + 19f_n - 5f_{n-1} + f_{n-2}\right). \quad (2.103)$$

This method is sometimes called the modified Adams method and is ascribed to Moulton (1926). The method can be applied only if the step length is constant. In the regions where the step length varies it is not necessary to use this method since at these altitudes the number density decays approximately exponentially. In these regions we again use the modified Euler method described in the section for the O^+ procedure. These methods are described, for example, in Hildebrand (1974).

Our H^+, He^+ and O^{++} momentum equations (2.29), (2.59) and (2.64) are in similar form to equation (2.101) and they are ready to be solved numerically by the methods described. Every time we calculate the number density we calculate the corresponding flux using the equations (2.37), (2.38'), (2.63) and (2.65') and this will require estimating $\frac{\partial n_i}{\partial t}$ (i = 1,2,3 and 4). This is approximated using equation (2.83a).

To start the numerical solution the equatorial value of n_i is required. This value at the equator is found using the searching procedure developed by Moffett and Murphy (1973). This involves searching for a value for the number density of H^+(or He^+ or O^{++}) at the equator that yields a solution which is such that the number density at the lower boundary agrees with the boundary condition to within a specified percentage. This is done by binary splitting at the upper boundary (the equator). For the time interval we adopt Δt = 15 mins. It is noted that sufficient accuracy can be obtained with this value of Δt (Moffett and Murphy, 1973). A 24 hours period of integration requires about 8 minutes on the Aston University ICL 1904S computer. On the more powerful CDC 7600 the 24 hours integration requires less than 20 seconds.

III DOWNWARD PROTON FLOW IN THE TOPSIDE IONOSPHERE

3.1 INTRODUCTION

The magnitude of downward H^+ velocities, parallel to the Earth's magnetic field, is investigated for mid-latitudes. The most rapid downward flow is likely to occur during the period following sunset. The falling temperatures and decaying O^+ layer may lead to rapidly changing pressure gradients in the topside ionosphere. A possible consequence is that some of the gravitational potential energy of the protonospheric plasma is converted into kinetic energy as the plasma flows towards the ionosphere.

The possibility of downward supersonic H^+ flow parallel to the magnetic field in a collapsing post-sunset ionosphere was investigated by Fontheim and Banks (1972). They found that under steady-state, isothermal, collisionless conditions a critical point (transition point from subsonic to supersonic flow) exists above 1000 km if the plasma temperature is below a certain limiting temperature, T_ℓ, which varies with latitude. For the more general case they found that the temperature gradient exerted a strong influence on the H^+ flow and their criteria for the existence of a critical point above 1000 km were complicated. If the temperature gradient was below a certain value, $\left(\frac{\partial T}{\partial r}\right)_0$, which is a function of latitude, a critical point exists when the plasma temperature is below the limiting temperature, T_ℓ.

However, when the temperature gradient is greater than $\left(\frac{\partial T}{\partial r}\right)_0$ the condition for the critical point to exist is that the plasma temperature must exceed T_ℓ. Fontheim and Banks concluded that there was a strong possibility of supersonic H^+ flow in the post-sunset ionosphere. However, they did note that their criteria were necessary but not sufficient conditions for supersonic H^+ flow to occur.

The criteria obtained by Fontheim and Banks were derived by a qualitative examination of the H^+ equations. Murphy and Moffett (1978) investigated proton flow in a collapsing post-sunset ionosphere by solving numerically the fully time dependent equations of continuity and momentum for O^+ and H^+ and the energy equations for ion and electron temperatures along a mid-latitude magnetic field tube. They found that the H^+ flow remained subsonic even when the temperatures satisfied the criteria of Fontheim and Banks. Even under extreme conditions downward supersonic flow did not occur.

Although the findings of Murphy and Moffett (1978) appear to disagree with Fontheim and Banks (1972) they are not in direct conflict since the criteria for the existence of a critical point are necessary but not sufficient conditions. Fontheim and Banks define a critical point as a point at which the flow becomes supersonic or a point at which a maximum in the mach number occurs. This definition is sensible for the isothermal, collisionless, steady-state case and what happens at the critical point depends on conditions at some other point of the field tube. In this chapter it is shown how such conditions can be incorporated in the model.

In this chapter an attempt is made to clarify the nature of downward H^+ flow at mid-latitudes. Initially we examine the isothermal case and extend the analysis of Fontheim and Banks by deriving an analytical expression for the limiting temperature. We also incorporate the conditions at the equator, or some other point of the field tube, into the equations so that the nature of a critical point can be determined. It is noted that, theoretically the isothermal assumption may not be too unrealistic parallel to the magnetic field because of the high conductivity in this direction. However, observational results indicate that there are altitude gradients in plasma temperatures at high altitudes (Serbu and Maier, 1970; Sanatani and Hanson, 1970; Bruce et al., 1974; Maher and Tinsley, 1977). It is also noted that H^+ is only likely to become supersonic, if at all, in the protonosphere. In the region where significant temperature gradients exist there is likely to be sufficient O^+ to keep the H^+ flow subsonic. The downward proton flow is restricted by the O^+ contribution to the polarisation field and collisions with O^+.

A thorough understanding of the isothermal case is useful before investigating the general case. An understanding of the way in which the energy is distributed amongst its different forms throughout the plasma is particularly useful.

The general case is also re-examined. In this situation the definition of a critical point is not so straightforward. In the calculations of Murphy and Moffett (1978) the field-aligned component of the polarisation field term plays an important role in allowing H^+ to flow downwards. This term was not included in the equations presented by Fontheim and Banks (1972) and this may affect their conclusions involving temperature gradients for the general case. An analysis similar to that presented by Fontheim and Banks is not possible when the polarisation field is included. We therefore refer to the full calculations of Murphy and Moffett to discuss the relative importance of the temperature gradient and the polarisation field.

3.2 Equations.

Here we write the H^+ momentum equation in the form

$$\frac{d\underline{v}_2}{dt} + \frac{1}{n_2 m_2}\underline{\nabla} P_2 + \frac{1}{n_e m_2}\underline{\nabla} P_e + (\underline{v}_2 - \underline{v}_1)\nu_{21}(1-\Delta_{12}) +$$

$$+ \frac{k}{m_2}\alpha_2 \underline{\nabla} T_e - \frac{k}{m_2}\frac{n_1}{n_e}(\alpha_{12} - \overset{*}{\alpha}_{12})\underline{\nabla} T_i - \underline{g} = 0 , \qquad (3.1)$$

where the variables are as defined in Chapter II.

The coefficients γ_2, α_{12} and α^*_{12} are thermal diffusion coefficients and they are given by equations (2.19), (2.20) and (2.21) respectively. The correction factor, Δ_{12}, is given by equation (2.22). Equation (3.1) is equivalent to equation (2.15) of Chapter II, except that the acceleration term, $\frac{d\underline{v}_2}{dt}$, is included here but has been omitted in equation (2.15). The acceleration term is included here because it may be important when the magnitude of H^+ velocities become large and possibly supersonic, and it is precisely these features that are being investigated in this chapter.

If the H^+ gas is to attain supersonic speeds it is only likely to occur in the protonosphere. We therefore restrict our attention to this region and neglect H^+ collisions with O^+. We also use the result that γ_2 is zero for singly charged ions (St Maurice and Schunk, 1977). Therefore the H^+ momentum equation becomes

$$\frac{d\underline{v}_2}{dt} + \frac{1}{n_2 m_2}\underline{\nabla} P_2 + \frac{1}{n_e m_2}\nabla P_e - \frac{k}{m_2}\frac{n_1}{n_e}(\alpha_{12} - \alpha^*_{12})\underline{\nabla} T_i - \underline{g} = 0 \tag{3.2}$$

with $\frac{d\underline{v}_2}{dt} = \frac{\partial \underline{v}_2}{\partial t} + \underline{v}_2 . \nabla \underline{v}$.

Using the identities

$$\underline{v}_2 . \nabla \underline{v}_2 = \underline{\nabla}\left(\frac{v_2^2}{2}\right) - \underline{v}_2 \times \mathrm{curl}\, \underline{v}_2 \quad ,$$

$$\frac{1}{n}\underline{\nabla} P = \nabla\left\{\int \frac{dP}{n}\right\} ,$$

and $$\underline{g} = \nabla\left\{\frac{g_0 r_0^2}{r}\right\} ,$$

where r is the radial distance, r_0 is the value of r at 1000 km and g_0 is the magnitude of the gravitational acceleration at 1000 km, equation (3.2) becomes

$$\nabla\left[\frac{v_2^2}{2} + \frac{1}{m_2}\int\frac{dP_2}{n_2} + \frac{1}{m_2}\int\frac{dP_e}{n_e} - \frac{g_0 r_0^2}{r}\right] = \underline{v}_2 \times \mathrm{curl}\,\underline{v}_2 - \frac{\partial \underline{v}_2}{\partial t}$$

$$+ \frac{k}{m_2}\frac{n_1}{n_e}(\alpha_{12} - \alpha_{12}^*)\underline{\nabla} T_i \qquad (3.3)$$

So far we have only assumed a collisionless plasma. In undisturbed magnetic conditions the plasma flows parallel to the magnetic field, i.e. $\underline{v}_2 = v_2\underline{e}_s$ where $\underline{e}_s$ is a unit tangent vector to a field line. With this assumption the term $\underline{v}_2 \times \mathrm{curl}\,\underline{v}_2$ has no component parallel to the magnetic field and therefore disappears when taking the scalar product of equation (3.3) with $\underline{e}_s$. Thus taking the scalar product of equation (3.3) with $\underline{e}_s$ and assuming a steady-state, i.e. $\frac{\partial v_2}{\partial t} = 0$, leads to

$$\frac{\partial}{\partial s}\left[\frac{v_2^2}{2} + \frac{1}{m_2}\int\frac{dP_2}{n} + \frac{1}{m_2}\int\frac{dP_e}{n_e} - g_0\frac{r_0^2}{r}\right] = \frac{k}{m_2}\frac{n_1}{n_e}(\alpha_{12} - \alpha_{12}^*)\frac{\partial T_i}{\partial s}$$

Integrating this equation leads to

$$\frac{v_2^2}{2} + \frac{1}{m_2}\int \frac{dP_2}{n_2} + \frac{1}{m_2}\int \frac{dP_e}{n_e} - g_0\frac{r_0^2}{r} = \frac{k}{m_2}\int\left(\frac{n_1}{n_e}(\alpha_{12} - \alpha_{12}^*)\,\frac{\partial T}{\partial s}\right)ds + f(L), \tag{3.4}$$

where L is the McIlwain coordinate. The function f(L) varies from field line to field line but is constant for a particular field line. This equation can be interpreted as a conservation of energy equation parallel to the magnetic field line for the H^+ gas in the protonosphere. The function on the left of equation (3.4) is similar to the Bernoulli function in fluid theory which is constant on vorticity-stream surfaces (see, for example, Frederick and Chang, 1965). In fact equation (3.4) is similar to Bernoulli's equation for a stream line.

To proceed from equation (3.4) we substitute $P_2 = n_2 kT_i$, $P_e = n_e kT_e$ and assume isothermal conditions, i.e. $\frac{\partial T_i}{\partial s} = 0$, $\frac{\partial T_e}{\partial s} = 0$. With the latter assumption the thermal diffusion term disappears and equation (3.4) reduces to the simpler form

$$\frac{v^2}{2} - g_0\frac{r_0^2}{r} + \frac{kT_i}{m}\log n + \frac{kT_e}{m}\log n_e = f(L) \quad , \tag{3.5}$$

where, for convenience, the suffix 2 has been dropped from the variables. Equation (3.5) fully accounts for the non-linear acceleration terms under the assumed conditions. In the region of interest $n_e \simeq n(H^+)$ since $n(O^+)$ is negligible and therefore equation (3.5) takes the form

$$\frac{v^2}{2} - g_0 \frac{r_0^2}{r} + \frac{k(T_i + T_e)}{m} \log n = f(L) . \tag{3.6}$$

For the H^+ continuity equation we recall equation (2.35) of Chapter II

$$\frac{\partial n}{\partial t} + B \frac{\partial}{\partial s}\left(\frac{nv}{B}\right) = P - L \quad , \tag{3.7}$$

where the variables are as defined in Chapter II and the suffices have been dropped since there is no ambiguity. H^+ ions are produced and lost via the charge exchange reaction

$$O^+ + H \rightleftarrows H^+ + O$$

and since there is negligible O and O^+ in the protonosphere, the reaction cannot proceed, i.e.

$$P - L = 0.$$

Adopting the steady-state assumption, equation (3.7) becomes

$$B \frac{\partial}{\partial s}\left(\frac{nv}{B}\right) = 0 \tag{3.8}$$

leading to

$$\frac{nv}{B} = h(L) , \tag{3.9}$$

where h is an arbitrary function of L. Thus along a given field line $\frac{nv}{B}$ is constant and adopting the equatorial values

$$\frac{nv}{B} = \frac{n_{eq} v_{eq}}{B_{eq}} , \tag{3.10}$$

where the suffix eq refers to the equator. Then substituting for n from equation (3.10) into equation (3.6) we get

$$\frac{v^2}{2} - g_0 \frac{r_0^2}{r} + \frac{k(T_i+T_e)}{m} \log \left(\frac{B n_{eq} v_{eq}}{v\, B_{eq}} \right) = f(L) .$$

As with h(L), f(L) can be evaluated at the equator for a particular field line. This leads to

$$\frac{v^2}{2} - g_0 \frac{r_0^2}{r} + \frac{k}{m}(T_i+T_e) \log \left(\frac{B n_{eq} v_{eq}}{v\, B_{eq}} \right) = \frac{v_{eq}^2}{2} - g_0 \frac{r_0^2}{r_{eq}} + \frac{k}{m}(T_i+T_e) \log n_{eq} \tag{3.11}$$

Equation (3.11) is solved for v using the Newton-Raphson procedure. The Newton-Raphson procedure for solving the equation

$$F(v) = 0$$

is

$$v_{n+1} = v_n - \frac{F(v_n)}{F'(v_n)} .$$

For this particular problem we rearrange equation (3.11) to obtain

$$F(v) = \frac{1}{2}(v^2 - v_{eq}^2) - g_0 r_0^2 \left(\frac{r_{eq} - r}{r_{eq} r} \right) + \frac{k}{m}(T_i + T_e) \log \left(\frac{B v_{eq}}{B_{eq} v} \right) . \tag{3.12}$$

With this approach values of v can be obtained for different values of r along a particular magnetic field line. Consequently a velocity profile is obtained for this field line revealing the nature of the flow.

An alternative approach for determining the nature of the flow is to determine , if it exists, the radial distance r^*, on a given field line, of the point at which the H^+ gas achieves the sound speed. This is carried out by setting $v = -c$ in equation (3.11), where c is the H^+ critical velocity in the H^+-e plasma given by (Stobel and Weber,1972)

$$c^2 = \frac{k}{m}(T_i + \frac{n}{n_e} T_e) \quad , \tag{3.13}$$

and since $n_e \simeq n$ (3.13) simplifies to

$$c^2 = \frac{k}{m}(T_i + T_e) \quad . \tag{3.13'}$$

Carrying out this substitution (3.11) can be put into the form

$$\frac{1}{2}(c^2 - v_{eq}^2) - g_0 r_0^2 \left(\frac{r_{eq} - r^*}{r_{eq} r^*} \right) + c^2 \log \left(\frac{B^* v_{eq}}{B_{eq} c} \right) = 0 \tag{3.14}$$

and then we solve this equation for r^*, again using the Newton-Raphson procedure. Setting the left hand side of (3.14) equal to $H(r^*)$, the Newton-Raphson scheme is

$$r^*_{n+1} = r^*_n - \frac{H(r^*)}{H'(r^*)} \ .$$

In either case we first have to determine the ion and electron temperatures, which we assume to be equal. To choose these temperatures with the aim of producing supersonic H^+ flow we are guided by the isothermal analysis of Fontheim and Banks (1972) which we have extended to derive an analytical expression for the limiting temperature.

From equation (3.8), we get

$$\frac{1}{v}\frac{\partial v}{\partial s} + \frac{1}{n}\frac{\partial n}{\partial s} + B\frac{\partial}{\partial s}\left(\frac{1}{B}\right) = 0$$

or

$$\frac{1}{n}\frac{\partial n}{\partial s} = -\left[\frac{1}{v}\frac{\partial v}{\partial s} + B\frac{\partial}{\partial s}\left(\frac{1}{B}\right)\right] \qquad (3.15)$$

and, adopting the assumptions used in deriving equation (3.6), the field-aligned component of the H^+ momentum equation, equation (3.2), takes the form

$$\frac{1}{2}\frac{\partial v^2}{\partial s} + \frac{k(T_i+T_e)}{mn}\frac{\partial n}{\partial s} = -\frac{\partial \phi}{\partial s} \ , \qquad (3.16)$$

where $\phi = g_0 \frac{r_0^2}{r}$ is the gravitational potential.

Equation (3.6) is, in fact, the integral of equation (3.16). Substituting for $\frac{1}{n}\frac{\partial n}{\partial s}$ from equation (3.15) into equation (3.16) and using equation (3.13), equation (3.16) can be put in the form

$$\left(\frac{c^2-v^2}{v}\right)\frac{\partial v}{\partial s} + c^2B\frac{\partial}{\partial s}\left(\frac{1}{B}\right) = \frac{\partial \phi}{\partial s} \tag{3.17}$$

This equation is similar to equation (6) of Fontheim and Banks (1972) except we have retained the term involving H^+ velocities to clarify the definition of a critical point. Equation (3.17) is only valid within the protonosphere since the O^+ contribution to the field-aligned electrostatic field has been neglected. This improves the possibility of supersonic H^+ flow.

Fontheim and Banks define a critical point to be a point at which the equation

$$c^2B\frac{\partial}{\partial s}\left(\frac{1}{B}\right) = \frac{\partial \phi}{\partial s} \tag{3.18}$$

is satisfied. This equation is obtained from equation (3.17) by either putting v=c or alternatively putting $\frac{\partial v}{\partial s} = 0$. Thus, as noted by Fontheim and Banks, the H^+ flow does not necessarily become supersonic at a critical point. It may simply be a point at which the H^+ velocity profile has reached a maximum, i.e. $\frac{\partial v}{\partial s} = 0$.

To proceed from equation (3.18) a dipole magnetic field is assumed. With this assumption it is shown in Appendix B that

$$B \frac{\partial}{\partial s}\left(\frac{1}{B}\right) = \frac{3\cos\theta(3+5\cos^2\theta)}{r(1+3\cos^2\theta)^{3/2}} ,$$

and that

$$\frac{\partial\phi}{\partial s} = g_0 \frac{r_0^2}{r^2} \frac{2\cos\theta}{(1+3\cos^2\theta)^{\frac{1}{2}}} ,$$

where θ is the colatitude. Since equation (3.18) is only satisfied at a critical point $r=r^*$ of a field line, on substituting these expressions into equation (3.18) the variables r,θ take on the values r^*,θ^* at this point. However, from the equation of a field line, $r=r_e \sin^2\theta$, we have $\sin^2\theta^* = \left(\frac{r^*}{r_0}\right)\sin^2\theta_0$ where θ_0 is the colatitude of the point on the field line at a radial distance r_0(1000 km) and thus θ^* can be eliminated. Carrying out these substitutions equation (3.18) can be arranged into the form

$$\frac{r^*}{r_0} = \frac{2g_0 r_0}{3c^2}\left\{\frac{4-3\sin^2\theta_0 \, {r^*}/{r_0}}{8-5\sin^2\theta_0 \, {r^*}/{r_0}}\right\}$$

or, using latitude ψ rather than colatitude θ

$$\frac{r^*}{r_0} = \frac{2g_0 r_0}{3c^2}\left\{\frac{4-3\cos^2\psi_0 \, {r^*}/{r_0}}{8-5\cos^2\psi_0 \, {r^*}/{r_0}}\right\} \qquad (3.19)$$

This equation is quadratic in ${}^{r^*}\!/_{r_0}$ and can be solved for the ratio ${}^{r^*}\!/_{r_0}$. The result is

$$\frac{r^*}{r_0} = \frac{6(g_0 r_0 \cos^2\psi_0 + 4c^2) \pm \left[36g_0^2 r_0^2 \cos^4\psi_0 - 192 g_0 r_0 c^2 \cos^2\psi_0 + (24c^2)^2\right]^{\frac{1}{2}}}{30c^2\cos^2\psi_0} \tag{3.20}$$

Here it is noted that although the numerical values of the limiting temperatures obtained by Fontheim and Banks were correct their form of equation (3.20) contained an error. For the solution with the positive square root, we substitute $r_0 = r_e\cos^2\psi_0$ in equation (3.20) and obtain

$$\frac{r^*}{r_e} = \frac{6(g_0 r_e \cos^4\psi_0 + 4c^2) + \left[36g_0^2 r_e^2 \cos^8\psi_0 - 192 g_0 r c^2 \cos^4\psi_0 + (24c^2)^2\right]^{\frac{1}{2}}}{30c^2}$$

The quantity inside the square root equals

$$(24c^2 - 4g_0 r_0 \cos^4\psi_0)^2 + 20 g_0^2 r_0^2 \cos^8\psi_0$$

i.e. the roots are always real. From the last equation we obtain

$$\frac{r^*}{r_e} \geq \frac{48c^2 + 2g_0 r_0 \cos^4\psi_0}{30c^2}$$

i.e. $\dfrac{r^*}{r_e} \geq \dfrac{48}{30}$

which is unphysical since it corresponds to a value of r^* which is larger than the equatorial radius of the field line.

For the solution with the negative square root, the ratio r^*/r_0 must be larger than unity in order for the critical point to lie above r_0 (1000 km). Below r_0 H^+ is no longer the sole constituent. For a critical point to exist above 1000 km we therefore require $r^*/r_0 \geq 1$

$$\text{i.e.}\quad \frac{6(g_0r_0\cos^2\psi_0+4c^2)-\left[36g_0^2r_0^2\cos^4\psi_0-192g_0r_0c^2\cos^2\psi_0+(24c^2)^2\right]^{\frac{1}{2}}}{30c^2\cos^2\psi_0} \geq 1$$

$$\text{or}\quad 6c^2(4-5\cos^2\psi_0)+6g_0r_0\cos^2\psi_0 \geq \left[36g_0^2r_0^2\cos^4\psi_0-192g_0r_0c^2\cos^2\psi_0+(24c^2)^2\right]^{\frac{1}{2}}$$

In this inequality, the second term is positive, the first is positive provided $\frac{4}{5} \geq \cos^2\psi_0$, i.e. $\psi_0 \geq 27^{\circ}$. Then the inequality can be squared for $27^{\circ} \leq \psi_0 \geq 90^{\circ}$ which covers the mid-latitude range. Carrying this out

$$36\left[c^4(16-40\cos^2\psi_0+25\cos^4\psi_0)+2r_0g_0c^2\cos^2\psi_0(4-5\cos^2\psi_0)+ \right.$$
$$\left. +r_0^2g_0^2\cos^4\psi_0\right] \geq \left[36g_0^2r_0^2\cos^4\psi_0-192g_0r_0c^2\cos^2\psi_0+(24c^2)^2\right].$$

After some manipulation this leads to the inequality

$$3c^2(5\cos^2\psi_0-8) \geq 2r_0g_0(3\cos^2\psi_0-4)$$

$$\text{or}\qquad 3c^2(8-5\cos^2\psi_0) \leq 2r_0g_0(4-4\cos^2\psi_0)$$

where $0 \leq \cos\psi_0 \leq \frac{4}{5}$. Then both sides are positive. Hence

$$c^2 \leq \frac{2r_0 g_0}{3} \cdot \frac{(4-3\cos^2\psi_0)}{(8-5\cos^2\psi_0)} \quad .$$

Assuming that the ions and electrons have a common temperature, i.e. $T_i = T_e = T$, then from (3.13) we have

$$c^2 = \frac{2kT}{m} \quad .$$

This leads to

$$T \leq \frac{r_0 g_0 m}{3k} \cdot \frac{(4-3\cos^2\psi_0)}{(8-5\cos^2\psi_0)} \quad . \tag{3.21}$$

If we define the limiting temperature, T_ℓ, to be

$$T_\ell = \frac{r_0 g_0 m}{3k} \cdot \frac{(4-3\cos^2\psi_0)}{(8-5\cos^2\psi_0)} \tag{3.22}$$

then inequality (3.21) becomes

$$T \leq T_\ell$$

i.e. if the plasma temperature is below the limiting temperature, T_ℓ, a critical point would exist and at this critical point one of the conditions $M = -1$ or $\frac{\partial v}{\partial s} = 0$ would be satisfied.

For the general case we recall the H^+ momentum equation given by (2.29) in Chapter II. Note that in equation (2.29) the acceleration term was neglected. Taking account of the acceleration term, $\frac{dv_2}{dt}$, and rearranging the H^+ momentum equation we get

$$\left[\frac{k}{m_2}\left(T_i + \frac{n_2}{n_e} T_e\right) - v_2^2\right]\frac{\partial}{\partial s}\log n_2 = -\left[g\sin I + \frac{k}{m_2}\,\frac{\partial}{\partial s}(T_i + T_e)\right.$$

$$+ \frac{k}{m_2}\,\frac{T_e}{n_e}\,\frac{\partial n_1}{\partial s} - \frac{k}{m_2}\,\frac{n_1}{n_e}\,\alpha\,\frac{\partial T_i}{\partial s} -$$

$$\left. - \nu_{20}\, u \cos I\right] - \frac{\phi_2}{n_2}\left[\nu_{20} + \right.$$

$$\left. + \nu_{21}\,(1-\Delta_{12}) + \frac{m_1}{m_2}\,\nu_{12}(1-\Delta_{12})\right] +$$

$$+ C\,\frac{m_1}{m_2}\,\frac{\nu_{12}(1-\Delta_{12})}{n_2} - \frac{\partial v_2}{\partial s} +$$

$$+ v_2^2 B\frac{\partial}{\partial s}\left(\frac{1}{B}\right) - \frac{J_2 v_2}{n_2} \qquad (3.23)$$

where

$$J_2 = P_2 - L_2 - \frac{\partial n_2}{\partial t}$$

and the other variables are as defined in Chapter II.

The H^+ continuity equation of (3.7) can be arranged in the form

$$\frac{\partial}{\partial s}\log n_2 = \frac{J_2}{n_2 v_2} - \frac{1}{v_2}\,\frac{\partial v_2}{\partial s} - B\,\frac{\partial}{\partial s}\left(\frac{1}{B}\right) \qquad (3.24)$$

Introducing the H^+ Mach number $M = {}^{v_2}/_{c}$ where c is given by equation (3.13) and substituting for $\frac{\partial}{\partial s}\log n_2$ from equation (3.24) into equation (3.23) and neglecting the O^+ flux, ϕ_1 compared to ϕ_2, the H^+ momentum equation takes the form

$$
\begin{aligned}
\left(\frac{M^2-1}{v_2}\right)\frac{\partial v_2}{\partial s} = {} & c\,B\,\frac{\partial}{\partial s}\left(\frac{1}{B}\right) + \left\{\frac{1}{nm}\left(\frac{\partial n_2}{\partial t} - P_2 + L_2\right) - \right. \\
& \left. - M\left(\nu_{20} + \nu_{21}(1-\Delta_{12})\right) - \frac{\partial M}{\partial t}\right\} - \\
& - \frac{1}{c}\left\{g \sin I + \frac{k}{m_2}\frac{\partial}{\partial s}(T_i + T_e) + \frac{k}{m_2}\frac{T_e}{n_e}\frac{\partial {}_{1}}{\partial s} - \right. \\
& \left. - \frac{k}{m_2}\frac{n_1}{n_e}\,\alpha\,\frac{\partial T_i}{\partial s} - \nu_{20}\,u \cos I + M\frac{\partial c}{\partial t}\right\}
\end{aligned}
\qquad (3.25)
$$

In the corresponding equation of Fontheim and Banks the O^+ contribution to the field-aligned electrostatic field and thermal diffusion terms were not included.

3.3. DISCUSSION

3.3.1 The isothermal, collisionless, steady state case.

We have extended the analysis of Fontheim and Banks who derived criteria for the existence of a critical point. Such a point must exist for supersonic flow to occur but the existence of a critical point is not sufficient to ensure supersonic flow for the isothermal case. The critical point discussed by Fontheim and Banks is a point at which there is a transition to supersonic flow or simply a point at which the H^+ velocity gradient is zero. This is clarified by equation (3.17). Which one occurs depends on conditions at some other point of the field line, such as number density and flux at the equator which is influenced by other physical conditions such as pressure gradients in the topside ionosphere.

Although we have assumed an isothermal protonosphere we note that this may not be too unrealistic because of the high conductivity along magnetic field lines. It is only in this region that the H^+ flow is likely to become supersonic if at all. As O^+ densities increase the H^+ flow is hindered in the topside ionosphere by collisions and the field-aligned electrostatic field.

Fontheim and Banks's criteria for the existence of a critical point in the isothermal, collisionless, steady-state is that the plasma temperature should be below a certain limit. They derived values of the limiting temperature for different field lines. We have derived an explicit analytical form for the limiting temperature. This is given in equation (3.22). These limiting temperatures range approximately from 925 K at L=2 to 1000 K at L=4. Figure 1 shows the limiting temperature plotted against latitude. As noted in the equations section, the equations used in deriving the limiting temperature inequality are valid only for the regions where H^+ dominates, i.e. inequality (3.21) is valid only in the mid-latitude regions and therefore only the mid-latitude range of figure 1 is applicable. We note that Fontheim and Banks obtained similar values for the limiting temperature. From figure 1 one can see that 695 K $\leq T_\ell \leq$ 1045 K. This means that if the plasma temperature is greater than 1045 K, a critical point would not exist, i.e. the H^+ flow will remain subsonic. Fontheim and Banks pointed out that such temperatures are probably low for immediate post-sunset conditions and therefore the H^+ flow would remain subsonic. Our analysis supports the subsonic flow idea under these conditions. Further, we show that when a critical point does exist it is a point at which the velocity gradient is zero. We demonstrate this by calculating velocity profiles. Velocity profiles for flux tubes at different L-values can be produced by solving equation (3.11). Starting with values of H^+ number density and flux at the equator, equation (3.11) is solved for the H^+ velocity. If the temperature is chosen to satisfy the inequality (3.21) the velocity profile would either exhibit a maximum or achieve supersonic values. Figure 2 shows two typical velocity profiles for L=3.5. At this L-value the limiting temperature (see equation (3.22)) takes the value 988 K. For the lower curve the plasma temperature, 700 K, satisfies inequality (3.21) and therefore a critical point exists. This velocity profile exhibits a maximum at the critical point rather than a transition to supersonic flow. For the upper curve the plasma temperature, 1200°K, is greater than the limiting temperature and, therefore, a critical point does not exist. For these two cases we have used the equatorial values 5×10^{2} cm^{-3} and 10^{7} cm^{-2} s^{-1} for the H^{+} number density and H^{+} flux respectively. It became evident from the upper curve and further calculations that the effect of increasing the plasma temperature was to push the critical point below the 1000 km level where our equations are not valid. If we set the plasma temperature equal to the limiting temperature the calculations produce a velocity profile with a maximum (i.e. critical point) at 1000 km.

Several sets of calculations were carried out, producing many velocity profiles in addition to those in Figure 2. However, the main features are illustrated in the curves of Figure 2. Even with fluxes as large as 10^{8} cm^{-2} s^{-1} at the equator, velocity profiles (with plasma temperature below the limiting temperature) exhibited maxima at the critical point rather than achieving the sound speed. In this context it is noted that the two-hemisphere calculations of Bailey et al.(1978) indicated equatorial fluxes only of order 10^{6} cm^{-2} s^{-1}. These calculations strengthen the conclusions of Fontheim and Banks (1972) who noted that supersonic flow was unlikely to occur because plasma temperatures usually exceed the limiting temperature. It appears that when a critical point does exist it is simply a point at which the velocity profile exhibits a maximum rather than a point at which there is a transition to supersonic flow.

Whether or not the H^+ velocity becomes supersonic in that part of the flux tube above 1000 km can be determined in a different way. We set $v = -c$ in equation (3.11) and then solve equation (3.11) for r. This determines the radial distance of the point on the field line where there is a transition to supersonic flow, if it exists. Our calculations show that such a point could not be found for realistic equatorial conditions. Because of this we adopted another approach by assuming that supersonic flow occurred at some point of the flux tube between 1000 km and the equator. We then solved equation (3.10) to determine the H^+ velocity at the equator. With respect to the location of the critical point the equatorial H^+ velocity is a minimum when the critical point is located at the lowest altitude for which the equations are valid, i.e. 1000 km. Even then results showed that we need to use supersonic flow across the equator to be able to produce such a critical point, and this is highly unlikely. This means that, for realistic conditions across the equator, the H^+ downwards flow will remain subsonic whether or not the plasma temperature is below its critical value.

It is noted that there is sufficient gravitational potential energy to produce supersonic H^+ flow. When the H^+ flow velocity is calculated with the assumption that all of the gravitational potential energy is converted to kinetic energy, the resulting H^+ velocity is 8.5×10^5 cm s^{-1} at 1000 km. This is greater than the sound speed, which is

3.5×10^{5} cm s^{-1}. For the case corresponding to the lower curve of Figure 2, we found that only 0.3% of the gravitational potential energy was converted to kinetic energy, and the remainder of this energy was absorbed in the pressure gradient term in the momentum equation.

3.3.2 The General Case

The previous discussion ignored the time-dependence of the variables, the temperature gradient and collisions between H^+ and O^+ and neutrals. In the general case we take account of these factors. The inclusion of the temperature gradient in the calculation may improve the chances of a supersonic H^+ flow. This will allow thermal energy to be converted to kinetic energy and it may also help to increase the amount of the gravitational potential energy that could be converted to kinetic energy. A very small amount of potential energy was converted to kinetic energy in the isothermal case. It is worth noting that observational results (Serbu and Maier, 1970; Sanatani and Hanson, 1970; Brace et al., 1974; Maher and Tinsley, 1977) suggest that there are substantial altitude gradients in plasma temperature at high altitudes.

In the analysis of Fontheim and Banks (1972) they neglected the contribution of O^+ to the field-aligned electrostatic field. This contribution appears in equation (3.25) via the term involving $\frac{\partial n_1}{\partial s}$. The importance of this contribution is shown in Figure 3, where we have compared the temperature altitude gradient, $\frac{\partial}{\partial s}(T_i + T_e)$, and the O^+ contribution to the field-aligned electrostatic field, $\frac{T_e}{n_e} \frac{\partial n_1}{\partial s}$, each term plotted against height and as a percentage of their sum. The data used to draw the two curves in Figure 3 are taken from the post-sunset calculations of Murphy and Moffett (1978). Figure 3 shows that $\frac{\partial}{\partial s}(T_i + T_e)$ and $\frac{T_e}{n_e} \frac{\partial n_1}{\partial s}$ are of the same order of magnitude up to approximately 1400 km. In their analysis, Fontheim and Banks calculated their criteria for the existence of a critical point at 1000 km. The omission of the O^+ contribution to the field-aligned electrostatic field throws some doubt on their findings. Also it is noted that in the derivation of their criteria, Fontheim and Banks used numerical values from the calculations of Nagy et al. (1968) who also neglected the O^+ contribution to the electrostatic field. The importance of the O^+ electrostatic field is emphasised by considering the situation in which O^+ and H^+ are in diffusive equilibrium. Under such conditions the H^+ momentum equation (3.1) can be put in the form

$$\frac{1}{n_2} \nabla P_2 + \frac{1}{n_e} \nabla P_e = m_2 \underline{g} \quad ,$$

where we have neglected thermal diffusion. Taking scalar product with $\underline{e}_s$ and substituting for P_2 and P_e gives

$$\frac{1}{n_2} \frac{\partial}{\partial s} n_2 T_i + \frac{1}{n_e} \frac{\partial}{\partial s} n_e T_e = - \frac{mg \sin I}{k} \qquad (3.26)$$

or $\frac{T_i}{n_e} \frac{\partial}{\partial s} n_2 + \frac{\partial T_i}{\partial s} + \frac{\partial T_e}{\partial s} + \frac{T_e}{n_e} \frac{\partial n_1}{\partial s} + \frac{T_e}{n_e} \frac{\partial n_2}{\partial s} = - \frac{mgsinI}{k}$

and multiplying through by $\frac{n_e}{T_e}$ we get

$$\left[\frac{T_i n_e}{n_2 T_e} + 1 \right] \frac{\partial n_2}{\partial s} + \frac{n_e}{T_e} \frac{\partial}{\partial s}(T_i + T_e) + \frac{\partial n_1}{\partial s} = - \frac{n_e mgsinI}{kT_e} \tag{3.27}$$

Similarly the O^+ momentum equation is

$$\left[\frac{T_1 n_e}{n_1 T_e} + 1 \right] \frac{\partial n_1}{\partial s} + \frac{n_e}{T_e} \frac{\partial}{\partial s}(T_i + T_e) + \frac{\partial n_2}{\partial s} = - \frac{n_e m_1 gsinI}{kT_e} \tag{3.28}$$

To eliminate $\frac{\partial n_1}{\partial s}$ from (3.27) multiply through by

$\left[\frac{T_i n_e}{n_1 T_e} + 1 \right]$ and subtract equation (3.28):

$$\left[\frac{T_i n_e}{n_1 T_e} + 1 \right] \left[\left\{ \frac{T_i n_e}{n_2 T_e} + 1 \right\} \frac{\partial n_2}{\partial s} + \frac{n_e}{T_e} \frac{\partial}{\partial s}(T_i + T_e) \right] - \frac{n_e}{T_e} \frac{\partial}{\partial s}(T_i + T_e) - \frac{\partial n_2}{\partial s}$$

$$= - \left[\frac{T_i n_e}{n_1 T_e} + 1 \right] \frac{n_e mgsinI}{kT_e} + \frac{n_e m_1 gsinI}{kT_e} \; .$$

Multiplying out

$$\left[\frac{T_i^2 n_e^2}{n_1 n_2 T_e^2} + \left\{\frac{1}{n_1} + \frac{1}{n_2}\right\} \frac{T_i n_e}{T_e}\right] \frac{\partial n_2}{\partial s} + \frac{T_i n_e^2}{n_1 T_e^2} \frac{\partial}{\partial s} (T_i + T_e) =$$

$$= - \frac{n_e g \sin I}{k T_e} \left[m_2 \left\{ 1 + \frac{T_i n_e}{n_1 T_e} \right\} - m_1 \right]$$

and multiplying through by $\frac{n_1 T_e}{T_i n_e^2}$ we get

$$\left[\frac{T_i}{n_2 T_e} + \frac{1}{n_2}\right] \frac{\partial n_2}{\partial s} + \frac{1}{T_e} \frac{\partial}{\partial s} (T_i + T_e) =$$

$$= - \frac{n_1 g \sin I}{k n_e T_i} \left[m_2 \left\{ 1 + \frac{T_i n_e}{n_1 T_e} \right\} - m_1 \right].$$

Multiplying through by $T_e/(T_i + T_e)$ we get

$$\frac{\partial}{\partial s} \left[\log \left\{ n_2 (T_i + T_e) \right. \right] =$$

$$= - \frac{g \sin I}{k (T_i + T_e)} \left[m_2 \left\{ \frac{T_e n_1}{n_e T_i} + 1 \right\} - m_1 \frac{T_e n_1}{n_e T_i} \right]$$

$$= - \frac{m_2 g \sin I}{k (T_i + T_e)} \left[1 + \frac{T_e n_1}{T_i n_e} \left\{ 1 - \frac{m_1}{m_2} \right\} \right]$$

i.e. $$\frac{\partial}{\partial s} \log\left\{n_2(T_i + T_e)\right\} = -\frac{m_2 g \sin I}{k(T_i + T_e)}\left[1 - 15\frac{n_1 T_e}{n_e T_i}\right] \qquad (3.29)$$

This equation describes the H^+ profiles when both O^+ and H^+ are in diffusive equilibrium. The occurrence of a maximum in the H^+ profile is a direct result of opposing effects of gravity and electrostatic field. This analysis shows how important the O^+ electrostatic field is in a diffusive equilibrium situation. Thus the omission of such an important effect in any calculation is not justifiable.

In our analysis of the isothermal case, we showed that the critical point is a point at which $v = -c$ or alternatively $\frac{\partial v}{\partial s} = 0$. The situation in the general case is different. By putting $v = -c$ ($M = -1$) in equation (3.25), we get an equation which differs from the equation obtained by setting $\frac{\partial v}{\partial s} = 0$ in equation (3.25). Setting $\frac{\partial v}{\partial s} = 0$ in equation (3.25) deletes the term on the LHS, but setting $M = -1$ in equation (3.25) deletes the term on the LHS and affects other terms on the RHS. The resulting two equations will only be identical with the additional collisionless, steady-state, isothermal assumptions. Consequently the conditions for a point to exist at which $M = -1$ will, in general, differ from the conditions for the existence of a point at which $\frac{\partial v}{\partial s} = 0$. Therefore, a point at which equation (3.25) is satisfied with $M = -1$ does not have the alternative of being a point at which H^+ speed reaches a maximum $\left(\frac{\partial v}{\partial s} = 0\right)$ as indicated by Fontheim and Banks.

In the post-sunset calculations of Murphy and Moffett (1978) the H^+ supersonic flow was never achieved. This is consistent with the fact that equation (3.25) with $M = -1$ has complex roots. On the other hand, there is always a point at which $\frac{\partial v}{\partial s} = 0$.

3.4 Conclusions.

For the isothermal, collisionless, steady state case we have shown that, at mid-latitudes, when a critical point exists, it is a point at which the velocity gradient is zero rather than a point at which there is a transition to supersonic flow. The only exception was when there was supersonic flow across the equator, which is unrealistic. An important reason for the H^+ flow not becoming supersonic is that a very small amount (0.3% for the case considered) of the available gravitational potential energy is converted to kinetic energy.

For the more complicated case it has been shown that the O^+ contribution to the field-aligned electrostatic field is important. This term, omitted by Fontheim and Banks, was of the same order of magnitude as the temperature gradient term on which they based their criteria for the existence of a critical point. In the post-sunset calculations of Murphy and Moffett (1978), the O^+ contribution to the field-aligned electrostatic field was included. Their results and our analysis showed that it is unlikely that H^+ flow will achieve supersonic speed at any time. If it does achieve such speeds then changes in temperatures have to be responsible for converting enough potential energy into kinetic energy. Finally it is noted that via the electrostatic field the O^+ layer affects the H^+ behaviour in a way that restricts H^+ downwards flow. This was shown in the post-sunset calculations of Murphy and Moffett. Thus, by including the O^+ field-aligned electrostatic field and the O^+ - H^+ collisions, the general case becomes more complicated and therefore the nature of H^+ flow cannot be determined by the application of simple criteria involving temperature and temperature gradients alone.

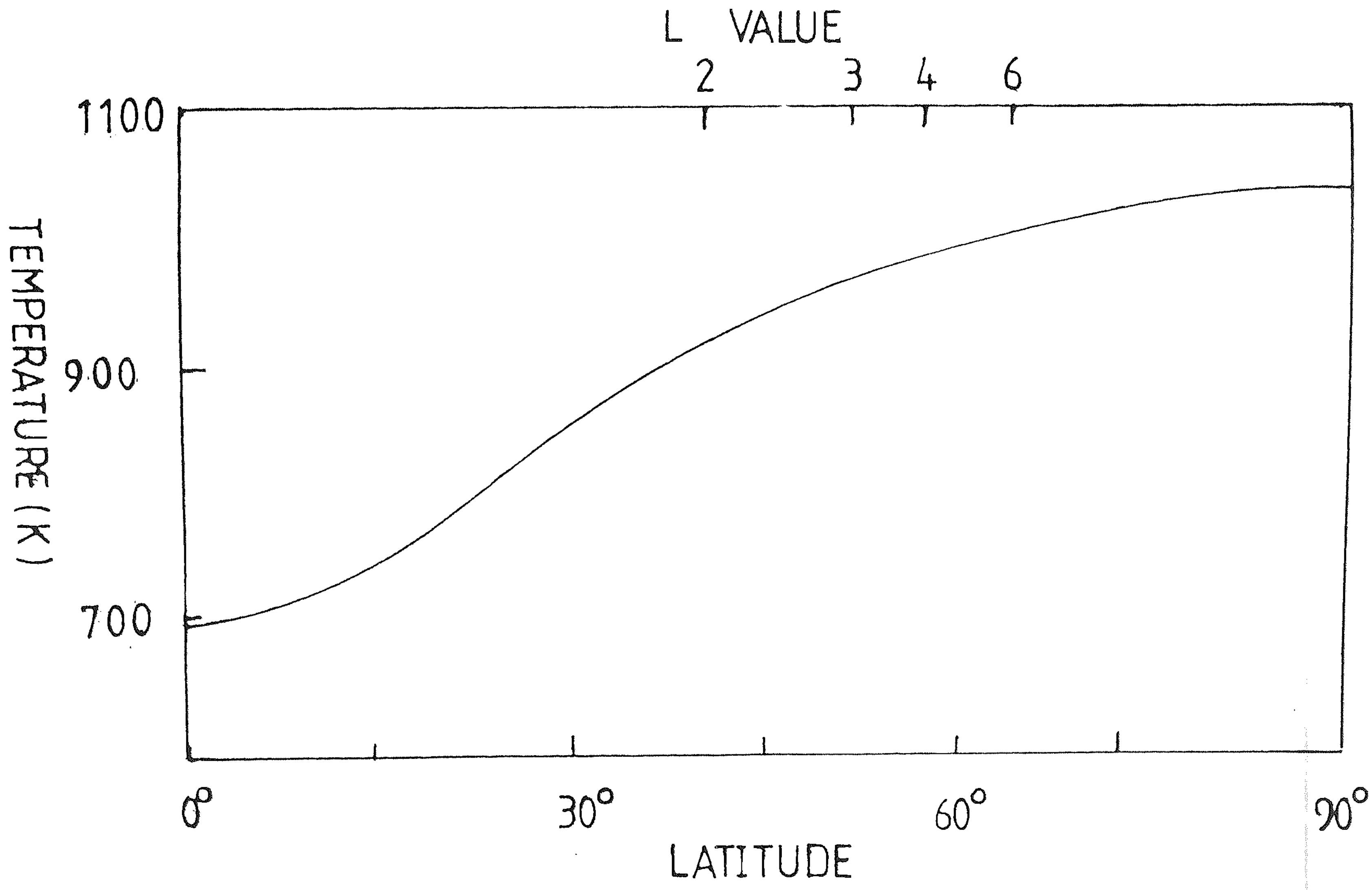

Figure 1. The limiting temperature plotted against latitude.

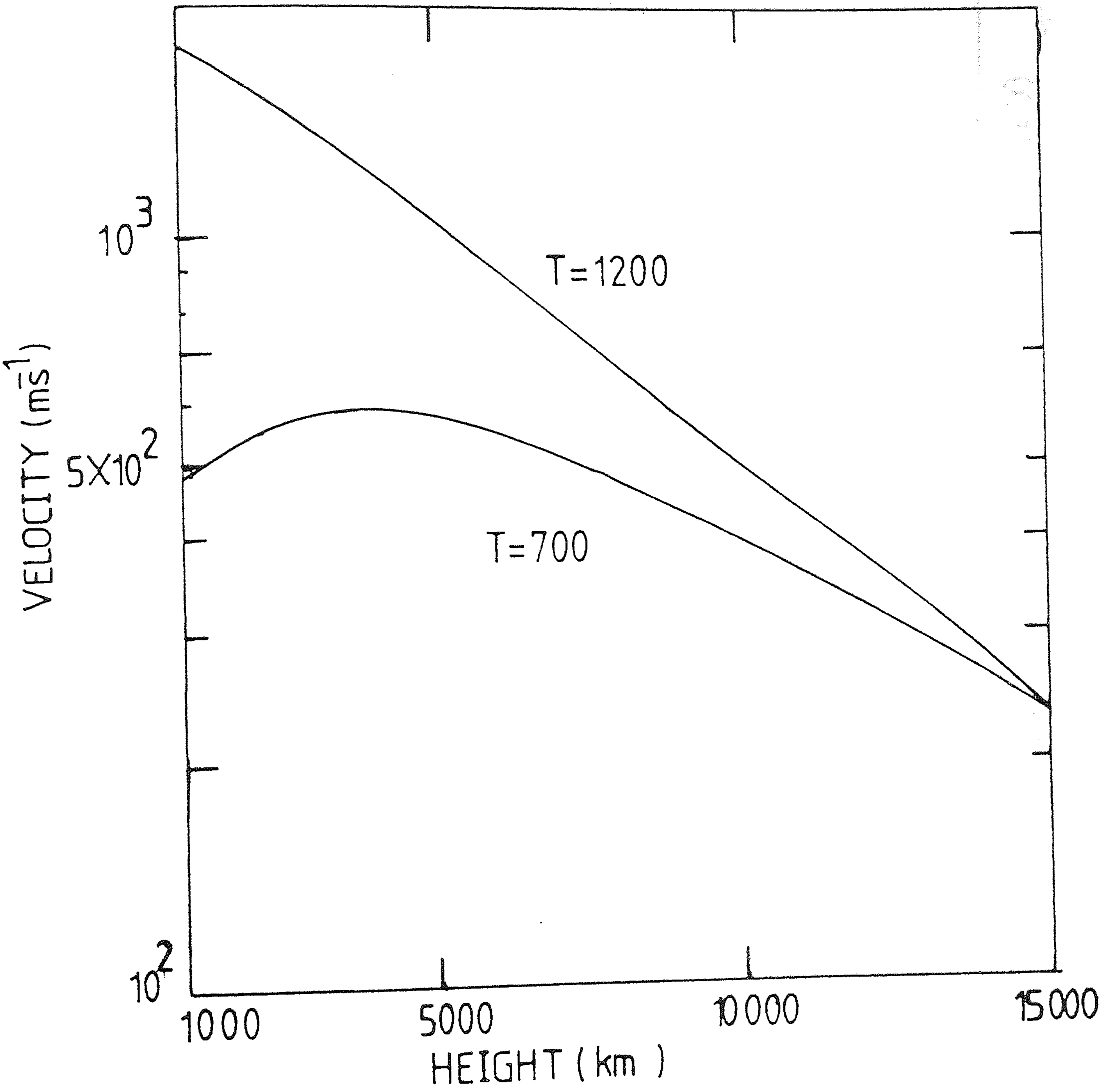

Figure 2. Velocity profiles for the L = 3.5 field line with T_e = 988k. The two curves correspond to two temperatures; one is less than T_e and the other is greater than T_e.

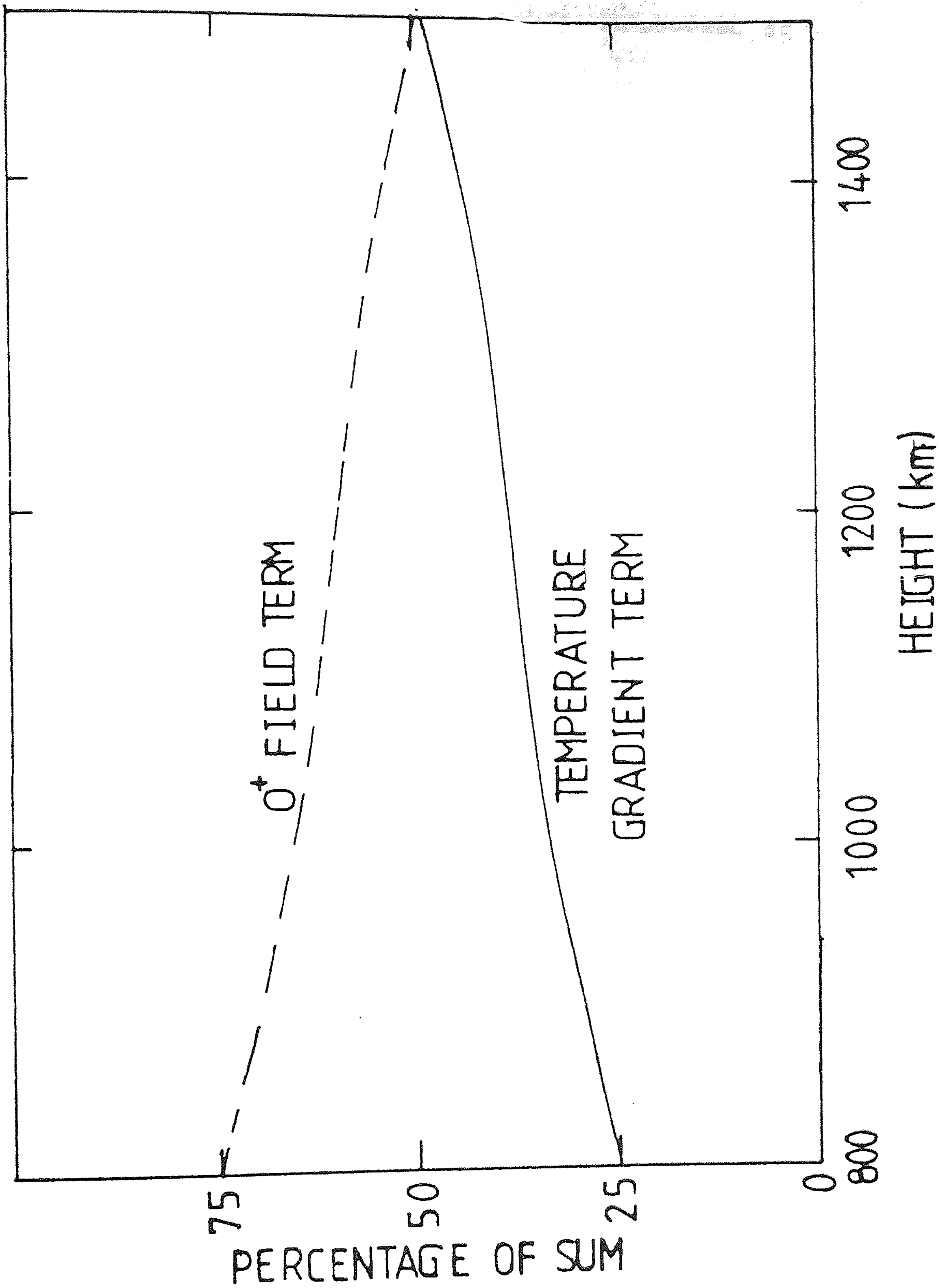

Figure 3. Comparison of $\frac{\partial}{\partial s}(T_i + T_e)$ and $\frac{T_e}{n_e}\frac{\partial}{\partial s}n(O^+)$ plotted against height and as a percentage of their sum.

IV BEHAVIOUR OF HE$^+$ IN THE MID-LATITUDE PLASMASPHERE UNDER SUNSPOT MINIMUM CONDITIONS.

4.1 INTRODUCTION

The first indication of the presence of neutral helium in the upper atmosphere came from the optical observations by Mironov (1959). However, it was Nicolet (1961) who showed that helium was an important constituent in the upper atmosphere. Following that, the theoretical studies of the helium ion distribution in the topside ionosphere were restricted to diffusive equilibrium (Mange, 1960; Hanson, 1962, 1965; Bauer, 1963, 1966; Kockarts and Nicolet, 1963; Angerami and Thomas, 1964; Taylor et al., 1963). Other authors also carried out theoretical studies to explain elementary structure of the He$^+$ layer (Bates and Patterson, 1962; Rush and Venkatesawaran, 1965; McElroy, 1965). Such studies were mostly concerned with the steady-state behaviour of the helium ions. Banks and Holzer (1969) examined the behaviour for both H$^+$ and He$^+$ ions and they found that at mid to high latitudes both H$^+$ and He$^+$ were likely to exist in a state of dynamic equilibrium with an outflow of ions from the ionosphere along geomagnetic field lines. Then most of the work that has been done on He$^+$ behaviour was concerned with the polar regions (Axford, 1968; Lemaire, 1972; Raitt et al., 1977, 1978). In the calculations of Raitt et al. (1977 and 1978), the results showed that the He$^+$ escape flux varies from a low value of

0.99×10^5 $cm^{-2}s^{-1}$ for solar minimum, summer, high magnetic activity conditions to a maximum 1-2 x $10^7 cm^{-2}s^{-1}$ for solar maximum, winter, low magnetic activity conditions. They attributed the variations mainly to changes in the neutral helium density. In mid-latitude regions, there were limited theoretical studies of the He^+ behaviour (Brinton et al., 1969; Schunk and Walker, 1970b; Mayer et al., 1972; Paresce et al., 1974). In these studies, the authors have assumed diffusive equilibrium or steady state.

Recently Murphy et al. (1979) conducted an initial study of the behaviour of He^+ in the mid-latitude regions. They solved the time-dependent He^+ momentum and continuity equations. The atmospheric conditions in their calculation were appropriate to sunspot maximum, and they took account of the two major ions, O^+ and H^+. Starting with a relatively low He^+ tube content, they solved the He^+ equations for a period of 8 days. In the study of Murphy et al. (1979), thermal diffusion was neglected in the He^+ calculations. They also limited the effects of the two major ions, O^+ and H^+, on He^+ by integrating the O^+/H^+ equations for four days and then using the O^+/H^+ results of the fourth day throughout their He^+ calculations. However, following a magnetic storm, four days is not sufficient for the H^+ tube content to reach total replenishment. Indeed, our O^+/H^+ (sunspot maximum) calculations, which we carried out for the O^{++} problem, in Chapter V, showed that after 24 days of integration the H^+ tube content still did not reach total replenishment. Consequently the H^+ tube content on the fourth day is still relatively low and, since the He^+ integration period (Murphy et al. , 1979) was eight days, the He^+ tube content may have reached higher values than it would have done if more H^+ was present. The results of Murphy et al. (1979) show an upflow during the day-time and downflow at night-time. Their results for sunspot maximum conditions suggested that little of the He^+ produced during the day-time is lost by recombination with N_2 and O_2 at night-time.

When a magnetic storm occurs the plasmapause and the magnetospheric convection region move to lower L-values so that the mid-latitude field lines are convected into the tail of the magnetosphere. After the magnetic storm the convection region moves to higher L-values, leaving closed mid-latitude field tubes with very low plasma concentration which the ionosphere then attempts to refill. Using a relatively low He^+ tube content which is typical of post-magnetic storm conditions, we investigate the He^+ replenishment and behaviour for L=3, by solving the O^+, H^+ and He^+ time dependent continuity and momentum equations treating He^+ as a minor ion and treating O^+ and H^+ as major ions. The O^+, H^+ and He^+ equations are solved for atmospheric conditions appropriate to sunspot minimum (at equinox). We have included thermal diffusion in the He^+ momentum equation since it may influence the behaviour of He^+ (Schunk and Walker, 1969). We mentioned earlier that Murphy et al.

(1979) limited the effects of O^+ and H^+ on He^+ by using O^+/H^+ results that correspond to the fourth day throughout the He^+ integration. We overcome this limitation by integrating O^+ and H^+ equations for 24 hours and then we integrate the He^+ equation for the same period and this process is repeated for every new day of the integration period.

4.2 Theoretical formulation

To investigate the daily behaviour of He^+ at mid-latitude regions, we numerically solve the time-dependent equations of continuity and momentum of O^+, H^+ and He^+ along a magnetic flux tube (dipole field) at L=3 (equatorial crossing height = 12740 km). The O^+, H^+ and He^+ equations are solved from a height of about 200 km to the equatorial plane. Normally the O^+, H^+ and He^+ equations are coupled with each other, but with the assumption that He^+ is treated as a minor ion, the dependence of the two major ions, O^+ and H^+, on He^+ is removed. Therefore, the He^+ calculation is carried out in two stages. The first stage is to solve the O^+/H^+ equations yielding O^+/H^+ number densities and fluxes for a period of 24 hours, to be used in the He^+ calculations. Having calculated the O^+/H^+ densities and fluxes, we then solve the He^+ continuity and momentum equations and obtain He^+ densities and fluxes for the same 24 hour period. This process is repeated to calculate the O^+, H^+ and He^+ number densities and fluxes for each day of a ten day period, starting at 06.15 local time on the first day. It should be noted that although we have solved the O^+/H^+ equations for the He^+ problem, the O^+/H^+ results will not be discussed in detail in this chapter, since such results have been presented in a previous work by Murphy et al., (1979). Here, we present the behaviour of some of the important O^+/H^+ variables in relation to their effect on He^+ behaviour. Figure 1 shows height profiles of O^+ and H^+ at midday and midnight on the eighth day of the integration. Figure 2 shows the behaviour of N_mF2, h_mF2, O^+/H^+ transition height (the height where $n(O^+) = n(H^+)$)and H^+ tube content on the eighth day. Figure 3 shows the behaviour of the field-aligned H^+ flux at 1000 km over a period of 24 hours on the eighth day. These will be discussed further in the results section when we consider their influence on He^+.

4.2.1 Equations

As mentioned in Chapter II, the O^+, H^+ and He^+ equations are derived using the formulation of St. Maurice and Schunk (1977).

O^+ equations

For regions below 2000 km we recall equation $(2.3\overset{3}{4})$ for the O^+ momentum equation

$$\nu_1 \frac{\partial n_1}{\partial t} = D_0 \frac{\partial^2 n_1}{\partial s^2} + D_1 \frac{\partial n_1}{\partial s} + D_2 n_1 + D_3 \qquad (4.1)$$

where the coefficients ν_1, D_0, D_1, D_2, D_3 are given by (2.34a-e). To calculate the O^+ fluxes we recall the O^+

continuity equation given by equation (2.38)

$$\phi_1(s,t) = -B(s)\int_s^{s_E} \frac{1}{B(s)}\left[P_1 - L_1 - \frac{\partial n_1}{\partial t}\right] ds \; . \qquad (4.2)$$

For the regions above 2000 km, we assume that O^+ is in diffusive equilibrium and we calculate O^+ number densities using equation (2.28) with $\phi_1 = 0$. Equation (2.28) with $\phi_1 = 0$ can be arranged in the form

$$\frac{\partial}{\partial s}\log n_1 = \left\{ -\left[g \sin I + \frac{k}{m_1}\frac{\partial}{\partial s}(T_i + T_e) + \frac{k}{m_1}\frac{T_e}{n_e}\frac{\partial n_2}{\partial s} \right.\right.$$

$$\left. + \frac{k}{m_1}\frac{n_2}{n_e}\alpha\frac{\partial T_i}{\partial s} - \nu_{10}\, u \cos I \right]$$

$$\left. + \frac{m_2}{m_1}\frac{\nu_{21}}{n_1}(1 - \Delta_{12})\phi_2 \right\} \Bigg/ \left[\frac{k}{m_1}\left(T_i + \frac{n_1}{n_e}T_e\right)\right] \qquad (4.3)$$

where the variables are as defined in Chapter II.

H^+ equations

For the H^+ momentum equation we recall equation (2.29)

$$\frac{\partial}{\partial s}\log n_2 = \left\{ -\left[g \sin I + \frac{k}{m_2}\frac{\partial}{\partial s}(T_i + T_e) + \frac{k}{m_2}\frac{T_e}{n_e}\frac{\partial n_1}{\partial s} \right.\right.$$

$$\left. - \frac{k}{m_2}\frac{n_1}{n_e}\alpha\frac{\partial T_i}{\partial s} - \nu_{20}\, u \cos I \right]$$

$$- \frac{\phi_2}{n_2}\left[\nu_{20} + \nu_{21}(1-\Delta_{12}) + \frac{m_1}{m_2}\nu_{12}(1-\Delta_{12})\right] +$$

$$+ C \frac{m_1}{m_2} \frac{\nu_{12} (1 - \Delta_{12})}{n_2} \Bigg\} \Bigg/ \left(\frac{k}{m_2} \left(T_i + \frac{n_2}{n_e} T_e \right) \right) \qquad (4.4)$$

with

$$\phi_2(s,t) = - B(s) \int_s^{s_E} \frac{1}{B(s)} \left(P_2 - L_2 - \frac{\partial n_2}{\partial t} \right) ds \qquad (4.5)$$

and

$$C(s,t) = - B(s) \int_s^{s_E} \frac{1}{B(s)} \left(P_1 + P_2 - L_1 - L_2 - \frac{\partial n_1}{\partial t} - \frac{\partial n_2}{\partial t} \right) ds \qquad (4.6)$$

where the variables are as in Chapter II.

He^+ equations

For the He^+ momentum equation we recall equation (2.59)

$$\frac{\partial}{\partial s} \log n_3 = \Bigg\{ - \Bigg[g \sin I + \frac{k}{m_3} \frac{\partial}{\partial s} (T_i + T_e) + \frac{k}{m_3} \frac{T_e}{n_e} \frac{\partial}{\partial s} (n_1 + n_2)$$

$$- \frac{k}{m_3} \beta \frac{\partial T_i}{\partial s} - \nu_{30} u \cos I \Bigg]$$

$$- \frac{\phi_3}{n_3} (\nu_{30} + \eta_{31} + \eta_{32})$$

$$+ \frac{\eta_{31}}{n_1} \phi_1 + \frac{\eta_{32}}{n_2} \phi_2 \Bigg\} \Bigg/ \left(\frac{k}{m_3} T_i \right) \qquad (4.7)$$

and the He^+ continuity equation is given by (2.63)

$$\phi_3 (s,t) = - B(s) \int_s^{s_E} \frac{1}{B(s)} \left(P_3 - L_3 - \frac{\partial n_3}{\partial t} \right) ds \qquad (4.8)$$

where the variables are as defined in Chapter II. The acceleration terms have been omitted from the O^+, H^+ and He^+ momentum equations since they are unlikely to have any significant effect on the results(Murphy and Moffett, 1978).

To solve the O^+, H^+ and He^+ continuity and momentum equations, we require expressions for the production and loss processes for each ion. Oxygen ions are produced by photoionisation of neutral atomic oxygen. From equations (1.8) and (1.14) this production rate, P_0, is given by

$$P_0 = I_\infty \eta \sigma_0 n(O) \exp(-\tau) \qquad (4.9)$$

where the variables are as defined in Chapter I. The optical depth, τ, is derived in Appendix A

$$\tau = \sigma \sum n(X) H(X) Ch(X,\chi) \ ,$$

where $Ch(X,\chi)$ is the Chapman function for constituent X, n(X) is the number density for constituent X, H(X) is the scale height of constituent X, χ is the solar zenith angle and the sum is over the neutral constituents atomic oxygen, nitrogen and molecular oxygen. The forms of Chapman function, $Ch(X,\chi)$, are derived in Appendix A for different values of the solar zenith angle, χ. The product $I_\infty \eta \sigma$ is chosen such that it gives a reasonable day-time value for N_mF2. The value used for the product, $I_\infty \eta \sigma_0$, is $3 \times 10^{-7} s^{-1}$. The value used for the absorption cross section, σ, is

1.5×10^{-17} cm^{-2} (Hinteregger et al., 1965). The solar zenith angle, χ, is given by

$$\cos\chi = \sin\delta\cos\theta + \cos\delta\sin\theta\cos\phi \qquad (4.10)$$

where

θ is the colatitude ,

ϕ is the hour angle ($\phi = 0$ at midday) ,

δ is the declination angle made by the radiation path with the equatorial plane.

For equinox conditions the declination angle, δ, is zero and (4.10) becomes

$$\cos\chi = \sin\theta\cos\phi \qquad (4.11)$$

Therefore equation (4.9) which gives O^+ production due to photoionization, becomes

$$P_0 = 1.5 \times 10^{-7} \exp\left[-1.5 \times 10^{-17} \sum n(X)H(X)Ch(X,\chi)\right] n(O)\,\mathrm{cm}^{-3}\mathrm{s}^{-1} \qquad (4.12)$$

Oxygen ions are also produced by the charge exchange reaction

$$H^+ + O \rightarrow H + O^+ \ . \qquad (4.13)$$

The reaction rate for this reaction is $2.2 \times 10^{-11}(T_i)^{\frac{1}{2}}$ cm^{-3}s^{-1} (Raitt et al., 1975) and the production due to this reaction is given by $2.2 \times 10^{-11}(T_i)^{\frac{1}{2}} n(O)n_2$ cm^{-3}s^{-1}

Including these O^+ production processes, the total O^+ production rate is

$$P_1 = P_0 + 2.2 \times 10^{-11} (T_i)^{\frac{1}{2}} n(O) n_2 \ . \qquad (4.14)$$

Oxygen ions are lost via the reverse of reaction (4.13), which is

$$O^+ + H \rightarrow O + H^+ \qquad (4.15)$$

with the reaction rate $2.5 \times 10^{-11} (T_n)^{\frac{1}{2}}$ (Raitt et al, 1975) and the O^+ loss due to reaction (4.15) is given by $2.5 \times 10^{-11} (T_n)^{\frac{1}{2}} n(H) n_1$. O^+ ions are also lost due to neutralisation via the ion-atom interchange reactions

$$O^+ + O_2 \rightarrow O_2^+ + O \qquad (4.16)$$

$$O^+ + N_2 \rightarrow NO^+ + N \qquad (4.17)$$

with the reaction rates $1.07 \times 10^{-9} (T_i)^{0.7}$ $cm^{-3} s^{-1}$ and $\frac{3.6}{T_i} \times 10^{-10}$ $cm^{-3} s^{-1}$ (Roble, 1975) respectively. The recombination coefficient for O^+ is therefore given by

$$\ell_1 = \left\{ 1.07 \times 10^{-9} (T_i)^{0.7} n(O_2) + 3.6 \times 10^{-10} \frac{n(N_2)}{T_i} \right\} cm^{-3} s^{-1} . \qquad (4.18)$$

The total rate of loss of O^+ ions is then

$$L_1 = \ell_1 n_1 + 2.5 \times 10^{-11} (T_n)^{\frac{1}{2}} n(H) n_1 \ . \qquad (4.19)$$

The H^+ ions are produced by photoionisation of neutral hydrogen and the H^+ production due to this process is given by

$$P(H) = 4.5 \times 10^{-7} \exp\left[-1.5 \times 10^{-17} \sum n(X) H(X) Ch(X,X) \right] n(H) cm^{-3} s^{-1}$$

(4.20)

where the variables are as defined before. Hydrogen ions are also produced by the exchange reaction (4.15) and the H^+ production due to reaction (4.15) is $2.5 \times 10^{-11}(T_n)^{\frac{1}{2}}n(H)n_1$. The total H^+ production is given by

$$P_2 = P(H) + 2.5 \times 10^{-11} (T_n)^{\frac{1}{2}}n(H)n_1 . \qquad (4.21)$$

H^+ ions are lost via the charge exchange reaction (4.13). This loss is given by

$$L_2 = 2.2 \times 10^{-11} (T_i)^{\frac{1}{2}}n(O)n_2 . \qquad (4.22)$$

Helium ions are produced by the photoionization of neutral helium and the production rate is taken to be

$$P_3 = P(He) = 6 \times 10^{-8} \exp\left[-1.5 \times 10^{-17} \sum n(X)H(X)Ch(X,X)\right] n(He) cm^{-3} s^{-1} \qquad (4.23)$$

where the variables are as before. Helium ions are lost via the reactions

$$He^+ + N_2 \rightarrow N + N^+ + He \qquad (4.24)$$

$$He^+ + O_2 \rightarrow O + O^+ + He \qquad (4.25)$$

with reaction rates 1.3×10^{-9} cm^{3}s^{-1} and 1.7×10^{-9} cm^{3}s^{-1}, respectively (Banks and Kockarts, 1973). The He^+ loss coefficient is therefore given by

$$\ell_3 = \left\{1.3 \times 10^{-9} n(N_2) + 1.7 \times 10^{-9} n(O_2)\right\}$$

and consequently

$$L_3 = \ell_3 n_3 cm^{-3} s^{-1} . \qquad (4.26)$$

It is noted that these production and loss processes depend on the distribution of the atmospheric constituents O_2, O, N_2, H and He. These distributions are approximated by using the Jacchia (1971) model atmosphere. This model is described in the next section.

After determining the production and loss processes, we proceed to solve numerically the O^+, H^+ and He^+ equations using the procedures described in Chapter II. The O^+ diffusion equation (4.1) is solved between the points s_N (around 2000 km) and s_M (around 200 km). At the upper boundary, s_N, we assume a condition of zero O^+ flux. At the lower boundary, s_M, photochemical equilibrium is assumed during the day-time and the condition is expressed as

$$n_1(s_M) = \frac{P_0(s_M)}{\ell_1(s_M)} \quad . \tag{4.27}$$

At night-time the lower boundary condition is given by

$$n_1(s_M) = \frac{\ell_1(s_{M-1})n_1(s_{M-1})}{\ell_1(s_M)} \quad . \tag{4.28}$$

After calculating the number densities below 2000 km, we then calculate O^+ fluxes for that region. Above 2000 km O^+ is in diffusive equilibrium and the O^+ number densities are calculated using equation (4.3) using the procedure described in Chapter II.

The H^+ and He^+ momentum equations are solved using the numerical procedure described in Chapter II. This procedure involves searching for a value of n(X) at the equator, where X is either H^+ or He^+ that leads to a solution which satisfies the physical lower boundary condition for each ion. We assume that H^+ is in chemical equilibrium at the lower boundary, i.e. the continuity equation reduces to $P_2 - L_2 = 0$ and this leads to the lower boundary value

$$n_2 = \frac{2.5 \times 10^{-11} T_n^{\frac{1}{2}} n(H) n_1}{2.2 \times 10^{-11} T_i^{\frac{1}{2}} n(O)} \quad . \tag{4.29}$$

This condition is applied at approximately 500 km. The values of n_2 between this altitude and 200 km are calculated assuming chemical equilibrium.

For He^+, the lower boundary condition is obtained by making a numerical approximation to the equation

$$\frac{\partial n_3}{\partial t} = P_3 - L_3 \quad , \tag{4.30}$$

which is the He^+ continuity equation with the divergence term neglected. Using the approximation

$$\frac{\partial n_3}{\partial t} \approx \frac{n_3(t) - n_3(t - \Delta t)}{\Delta t}$$

and substituting for P_3 and L_3 equation (4.30) leads to

$$n_3(t) \simeq \frac{(\Delta t \times P_3 + n_3(t-\Delta t))}{(1 + \Delta t \times \ell_3)} \quad . \qquad (4.31)$$

This equation is applied below 400 km. In the day-time, the time derivative in equation (4.30) is negligible and the lower boundary condition is equivalent to photochemical equilibrium. At night-time, there is no production and the application of (4.31) allows the He^+ number density to decay at lower altitudes.

4.2.2 The Neutral Atmosphere Model

The distribution for the neutral constituents, O, O_2, N_2, H and He is calculated using the model atmosphere of Jacchia (1971).

The global exospheric temperature, given by Jacchia (1965), is

$$T_\infty = T_0(1 + R\sin^{m'}\Theta\left\{1 + \frac{R(\cos^{m'}\eta - \sin^{m'}\Theta)}{1 + R\sin^{m'}\Theta}\cos^{n'}\frac{\bar{\Phi}}{2}\right\}, \qquad (4.32)$$

where $\Theta = (\pi/2 - \theta + \delta)/2$,

$\eta = (\pi/2 - \theta - \delta)/2$,

$\bar{\Phi} = \phi + \beta' + P'\sin(\phi + \gamma') \qquad -\pi < \bar{\Phi} < \pi$.

In these equations θ is colatitude and ϕ is the hour angle of the sun measured from noon. For equinox conditions the declination of the sun, δ, is zero. In the last equations

T_0 is the minimum night-time temperature, $(1 + R)T_0$ is the maximum night-time temperature and the parameters R, m', n', β', P' and γ' correspond to Jacchia (1971) parameters R,m, n, β, P and γ. The values of these parameters are

$$m' = 2.2 \ , \quad n' = 3.0 \ , \quad R = 0.3 \ ,$$
$$\beta' = -37^0 \ , \quad P' = +6^0 \ \text{and} \ \gamma' = +43^0 .$$

The modified Jacchia neutral temperature profile presented by Walker (1965) is

$$T = T_\infty - (T_\infty - T_{120})\exp(-\sigma\xi) \ , \tag{4.33}$$

where T_{120} is the neutral temperature at 120 km, σ is given by

$$\sigma = \left(s + \frac{1}{r_0 + 120} \right) \text{km}^{-1} \ ,$$

the parameter s given by Jacchia (1965b) is

$$s = 0.0291 \exp(-X^2/ 2) \ \text{km}^{-1}$$

$$\text{with } X = \frac{T_\infty - 800}{750 + 1.722 \times 10^{-4} (T_\infty - 800)^2}$$

and ξ is the geopotential height given by

$$\xi = \frac{(z - 120)(r_0 + 120)}{r_0 + z} \ \text{km} \ ,$$

where z is the altitude and r_0 is the Earth's radius, both in kilometers. Using the approximation (4.33), Walker (1965) integrated the diffusive equilibrium equation for the neutral constituents to obtain an analytical expression for the distributions of O, O_2, N_2, H and He. The result is

$$n = n_{120} \left(\frac{1 - a}{1 - a \exp(-\sigma\xi)} \right)^{1+\gamma} \cdot \exp(-\sigma\gamma\xi) \ , \qquad (4.34)$$

where n is the number density, n_{120} is the number density at 120 km,

$$a = \frac{T_\infty - T_{120}}{T_\infty} \ ,$$

α is the thermal diffusion coefficient (equal to - 0.38 for He and zero for N_2, O_2, O and H), and

$$\gamma = \frac{m(X) g_{120}}{\sigma k \ T_{120}} \ ,$$

where m(X) is the molecular mass of constituent X, g_{120} is the gravitational acceleration at 120 km and equal to 944.1 cm. s^{-1} ,k is the Boltzman's constant and the other variables are as defined before. For the minimum night-time temperature, T_0, and the temperature at 120 km, T_{120}, we used the following values T_0 = 700°K and T_{120} = 310°K.

For the neutral constituent number densities at 120 km we have adopted the following values:

$$n_{120}(O) = 1.11 \times 10^{11} \text{ cm}^{-3} \ , \quad n_{120}(O_2) = 2.99 \times 10^{11} \text{ cm}^{-3} \ ,$$

$n_{120}(N_2) = 2.27 \times 10^{11}\ cm^{-3}$ and $n_{120}(He) = 1.6 \times 10^{7}\ cm^{-3}$.

Figure 4 shows the variation with local time of the concentrations of O, O_2 and N_2.

The value of hydrogen at 120 km is chosen such that equation (4.34) gives a specified value for n(H) at 400 km. The variation of atomic hydrogen at 400 km used in these calculations is based on the results of Brinton and Mayr (1972) and is $\left\{2.2 + 0.65 \sin\left(\frac{\pi T}{43200}\right)\right\} 10^{5}\ cm^{-3}$,

where T is the local time in seconds. Figure 5 shows the atomic hydrogen variation at 400 km over 24 hours. Figure 6 shows the He number densities profiles at mid-day and midnight.

For the meridional neutral wind we have used the same model as Murphy et al. (1976).

For the electron and ion temperatures, we adopt the following. For altitudes at and below 1000 km the observed values of Evans (1967) are combined with those of Brace et al.(1967). This involves interpolation with respect to height and time. For altitudes higher than 1000 km we set $T_i = T_e$ and we constructed a model to calculate these temperatures. Observational results (Serbu and Maier, 1970; Sanatani and Hanson, 1970; Brace et al., 1974; Maher and Tinsley, 1977) suggested that there are substantial altitudes gradients in plasma temperature at high altitudes. We therefore imposed a uniform gradient in our ion and electron temperatures above 1000 km. The value of this uniform gradient is 5×10^{-6} cm^{-1} during the day-time and 2.5×10^{-6} cm^{-1} during the night-time. Around sunrise and sunset we assume the gradient to vary linearly between the day-time and night-time. Figure 7 shows the electron and ion temperatures variation over 24 hours for selected altitudes. Further details of electron and ion temperatures are given by Murphy et al. (1976).

4.3 Results

As mentioned earlier the He^+ calculations are carried out for a period of ten days starting at 06.00 local time on the first day. The integration is started with a relatively low He^+ tube content (all tube contents are quoted for the magnetic tube at L = 3 with a cross section of 1 cm^2 at 1000 km). The sets of calculations carried out are summarized in Table 1. We first discuss our standard model A. Our initial He^+ tube content is approximately 4×10^{10} cm^{-2} and the corresponding He^+ equatorial number density is 0.64 cm^{-3}. Even with this relatively low He^+ tube content which characterises conditions in the subsonic recovery phase following a magnetic storm at sunspot minimum, there are downward fluxes of He^+ through the 1000 km level of magnitude 10^5 cm^{-2} s^{-1} in the evening (the corresponding tube content is 1.4×10^{11} cm^{-2}). In the sunspot maximum calculations of Murphy et al. (1979), they noticed similar behaviour with downward He^+ fluxes of magnitude 8×10^5 cm^{-2} s^{-1} (the corresponding tube content was of magnitude 3.8×10^{11} cm^{-2}).

In these calculations He^+ continues to flow downwards through the 1000 km level in the evening and the early morning hours throughout the ten day integration period. Figure 8 shows the behaviour of the He^+ flux at 1000 km and 4400 km for day 9. Contrary to this, the H^+ fluxes were upwards on the first two days of the integration and started to flow downwards in the evenings from day 3 onwards. In the morning hours H^+ fluxes were upwards until the 7th day of the integration period where the H^+ tube content reached a relatively large value (7.07×10^{13} cm^{-2}); then it started to flow downwards in the early morning hours. In the sunspot maximum calculations of Murphy et al. (1979), they found that H^+ and He^+ flows oppose each other in the early morning hours throughout the integration period. This may be partly due to the fact that they have used the same daily behaviour pattern for O^+/H^+ throughout their calculations. Murphy et al. (1979) calculated O^+/H^+ results for four days and used the O^+/H^+ behaviour pattern of the fourth day throughout the integration period for He^+. Consequently the day to day change of H^+ was not allowed to influence He^+; the H^+ tube content of the fourth day was relatively low. In addition, at sunspot maximum, Bailey et al. (1979) have suggested that H^+ can flow upwards throughout the night for several nights following a magnetic storm, whereas at sunspot minimum a down flow of H^+ is more likely at night (Murphy et al. 1976). The contrasting flows of H^+ and He^+ are enhanced by the fact that helium ions are four times heavier than hydrogen ions. However, this feature and the different behaviours of H^+ at sunspot minimum and sunspot maximum can be associated with the production processes for the two ions.

We mentioned earlier that the only production process for helium ions in our model is photoionization. Consequently any production at night occurs high in the magnetic flux tube (i.e. in the part of the tube that lies outside the Earth's shadow) and relatively little He^+ is produced. Therefore He^+ would be expected to flow downwards at night. Production and loss of H^+ arises from the reversible charge exchange reaction

$$O^+ + H \rightleftarrows O + H^+$$

and there is either a net production or a net loss of the H^+ above 450 km (H^+ and O^+ are in chemical equilibrium below this level). Thus the direction of the H^+ flow through the 1000 km level is largely influenced by the net production from this reaction, which in turn depends upon the relative concentration of the constituents involved. Consequently, when H^+ densities are relatively low, there can be a net production of H^+ at night-time that results in upward flow of H^+.

The results of the He^+ calculations for the first day are characterized by a rapid increase in the He^+ tube content. On the first day the He^+ tube content increased from 4×10^{10} cm^{-2} at 06.15 local time to 1.433×10^{11} cm^{-2} at midnight. From Figure 10 it is noted that on the early days of the integration very little of the He^+ produced during the day-time is lost during the night-time. As the integration continues, the He^+ tube content net increase gets smaller and at day eight the He^+ tube content net increase was just 1.33×10^{10} cm^{-2} (Figure 11) compared to 1.2×10^{11} cm^{-2} on the second day. After eight days of integration the He^+ tube content began to decrease. One might expect the He^+ layer to reach a state where it repeats its daily behaviour from day to day. In the sunspot maximum calculation of Murphy et al.(1979), the He^+ tube content continued to increase and its net increase on the eighth day was as high as 2.5×10^{11} cm^{-2}. However, since Murphy et al. (1979) used the O^+/H^+ results of the fourth day throughout their calculations, their H^+ densities, from the fifth day of the He^+ integration period onwards, are under-estimated. Greater H^+ densities and smaller He^+ densities would probably have resulted if the post-storm replenishment of the H^+ had been allowed to continue. For the calculations carried out here the H^+ tube content reached the value 8.8×10^{13} cm^{-2} on the ninth day compared to 5.5×10^{13} cm on the fourth day. Thus our results appear to indicate that the day to day increase in the H^+ tube content limits the day to day increase in He^+ tube content to the extent that the He^+ content actually starts to decrease from the eighth day onwards. We carried out two tests to investigate the He^+ behaviour. In the first test (model B, see Table 1) we carried out calculations similar to Murphy et al. (1979) but with sunspot minimum parameters. We repeated the He^+ calculations using the same daily pattern of behaviour for the O^+/H^+ number densities and fluxes for each day of the He^+ integration. The O^+/H^+ results of the fourth day were used to calculate the He^+ number densities and fluxes over ten days. The results of these calculations were similar to those presented by Murphy et al. (1979), namely our He^+ tube content continued to increase even after ten days of integration. For these new calculations (set B) the He^+ tube content at the end of the eighth day was 7.9×10^{11} cm^{-2} compared with 6.2×10^{11} cm^{-2} from our standard results. In Figure 10 we show a comparison between the two He^+ tube content variations over ten days. It is clear that the He^+ content is suppressed as the H^+ content continues to increase. This results in the He^+ content reaching its maximum on the eighth day and the He^+ content will probably continue to decrease until H^+ is fully replenished. It is not possible to determine the extent to which an increasing He^+ content limits the H^+ replenishment from these results since He^+ is treated as a minor ion. This limitation is removed in Chapter VI.

To examine how the build-up of H^+ limits the He^+ replenishment we have repeated the calculations of the ninth day with He^+ - H^+ collision frequency reduced by a factor of 5 (model C, see Table 1) compared to model A. This allowed the He^+ ions to flow more freely. The result shows a substantial increase in the He^+ tube content. Figure 12 shows a comparison between the two He^+ tube contents for models A and C. It therefore appears that the fall off in the He^+ content from day eight onwards, is associated with the larger He^+ - H^+ collision frequency due to the continuing replenishment of H^+. As this collision frequency increases throughout the post-storm replenishment the diffusion of He^+ through H^+ is impeded. It is therefore harder for the He^+ that is produced during the day-time to escape to greater altitudes. This results in more recombination of He^+ and less upward flow.

Figure 9 shows the eighth day He^+ profiles at different local times and the He^+ midday profile for the first day of the integration period. The He^+ profiles exhibit single peaks during the early days of the integration period. These peaks are around 450 km during the day-time and about 800 km during the night-time. At later stages of the integration when the He^+ tube content is sufficiently large, the He^+ profiles exhibit two peaks, with the upper peaks being a result of the balance between diffusion and the electrostatic field which is strongly influenced by O^+. The lower peak results from production processes and consequently disappears at night-time since He^+ is produced by photoionization. We have already noted that the small amount of He^+ that is produced during the night-time is produced high in the magnetic flux tube, outside the Earth's shadow.

From Figure 9 we notice that when two peaks are present they are very close to each other. They are separated only by about 100 km. In the sunspot maximum calculations of Murphy et al. (1979) the two peaks were well separated. A possible explanation for this difference is that at sunspot minimum the O^+ number densities are smaller than at sunspot maximum. Consequently the electrostatic field will be weaker at sunspot minimum and this results in the He^+ upper peak forming at lower altitudes.

Because of the day-time double peaks and the night-time single peaks in the He^+ profiles, we do not present the diurnal behaviour of the maximum number density in the He^+ profiles. Instead we show the number density variation at different altitudes. Figure 13 shows the He^+ number density variation at selected heights on the eighth day.

Although there are some differences, the results, in general, are similar to those presented by Murphy et al. (1979). Via its contribution to the electrostatic field the O^+ layer has a strong influence on He^+ behaviour at all heights but particularly at lower altitudes. During the day-time He^+ is displaced upwards by the O^+ layer producing a day-time maximum at greater altitudes. During the evening the He^+ collapses on top of the decaying O^+ layer. This results in a rapid increase in He^+ concentrations at lower heights. However, the increase is short lived. In the later evening hours recombination dominates at lower heights leading to a decrease in the He^+ densities. Mathematically the behaviour of He^+ at these altitudes depends on whether the divergence or recombination loss term dominates in the continuity equation. The pre-midnight decrease in the He^+ number density at 700 km, for example, differs from the results presented by Murphy et al. (1979). In the calculation of Murphy et al. the influx of He^+ was more than sufficient to offset the loss due to recombination.

Comparing Figure 13 to the corresponding results of Murphy et al. (1979) we see that the main differences in the time variations occur at lower altitudes. The results of Murphy et al. (1979) show a deeper day-time trough. Apart from the different sunspot parameters our model B is similar to the model used by Murphy et al. (1979). To investigate these differences at lower altitudes we compare the results at 700 km from our model B to the results from our standard model (see Table 1). The He^+ number densities at 700 km for these two models are shown in Figure 14 for the eighth day, along with corresponding H^+ densities. The results from our model B also produce a deep day-time trough. It therefore appears that the deep trough results from the artificially enforced lower H^+ densities used in model B and the model of Murphy et al. (1979). The lower H^+ densities allowed enhanced He^+ diffusion.

The results of Figure 13 and of Murphy et al. (1979) also differ at lower altitudes in the late evening and early morning periods. A similar difference is also apparent in the model A and model B results of Figure 14. Concentrating on the results of Figure 14, these differences can be linked to the fact that, on day eight, the He^+ content for the B model is considerably greater than the content for the A model (see Fig. 10). Consequently a greater downward flow of He^+ would be expected for the B model at night-time. For the broken curve (model A) there is not sufficient downward flow of He^+ to allow the divergence term in the continuity equation to offset the loss term associated with recombination.

In general there is less variation in the number densities at all heights shown in Figure 13 compared to the corresponding curves shown in Murphy et al. (1979). This can be explained in terms of the limited He^+ diffusion associated with the greater H^+ number densities.

Unfortunately it is not possible to provide a comparative description of the behaviour of He^+ at sunspot minimum and sunspot maximum. The differences between the sunspot maximum results of Murphy et al. and the sunspot minimum results presented here are dominated by the fact that Murphy et al. used the same O^+/H^+ behaviour on each day of the He^+ integration period.

4.4 Conclusions

The O^+, H^+ and He^+ time-dependent continuity and momentum equations have been solved using the procedure described in Chapter II with He^+ being treated as a minor ion. The effect of the two major ions, O^+ and H^+, on He^+ have been taken into account and thermal diffusion has been included. We have examined the behaviour of the He^+ number densities and fluxes over a period of ten days, beginning with a relatively low He^+ tube content on the first day. This low content is chosen to characterize conditions in the subsonic recovery phase following a magnetic storm at sunspot minimum.

Throughout the whole integration period He^+ flowed upwards during the day-time and downwards at night-time. Even on the first day there was a return flow of He^+ at night-time. The He^+ profiles exhibit single peaks during the early days of the integration period. These peaks are around 450 km during the day-time and around 800 km during the night-time. After four days of integration the He^+ profiles exhibit double peaks during the day-time hours and whenever these double peaks exist they are very close to each other. This is due to a relatively weak electrostatic field compared to the sunspot maximum results of Murphy et al. (1979) where the peaks were widely spaced during the day-time.

The He^+ tube content started from about 4×10^{10} cm^{-2} and increased, reaching a maximum value of 6.8×10^{11} cm^{-2} on the eighth day of the integration when it began to decrease. This behaviour of the He^+ tube content is due to the large amount of H^+ present at the later stages of the integration period. The He^+ tube content will probably continue to decrease until the H^+ reaches full replenishment. In the sunspot maximum calculations of Murphy et al. (1979) the He^+ tube content did not reach a maximum but continued to increase throughout the entire integration period. Our results indicate that this was not due to the sunspot maximum parameters but was a result of solving the O^+/H^+ equations for four days and using the results from the fourth day on every day of the He^+ integration period. This was confirmed by repeating our sunspot minimum calculations with a similar restriction. In such calculations the H^+ concentrations are under-estimated from the fifth day of the He^+ integration period onwards. Consequently the He^+ can diffuse more freely.

Calculations were carried out with the He^+ - H^+ collision frequency reduced by a factor of five; the He^+ tube content increased substantially. Consequently He^+ - H^+ collisions are important and help restrict He^+ to lower altitudes during the later stages of replenishment following a magnetic storm. In the later stages of replenishment, less H^+ flows upwards during the daytime and more H^+ flows downwards at night-time. Consequently the decrease in the net upward flux of H^+ causes a decrease in the net upward flow of He^+ and more He^+ recombines at lower altitudes.

The He^+ number density variation at all heights is strongly influenced by the O^+ electrostatic field, resulting in a daytime trough at low altitudes and a daytime maximum at greater altitudes. The decay of O^+ in the evening leads to an evening maximum in the He^+ concentration at lower altitudes and a decrease in He^+ concentration at higher altitudes. It therefore appears that the behaviour of He^+ is strongly influenced by the O^+ contribution to the electrostatic field, but that the behaviour is dampened in the later stages of replenishment due to collisions with H^+.

The calculations of Murphy et al. (1979) indicated that He^+ was lost by magnetic storms rather than converted to neutral helium leading to a loss process for neutral helium. However,it appears that this feature of their results was a consequence of the use of the O^+/H^+ results of the fourth day throughout the He^+ integration period. Our calculations indicate that the way in which He^+ is lost depends on the frequency of the magnetic storms. If the period between the magnetic storms is less than eight days then the He^+ will be lost via magnetic storms, but during magnetically quiet periods (greater than eight days) He^+ is lost by recombination with O_2 and N_2 producing neutral helium.

A	Standard model in which both H^+ and He^+ are allowed to replenish from day to day over the integration period. He^+ is treated theoretically as a minor ion. Sunspot minimum parameters are described in section (4.22)
B	As in set A except that only He^+ is allowed to replenish from day to day. O^+/H^+ calculations are carried out for four days and the behaviour on the fourth day is used throughout the He^+ calculations. Similar calculations were carried out by Murphy et al. (1979) but with sunspot maximum conditions.
C	As in set A but with the He^+ - H^+ collision frequency reduced by a factor of 5.

Table 1

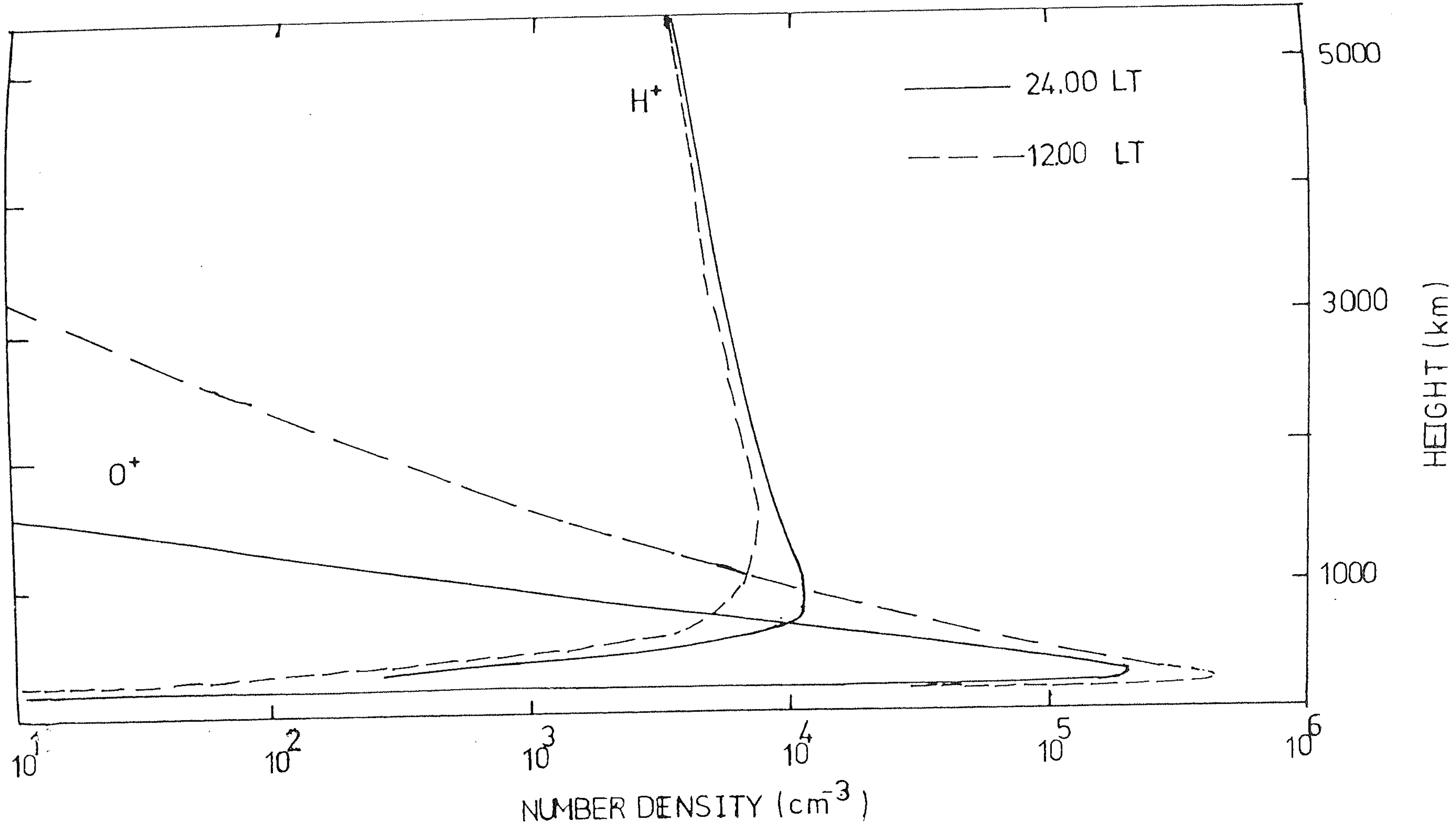

Figure 1. Height profiles of O^+ and H^+ at midday and midnight on day eight of the integration period.

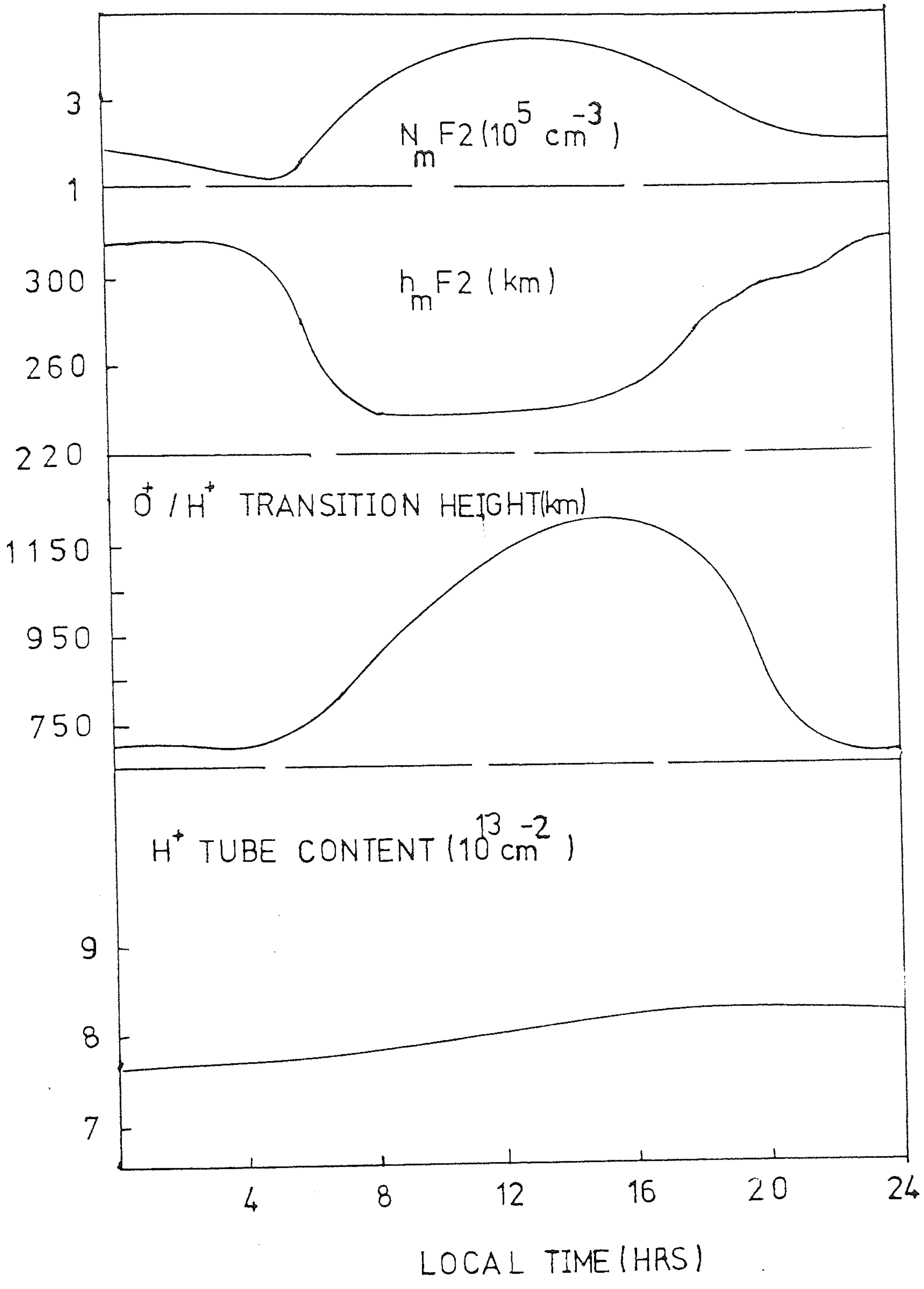

Figure 2. Diurnal variations of N_mF2, h_mF2, O^+/H^+ transition height (height at which $n(O^+) = n(H^+)$) and H^+ tube content on day eight of the integration period.

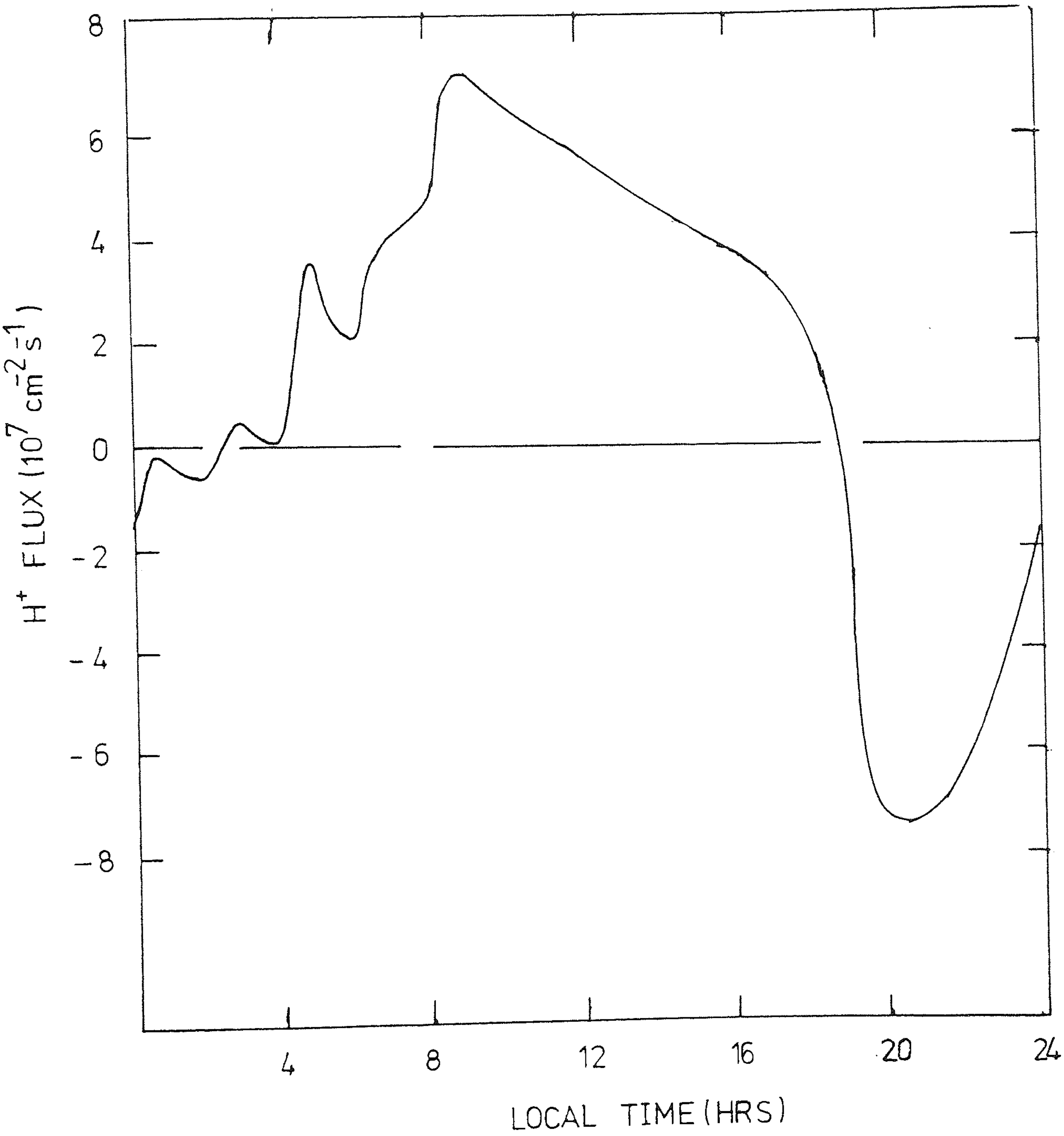

Figure 3. Diurnal variation of the H^+ flux through the 1000 km level on day eight of the integration period.

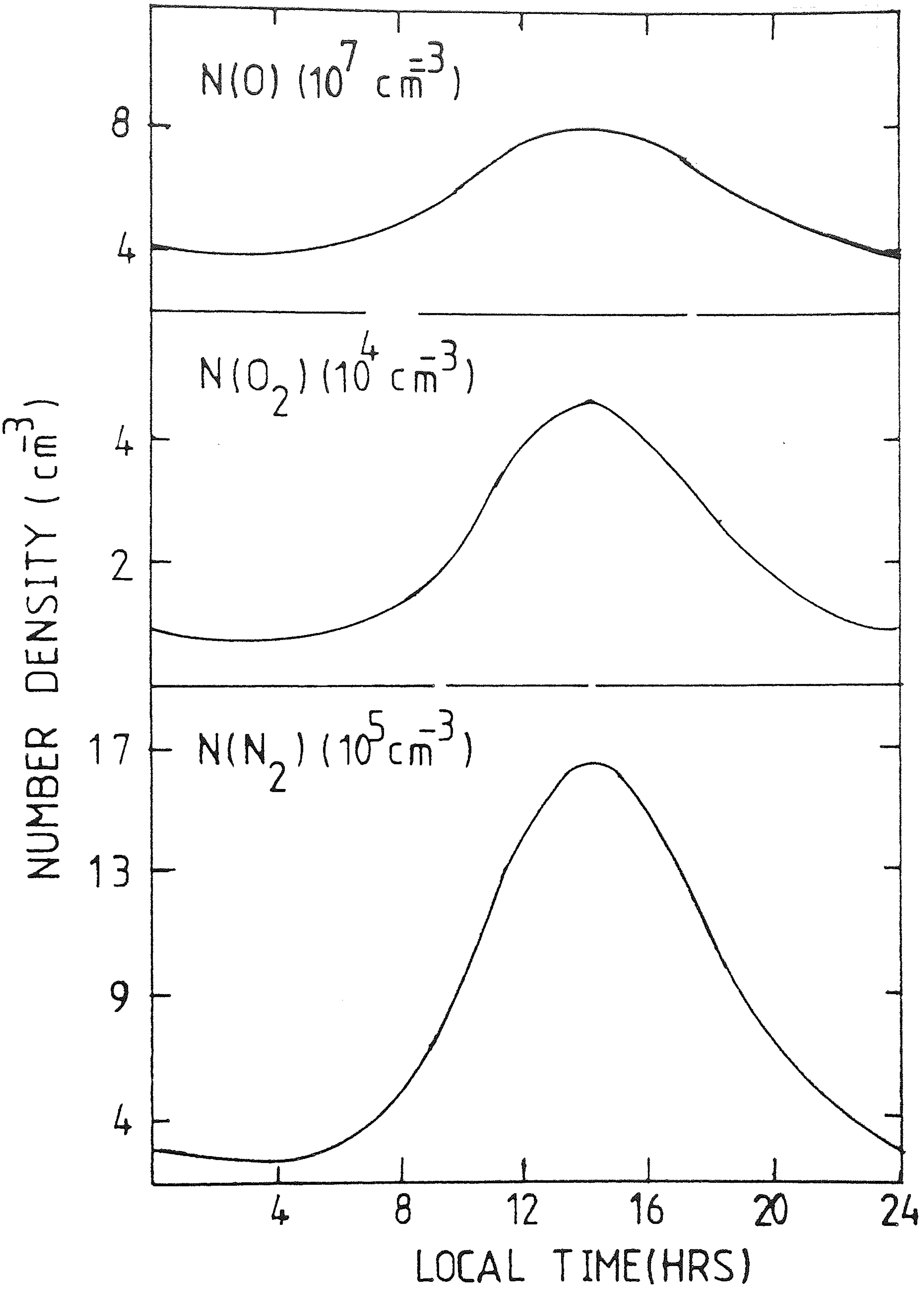

Figure 4. The diurnal variation of the number densities of the neutral constituents, O, O_2 and N_2 at 300 km for sunspot minimum conditions.

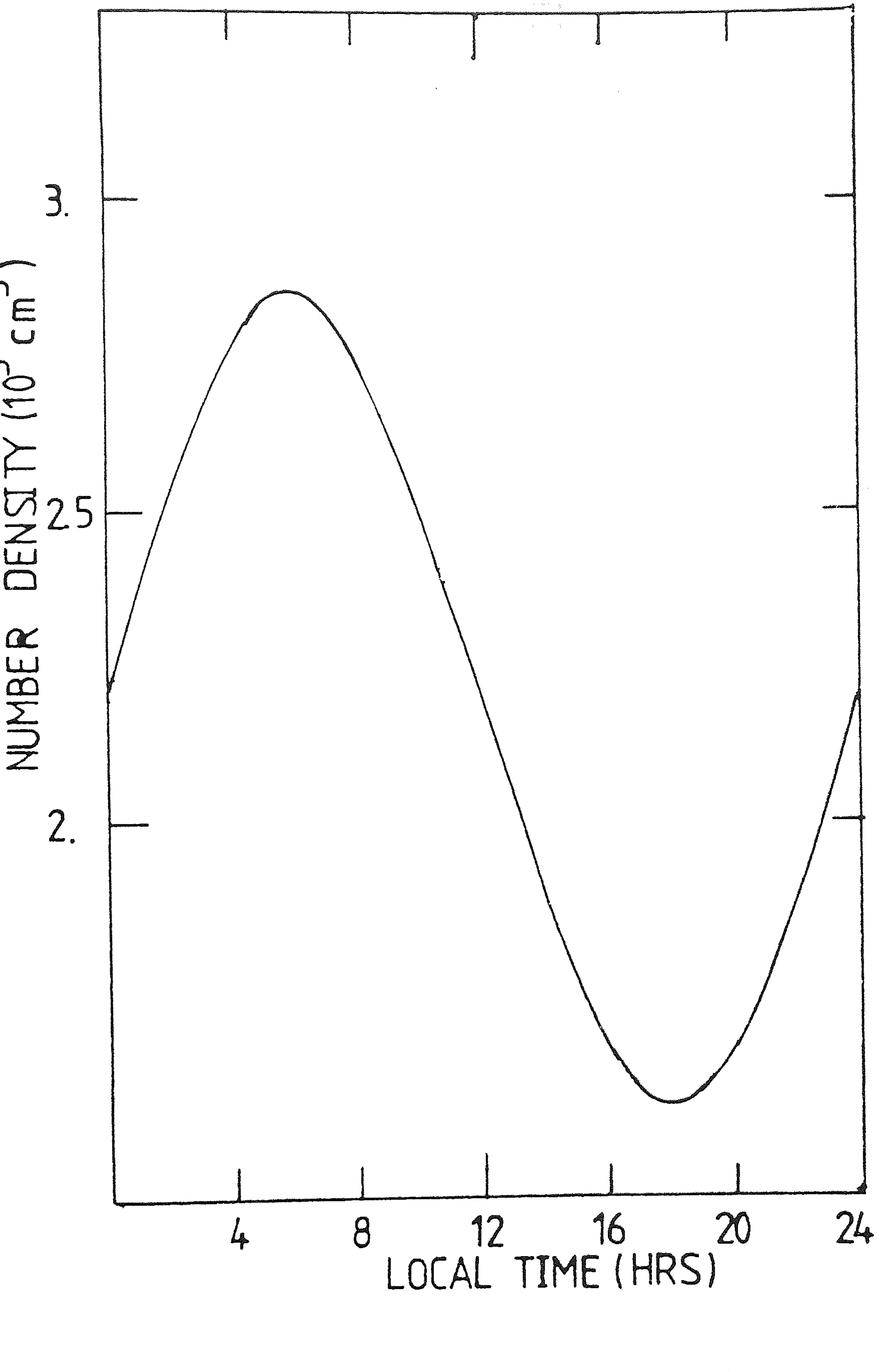

Figure 5. The diurnal variation of the number density of atomic hydrogen at 400 km for sunspot minimum conditions.

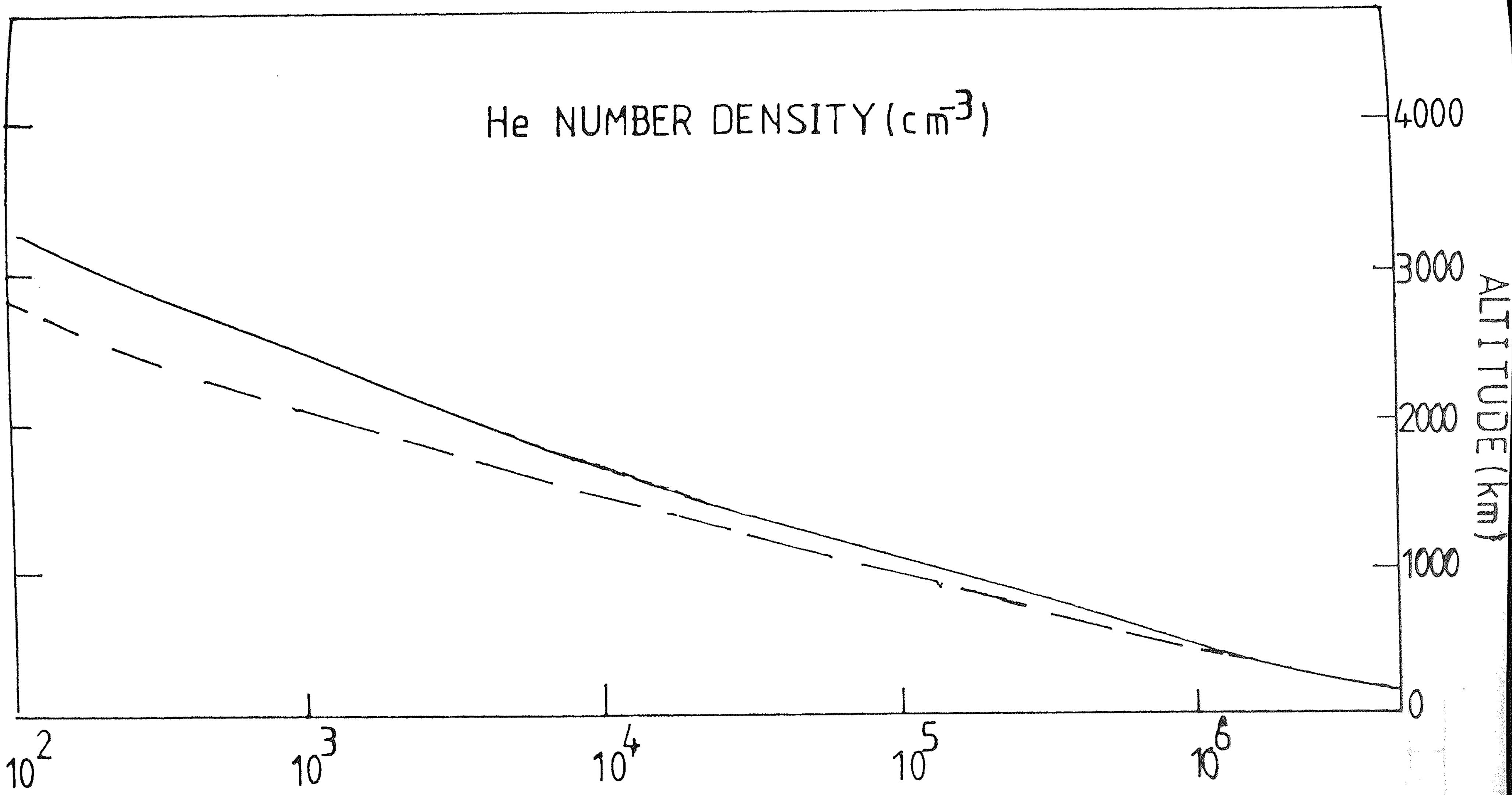

Figure 6. Altitude profiles for the neutral helium density at midday and midnight for sunspot minimum conditions.

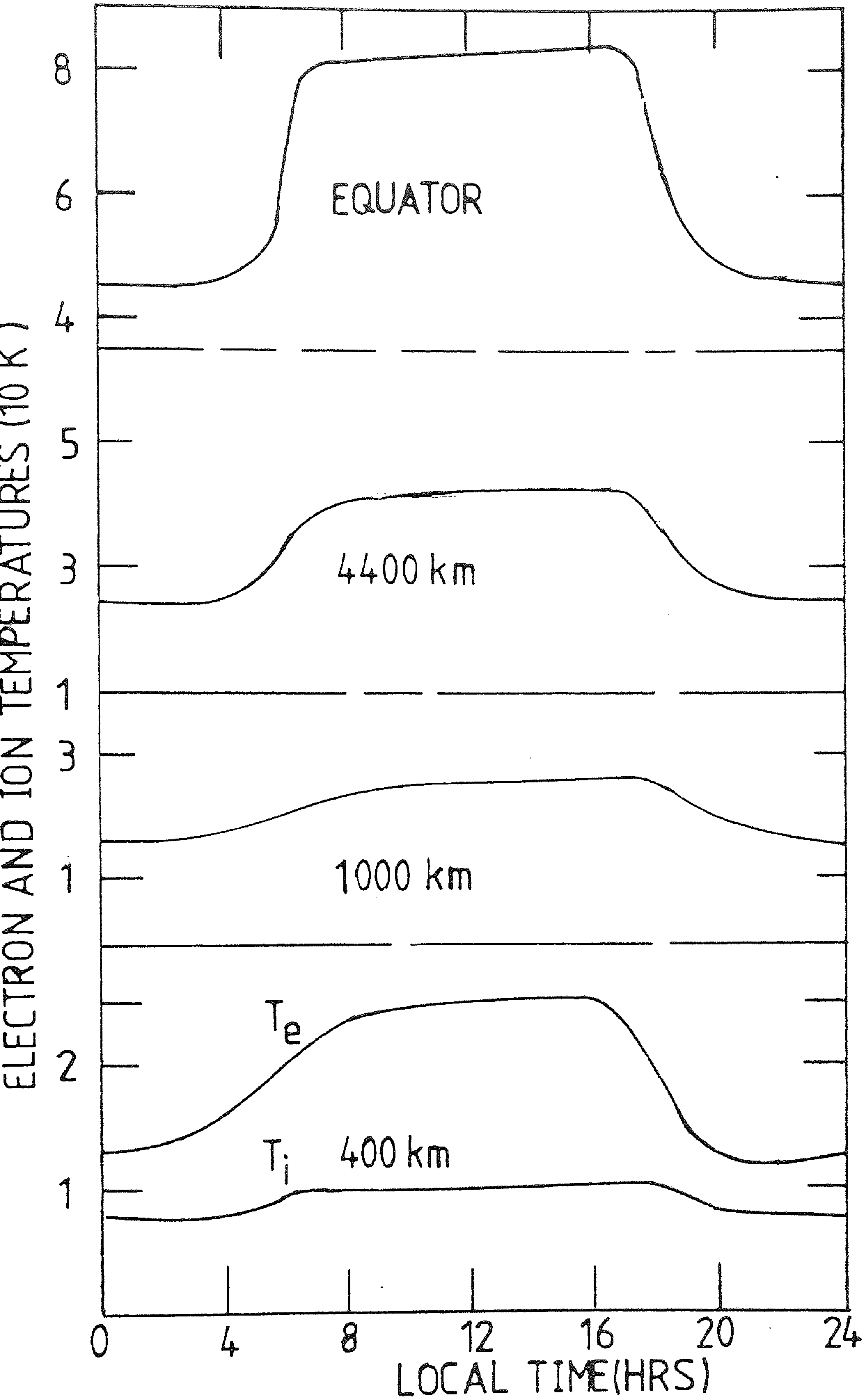

Figure 7. Diurnal variations of electron and ion temperatures at selected altitudes (at and above 1000 km $T_i = T_e$).

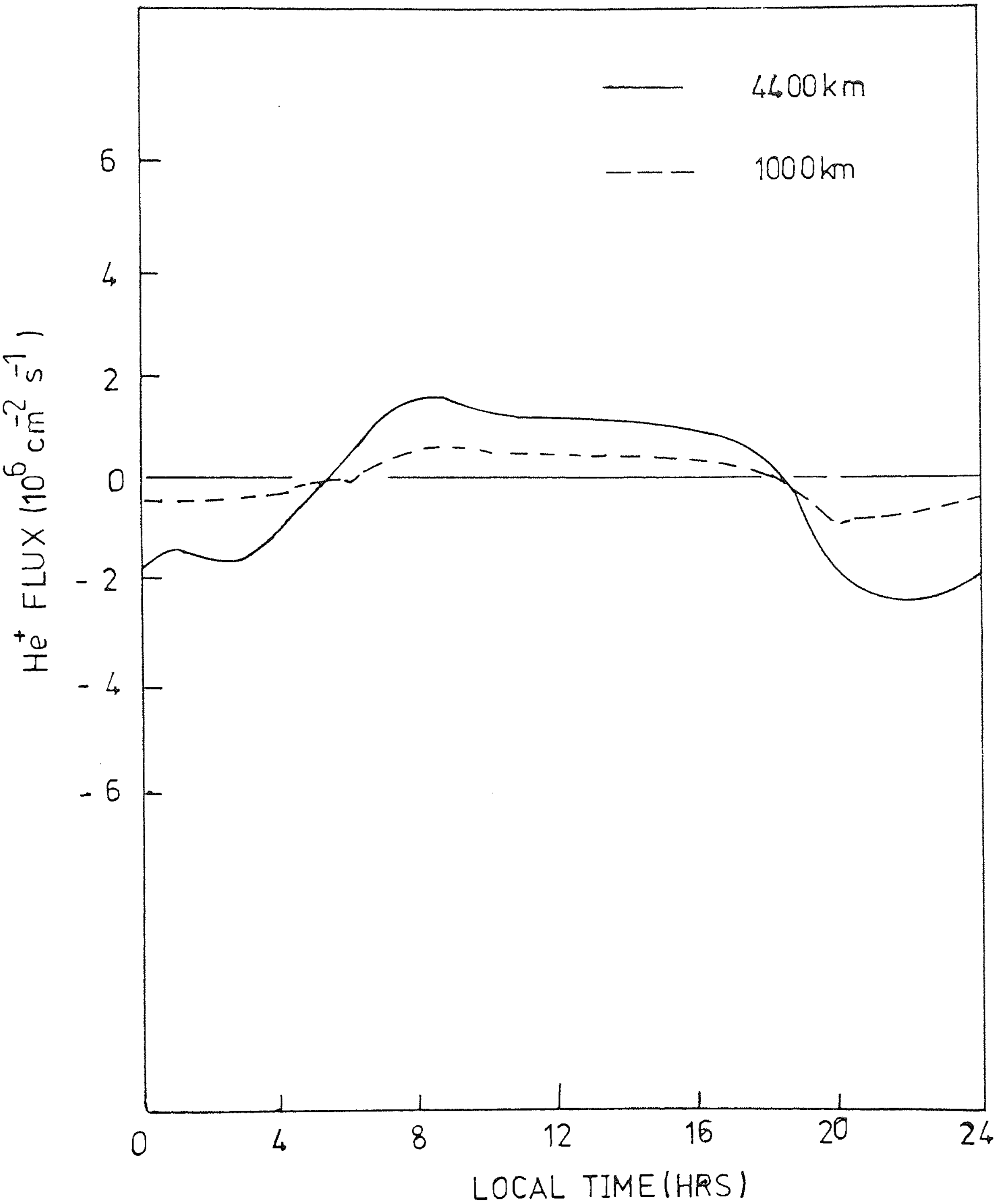

Figure 8. The diurnal variations of He$^+$ flux through the 4400 km and 1000 km levels on the eighth day of the integration period (set A).

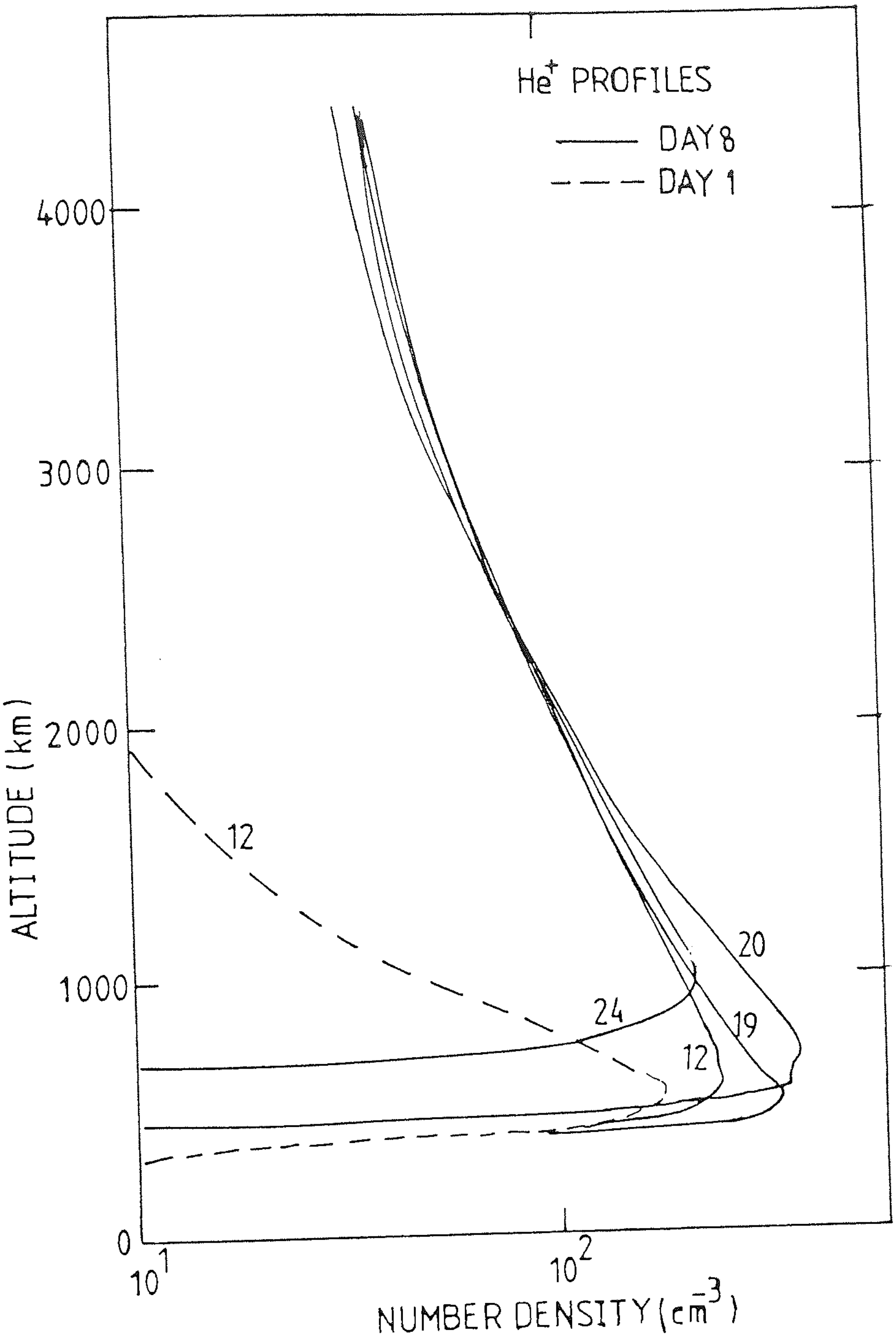

Figure 9. He$^+$ altitude profiles at selected local times on day eight (set A) compared to midday profile of the first day of the integration period. The selected local times are indicated on the curves.

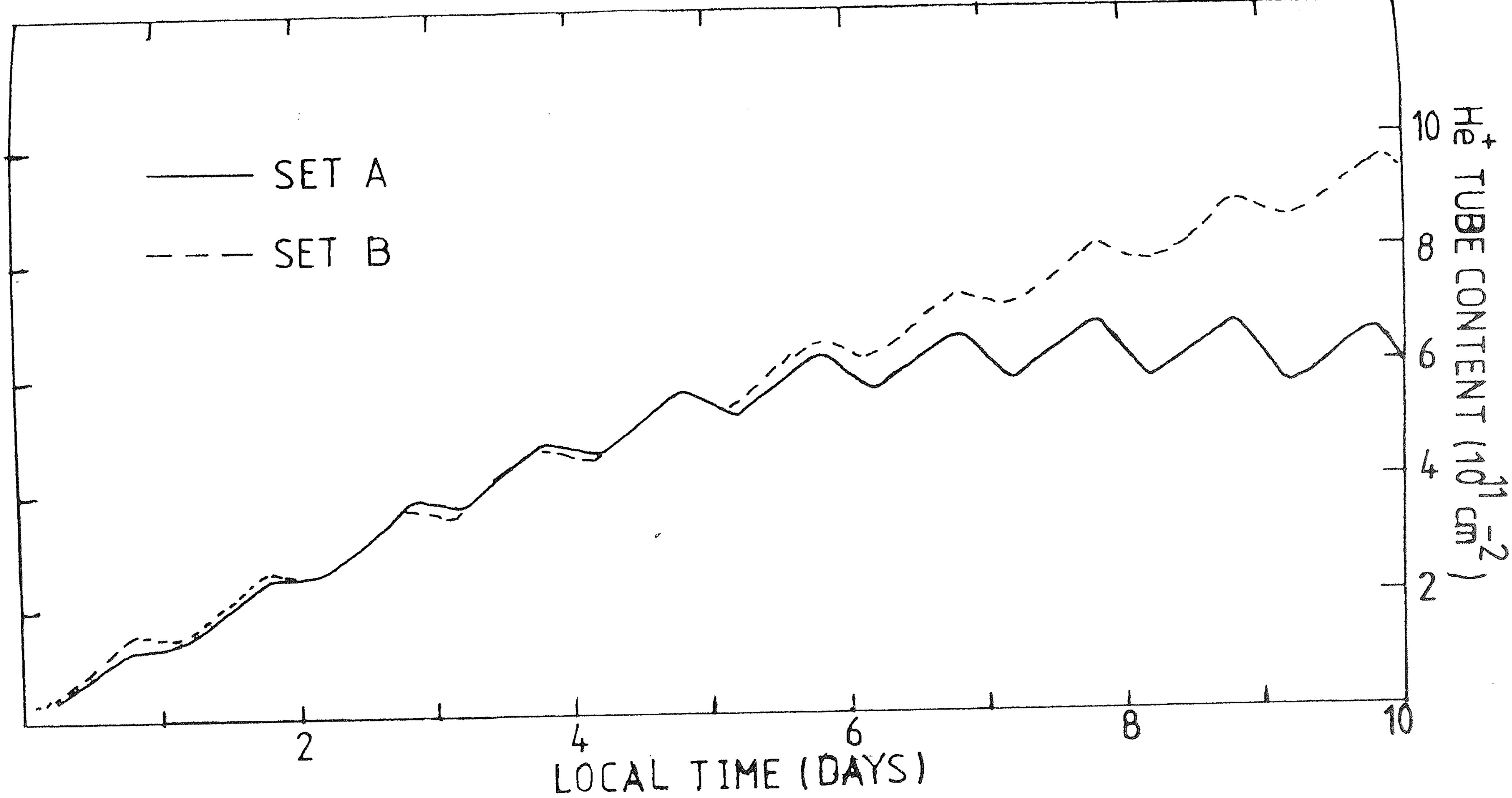

Figure 10. A comparison between the He$^+$ tube contents of sets A and B of the calculations (see Table 1).

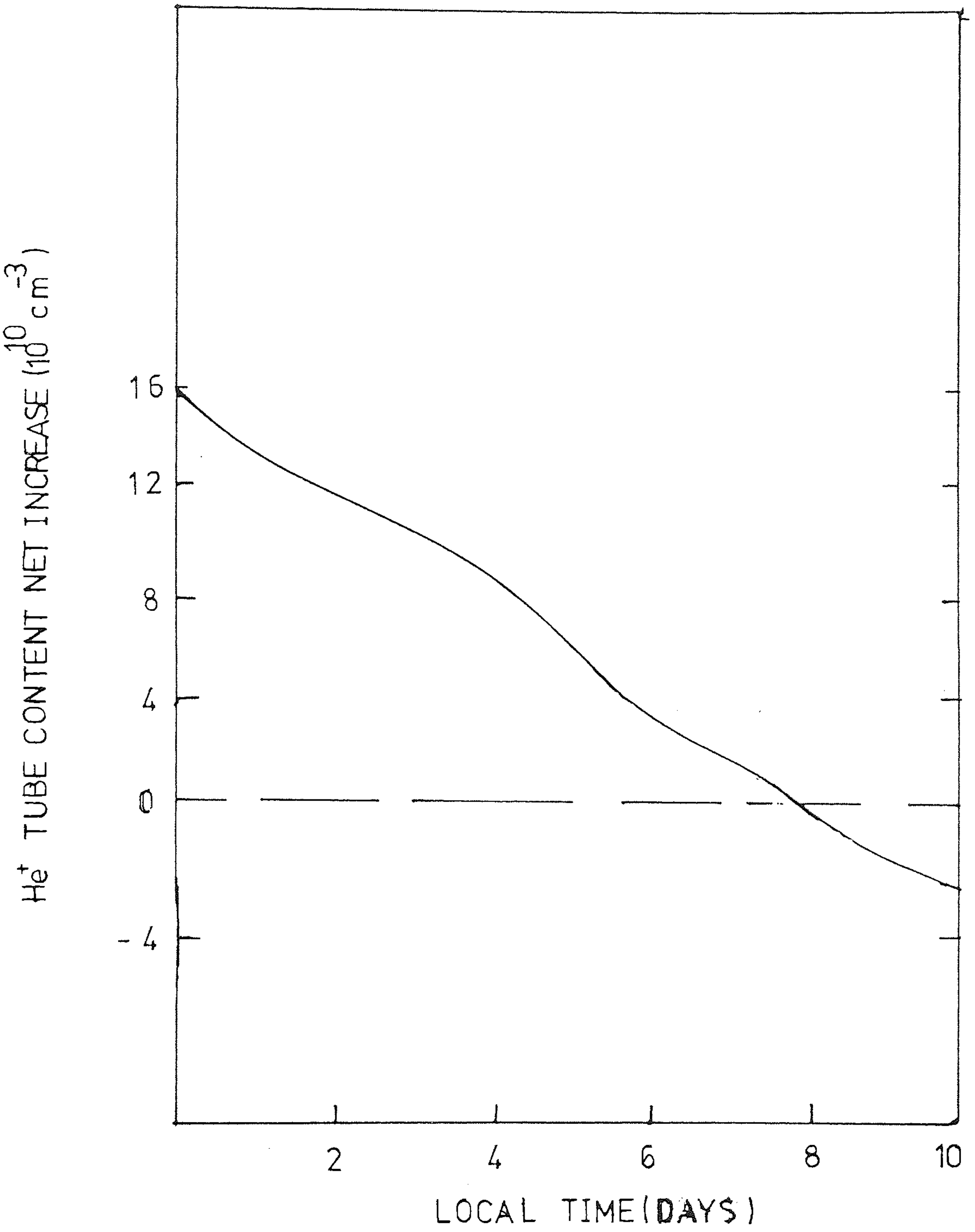

Figure 11. The behaviour of the net increase of the He^+ tube content from day to day for set A of our calculations.

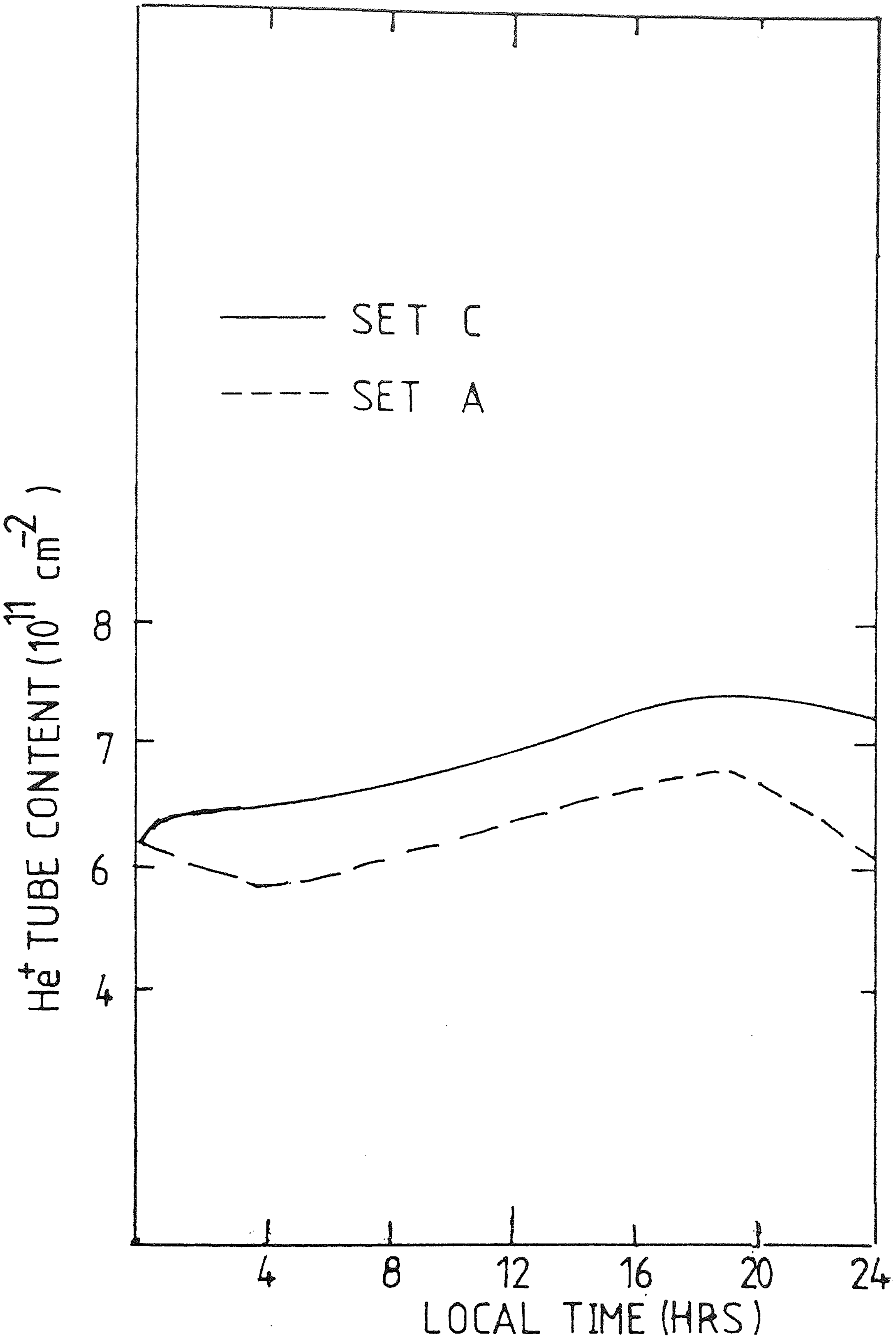

Figure 12. A comparison between the He^+ tube contents of sets A and C (see Table 1) on the ninth day of the integration period.

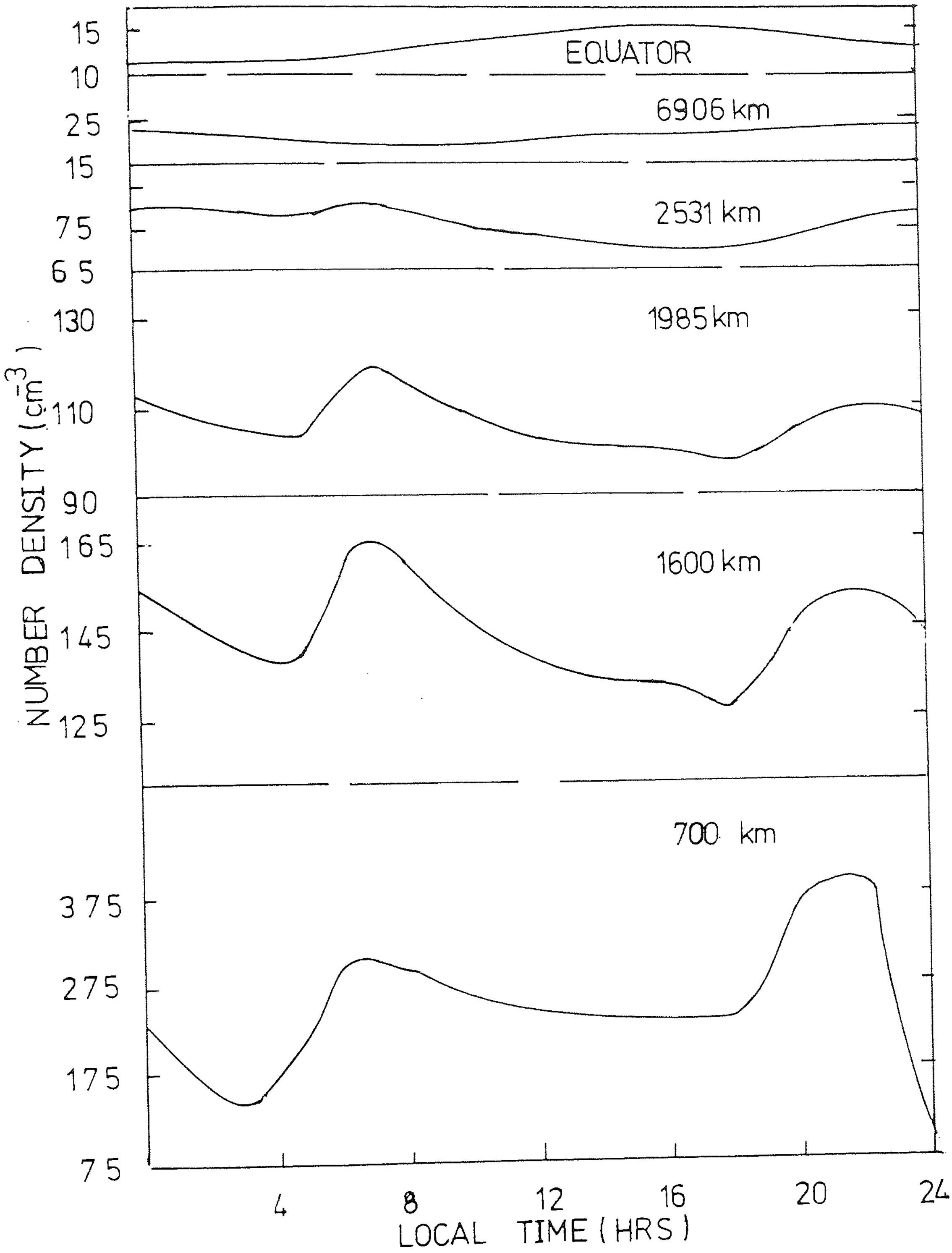

Figure 13. The diurnal variation of He^{+} number density at selected altitudes on the eighth day of the integration period for set A.

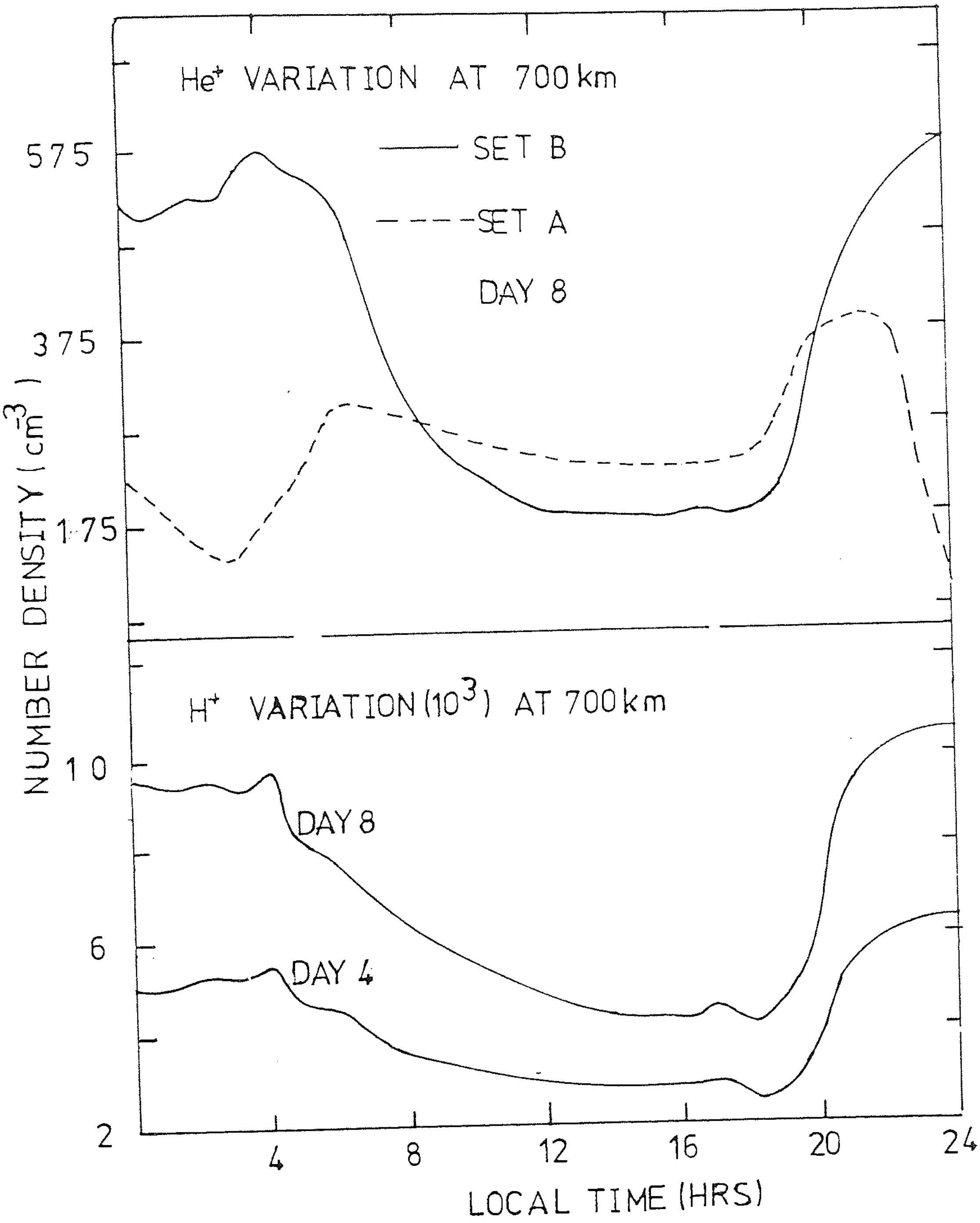

Figure 14. The diurnal variation of He^+ number density at 700 km for sets A and B on day eight with the corresponding H^+ diurnal variations at the same altitude.

V. A THEORETICAL STUDY OF DOUBLY CHARGED ATOMIC OXYGEN IN THE MID-LATITUDE PLASMASPHERE

5.1 Introduction

Doubly charged oxygen ions, O^{++}, were observed in 1967, when Hoffman (1967) reported the detection of the doubly charged ions of oxygen and nitrogen in the topside ionosphere using the mass spectrometer on Explorer 31. Since then, only limited works concerning O^{++} have been carried out. Such works were carried out by Nakada and Singer (1968), Schunk and Walker (1969), Walker (1970) and Heelis et al. (1972). In the work of Nakada and Singer (1968) they assumed a steady state and calculated the concentration of O^{++}, O^{+}, He^{+} and other ions for different conditions. In their study they pointed outthe importance of thermal diffusion at altitudes higher than 1000 km. They also pointed out that with a certain temperature gradient $\left(\frac{\partial T}{\partial r} \geq 2 \times 10^{-5}\ K/cm\right)$ thermal diffusion exceeds pressure diffusion at all altitudes above 1000 km and there was a possibility that the O^{++} concentrations will be greater than the H^{+} concentrations beyond 2.5 Earth radii. In the work of Walker (1970), he solved the O^{++} equations for a limited range of altitudes in the topside ionosphere. Walker (1970) neglected the effect of the chemical loss processes for the doubly charged oxygen ions, assuming that the rate coefficient for the chemical reactions resulting in loss of O^{++} were too small to affect the calculations. Walker's results showed that the O^{++} density increases slowly with altitude and the ratio O^{++}/O^{+} was about 10^{-2} at 500 km. A common difficulty in the early O^{++} studies was the uncertainty of the O^{++} chemical loss rates. Since that early work on O^{++}, considerable work has been carried out to determine the O^{++} chemical loss processes and their reaction rates (Breig et al., 1977; Johnson and Biondi, 1978; Victor and Constantinides, 1979; Howorka et al., 1979 and Geiss and Young, 1981). Breig et al. (1979) analysed the O^{++} measurements made by the Atmosphere Explorer C satellite for altitudes where photochemical equilibrium conditions prevail to determine the photochemical sources and sinks of O^{++}. They found that the O^{++} ions were produced mainly by the photonization of O^{+} and they pointed out that the ionization of the neutral atomic oxygen could be a major source for O^{++} at lower altitudes. Breig et al. (1977) also suggested that O^{++} could be lost through the chemical reactions

$$O^{++} + O \rightarrow O^{+} + O^{+} \qquad (5.1)$$

$$O^{++} + N_2 \rightarrow O^{+} + \text{Products} \qquad (5.2)$$

$$O^{++} + O_2 \rightarrow \text{Products} \quad . \qquad (5.3)$$

The reaction rate coefficients for the reactions (5.1), (5.2) and (5.3) will be given in section 5.3.

More recently Geiss and Young (1981) conducted a study to investigate the high values of O^{++} and its presence at high altitudes in the Earth's plasmasphere and also the magnetosphere. Although Geiss and Young (1981) solved the O^{++} equations they did not solve the O^{+}/H^{+} equations but rather they constructed a model based on some observations and the sunspot minimum calculations of Murphy et al. (1976). In their model they used constant bulk flow velocities below 2000 km and they did not differentiate between the O^{+} and the H^{+} velocities, i.e. both were assumed to have the same velocity. Geiss and Young found that thermal diffusion was the only possible explanation for the observations of $O^{++}/ O^{+} \sim 1$ in the equatorial plasmasphere. They also noted that there was a threshold temperature gradient between ionosphere and equatorial plasmasphere, corresponding to an equatorial temperature at $L = 3$ of 5000°K, below which thermal diffusion becomes ineffective.

In this work we investigate the O^{++} behaviour at all altitudes above 200 km for $L = 3$. This is achieved by solving the time-dependent continuity and momentum equations of O^{+}, H^{+} and O^{++}. The integration is carried out for a period of twenty days for our standard model. In these calculations O^{++} is treated as a minor ion with O^{+} and H^{+} treated as major ions. In our standard set of calculations we use similar temperature profiles to Geiss and Young (1981). Since these temperatures, based on GEOS 1 data at the equator, have little diurnal variation, we also perform a set of calculations in which the diurnal variation of the temperature is more pronounced. The latter temperature model was used in the study of O^+/H^+ behaviour at sunspot maximum by Bailey et al. (1979). These two temperature models are described in section 5.3.

5.2 Equations.

As seen in Chapter II, the O^+, H^+ and O^{++} continuity and momentum equations were derived using the formulation of St. Maurice and Schunk (1976). Referring to equations (2.64) and (2.65) of Chapter II, the O^{++} continuity equation is given by

$$\frac{\partial n_4}{\partial t} + B \frac{\partial}{\partial s} \left(\frac{\phi_4}{B} \right) = P_4 - L_4 \qquad (5.4)$$

and the O^{++} momentum equation takes the form

$$\begin{aligned} \frac{kT_i}{m_4} \frac{\partial}{\partial s} (\log(n_4)) = & -g \sin I - \frac{k}{m_4} \frac{T_e}{n_e} \frac{\partial n_e}{\partial s} - 0.392 \frac{k}{m_4} \frac{\partial T_e}{\partial s} \\ & - \frac{k}{m_4} \frac{\partial T_i}{\partial s} + \frac{k}{m_4} \beta \frac{\partial T_i}{\partial s} - \Big[\nu_{41} (1 - \Delta_{41}) + \\ & + \nu_{42} (1 - \Delta_{42}) \Big] \frac{\phi_4}{n_4} + \frac{\nu_{41}}{n_1} (1 - \Delta_{41}) \phi_1 + \\ & + \frac{\nu_{42}}{n_2} (1 - \Delta_{42}) \phi_2 \end{aligned} \qquad (5.5)$$

where the variables are as defined in Chapter II. The terms involved in the last equation arise from gravity, the electrostatic field, the partial pressure gradient in the O^{++} gas, thermal diffusion and collisions with the major ions, O^+ and H^+. Although the O^{++}, O^+ and H^+ equations are coupled, the assumption that O^{++} is a minor ion removes the dependence of O^+ and H^+ on O^{++}. This means, the two calculations can be separated and therefore solve the O^+ and H^+ equations first to obtain the number densities and fluxes of the two major ions. These densities and fluxes are then available to carry out the O^{++} calculations. As noted in Chapter II, the O^+ equations are solved using the Laasonen procedure and the H^+ and O^{++} equations are solved using the searching method with the numerical integration achieved via a predictor-corrector method. Thus, for O^{++} a search is carried out to find a suitable value for $n(O^{++})$ at the equator which produces an acceptable solution, i.e. a solution that agrees with the physical condition at the lower boundary.

The lower boundary condition for O^{++} is obtained by making a numerical approximation to the equation

$$\frac{\partial n_4}{\partial t} = P_4 - L_4 \quad , \tag{5.6}$$

which is the O^{++} continuity equation with the divergence term neglected. Using the approximation

$$\frac{\partial n_4}{\partial t} = \frac{n_4(t) - n_4(t - \Delta t)}{\Delta t}$$

and the fact that $L_4 = \ell_4 n_4$, equation (5.6) takes the form

$$n_4(t) = \frac{P_4 \Delta t + n_4(t - \Delta t)}{1 + \Delta t \ell_4} \quad .$$

In the daytime, $\frac{\partial n_4}{\partial t}$ is negligible and the lower boundary condition is equivalent to photochemical equilibrium. At night-time when $P_4 \simeq 0$, the application of (5.7) causes the O^{++} number density to decay at lower altitudes. The lower boundary condition is imposed at a height of 650 km and the O^{++} number density helow this height is calculated using equation (5.7).

The numerical integration of equations (5.5) is carried out for $L = 3$, from the equator (at about 12739 km) to about 200 km down the field line. The integration period for our standard set of calculations is twenty days.

5.3 Atmospheric Parameters

O^{++}- Production Processes.

The doubly charged oxygen ions are produced by the photoionization of O^+ (Walker, 1970; Breig et al, 1977; Victor and Constantinides, 1979; Geiss et al., 1978). We adopt the value of rate coefficient used by Geiss and Young (1981) which is $1.6 \times 10^{-7}\ s^{-1}$. Therefore the production rate for this process is given by

$$P_4(O^+) = 1.6 \times 10^{-7} \exp\left[-1.5 \times 10^{-17} \sum_i \tau_i\right] n(O^+) \mathrm{cm}^{-3}\ \mathrm{s}^{-1}, \qquad (5.8)$$

where τ is the optical depth, given in Appendix A, and the sum is over the neutral constituents atomic oxygen, nitrogen and molecular oxygen.

The other production source which we consider for O^{++} is the double photoionization of atomic oxygen (Victor and Constantinides, 1979). Victor and Constantinides (1979) pointed out that this process is very important and could dominate at lower altitudes. They estimated the rate coefficient for this process to be $2 \times 10^{-9}\ \mathrm{s}^{-1}$. However, for comparison, we adopt the value used by Geiss and Young (1981) which is $1.5 \times 10^{-9}\ \mathrm{s}^{-1}$. Thus the production rate from this source is taken as

$$P_4(O) = 1.5 \times 10^{-9} \exp\left[1.5 \times 10^{-17} \sum_i \tau_i\right] n(O) \mathrm{cm}^{-3}\ \mathrm{s}^{-1} \qquad (5.9)$$

where the variables are as given before.

The O^{++} ions are produced by Auger process following K shell ionization. We neglected the effect of this process since it has been shown (Victor and Constantinides, 1979) that this process is negligible compared with the previous two processes. Thus the total O^{++} production is given by

$$P_4 = P_4(O^+) + P_4(O)$$

The O^{++} Loss Processes.

The O^{++} ions are lost via the charge exchange reactions (Breig et al., 1977).

$$O^{++} + O \xrightarrow{k_1} O^{+} + O^{+} \quad ,$$

$$O^{++} + N_2 \xrightarrow{k_2} \text{Products} \quad ,$$

and
$$O^{++} + O_2 \xrightarrow{k_3} \text{Products} \quad .$$

The reaction rate k_1 has been estimated by Breig et al. (1977) to be 1×10^{-11} $cm^{-3}s^{-1}$. The other reaction rates, k_2 and k_3, have been measured by Johnson and Biondi (1978) and Howorka et al. (1979). We adopt the values 1.4×10^{-9} $cm^{-3}s^{-1}$ for both k_2 and k_3. These values were also used by Geiss and Young (1981). We have neglected the O^{++} losses due to charge exchange with H and He since they have been shown to have minor effects on the O^{++} results (Geiss and Young). Thus the total loss term for the O^{++} ions is given by

$$L_4 = (10^{-11} n(O) + 1.4 \times 10^{-9} n(O_2) + 1.4 \times 10^{-9} n(N_2) n(O^{++}) \qquad (5.10)$$

with the neutral constituents O, O_2 and N_2 calculated using the neutral atmosphere described in Chapter IV with atmospheric conditions appropriate to sunspot maximum. The neutral parameters at 120 km are given by

T_0 = 1000 K (915 for set B), T_{120} = 350 K ,

$n_{120}(O) = 1.2 \times 10^{11}\ \text{cm}^{-3}$, $n_{120}(O_2) = 5 \times 10^{10}\ \text{cm}^{-3}$,

$n_{120}(N_2) = 3. \times 10^{11}\ \text{cm}^{-3}$.

The value of 1000 K is used to be consistent with Geiss and Young (1981). The variation of atomic hydrogen at 500 km used in these calculations is based on the results of Brinton and Mayr (1972) and is

$$H_{500}(T) = 10^{4}(6.15 + 1.55 \sin(\Omega \times T + 0.5236)) \qquad (5.11)$$

where T is local time in seconds and $\Omega = 7.2722 \times 10^{-5}$.

Two different models are used for the ion and electron temperatures. We use the temperature profiles described by Geiss and Young (1981) for set A of our calculations (see Table 1). These temperature profiles are calculated using the form

$$T = C_1 + \frac{C_2}{r^2}, \qquad (5.12)$$

where r is the distance from the centre of the Earth. The constants C_1 and C_2 are determined by the temperatures at the equator (8000 K for daytime and 7000 K during night-time) and 1000 km (2400 K for the daytime and 2000 K for the night-time) and we restrict the temperature not to be less than 1000 K at the lower altitudes. For this set of calculations T_i(ion temperature) = T_e(electron temperature) at all altitudes. As noted by Geiss and Young (1981) the equatorial temperatures are based on data from GEOS 1.

For set B (see Table 1), we adopt the following. For altitudes below 900 km, the electron temperatures, T_e, are based on data obtained at Millstone Hill (L = 3.2) and supplied by J. V. Evans and J. E. Salah (private communication with G. J. Bailey). Less information is available on temperatures for altitudes greater than 900 km and therefore a model is constructed. Observational results (Serbu and Maier, 1970; Sanatani and Hanson, 1970; Brace et al, 1974; Maher and Tinsley, 1977) suggested that there are substantial altitude gradients in plasma temperatures at high altitudes. We have therefore imposed a uniform gradient in T_e above 900 km. The value of this gradient is 0.8 $\mathrm{K\,km^{-1}}$ during the daytime and 0.4 $\mathrm{K\,km^{-1}}$ during the nighttime. Around sunrise and sunset, we assume the gradient to vary linearly between the day and night.

The ion temperature, T_i, is obtained at all altitudes by equating the ion thermal energy input from electron-ion collisions to that lost through ion-neutral collisions (Bailey et al., 1979). At high altitudes T_i equals T_e.

Figure 1 shows the variations of the neutral concentrations of O, O_2 and N_2 with local time at 300 km and the variation of the atomic hydrogen at 500 km. Figure 2a shows the variation with local time of the two temperature models at selected altitudes. Figure 2b shows the temperature profiles used in our standard set (set A).

Although we have carried out O^+/H^+ calculations for sunspot maximum conditions, the O^+/H^+ results will not be discussed in detail in this chapter since such results have been given by Bailey et al. (1979). Therefore the O^+/H^+ results will only be discussed where they affect the O^{++} calculations. In Figure 3a, we show the behaviour of N_mF2 and h_mF2 on day eight for the two sets of calculations A and B. Figure 3b shows the behaviour of O^+-flux through the 750 km level and H^+-flux through 1000 km over twenty-four hours on day eight (set A) and in Figure 3c we show the H^+-content over twenty days.

Finally it is noted that we have carried out some additional calculations to investigate the important physical processes. In these additional calculations either the standard set of parameters or terms in the O^{++} momentum equation have been modified. These modifications are summarized in Table 1.

5.4 Results.

The O^+, H^+ and O^{++} number densities and fluxes are calculated along a mid-latitude magnetic flux tube at $L = 3$ from an altitude of 200 km to the equator (at an altitude of 12739 km). It has already been noted that O^{++} is treated as a minor ion. Thus first we calculate the O^+/H^+ results over the complete integration period and determine the O^{++} results using the corresponding O^+/H^+ variables at each fifteen minute stage of the integration period (a time step of fifteen minutes was used). Low initial O^{++}(and H^{+}) densities were chosen to characterize conditions in the subsonic recovery phase following a magnetic storm. The initial O^{++} profile was calculated assuming chemical control at low altitudes and diffusive equilibrium at greater altitudes. The tube content of this O^{++} profile was 8.6×10^{8} cm^{-2} (as in previous chapters all flux tube contents are quoted for a magnetic flux tube at $L = 3$ with a cross section of 1 sq cm at 1000 km altitude) and the maximum and the equatorial values of $n(O^{++})$ were 2.0 cm^{-3} and 1.1×10^{-2} cm^{-3} respectively.

We produce several sets of results. The parameters for our standard set A are similar to those used by Geiss and Young (1981). The other results are produced to investigate the effect of various physical processes and are obtained by varying some of the parameters in the standard set. These variations are summarized in Table 1.

With the obvious exception of the behaviour of O^{+} at the equator, in general O^{+}/H^{+} behaviour is only discussed in relation to its influence on the behaviour of O^{++}. Detailed theoretical studies of O^{+}/H^{+} behaviour following a magnetic storm have already been carried out (Murphy et al., 1976; Bailey et al., 1977; Bailey et al., 1979). Some of the important O^{+}/H^{+} parameters are shown in Figure 3b for the eighth day of the integration period, whereas there is little change in the behaviour of O^{+} over each day of the integration period. The H^{+} number densities increase from day to day throughout the post storm replenishment period. Therefore we show the behaviour of the H^+ content over the twenty day integration period in Figure 3c.

We first discuss the behaviour of O^{++} in our standard set A where we have tried to retain similar parameters to those used by Geiss and Young (1981). In particular we use similar temperature profiles. However, our model differs from that used by Geiss and Young (1981) in that they do not solve the O^+/H^+ continuity and momentum equations. Instead, they construct model O^+ and H^+ densities and fluxes based on observations from GEOS 1 and OGO 6 and calculations of Murphy et al. (1976). In our model the O^+/H^+ calculations have been carried out using the same neutral atmosphere and ion and electron temperatures as used in the O^{++} calculations. This consistency may be important when discussing the ratio $n(O^{++})/n(O^+)$. Because of this our calculated equatorial O^+ values differ from those used by Geiss and Young (1981) which were based on GEOS 1 mass spectrometer data. These authors used values of 0.3 cm^{-3} and 1 cm^{-3} for equatorial $n(O^+)$ in the night-time and daytime respectively. The variation of O^+ (and O^{++}) at the equator, obtained from our calculations, is displayed in Figure 4 for the first twelve days of the integration period. Although our daytime maximum of approximately 1.2 cm^{-3} does not vary significantly from the values used by Geiss and Young (1981), our night-time values drop to around 5×10^{-2} cm^{-3}. It was suggested by Geiss and Young that the daily O^+ variation at the equator, obtained from theoretical calculations, may be exaggerated by assuming that 0^+ is in diffusive equilibrium above a certain altitude in the topside ionosphere. In all of the results presented here we have assumed that 0^+ is in diffusive equilibrium above 2000 km. However, we have varied this altitude to examine its influence on 0^+ at the equator and found very little difference in the results. To replace this assumption by the equinox condition of zero flux at the equator it would be necessary to take much smaller step lengths at greater heights compared to those used at present (see section 2.4). This would result in a considerable increase in the amount of computer time needed to calculate the densities and fluxes of all three ions. In addition, we note that 0^+ is in pseudo-diffusive equilibrium in the topside ionosphere due to the lack of importance of collisions compared to other processes. It is interesting to note that for the 0^+ - H^+ collision term to be comparable to the gravitational acceleration term in the 0^+ momentum equation in the topside ionosphere, the 0^+ ions would need to be flowing with a Mach number of 5 or more. The value has been determined from our results between 1500 km and 2000 km at midday on the eighth day of the integration period. The corresponding 0^+ fluxes would be of the order 10^9 cm^{-2} s^{-1}. It therefore appears that the variation of 0^+ at the equator is not strongly influenced by the assumption of diffusive equilibrium above 2000 km. Thus the variation of 0^+ at the equator, obtained from the limited GEOS 1 mass spectrometer data, leaves an interesting problem to be resolved. In addition, an interesting feature of the behaviour of O^+ at the equator is evident in Figure 4. The maximum daytime number density of O^+ at the equator falls steadily throughout the integration period. We have not examined this feature in detail but it is probably linked to the increasing H^+ content. It cannot be linked to O^{++} behaviour since O^{++} is treated as a minor ion and therefore has no influence on O^+ behaviour in our model. Note also that a similar feature is probably not evident in the O^{++} behaviour because of the prominent role of thermal diffusion which we discuss in more detail later.

Apart from the night-time behaviour of O^+ at the equator the results of our standard set are in general agreement with the results of Geiss and Young (1981). From Figure 4 it is clear that the O^{++} concentrations exceed the O^+ concentrations at the equator from the fifth day onwards, and that the O^{++} concentrations continue increasing throughout the integration period. This is also evident in Figure 5 where we show the equatorial value of the ratio $n(O^{++})/n(O^+)$ for 13.00 LT on each day of the integration period.

The results of our standard set A are in agreement with the findings of Geiss and Young, that thermal diffusion is responsible for large amounts of O^{++} at the equator. Starting from the end of day seven for set A, we have repeated the O^{++} calculations for days eight, nine and ten with the thermal diffusion term omitted from the O^{++} momentum equation (set C). The dot-dashed curve of Figure 4 shows the resulting O^{++} densities at the equator. The conclusions are self-evident in Figure 4. As soon as thermal diffusion is omitted the O^{++} number densities fall rapidly at the equator. No regular diurnal pattern of behaviour of the equatorial O^{++} number density is evident over the three days for which thermal diffusion was omitted. This irregular behaviour is a consequence of there being too much O^{++} in the flux tube for this parameter set at the start of the eighth day and the behaviour would probably continue until the O^{++} tube content falls to a sufficiently low value. However, these results emphasize the importance of thermal diffusion and its influence on the O^{++} flux tube content and O^{++} number densities near the equator.

In Figure 6 we show the diurnal variation of O^{++} at selected altitudes for sets A, C and D on day eight (see Table 1). In particular the dashed curve gives some indication of how the O^{++} layer redistributes itself when thermal diffusion is neglected. The O^{++} layer rapidly collapses with O^{++} number densities decreasing at greater altitudes. At 2500 km $n(O^{++})$ initially increases due to an influx from greater altitudes, but decreases after about an hour due to the O^{++} flowing to even lower altitudes. This decrease is offset at 08.00 LT when the daytime temperature profile is introduced. In the absence of thermal diffusion O^{++} behaviour is strongly influenced by the O^{+} contribution to the polarization electric field, which in turn depends on the electron temperature. The dot-dashed results (set D) shown in Figure 6 have been obtained by solving the O^{++} equations with the polarization electric field decreased by a factor of 100 in the O^{++} momentum equation. The initial distributions were taken from the end of the seventh day for set A. The effect is as expected. More O^{++} is allowed to remain at lower altitudes with the consequence that there is less O^{++} at greater altitudes. At 04.00 LT, for example, the equatorial value of $n(O^{++})$ drops from 2.0 cm^{-3} for the standard set A to 1.5 cm^{-3} for set D.

The effect of thermal diffusion on the O^{++} layer is also illustrated in Figure 7 where we compare O^{++} height profiles at midday on the eighth day for the standard set A and set C in which thermal diffusion is neglected. Over the range 2000 - 7000 km approximately there is a marked difference between the O^{++} scale heights in the two profiles. The explanation is clearly evident from Figure 8 where we show the height profiles of the thermal diffusion term and O^{+} contribution to the polarization field term corresponding to curve A of Figure 7. These terms from the O^{++} momentum equation are given in the same units as gravity. The significant point is that thermal diffusion becomes the dominant term from just below 2000 km upwards.

Returning to Figure 5, it can be seen that the O^{++}/O^{+} ratio at the equator is only increasing very slightly after 15 days. Note that this figure only shows the O^{++}/O^{+} ratio for 13.00 LT on each day for easy comparison with Figure 3 of Geiss and Young (1981). After twenty days this ratio has only reached a value of 3.2 compared to approximately 10 in the results of Geiss and Young (1981), and it certainly looks as though it would not exceed 4 if we continued our results for a further twenty days. The corresponding O^{++} concentrations for the twentieth day are 3.3 cm^{-3} (set A) and approximately 10 cm^{-3} (Geiss and Young, 1981). Although we have used the same temperature profiles as Geiss and Young, this difference arises almost entirely from thermal diffusion effects. At 1000 km the thermal diffusion coefficient in the O^{++} momentum equation of Geiss and Young is a factor of four larger than the value arising in our results. Sample values of the thermal diffusion coefficient are shown in Table 2, where we compare our values to those used by Geiss and Young. Our values have been taken from mid-day on the eighth day and we have used the daytime 'day-infinity' values of $n(O^+)$ and $n(H^+)$ to calculate the values used by Geiss and Young. From Table 2 it can be seen that the difference in the values arises partly from the different formulations of the thermal diffusion coefficient and partly from the different values of the ratio $n(H^+)/n(O^+)$. We calculate the O^{++} thermal diffusion coefficient using the formulation of St. Maurice and Schunk (1976), whereas Geiss and Young use

$$\alpha = 11.2 - \frac{18}{n(H^+)/n(O^+) + 2.22} \qquad (5.13)$$

to calculate the O^{++} thermal diffusion coefficient. Using this expression with our ratio $\frac{n(H^+)}{n(O^+)} = 0.0968$ at 1000 km over-estimates the O^{++} thermal diffusion coefficient, from the results of set A which uses the formulation of St. Maurice and Schunk (1977), by 85%. When the ratio used by Geiss and Young at 1000 km, $n(H^+)/n(O^+) = 2.5$, is substituted into the above expression it takes the value 7.39 compared to 1.85 obtained in our standard set A. It therefore appears that the O^{++} number densities at the equator, calculated by Geiss and Young (1981) are over-estimated due to the use of equation (5.13). Their equatorial O^{++} number densities are also enhanced, compared to ours, due to the fact that their ratio $n(H^+)/n(O^+)$ is greater than the value calculated in our results. This indicates the sensitivity of the equatorial O^{++} number densities to the ratio $n(H^+)/n(O^+)$ or the $O^+ - H^+$ transition height. Thus large values of $n(H^+)/n(O^+)$ in the topside ionosphere or equivalently low $O^+ - H^+$ transition heights provide favourable conditions for large amounts of O^{++} to exist at the equator. Indeed, it would be more favourable for temperature gradients to exist above the $O^+ - H^+$ transition height rather than below the transition height.

To examine the effects of the $O^{++} - O^+$ collision frequency we have calculated results for day eight with this collision frequency reduced by a factor of 100 (set E). This resulted in a reduction in O^{++} number densities at almost all altitudes. The exception was at altitudes below approximately 750 km just after 20.00 LT. The switch to night-time temperature profiles resulted in a sudden collapse of the O^+ profile and for set A O^{++} ions below 750 km are dragged into the recombination region. The reduction of the drag-term by a factor of 100 excludes this effect from set E. Consequently O^{++} number densities for set E exceeded corresponding number densities for set A, at 750 km for example, for a short period just after 20.00 LT. Returning to the general effect, the O^{++} tube content changed from a value of 1.062×10^{11} cm^{-2} at the end of the seventh day to 1.168×10^{11} cm^{-2} and 8.311×10^{10} cm^{-2} for set A and E respectively at the end of the eighth day. For set E the O^{++} tube content decreased steadily throughout the day and there was a downward flux of O^{++} at almost all altitudes throughout the day. The maximum downward flux through 1000 km occurred at 21.00 LT and had magnitude 5.815×10^5 cm^{-2} s^{-1}. The reduction in O^{++} - O^+ collision frequency allowed the O^{++} ions to diffuse relatively freely through the O^+ layer to regions of high recombination. The reduction in the O^{++} content indicates that less than eight days are required for the O^{++} layer to reach total replenishment with this reduced collision frequency. It therefore appears that the O^{++} - O^+ collision frequency is an important parameter influencing the O^{++} contents, the replenishment time and the amount of O^{++} at the equator. However, the latter was only slightly affected. At 18.00 LT, for example, the O^{++} number densities at the equator for sets A and E on the eighth day are 2.2 cm^{-3} and 1.8 cm^{-3} respectively. The situation is clarified in Figure 7 where the midday profiles for sets A and E are shown. As expected, the bottom of the layer has the main reduction due to the reduced collision frequency.

Thermal diffusion restricts the downward flow of O^{++} from the top of the layer.

The role of the O^{++} - O^{+} collision frequency leads to the conclusion that large amounts of O^{++} are more likely to be present at the equator at sunspot maximum rather than sunspot minimum. This situation may be counteracted by the lower values of the O^{++} thermal diffusion coefficient due to the high O^{+} - H^{+} transition altitude. However, if one also considers the production mechanisms and the importance of temperature gradients, it does appear that sunspot maximum conditions are more favourable than sunspot minimum conditions for O^{++} to exist in appreciable quantities at the equator.

The results of our calculations for set B showed considerably different behaviour to the results of set A. As indicated in Table 1, sets A and B differ in that different model temperature profiles are used. The diurnal variation of the temperatures at selected heights are shown in Figure 2a for sets A and B. Starting with the same initial profiles as set A, the results for set B were produced over a fourteen day integration period. One of the main differences between the results of set A and set B is that the daytime equatorial value of the ratio $n(O^{++})/n(O^{+})$ is considerably less than unity on each day of the fourteen day integration period. This feature is apparent in Figure 5 and is caused mainly by the large amount of O^{+} at the equator resulting from the temperature model of set B. In Figure 9 we show O^+ profiles at 08.00 LT on the eighth day, for sets A and B, with the corresponding temperature profiles. The time 08.00 LT is chosen since it is the time at which a maximum in the equatorial O^+ number density occurs. The temperature profiles deviate rapidly in the approximate altitude region 500 - 1200 km, producing a substantial difference in the O^+ scale height over the same region. Consequently this difference in temperature gradients below 1200 km results in a substantial difference in the amount of O^+ at the equator. The equatorial values of the O^+ number density for the profiles shown in Figure 9 are 0.56 cm^{-3} (set A) and 16.2 cm^{-3} (set B).

The difference between the O^{++} number densities for sets A and B at the equator are not so pronounced as for O^+. In Figure 10 the diurnal variation of the equatorial O^{++} number densities is shown for sets A and B on the eighth day and the B values are slightly more than a factor of two lower than the A values at most. Also, apart from the first two days, the O^{++} tube content for set B is lower than the corresponding content for set A (see Figure 12). These features are mainly a consequence of the more rapid fall in the temperature at night-time in set B model compared to the set A model. However, a contributory factor is again the temperature gradients below 1200 km, which raises the O^+ - H^+ transition height to 3000 km for set B compared to 1450 km for set A (values are quoted for 08.00 LT on day eight corresponding to Figure 9). As noted above, the raising of this transition height results in lower values for the ratio $n(H^+)/n(O^+)$ which leads to lower values of the O^{++} thermal diffusion coefficient. Consequently, although thermal diffusion plays a major role in both sets of calculations it has less effect in set B than it does in set A. It therefore appears that high equatorial temperatures alone do not imply that the number densities of O^{++} exceed the number densities of O^+ at the equator. The altitude range in which significant temperature gradients exist is important. The effects of thermal diffusion on O^{++} transport are enhanced when such temperature gradients exist above the O^+ - H^+ transition altitude rather than below it.

The diurnal variations of O^+ and O^{++} number densities at the equator for the eighth day of set B are shown in Figure 11. As discussed above, and illustrated in Figure 5, the O^{++} number densities are considerably lower than the O^+ number densities during the daytime. At night-time the situation is reversed. The O^+ layer decays due to the absence of photoionization production and aided by the falling temperatures. In fact, referring to Figures 2a and 11, the diurnal behaviour of O^+ at the equator shows a marked resemblance to the diurnal behaviour of the electron temperatures. The decay of the equatorial O^{++} number densities at night is impeded by thermal diffusion and the difficulty in diffusing through the O^+ layer to regions of high recombination.

In Figure 10 the diurnal variation of the O^{++} number density at selected heights for sets A and B on day eight is illustrated. Apart from regions near the equator it appears that it is difficult to predict the diurnal pattern of behaviour of O^{++} at a given altitude. The behaviour near the equator appears to fit in with the different temperature models used for sets A and B (see Figure 2a). To explain the behaviour at other altitudes we first note, for day eight, O^{++} tube contents for set B are lower than the corresponding contents for set A (Figure 12.) Thus generally one would expect the O^{++} number densities for set B to be lower than the corresponding densities for set A. Secondly we note that, at night, the temperatures for set B fall more rapidly than the temperatures for set A, particularly so at great altitudes (see Figure 2a). This is also the cause of the more rapid decrease in the O^{++} content at night for set B compared to set A. Consequently there is a greater downward O^{++} flux at night-time for set B than for set A. Corresponding to Figure 10, the downward O^{++} fluxes through 1000 km, at 03.00 LT for example, are 9×10^{4} cm^{-2} s^{-1} and 10^{6} cm^{-2} s^{-1} for sets A and B respectively. As a result, for set B, the diurnal behaviour of the O^{++} number density at some altitudes below approximately 2000 km has a maximum in the early morning hours. For set A there is relatively little difference between the daytime and night-time temperatures (Figure 2a) and the O^{++} layer is fairly well supported by thermal diffusion at night. Consequently, in set A, insufficient O^{++} flows down to altitudes at and below 1500 km to produce night-time maxima as in set B. For set A, this behaviour occurs at greater altitudes, e.g. 2500 km in Figure 10. Finally, we note that the effect of the change from night-time to daytime temperature at 08.00 LT and from daytime to night-time temperatures at 20.00 LT is evident in the set A curves of Figure 10, particularly at 2500 km. The minimum in the O^{++} variation at 750 km, that occurs at 21.00 LT, is an indirect result of the change to night-time temperatures at 20.00 LT. The temperature change caused the O^{+} layer to suddenly collapse and O^{++} was dragged to regions of high recombination. The diurnal variation of the O^{+}-flux at 750 km for day eight is shown in Figure 3b.

In the results for set B the O^{++} content starts to decrease after about ten days. This feature results from our night-time temperature profiles. The equatorial values fall as low as 5300 K in the early hours of the morning for set B (Figure 2a). Consequently there is a greater return flux of O^{++} for set B than for set A. For set A the night-time temperatures are sufficiently large to limit downward flowing O^{++} via thermal diffusion. In fact, as well as falling more rapidly at night-time, the flux tube contents for set B increase more rapidly in the daytime. This again is linked to the daytime temperatures used in the set B calculations, which indirectly enhance the production of O^{++} from O^{+}. From Figure 9 it is clear that there is a greater net production of O^{++} from this source for set B compared to set A.

We repeated the calculations of the twentieth day of set A with O^{++} - H^{+} collision frequency reduced by a factor of five (set F, see Table 1). The values of the O^{++} number density at the equator were only slightly larger than the corresponding results of set A. However, the net increases in O^{++} content for the twentieth days of sets A and F were 2×10^{9} cm^{-2} and 9×10^{9} cm^{-2} respectively (the net increase in the O^{++} content on the second day for set A was 1.735×10^{9} cm^{-2}). Thus the replenishment of O^{++} is impeded by H^{+} in later stages of recovery. The increasing H^{+} densities make it less easy for O^{++} to diffuse to great altitudes. In Chapter IV it was noted that H^{+} exerted a similar (and more emphasized) influence on He^{+}. Although the reduction in O^{++} - H^{+} collision frequency appears to produce a significant effect in the O^{++} content it is noted that it is only a secondary effect compared to the influence of temperatures and the O^{++} - O^{+} collision frequency. In addition we note that the effect is less evident when the O^{++} - H^{+} collision frequency is reduced on the eighth day.

5.5 Conclusions.

This work supports the findings of Geiss and Young (1981) that thermal diffusion plays a dominant role in influencing the behaviour of O^{++} in the topside ionosphere and provides the main contributing factor that can account for large amounts of O^{++} at the equator. The polarization electric field only plays a secondary role but does help to increase the amount of O^{++} at the equator. When the polarization field was decreased by a factor of one hundred on the eighth day, $n(O^{++})$ was 25% lower at the equator at the end of the day, compared to calculations carried out with normal polarization field. However, when the calculations of the eighth day were repeated with thermal diffusion neglected in the O^{++} calculations, the equatorial value of $n(O^{++})$ fell dramatically.

Although we support the findings of Geiss and Young our results indicate that the effects of thermal diffusion are enhanced in their calculations, compared to ours, due to their formulation of the thermal diffusion coefficient and constructed profiles for O^+ and H^+. A typical comparison showed that, at 1000 km, the value of the thermal diffusion coefficient used by Geiss and Young was four times larger than the value that arose in our calculations. Consequently the results of Geiss and Young showed a more rapid increase in the equatorial ratio $n(O^{++})/n(O^+)$. The daytime value of this ratio (13.00 LT) determined by Geiss and Young was approximately a factor of three greater than ours after twenty days.

The dependence of the O^{++} thermal diffusion coefficient on the ratio $n(H^+)/n(O^+)$ (St. Maurice and Schunk, 1977), and the importance of thermal diffusion for O^{++} would suggest that large amounts of O^{++} are more likely to occur at the equator when the O^+ - H^+ transition altitude is low. On the other hand the O^{++} - O^+ collision frequency appears to have an important influence on the O^{++} content. When the collision frequency is low O^{++} can diffuse more freely through the O^+ layer to regions of high recombination. Thus the former favours lower O^+ number densities such as at sunspot minimum, and the latter favours higher O^+ densities, such as at sunspot maximum. Although sunspot maximum O^+ number densities will result in smaller values of the O^{++} thermal diffusion coefficient compared to sunspot minimum, this may well be offset by the sunspot maximum temperature gradients. When the production processes are also brought into consideration it appears that daytime values of $n(O^{++})/n(O^+)$ exceeding unity at the equator are more likely to occur at sunspot maximum rather than sunspot minimum.

High equatorial temperatures do not imply that the ratio $n(O^{++})/n(O^+)$ will exceed unity at the equator. The altitude range over which large temperature gradients exist is important. The effects of thermal diffusion on O^{++} will be more pronounced if the temperature gradients exist above the O^+ - H^+ transition altitude rather than below it.

There is a strong link between the diurnal behaviour of O^{++} number densities at selected altitudes and the diurnal variations in temperatures. As the temperatures fall at night-time O^{++} flows downwards from the higher regions of the flux tube producing night-time maxima in the diurnal variation of the O^{++} number density at lower altitudes. The more pronounced the fall in the temperature at night-time the lower the altitudes at which the night-time maxima occur.

In one set of calculations that we carried out the O^{++} flux tube content and equatorial number density stopped increasing from day to day after about fourteen days. This feature, which did not arise in the calculations of Geiss and Young (1981), was mainly caused by the magnitude of temperature decay at night.

Our calculations indicate that the diurnal variation of O^+ at the equator is strongly influenced by the diurnal variation in temperature. The equatorial O^+ values used by Geiss and Young (1981) were based on data from GEOS 1 mass spectrometer and only varied between 0.3 cm^{-3} and 1 cm^{-3}. Although this variation seems to be relatively small it is consistent with the small change in the equatorial temperatures used by Geiss and Young which were based on GEOS 1 mass spectrometer. However, it does appear that further investigation of O^+ behaviour at the equator is needed. Another interesting feature of the behaviour of O^+ at the equator was the decrease in the daily maximum value throughout the integration period that arose in one set of our calculations.

TABLE 1

A	Standard set. Parameters similar to those used by Geiss and Young (1981). Results were produced for a twenty day integration period.
B	Different temperature model. The variation of T_i, T_e at selected altitudes are shown in Figure 2a. Results were produced for a fourteen day integration period.
C	Thermal diffusion is neglected in the O^{++} equations for days 8, 9 and 10 only. The first seven days are identical to A.
D	The polarization electrostatic field is reduced by a factor of 100 (eighth day only).
E	The O^{++} - O^+ collision frequency is reduced by a factor of 100 (eighth day only).
F	The O^{++} - H^+ collision frequency is reduced by a factor 5 (day 20 only).

TABLE 2

	Values taken from the results of set A for midday, Day 8.	Values used by Geiss and Young, daytime, Day ∞	Formulation used by Geiss and Young with $n(H^+)/n(O^+)$ taken from set A, midday, Day 8.
Equator	9.60	11.18	11.20
1000 km	1.85	7.39	3.43

Table 2: Values of the O^{++} thermal diffusion coefficient.

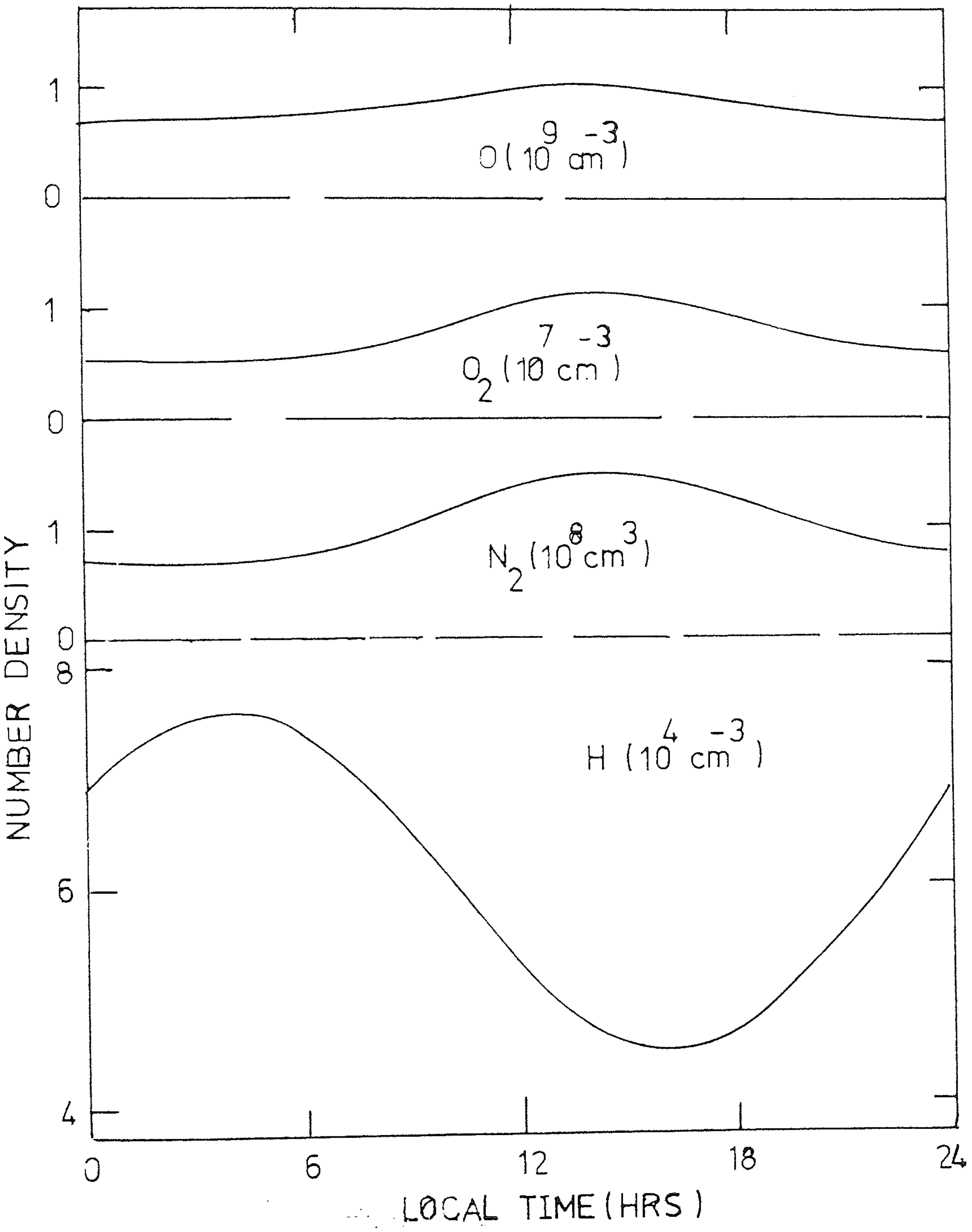

Figure 1. The diurnal variation of the number densities of the neutral constituents, O, O_2, N_2 at 300 km and H at 500 km.

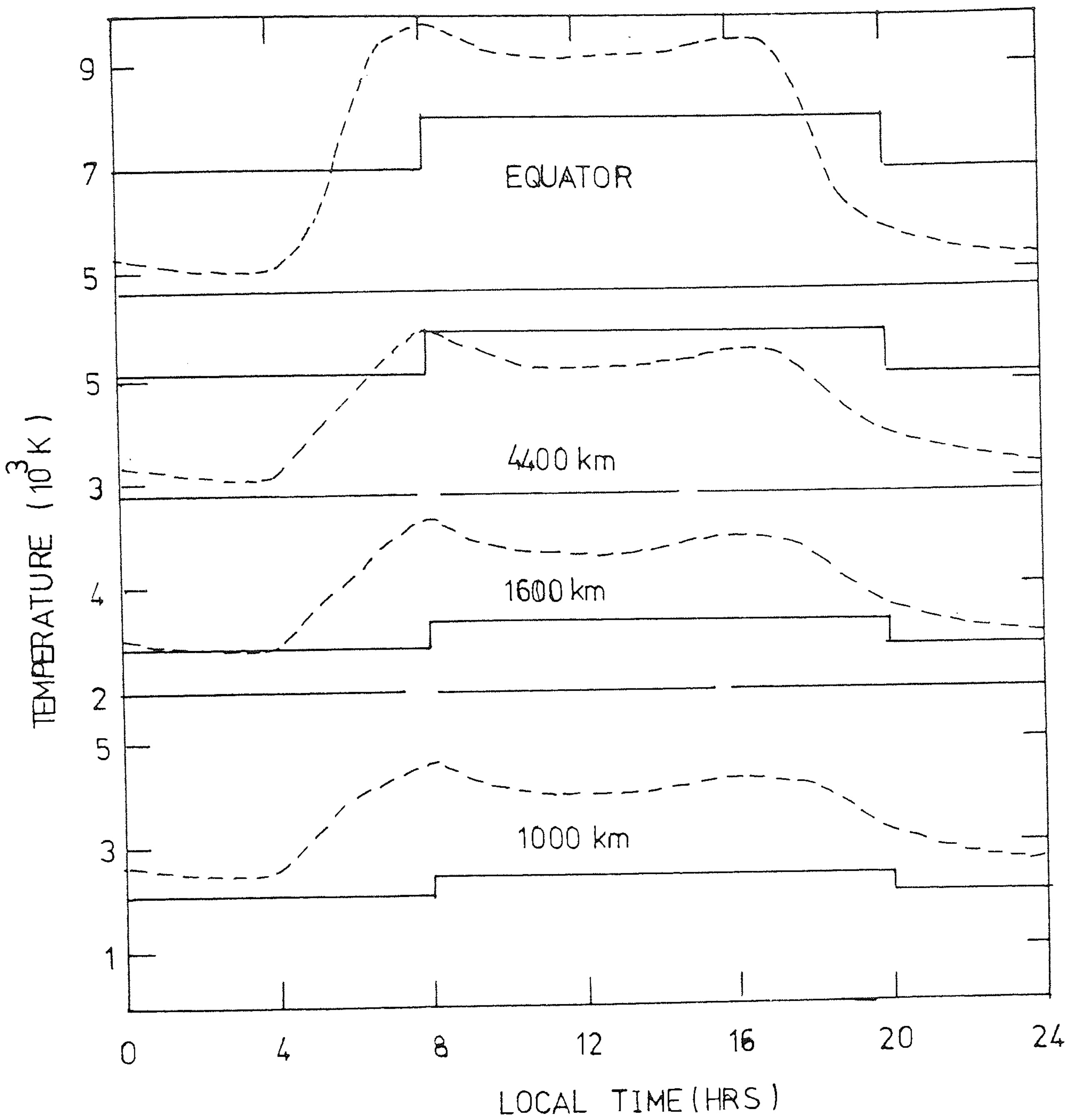

Figure 2a. The diurnal variation of the electron and ion temperatures at selected heights for model A (solid line) and model B (dashed line).

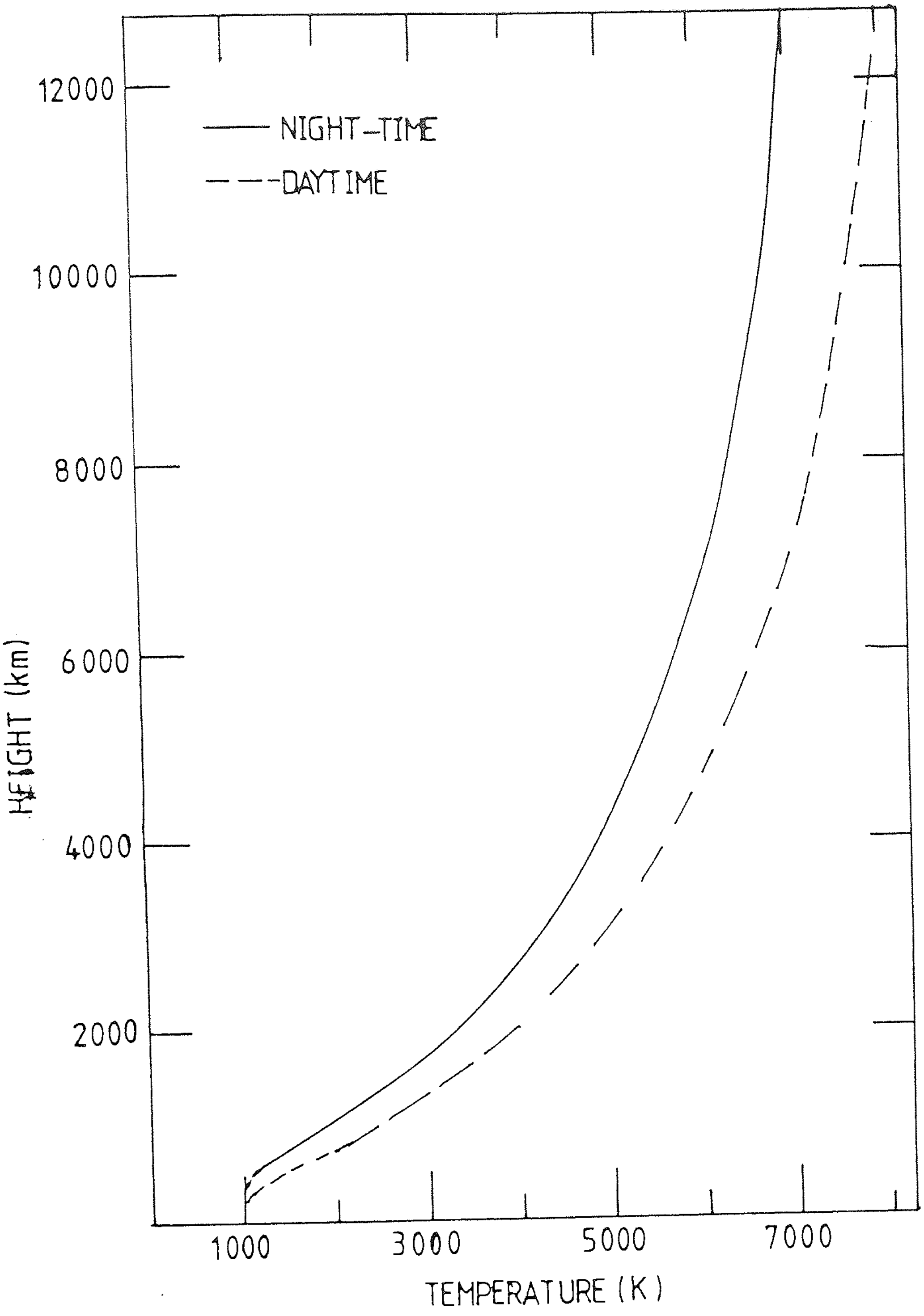

Figure 2b. Altitude profiles for the electron and ion temperatures for model A at daytime and night-time.

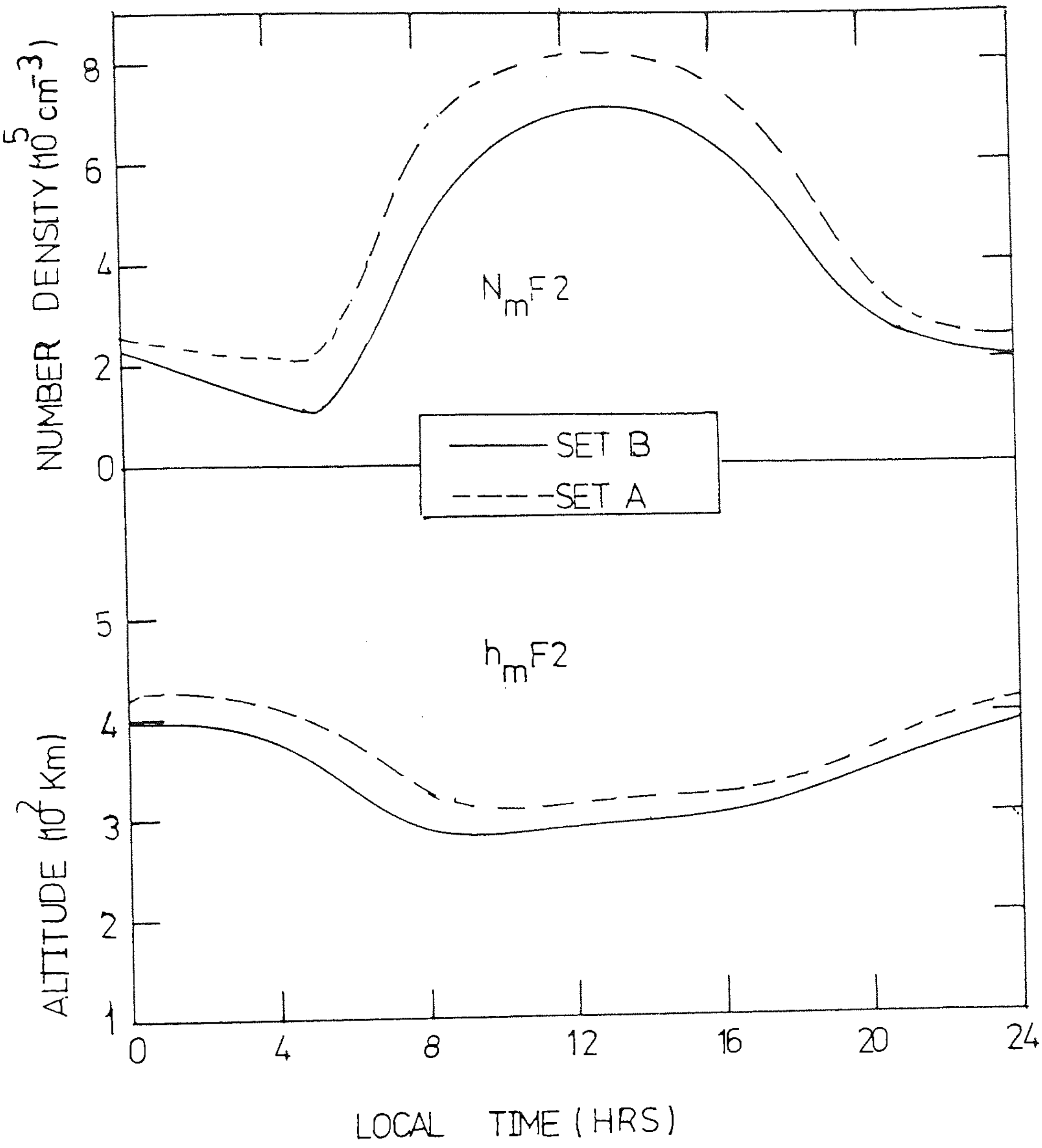

Figure 3a. The diurnal variation of N_mF2 and h_mF2 for day eight of the integration period of sets A and B.

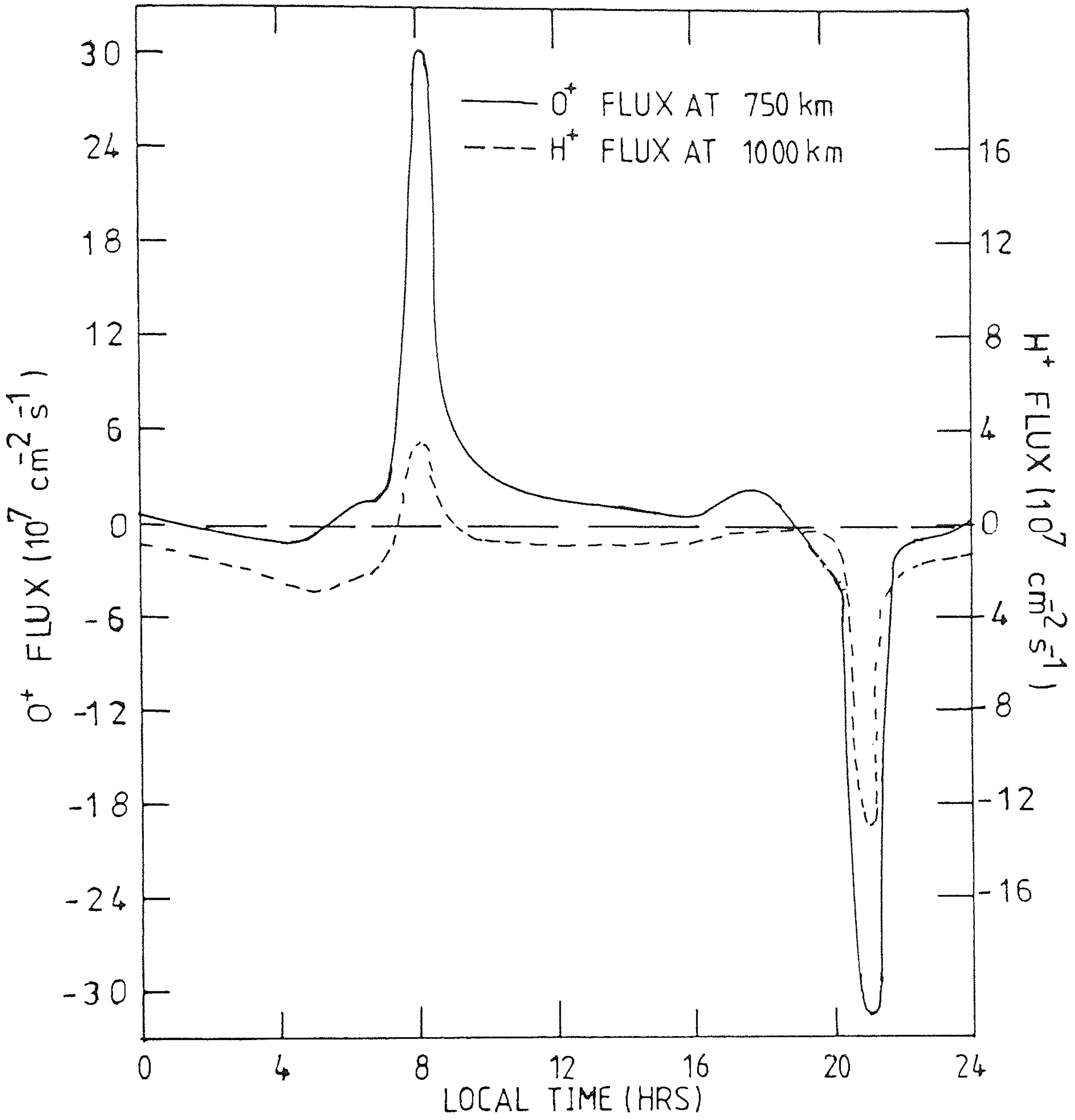

Figure 3b. The diurnal variation of the O^+-flux (solid line) and the H^+-flux (dashed line) for day eight of the integration period for set A.

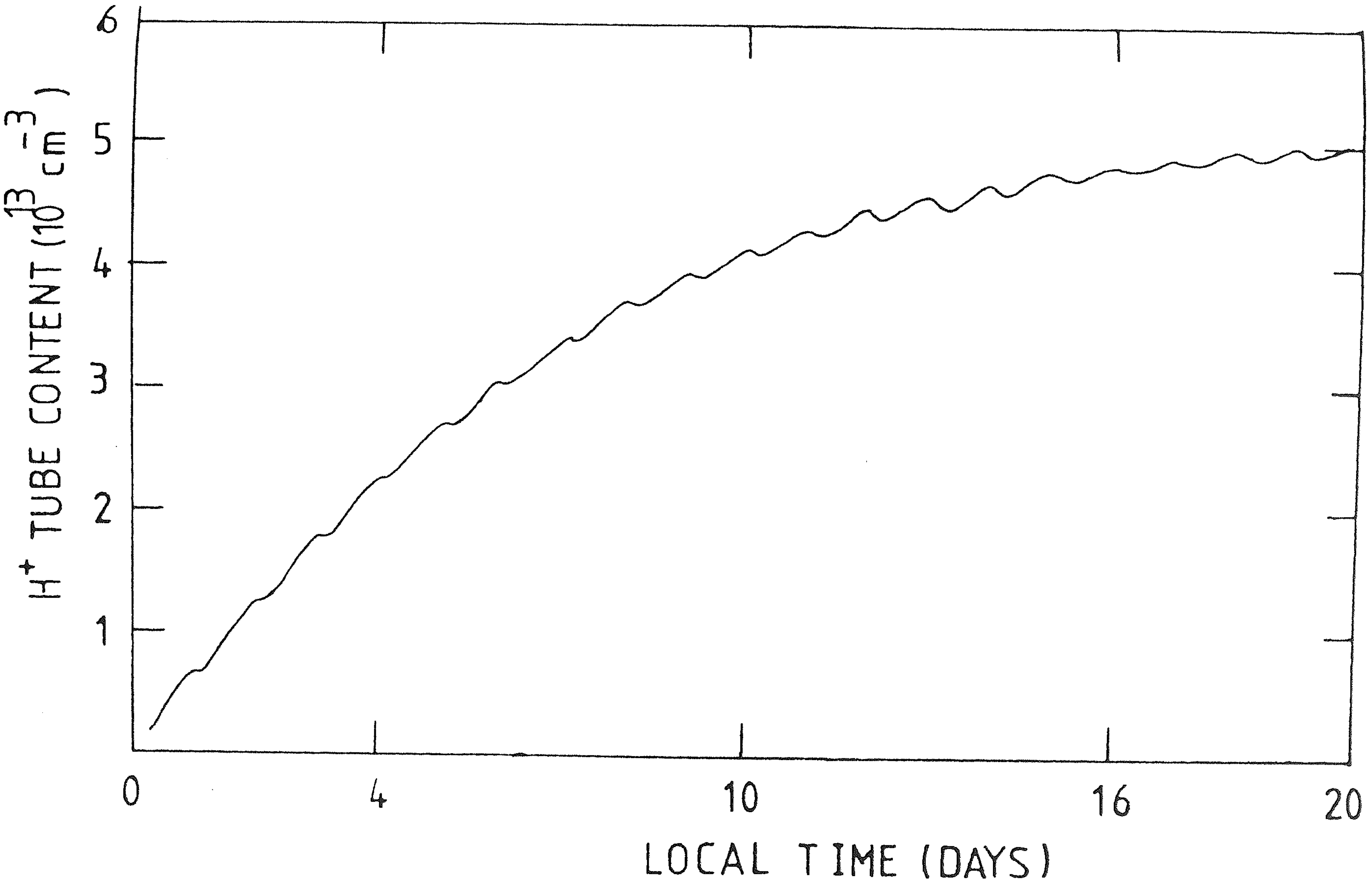

Figure 3c. The behaviour of H^+-content over twenty days for set A. The content is for a flux tube at L = 3 with a cross section of 1 sq. cm. at 1000 km altitude.

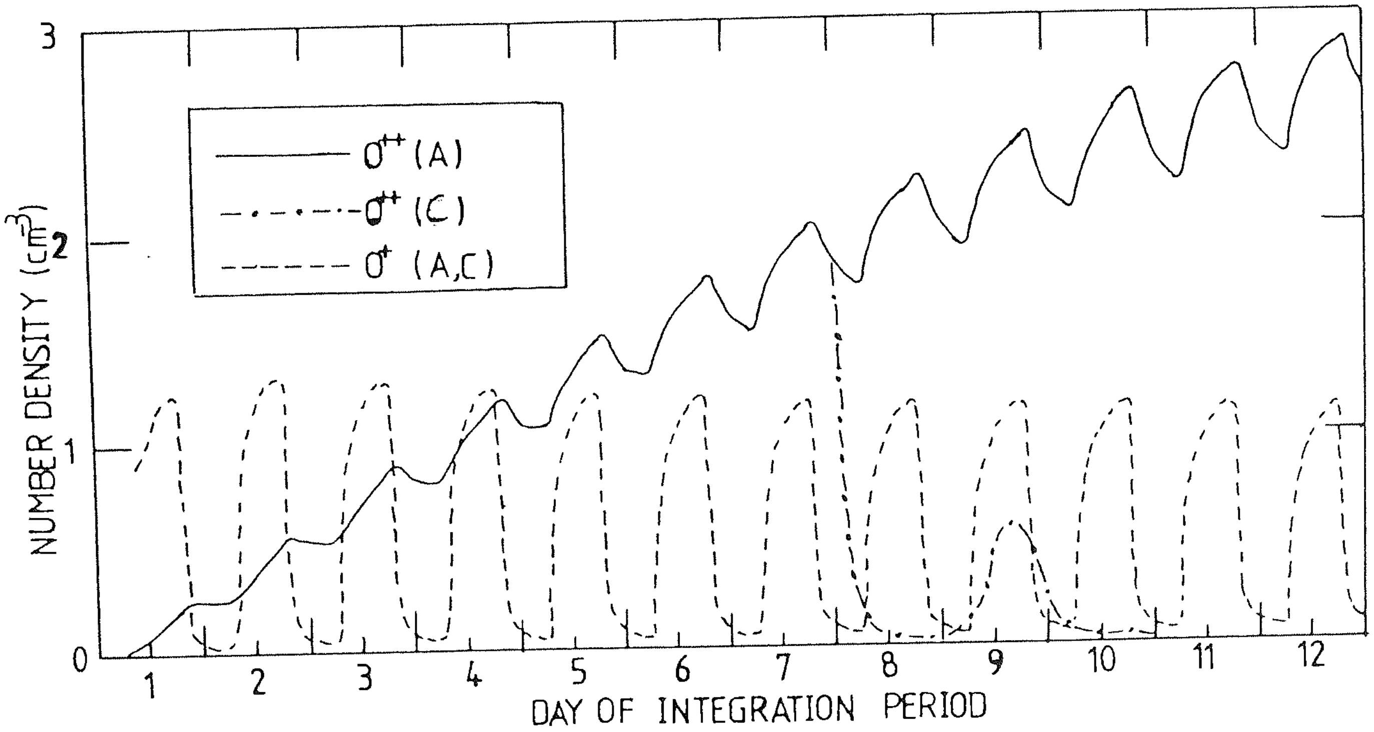

Figure 4. The behaviour of O^{++} and O^{+} number densities at the equator over the first twelve days of the integration period for the standard set A. For days 8, 9 and 10, equatorial O^{++} values are also shown for set C in which thermal diffusion has been neglected (see Table 1).

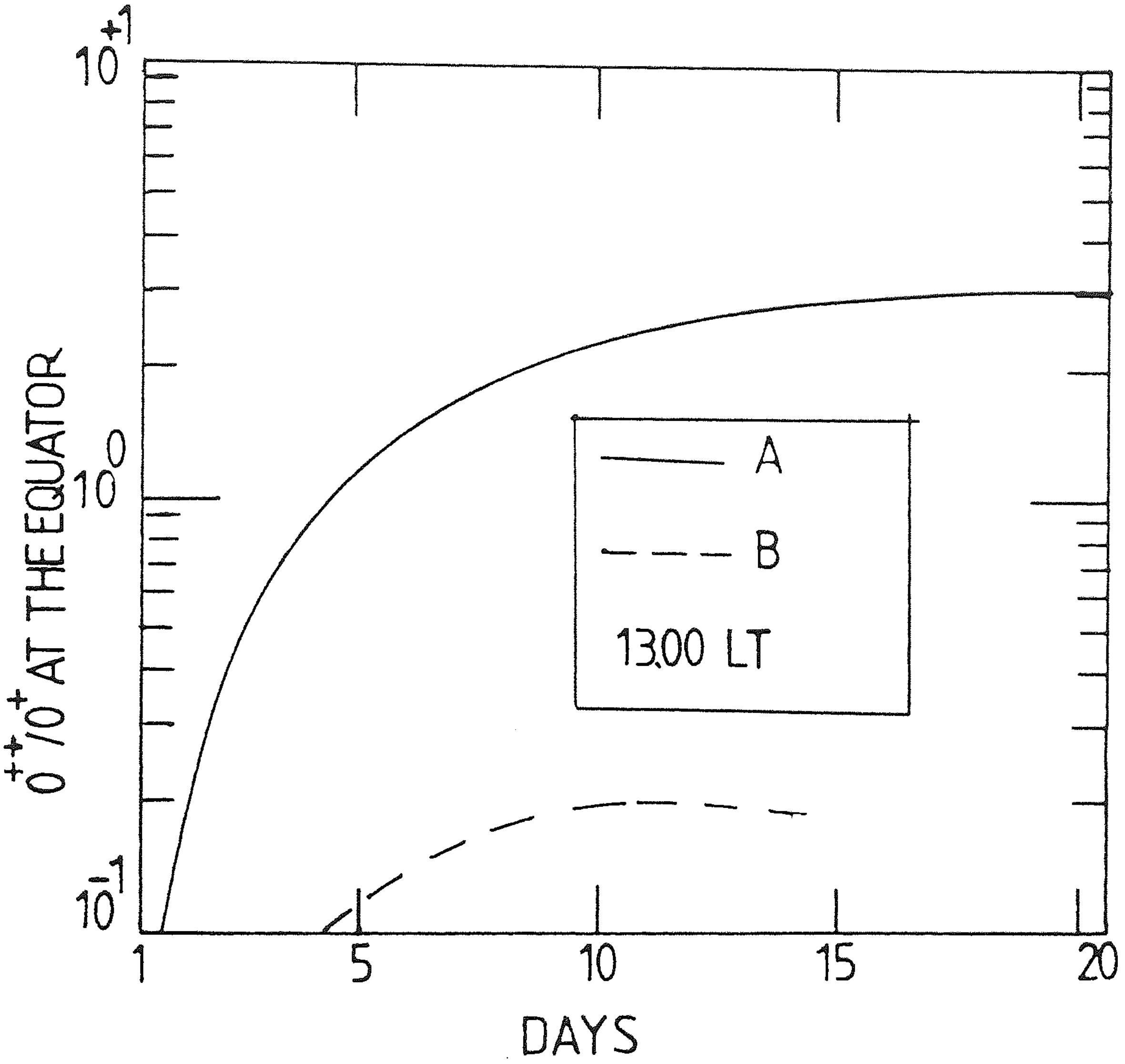

Figure 5. The behaviour of $n(O^{++})/n(O^{+})$ at the equator for set A (integration period 20 days) and set B (integration period 14 days). Only values at 13.00 LT have been plotted and therefore daily variations have been suppressed.

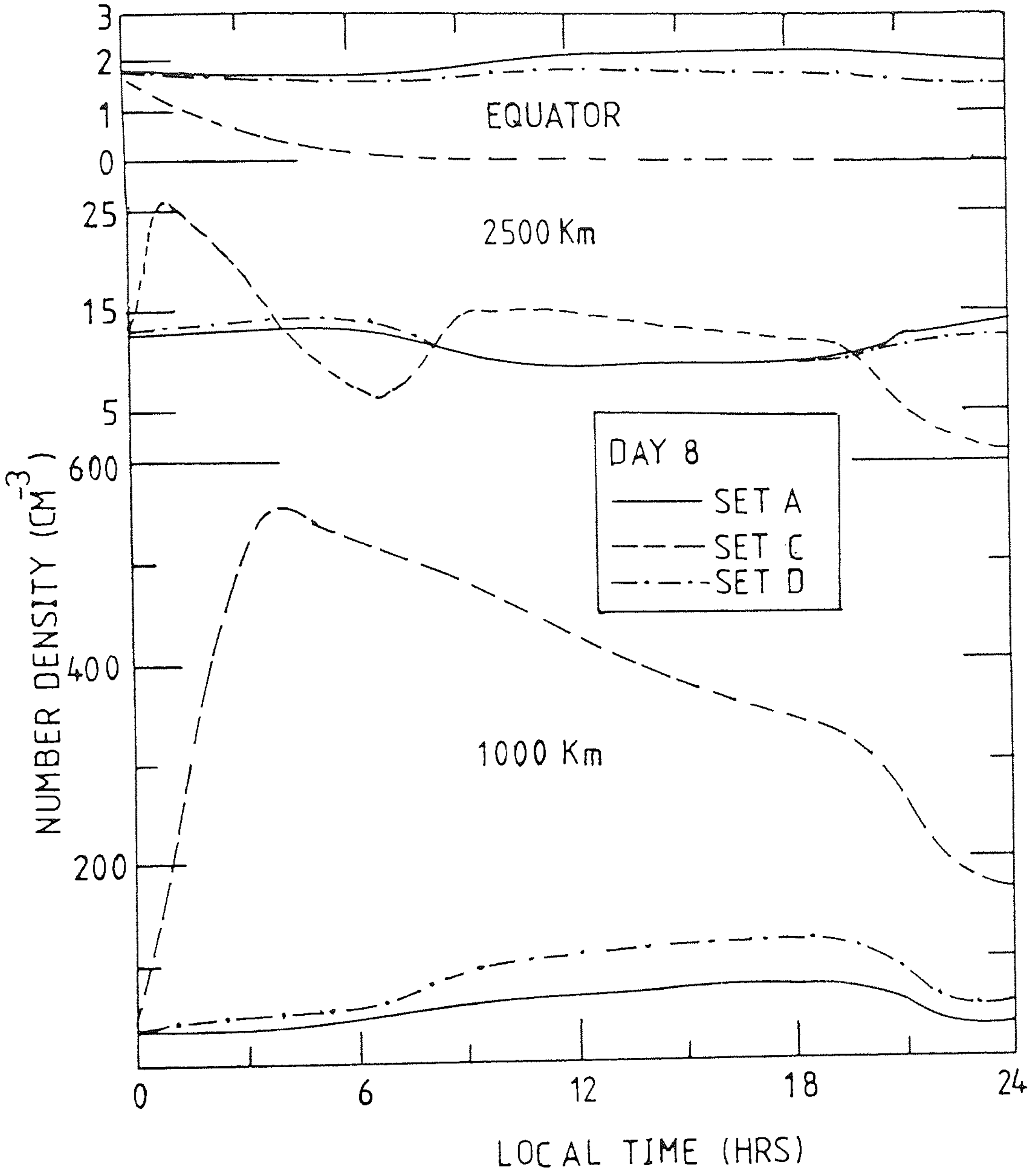

Figure 6. The diurnal variation of the O^{++} number density at selected altitudes on the eighth day. The figure compares the standard set A with set C (thermal diffusion neglected) and set D (polarization field reduced).

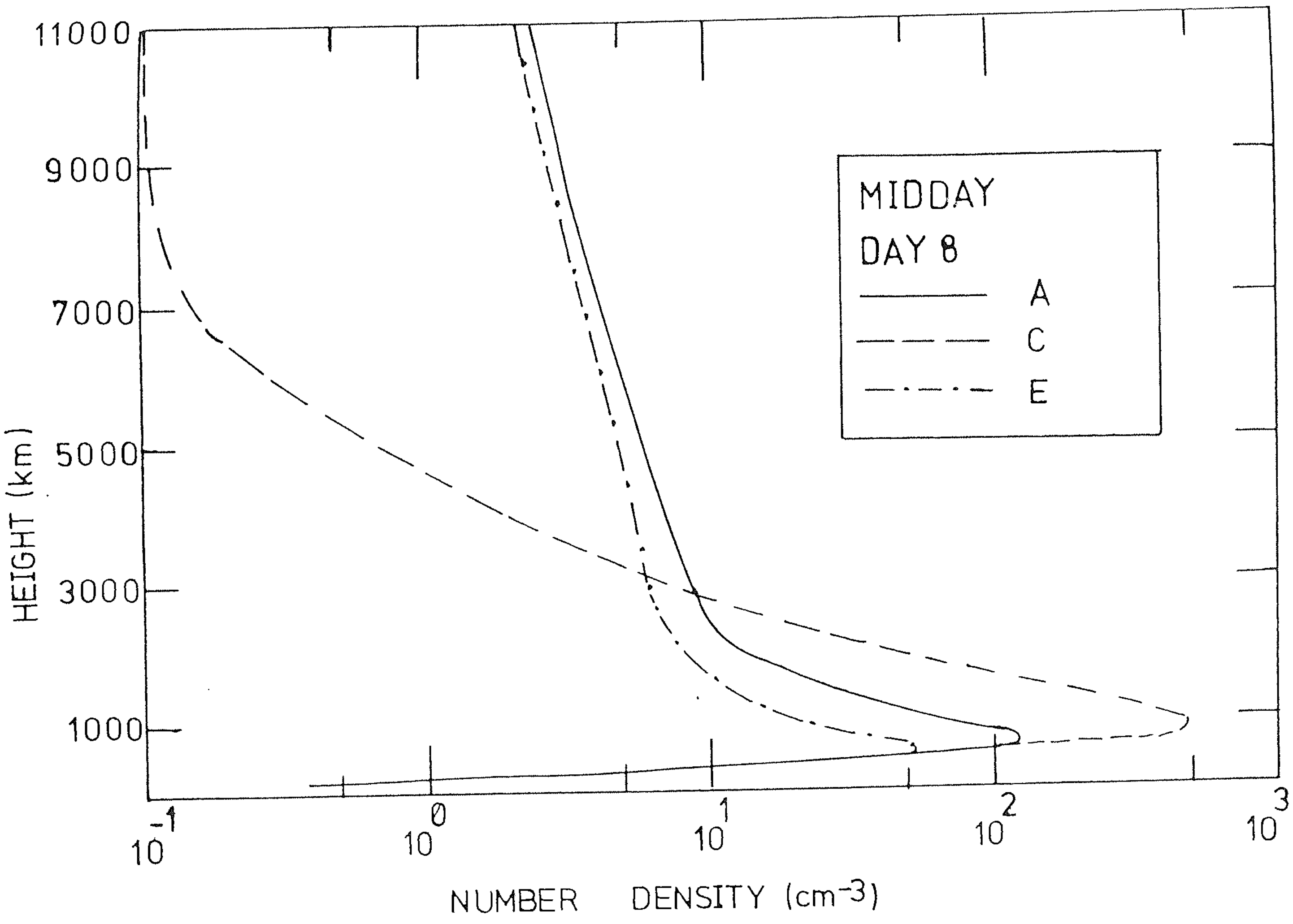

Figure 7. O^{++} height profiles for the standard set A, set C (thermal diffusion neglected) and set E (O^{++}-O^{+} collision frequency reduced by a factor of 100). The profiles are taken from midday on the eighth day of the integration period.

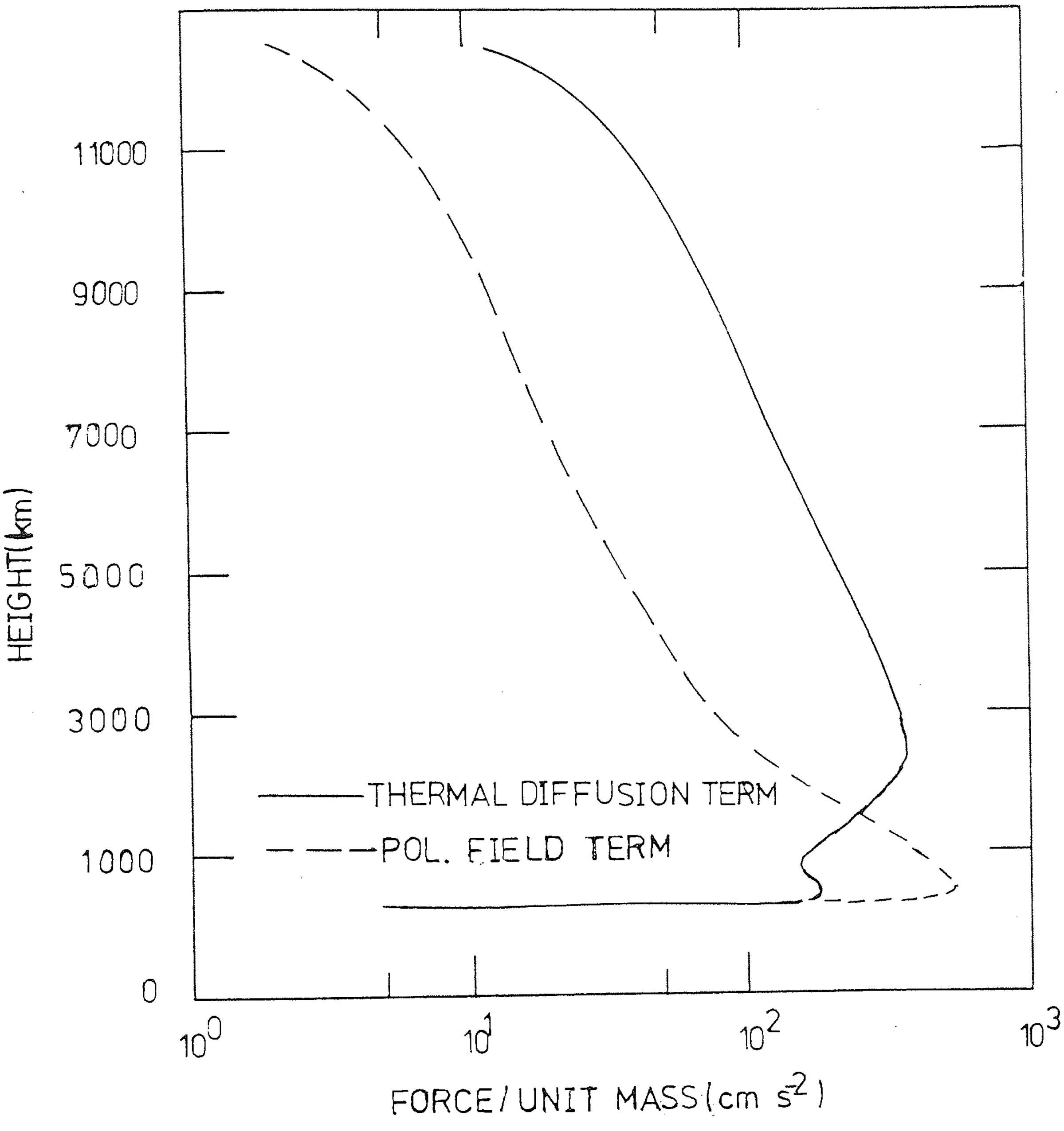

Figure 8. Height profiles of the thermal diffusion and the polarization field terms corresponding to curve A of Figure 7.

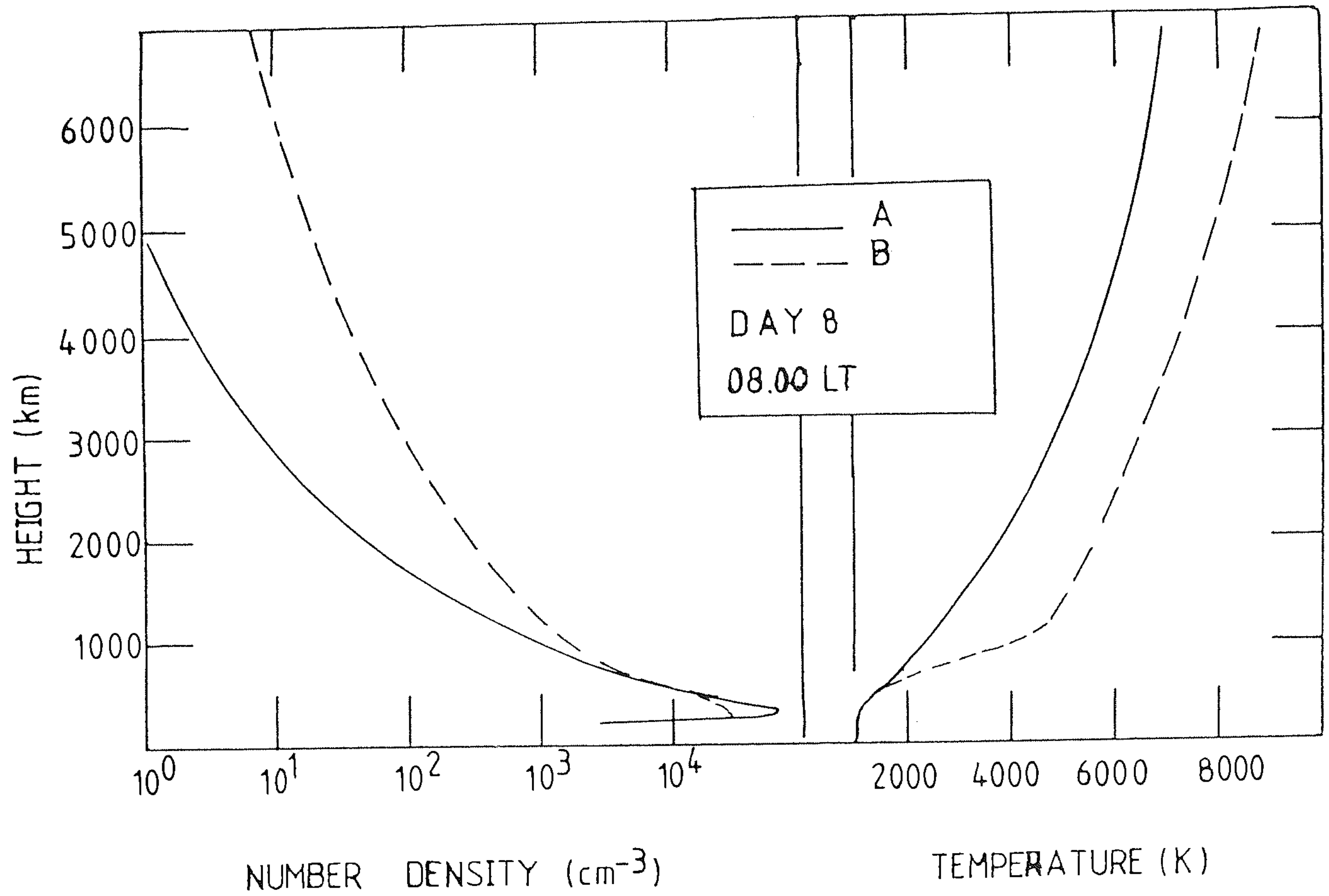

Figure 9. Height profiles of O^+ for sets A and B with the corresponding temperatures. The 08.00 LT is chosen since it is the time at which a maximum in the equatorial O^+ number density occurs.

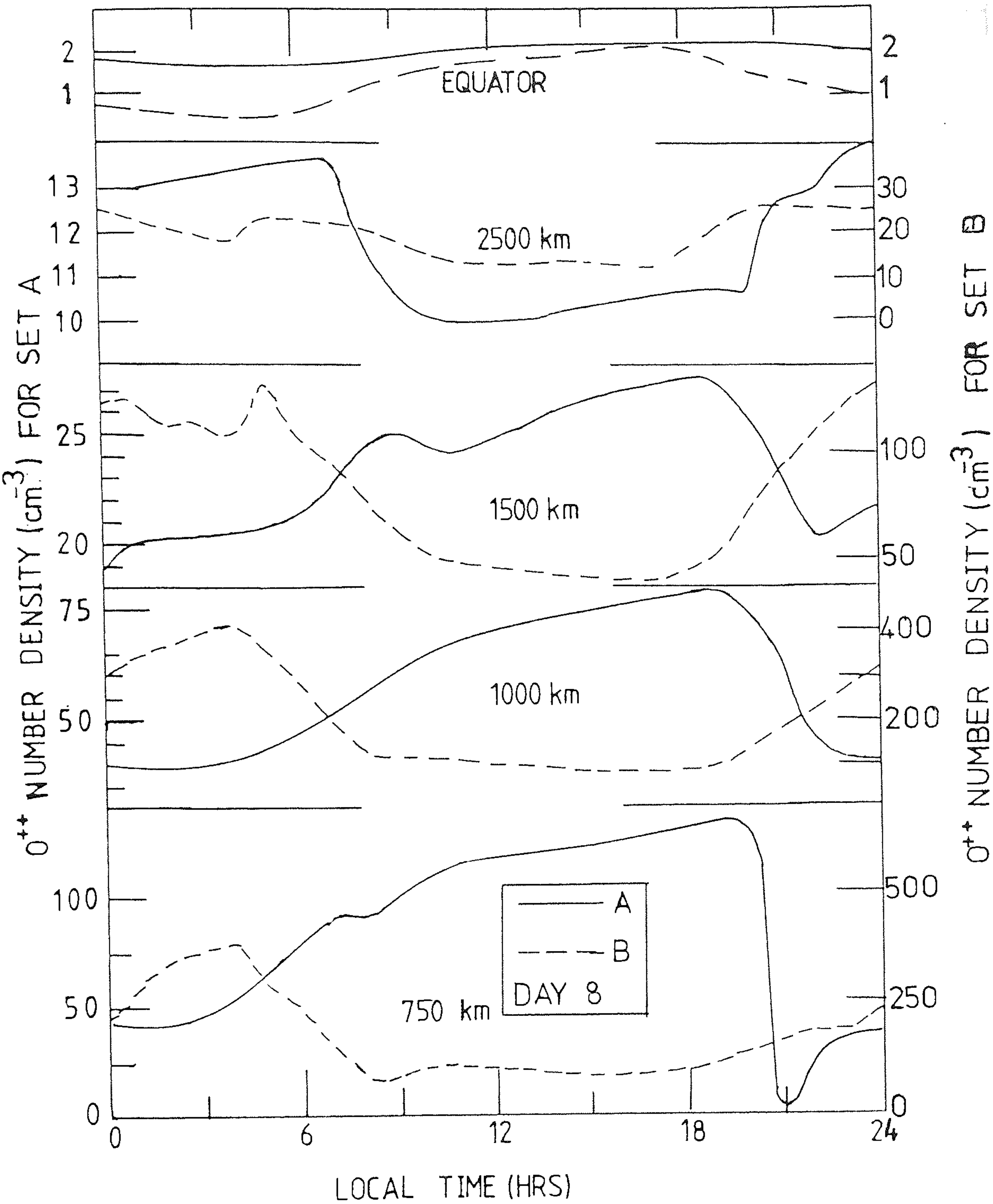

Figure 10. Diurnal variation of O^{++} number density at selected heights for sets A and B (see Table 1).

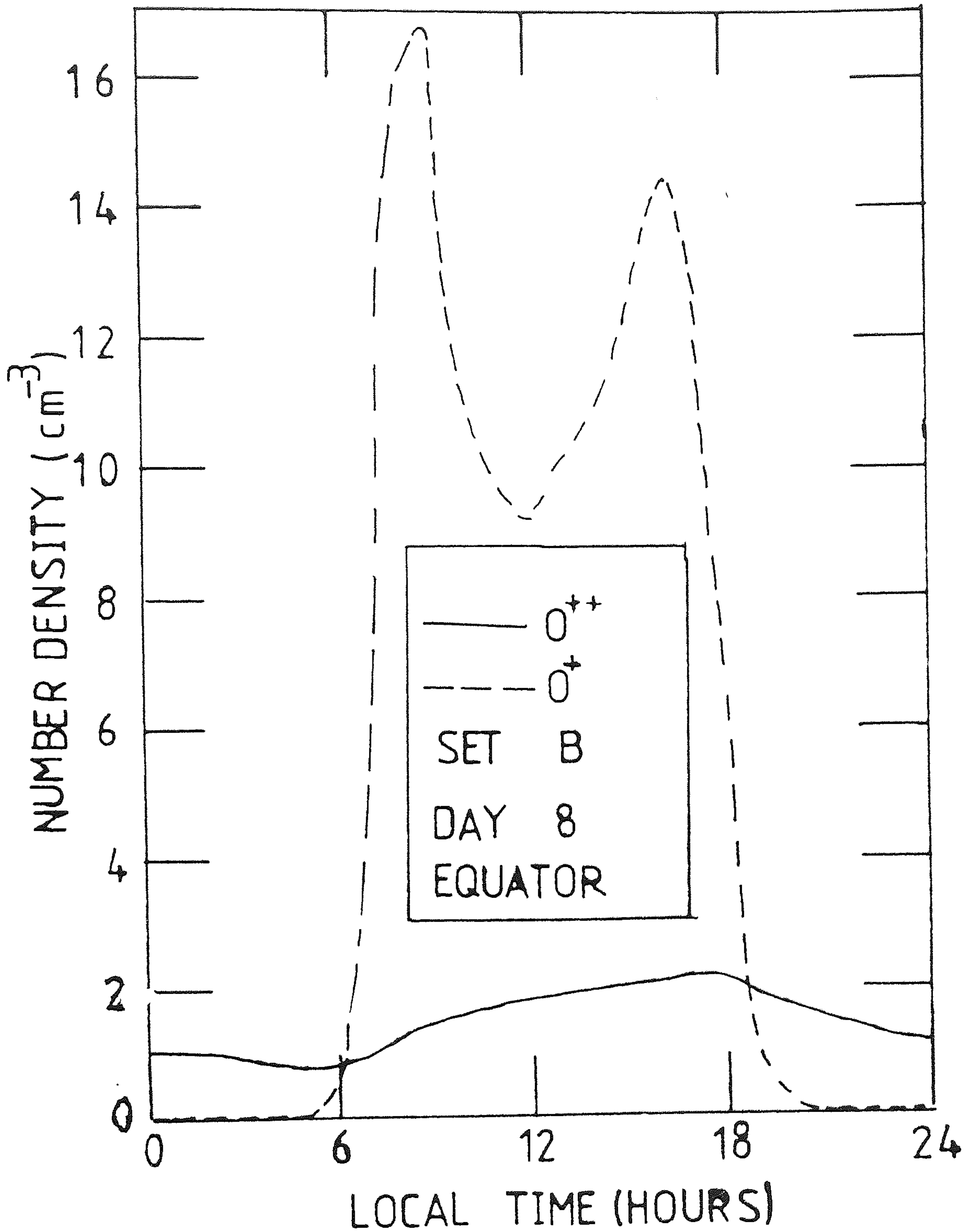

Figure 11. The diurnal variation of O^+ and O^{++} number densities at the equator for the eighth day of set B calculations. In the early morning and late evening the O^+ values are of the order $10^{-2} - 10^{-3}$ cm^{-3}.

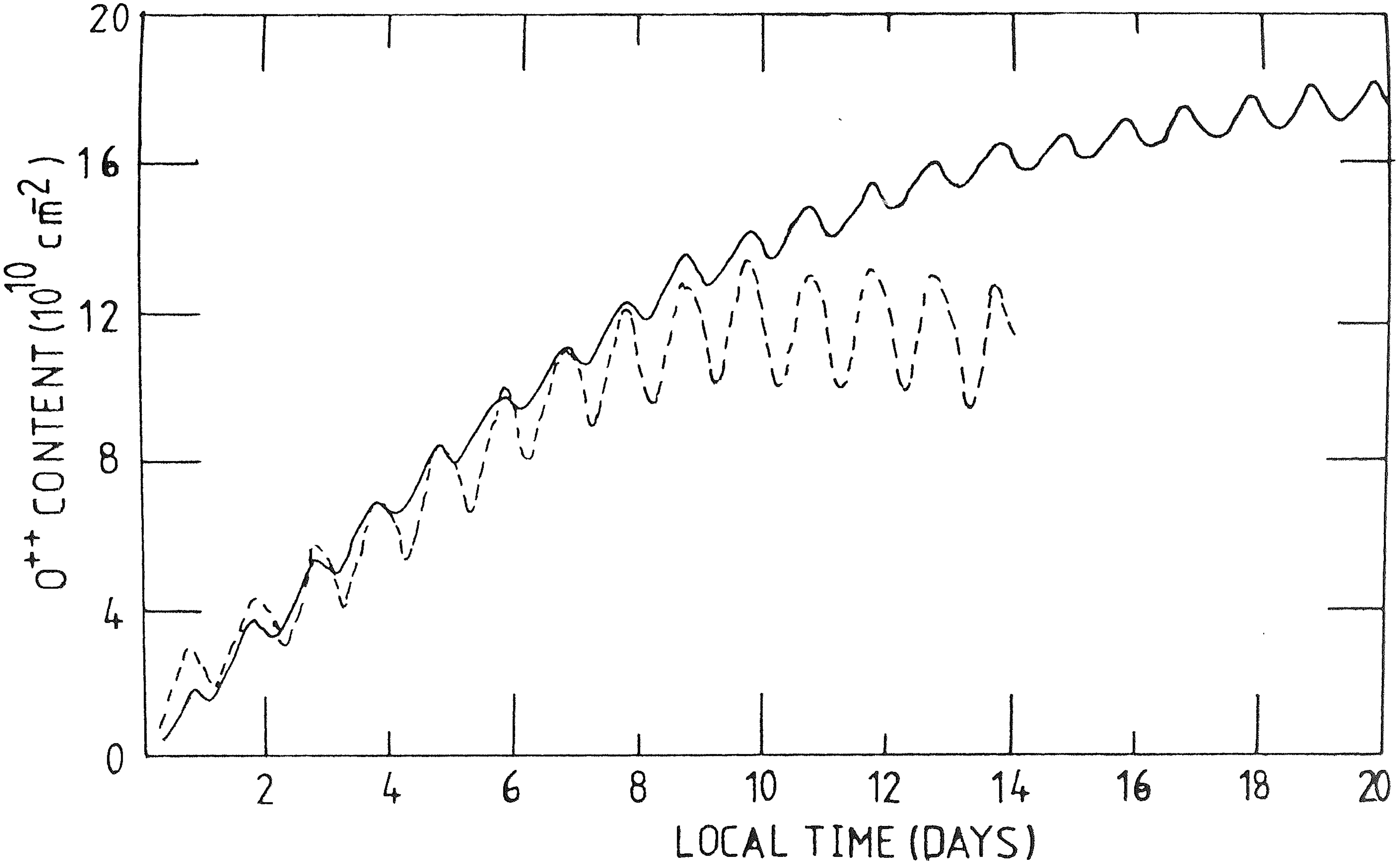

Figure 12. The O^{++}-content behaviour over the integration period (20 days for set A and 14 days for set B).

VI A COMPARATIVE STUDY OF H^+ AND HE^+ AT SUNSPOT MINIMUM AND SUNSPOT MAXIMUM IN THE MID-LATITUDE PLASMASPHERE

6.1 Introduction

Detailed studies of O^+ and H^+ behaviour at sunspot minimum and sunspot maximum have been carried out by Murphy et al.(1976) and Bailey et al.(1979) respectively. In Chapter IV the time-dependent behaviour of He^+ at mid-latitudes was investigated for sunspot minimum conditions. Starting from a relatively low He^+ tube content, typical of post-magnetic storm conditions, He^+ results were calculated for a period of ten days. From these results the replenishment and diurnal behaviour of He^+ throughout the ten day period were examined. Here we extend that work concentrating on the comparative behaviour of H^+ and He^+ throughout the period when the light ion content of a mid-latitude magnetic flux tube is being replenished. In addition we have compared some features of H^+ and He^+ behaviour at sunspot minimum to the behaviour at sunspot maximum. In this study our attention is mainly devoted to light ion contents and fluxes.

In a study of the polar ionospheric hole Murphy et al. (1981) demonstrated that, when modelling situations in which O^+, H^+ and He^+ can have comparable number densities, the use of a formulation which treats O^+ and H^+ as major ions and He^+ as a minor ion can lead to erroneous H^+ and He^+ results. In such situations it is appropriate to use the formulation of Quegan et al.(1981). With this formulation He^+ can be treated theoretically as a major ion along with O^+ and H^+. At mid-latitudes it is usually reasonable to assume that He^+ is a minor ion and, as in Chapter IV, the formulation of St.-Maurice and Schunk (1977), which allows for two major ions and a number of minor ions, can be used. However, in this study, since we are concentrating on the relative behaviour of the two light ions, it seems appropriate to use the theoretical formulation of Quegan et al.(1981).

One of the interesting features that arose in Chapter IV was the behaviour of the He^+ content at sunspot minimum, which reached a maximum on the eighth day and then started to decrease as the H^+ content continued rising. It was found that as the H^+ content increased it became less easy for the He^+ to diffuse upwards during the daytime. Thus the increasing H^+ number densities gradually caused more He^+ to remain at altitudes where recombination could take place. This feature was not evident in the study of He^+ behaviour of Murphy et al.(1979) at sunspot maximum. However, as noted in Chapter IV, it was not clear whether the different He^+ behaviour was due to the parameters used by Murphy et al.(1979) or the way in which they calculated the O^+/H^+ number densities and fluxes. This point is further investigated here. In addition, with He^+ treated as a minor ion in Chapter IV, the model did not allow He^+ to influence the H^+ behaviour. This restriction is removed in this study and the behaviour of the H^+ and He^+ contents is again examined.

6.2 Theoretical formulation.

In Chapter IV we examined the behaviour of He^+ as a minor ion. Consequently the influence of He^+ on the other two major ions was neglected. In this chapter He^+ is treated as a major ion along with O^+ and H^+ and we investigate how this approach affects H^+ as well as He^+ itself. The time-dependent equations for the three ions O^+, H^+ and He^+ are coupled and we solve them numerically as follows. We start by solving the O^+ equations at time t using the H^+ and He^+ number densities and fluxes from $t - \Delta t$ where $\Delta t = 15$ mins. Having calculated the O^+ profiles at time t we then calculate H^+ number densities and fluxes using the O^+ profiles at t and the He^+ number densities and fluxes at $t - \Delta t$. This is followed by the calculation of the He^+ number densities and fluxes at t using O^+ and H^+ results from time t. This order of calculations is carried out at every new time over a fourteen day integration period. Although we have solved the O^+ equations, its behaviour will not be discussed since it has been investigated in detail in previous works (Murphy et al.,1976; Bailey et al.,1979). However, here we present the behaviour of N_mF2 and h_mF2 for day eight and these are shown in Figure 1. These quantities vary little from day to day.

6.2.1. Equations.

Recall that in Chapter II, section (2.3) we derived the O^+, H^+ and He^+ time-dependent equations using the formulation of Quegan et al.(1981). We summarize these equations as follows.

O^+-Equations

For regions below 2000 km the O^+ diffusion equation is given by equation (2.77) and it is

$$n_1 \frac{\partial n_1}{\partial t} = D_0 \frac{\partial^2 n_1}{\partial s^2} + D_1 \frac{\partial n_1}{\partial s} + D_2 n_1 + D_3 \tag{6.1}$$

where the variables n_1, D_0, D_1, D_2 and D_3 are defined following equation (2.77). Using equation (6.1) we calculate the O^+ number densities between the lower boundary (200 km) and 2000 km. The corresponding O^+-fluxes are calculated using (2.38) which is

$$\phi_1(s,t) = -B(s) \int_s^{s_{2000}} \frac{1}{B(s)} \left(P_1 - L_1 - \frac{\partial n_1}{\partial t} \right) ds \ , \tag{6.2}$$

where the variables are as in Chapter II. For regions above 2000 km, we again assume that O^+ is in diffusive equilibrium and the O^+ number densities are calculated using equation (2.79) with the suffices 1 and 2 interchanged and $\phi_1 = 0$. Equation (2.79) with the above changes is given by

$$\frac{k}{m_1}\left[T_i + \frac{n_1}{n_e} T_e\right]\frac{\partial}{\partial s} \log(n_1) = - g \sin I - \frac{k}{m_1}\left[\frac{\partial}{\partial s}(T_i + T_e) + \right.$$
$$\left. + (\beta_1 - \beta_{12} - \beta_{13})\frac{\partial T_i}{\partial s} + \frac{T_e}{n_e}\frac{\partial}{\partial s}(n_2 + n_3)\right] +$$

$$+ \eta_{12} u_2 + \eta_{13} u_3 + (R_{132} - R_{123})(u_2 - u_3) +$$

$$+ \nu_{10} u \cos I. \qquad (6.3)$$

where the variables are as in Chapter II.

H^+ - Equations

For the H^+ momentum equation we recall equation (2.80)

$$\frac{k}{m_2}\left[T_e + \frac{n_2}{n_e} T_e\right]\frac{\partial}{\partial s} \log(n_2) = - g \sin I - \frac{k}{m_2}\left[\frac{\partial}{\partial s}(T_i + T_e)\right.$$

$$\left. + (\beta_2 - \beta_{21} - \beta_{23})\frac{\partial T_i}{\partial s} + \frac{T_e}{n_e}\frac{\partial}{\partial s}(n_1 + n_3)\right]$$

$$- \left[\frac{\eta_{21}(n_1 + n_2) + \eta_{23}}{n_2} + \frac{R_2}{n_1}\right] \phi_2$$

$$+ \left(\eta_{21} + \frac{R_2}{n_1}\right) C + (\eta_{23} - R_2) u_2$$

$$+ \nu_{20} u \cos I. \qquad (6.4)$$

with

$$\phi_2(s,t) = -B(s) \int_s^{s_E} \frac{1}{B(s)} \left(P_2 - L_2 - \frac{\partial n_2}{\partial s}\right) ds \qquad (6.5)$$

and

$$C(s,t) = -B(s) \int_s^{s_E} \frac{1}{B(s)} \left(P_1 + P_2 - L_1 - L_2 - \frac{\partial n_1}{\partial t} - \frac{\partial n_2}{\partial t}\right) ds \qquad (6.6)$$

and the other variables are as in Chapter II.

He$^+$- Equations:

For the He$^+$ momentum equation we recall equation (2.81)

$$\begin{aligned}\frac{k}{m_3}\left[T_i + \frac{n_3}{n_e}T_e\right]\frac{\partial}{\partial s}\log(n_3) = {} & -g\sin I - \frac{k}{m_3}\left[\frac{\partial}{\partial s}(T_i + T_e) + \frac{T_e}{n_e}\frac{\partial}{\partial s}(n_1 + n_2)\right. \\ & \left. + (\beta_3 - \beta_{31} - \beta_{32})\frac{\partial T_i}{\partial s}\right] + \eta_{31}(u_1 - u_3) \\ & + \eta_{32}(u_2 - u_3) + (R_{321} - R_{312})(u_1 - u_2) \\ & + \nu_{30}\, u\cos I. \qquad (6.7)\end{aligned}$$

and the He$^+$ flux is given by

$$\phi_3(s,t) = -B(s)\int_s^{s_E}\frac{1}{B(s)}\left(P_3 - L_3 - \frac{\partial n_3}{\partial t}\right)ds \qquad (6.8)$$

where the variables are as in Chapter II.

The production and loss for the ions O$^+$, H$^+$ and He$^+$, P_1, L_1, P_2, L_2, P_3 and L_3 are the same as in equations (4.14), (4.19), (4.21), (4.22), (4.23) and (4.26) respectively.

6.2.2 The Atmospheric Parameters.

The atmospheric parameters to be used in the calculations of this chapter are given in Chapter IV for the sunspot minimum conditions and in Chapter V for the sunspot maximum conditions, except the sunspot maximum value of neutral helium density at 120 km, which is given by $n(\mathrm{He})_{120} = 3 \times 10^{7} \mathrm{cm}^{-3}$. Figure 2 shows a height profile for n(He) at mid-day and midnight.

For the neutral wind we adopt the model used by Bailey et al.(1979). Figure 3 shows the diurnal variation of the neutral wind.

For the electron and ion temperatures we use the model described in Chapter IV for sunspot minimum and model B of Chapter V for sunspot maximum.

Equations (6.1), (6.3), (6.4) and (6.7) are solved numerically using the procedures described in Chapter II with the boundary conditions as in section (4.2.1).

6.3 Results.

The densities and fluxes of O^+, H^+ and He^+ have been calculated along a mid-latitude flux tube (L = 3) from an altitude of 200 km to the equator, by solving the time dependent equations of continuity and momentum for the three ions. The equations were obtained using the theoretical formulation of Quegan et al.(1981) which allows for three major ions. Low initial contents of H^+ and He^+ were chosen to characterize conditions following light ion depletion via a magnetic storm (see Figures 4a and 4b). Two sets of results are produced over an integration period of fourteen days using the sunspot minimum parameters described in

Chapter IV and the sunspot maximum parameters described in Chapter V.

In Figure 4a, 4b, we show the calculated behaviour of the H^+ and He^+ flux tube contents for sunspot minimum and sunspot maximum respectively over a period of fourteen days starting from the low H^+ and He^+ flux tube content. Note that those figures have different scales for the H^+ and He^+ contents. From Figure 4a it can be seen that, at sunspot minimum, the He^+ tube content reaches a maximum value after eight days of replenishment and then starts to decrease. This behaviour was noted in Chapter IV where He^+ was treated theoretically as a minor ion and was attributed to the increasing $He^+ - H^+$ collision frequency. The He^+ flow becomes increasingly influenced by the H^+ flow as the H^+ number densities continue to increase. The maximum value achieved by the He^+ flux tube content was $7.75 \times 10^{11} cm^{-2}$ in these calculations compared to $6.8 \times 10^{11} cm^{-2}$ in Chapter IV. Thus the maximum value of the He^+ flux tube content is under-estimated by approximately 12% when He^+ is treated theoretically as a minor ion for the sunspot minimum conditions. This feature also arose in the work of Murphy et al.(1981) who noted that when He^+ is treated theoretically as a minor ion H^+ densities are over-estimated and He^+ densities are under-estimated. They also noted that the over-estimation of the H^+ densities is mainly due to the omission of He^+ in the polarization field term in the H^+ momentum equation, whereas the under-estimation of He^+ densities resulted from the magnitude of thermal diffusion effects arising from the two formulations, i.e. St.-Maurice and Schunk(1977) and Quegan et al.(1981). In addition, Murphy et al.(1981) noted that the He^+ - H^+ collision frequency had little influence on He^+ behaviour in the polar ionosphere hole. The situation is different at mid-latitudes with the lighter H^+ densities. It has already been noted that the He^+ - H^+ collision frequency plays an important role in limiting the He^+ number densities. From Figure 4a it can be seen that, in agreement with the sunspot minimum calculations of Murphy et al.(1976), the H^+ content will require a large number of days before it is totally replenished, i.e. when the net increase in the tube content over a twenty-four hour period is zero.

Before discussing the light ion tube contents at sunspot maximum we examine the H^+ and He^+ fluxes through 1000 km at sunspot minimum. In Figure 5a we show how those fluxes change from day to day at 09.00 LT and 21.00 LT. These local times have been selected since they are approximately the local times at which the maximum upward and maximum downward fluxes occur respectively. The outstanding feature is that the H^+ fluxes change significantly over the replenishment period whereas there is relatively little change in the He^+ fluxes. In fact the upward He^+ flux at 09.00 LT only varies between $1.4 \times 10^6 \, cm^{-2} s^{-1}$ and $2 \times 10^6 \, cm^{-2} s^{-1}$ over the entire integration period. However, the upward H^+ flux is approximately $1.34 \times 10^8 \, cm^{-2} s^{-1}$ on the first day and it appears that it may level off at a value around $5 \times 10^7 \, cm^{-2} s^{-1}$ in the later stages of replenishment, although a magnetic storm may well occur before this value is achieved (Park, 1974). Thus these results indicate that the upward H^+ fluxes through 1000 km can vary by factors of 2-3 throughout the replenishment period at sunspot minimum.

The variation of upward H^+ flux throughout the replenishment period contrasts sharply with the work of Murphy et al.(1976). Their sunspot minimum calculations indicated that the upward H^+ flux during the day varied little throughout the replenishment period. Murphy et al.(1976) only carried out O^+/H^+ calculations and consequently the effect of He^+ on these two runs was not included. The difference between the results presented here and those presented by Murphy et al.(1976) may therefore result from the inclusion of He^+ as a major ion in our calculations. Although this has some effect a closer examination of the calculations carried out in Chapter IV shows it is not the main factor. In Chapter IV the behaviour of He^+ at sunspot minimum was investigated. He^+ was treated as a minor ion and consequently O^+ and H^+ densities and fluxes were calculated initially. Thus the H^+ behaviour was not influenced by He^+. However, the day to day behaviour of the daytime upward H^+ flux followed a similar behaviour to that presented in Figure 5a. It therefore appears that the day to day changes in the upward H^+ flux that arises in our calculations arises from collisional processes. In the formulations of St.-Maurice and Schunk(1977), used in Chapter IV, and Quegan et al.(1981) used in this chapter, the collision frequencies ν_{ij} that appear in the momentum equation are multiplied by $(1 - \Delta_{ij})$ where Δ_{ij} is the correction factor. Taking i and j to refer to O^+ and H^+ respectively, the correction factor Δ_{ij} decreases as the ratio $n_i/n_j = n(O^+)/n(H^+)$ decreases (see Table 4 of St.-Maurice and Schunk,1977). Thus at a given height Δ_{ij} decreases from day to day throughout the replenishment period and consequently the H^+ flow is further impeded by O^+. The correction factor Δ_{ij} was not included in the work of Murphy et al.(1976).

We have highlighted the correction factor as a possible explanation for the difference between our results and those presented by Murphy et al.(1976). However, it is noted that it is not the single cause of the decrease in the day to day upward flux of H^+. As the H^+ content builds up the H^+ partial pressure gradient will resist the upward flow of H^+. In addition, the increasing ratio $n(H^+)/n(O^+)$ will lead to a smaller net production from the charge exchange reactions that create and destroy H^+. These latter processes were also in the model of Murphy et al.(1976). Further calculations will be necessary to evaluate the importance of each of those processes.

From Figure 5a it can be seen that the He^+ flux at 09.00 LT initially increases from day to day and then starts to decrease. A possible explanation can be given in terms of the O^+ contribution to the polarization electric field and $He^+ - H^+$ collisions. Initially the O^+ contribution to the polarization electric field is suppressed due to the charge exchange reaction

$$O^+ + H \longrightarrow O + H^+ .$$

Murphy et al.(1976) noted that upward daytime H^+ fluxes can suppress N_mF2 by about 15%. As the H^+ number densities build up the net loss of O^+ from this reaction decreases and the O^+ polarization field may have more influence on He^+. Simultaneously, the increasing H^+ densities and decreasing upward H^+ fluxes limit the upward flow of He^+. Thus the opposing effects of the O^+ contribution to the polarization field and the $He^+ - H^+$ collision frequency may explain the behaviour of the He^+ flux in the morning throughout the replenishment period.

Both the downward H^+ and He^+ fluxes through 1000 km at 21.00 LT increase in magnitude throughout the replenishment period. The day to day increase in the return flow of H^+ at night-time is simply a consequence of the H^+ content increasing. However, it appears that there are two factors that influence the return flow of He^+. Similar to H^+ the increasing He^+ content is a contributory factor. The second factor is the return flow of H^+ which drags the He^+ with it. It is those two factors which cause the irregular day to day behaviour of the He^+ flux after day eight. After day eight the He^+ content starts to decrease (Figure 4a). This causes a decrease in the magnitude of the return flow of He^+ in the evening which is soon offset by the increased drag with H^+. Again, after the thirteenth day, the return flow of He^+ decreases due to the decreasing He^+ content. From Figure 5a the calculated maximum return flux of H^+ at sunspot minimum is slightly bigger than $10^8 cm^{-2} s^{-1}$ whereas the maximum return flux of He^+ is approximately $3.3 \times 10^6 cm^{-2} s^{-1}$. However, for the parameters used here, these values are only achieved after exceptionally long quiet spells.

Comparing Figure 4b with Figure 4a it appears that the H^+ and He^+ tube contents rise sharply at sunspot maximum compared to their behaviour at sunspot minimum. It is clear that many days are required for complete replenishment to be achieved. However, a closer examination shows that, at sunspot minimum, the H^+ content rises more rapidly over the first four days than at sunspot maximum. In fact, the two H^+ content curves do not cross until day ten. Since magnetic storms occur more frequently than every ten days (Park,1974) our results indicate that greater H^+ tube contents should occur at sunspot minimum compared to sunspot maximum. This mainly results from greater neutral hydrogen densities at sunspot minimum (see Figure 5, Chapter IV and Figure 1, Chapter V). Murphy et al.(1976) showed that the H^+ tube content increased far more rapidly with greater neutral hydrogen densities. In fact, one may expect a greater difference between the H^+ tube contents at sunspot minimum and sunspot maximum when examining our corresponding neutral hydrogen densities. However, there are further factors which complicate the situation such as temperatures and the O^+ number densities which influence the production of H^+, collisions of H^+ and in particular the O^+ contribution to the polarization field which accelerates H^+.

It is the behaviour of the H^+ tube content at night-time that causes the sunspot minimum and sunspot maximum curves for H^+ to cross at day ten. Although the sunspot minimum curve rises more rapidly initially the main increase is between sunrise and sunset, apart from the first few days, and there is soon a decrease in the content at night-time due to the collapsing O^+ layer. At sunspot maximum, due to the larger O^+ densities, production of H^+ often continues throughout the night and the H^+ is driven upwards by the O^+ contribution to the polarization field.

In Chapter IV it was noted that the He^+ results of Murphy et al.(1979) for sunspot maximum were strongly influenced by their H^+ number densities, which were under-estimated after the fourth day of the integration period. Consequently the He^+ densities were over-estimated and this cast some doubt on their conclusion that the depletion of magnetic flux tubes by magnetic storms provides a loss process for neutral helium at sunspot maximum. The results presented here remove that doubt and confirm the results of Murphy et al.(1979). In addition, as noted in Chapter IV, whether or not light ion depletion provides an effective loss process for neutral helium at sunspot minimum depends on the frequency of magnetic storms compared to the number of days needed for the He^+ content to reach its maximum. This was eight days in our calculations but could be less with different parameters such as higher temperatures. In any case the He^+ contents were smaller at sunspot minimum compared to sunspot maximum.

In Figure 5b for sunspot maximum, we show the H^+ and He^+ fluxes through 1000 km at 09.00 LT and 21.00 LT. Similar to the sunspot minimum results the upward daytime He^+ flux hardly varies from day to day throughout the replenishment period. This He^+ flux settles out at around $2.2 \times 10^6 cm^{-2} s^{-1}$ towards the end of the integration period at sunspot maximum, compared to $1.4 \times 10^6 cm^{-2} s^{-1}$ at sunspot minimum. The magnitude of the downward He^+ flux increases throughout the integration period, but is less than the corresponding sunspot minimum results due to the resistance of the O^+ contribution to the polarization field. The H^+ flux at 21.00 LT in Figure 5b emphasizes the point, already noted by Bailey et al.(1979), that the H^+ flux is often upwards during the night-time at sunspot maximum.

6.4 Conclusions.

At sunspot minimum He^+ is certainly a minor ion. If the He^+ tube content is not depleted by magnetic storms its magnitude is limited by H^+. Our results indicate that, during the later stages of long quiet periods, it becomes more difficult for He^+ to diffuse upwards through H^+. In addition, downward flowing H^+ drags He^+ into the recombination region. Consequently collisions between He^+ and H^+ play an important role in the behaviour of He^+ at sunspot minimum.

At sunspot minimum the He^+ tube content reached a maximum after eight days. By comparing results obtained using the theoretical formulations of St.-Maurice and Schunk (1977) and Quegan et al.(1981) we have found that this maximum is under-estimated by approximately 12% if He^+ is treated theoretically as a minor ion. However, in general, for mid-latitudes, the formulation of St.-Maurice and Schunk (1977) in which O^+ and H^+ are treated as major ions and He^+ is treated as a minor ion, provides a sufficiently accurate description of the behaviour of O^+, H^+ and He^+ at sunspot minimum. In general the He^+ densities were under-estimated and the H^+ densities were over-estimated when He^+ was treated as a minor ion. This effect may be more pronounced at sunspot maximum but at present we have not carried out sunspot maximum calculations using the formulation of St.-Maurice and Schunk(1977).

In contrast to the work of Murphy et al.(1976) we found that the upward daytime fluxes of H^+ decreased from day to day throughout the replenishment period at both sunspot minimum and sunspot maximum. Further calculations will be necessary to evaluate the importance of the various physical processes that influence this behaviour. However, contributory factors include the H^+ partial pressure gradient, the production of H^+ and the diffusion correction factor. The latter was not included in the work of Murphy et al. (1976). It is noted that this behaviour was not caused by the inclusion of He^+ as a major ion. In fact, via its contribution to the polarization field, He^+ helps to accelerate H^+ to higher altitudes. However, there was little day to day change in the daytime upward He^+ fluxes throughout the replenishment period at both sunspot minimum and sunspot maximum.

The magnitude of the night-time return fluxes of H^+ and He^+ increase from day to day as the contents increase throughout the replenishment period. Particularly at sunspot minimum, the return flow of He^+ is enhanced by downward flowing H^+. After eight days of replenishment the downward fluxes of H^+ and He^+ were $7.5 \times 10^7 cm^{-2} s^{-1}$ and $2.5 \times 10^6 cm^{-2} s^{-1}$ respectively at 21.00 LT for our sunspot minimum calculations. In our sunspot maximum calculations the H^+ flux at 21.00 LT on the eighth day was still upward but small in magnitude. The corresponding He^+ flux was downward with magnitude $8 \times 10^5 cm^{-2} s^{-1}$. The O^+ polarization field plays a major role in limiting the flow of both ions.

Our results indicate that H^+ tube contents are greater at sunspot minimum compared to sunspot maximum. For the He^+ tube contents the opposite is true. These features are mainly associated with the densities of the corresponding neutral constituents.

At sunspot maximum magnetic storms provide an effective loss process for neutral helium and neutral hydrogen. The H^+ and He^+ flux tube contents are depleted via the magnetic storms and the flux tubes are then replenished at the expense of the corresponding neutral constituents. A similar situation exists at sunspot minimum for neutral hydrogen. However, the situation is slightly different for neutral helium at sunspot minimum. After eight days of replenishment the He^+ tube content starts to decrease as H^+ drags He^+ into the recombination region, where it is converted back to neutral helium. With a different set of parameters this may take place in a shorter time.

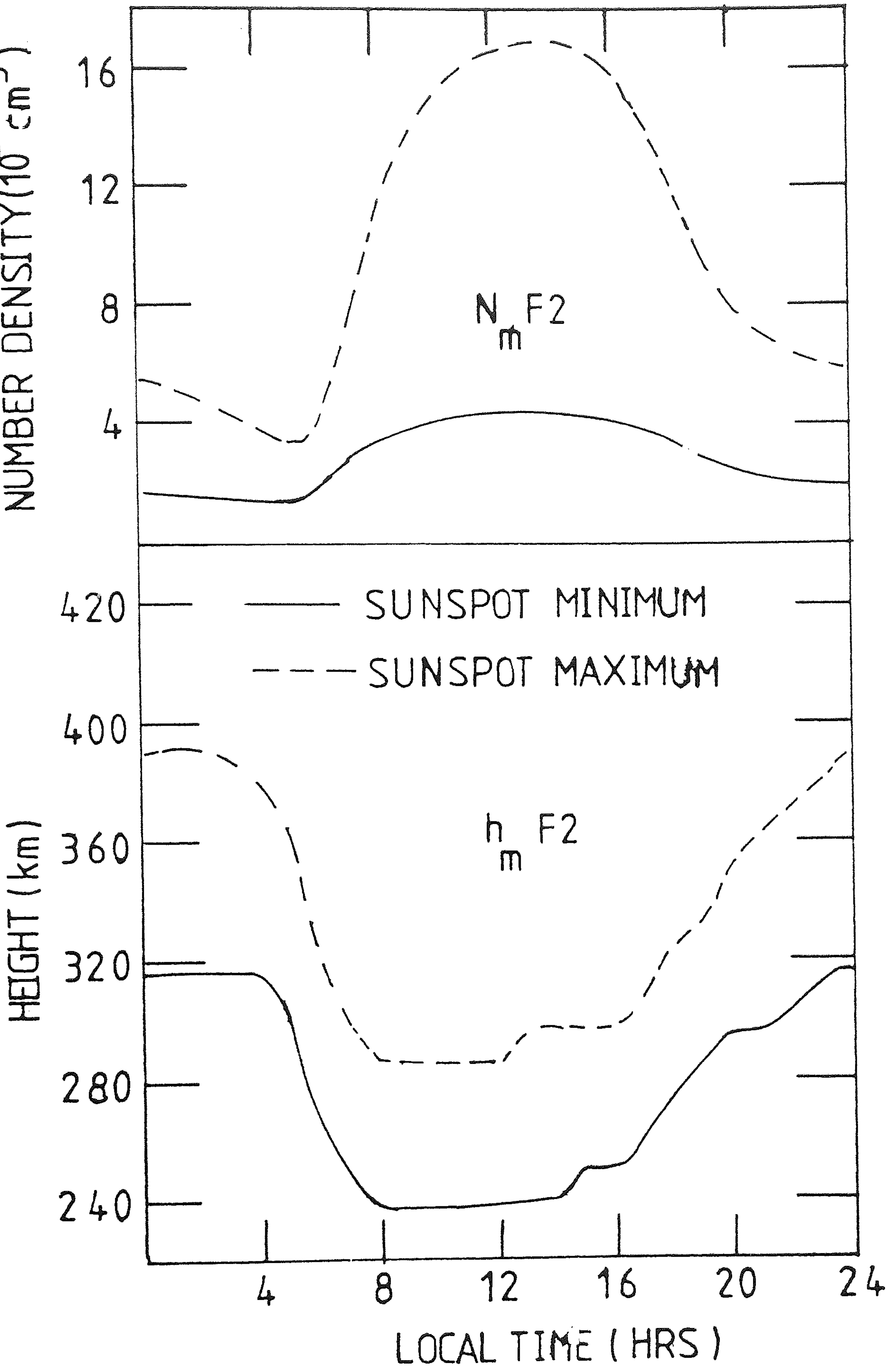

Figure 1. The diurnal behaviour of N_mF2 and h_mF2 on day eight for each set of calculations.

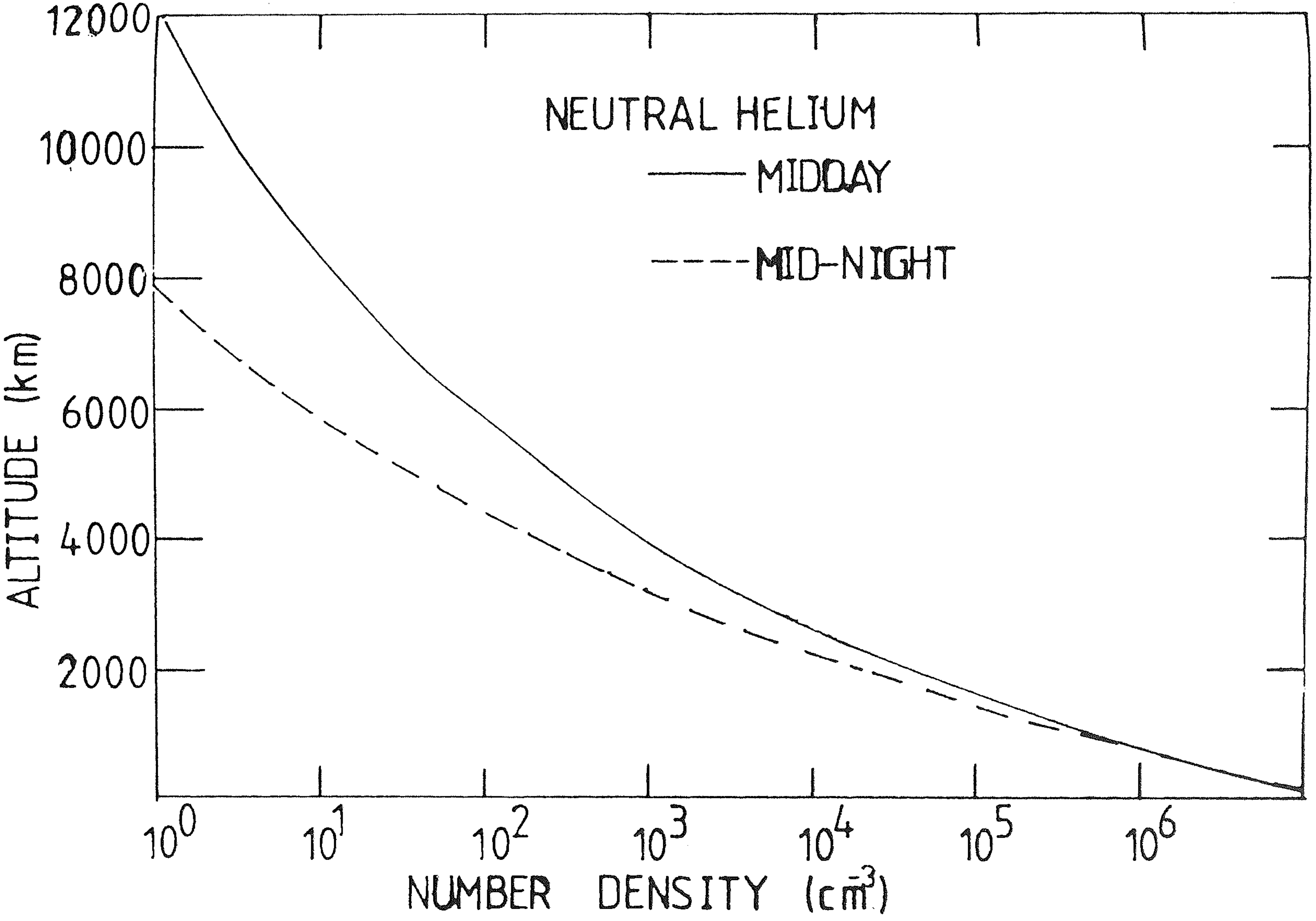

Figure 2. Height profiles of the neutral helium density at midday and midnight for sunspot maximum.

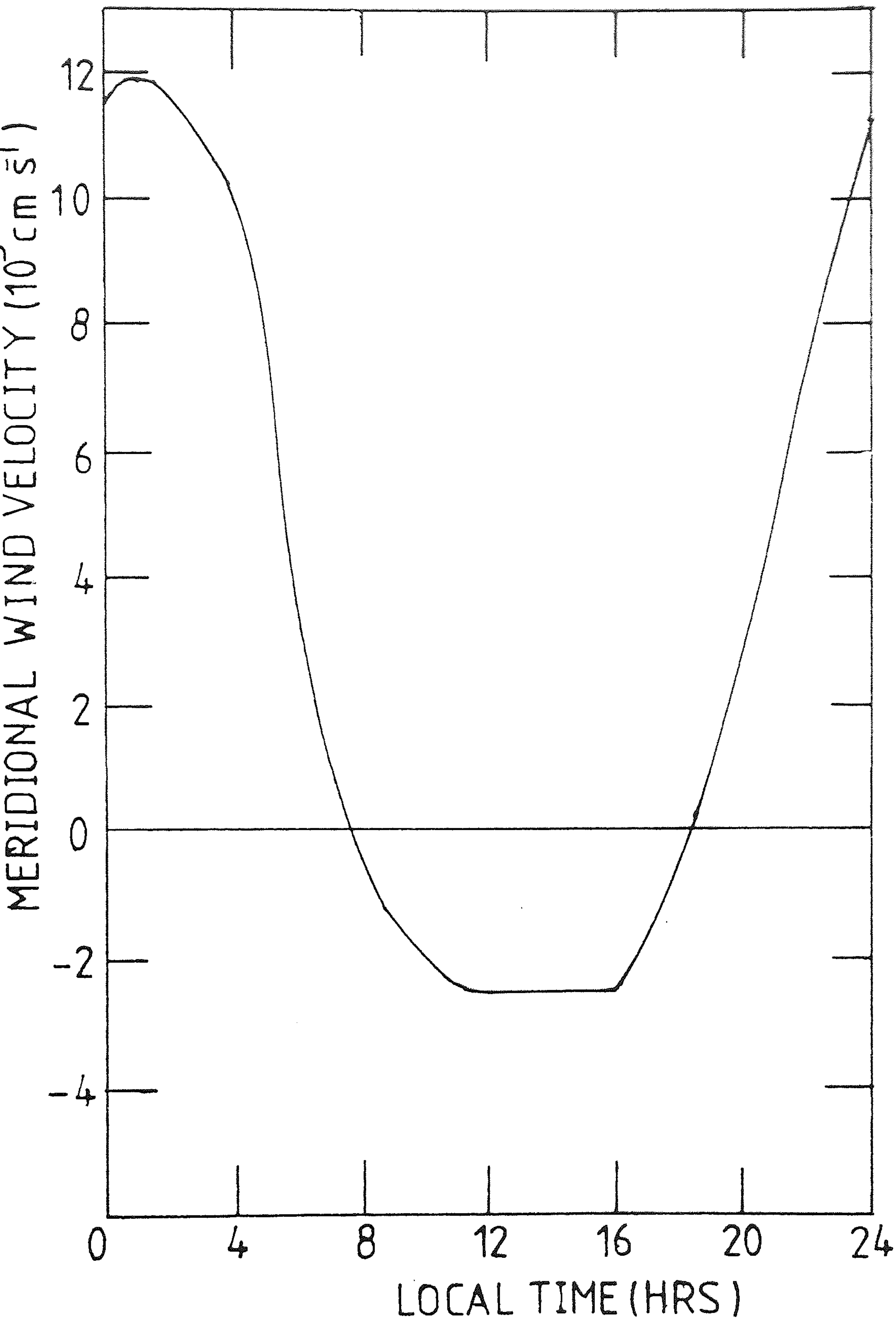

Figure 3. The diurnal variation of the neutral wind velocity over 24 hours.

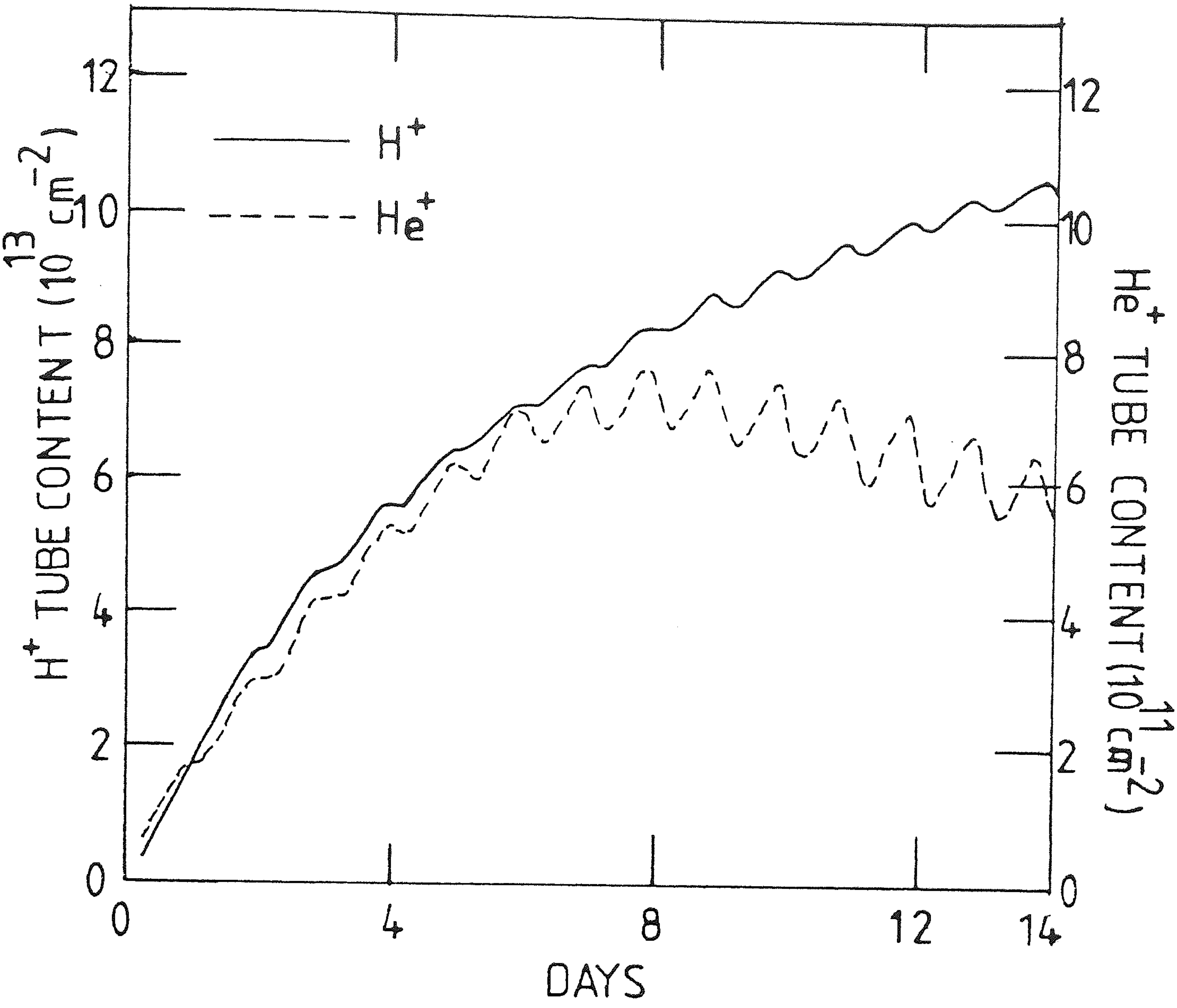

Figure 4a. The variation of the flux tube content for H^+ (solid line) and He^+ (dashed line) at sunspot minimum over the integration period.

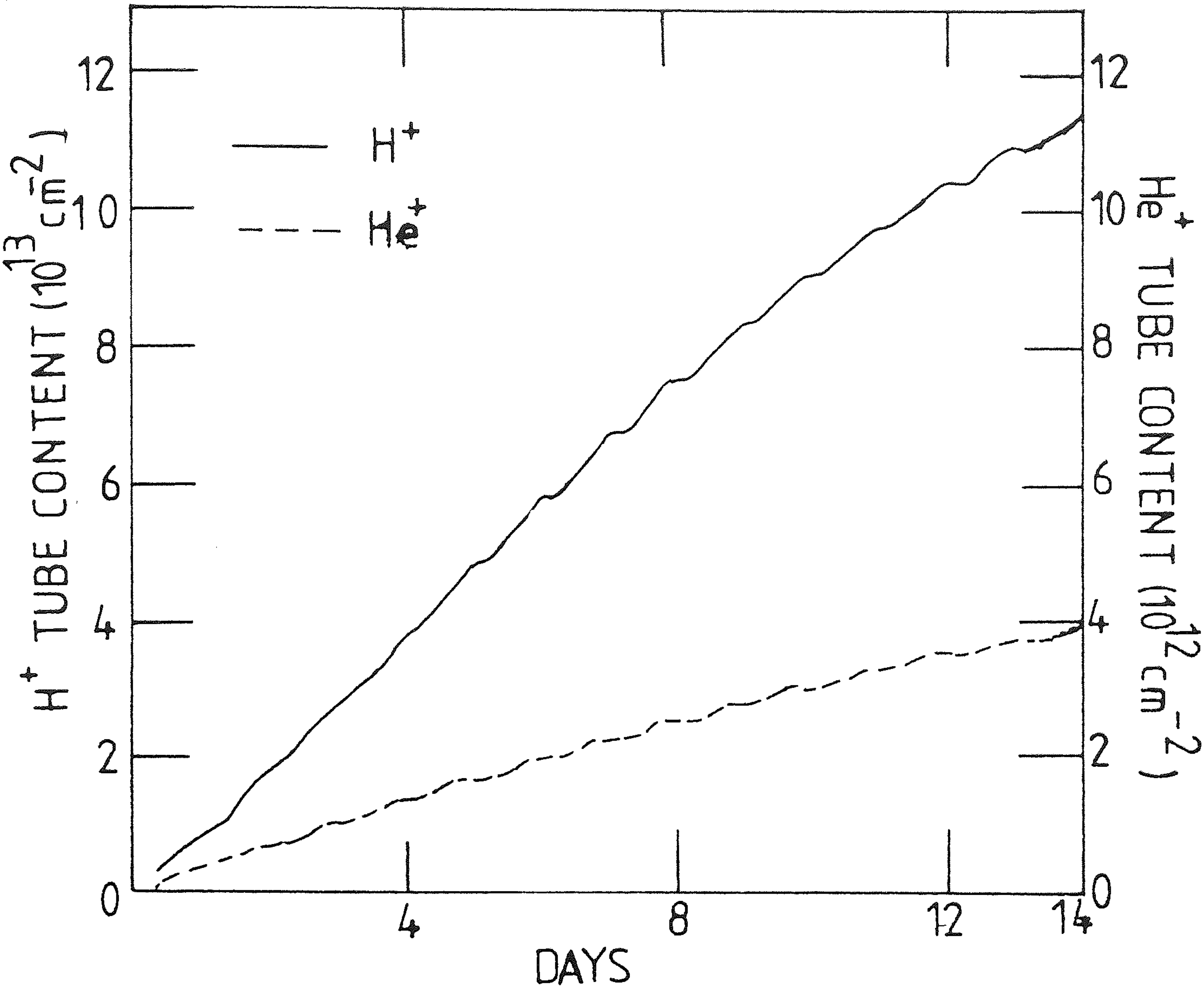

Figure 4b. The variation of the flux tube content of H^+ (solid line) and He^+ (dashed line) at sunspot maximum over the integration period.

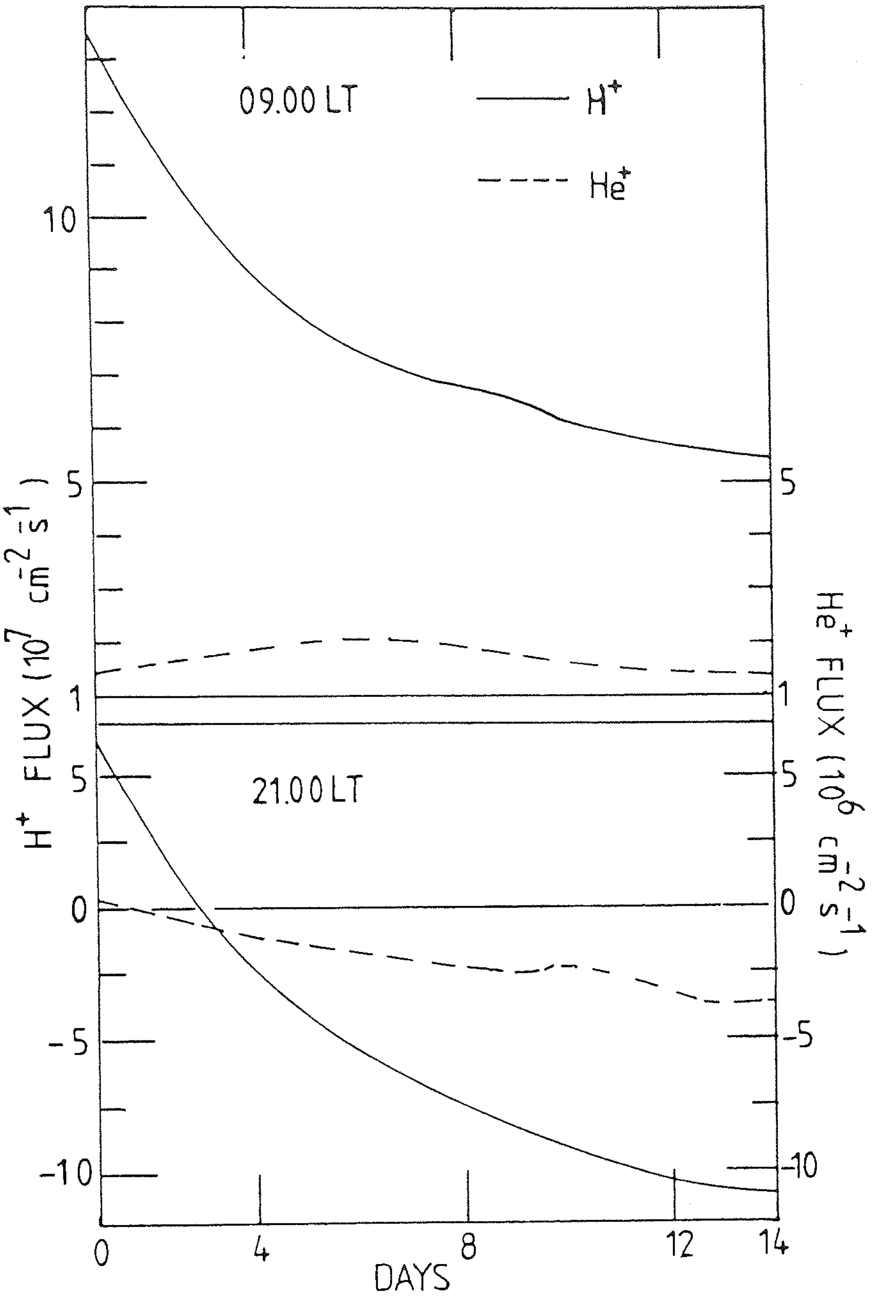

Figure 5a. Sunspot minimum H^+ and He^+ fluxes through 1000 km at the specified times on each day of the integration period.

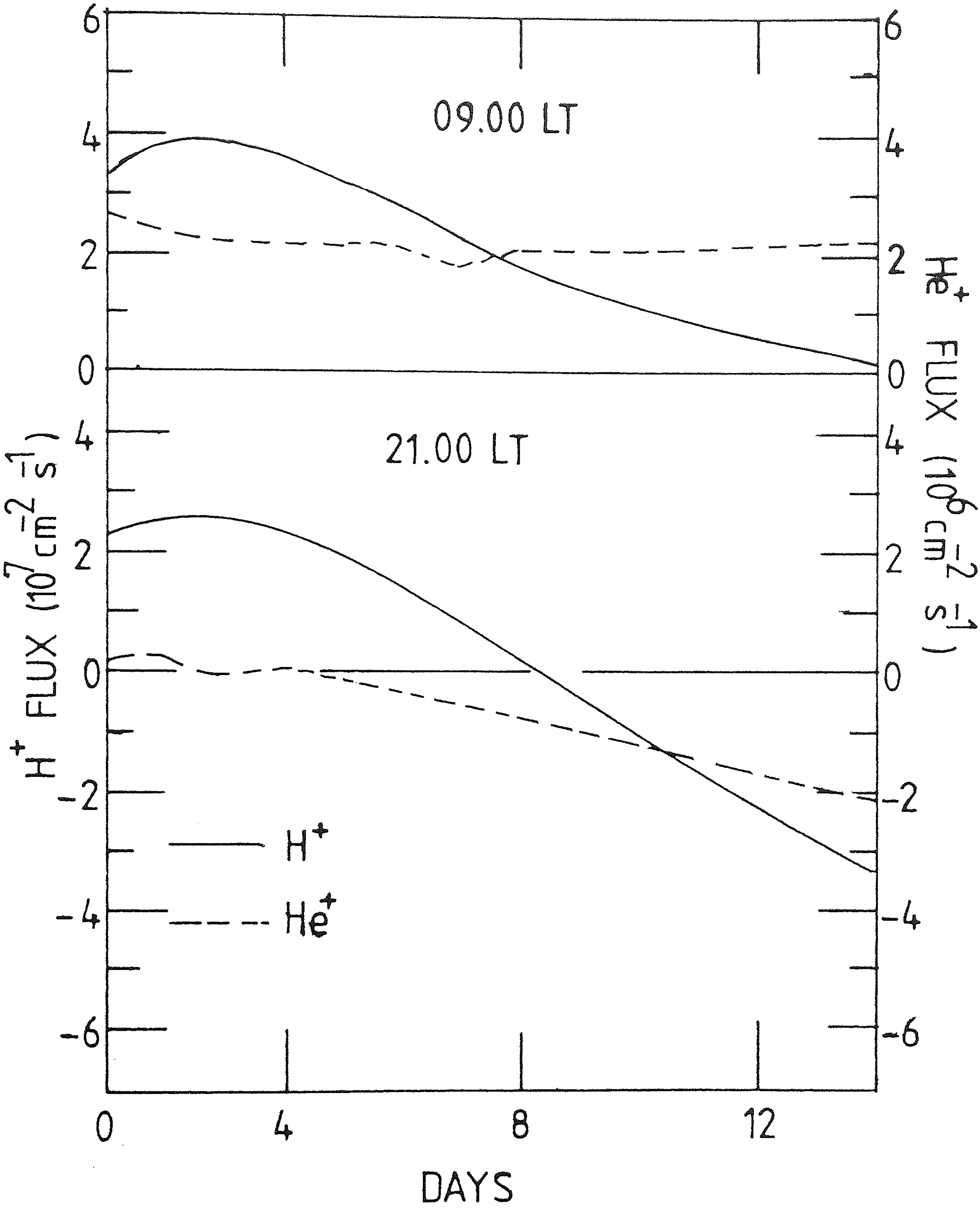

Figure 5b. Sunspot maximum H^+ and He^+ fluxes through 1000 km at the specified times on each day of the integration period.

APPENDIX A

EVALUATION OF OPTICAL DEPTH

The evaluation of the optical depth, τ, is necessary to calculate the photoionization production rate of ions. It was introduced in Chapter I and, according to equation (1.15) is given by

$$\tau = \int_{-\infty}^{s_p} \sigma n ds , \qquad (A.1)$$

where s is the distance along a radiation path, increasing from the sun to the point P, σ is the cross section for the absorption of the radiation and n is the neutral number density. It is clear that τ gives the number of molecules and atoms along the radiation path that absorb photons.

Since the neutral density is usually expressed as a function of height we make the substitution

$$ds = - dh \sec \chi , \qquad (A.2)$$

where h denotes altitude and χ is the solar zenith angle given by equation (4.10). Thus equation (A.1) becomes

$$\tau = \int_{h_p}^{\infty} \sigma n \sec \chi \, dh \qquad (A.3)$$

The plane Earth approximation.

A common assumption, when the point P is on the sunward side of the Earth, is that the variation of sec χ along the radiation path is sufficiently small to take sec χ outside the integral (A.3). This assumption is only valid when P is well away from sunset and sunrise, since sec χ varies rapidly as $\chi \to \pi/2$. Assuming, in addition, that σ is constant along the ray path and using the result

$$\int_h^\infty n dh = n(h)H(h) ,$$

where H(h) is the scale height of the neutral gas leads to the plane Earth approximation

$$\tau = \sigma n(h)H(h)\sec\chi \quad . \tag{A.4}$$

Determination of $\tau(h,\chi)$ near sunset and sunrise.

Near sunset and sunrise secχ varies rapidly and cannot be taken outside the integral (A.3). In addition, the substitution (A.2) introduces a singularity into the integral expression for the optical depth. Thus special consideration must be given to the evaluation of τ when χ is close to $\pi/2$.

With reference to Fig. 1, suppose that L is a point sufficiently close to G so that the length ξ is small compared to the radial distance of G for any point P between G and L. Then if s = 0 at G we have

$$r_G^2 + s^2 = (r_G + \xi)^2$$

which leads to

$$\xi = \frac{s^2}{2r_G} \qquad (A.5)$$

since ξ is small compared to r_G. To evaluate τ at some fixed point P between G and L we split the integral (A.1) into two parts:

$$\tau = \int_{-\infty}^{s_L} \sigma n ds + \int_{s_L}^{s_p} \sigma n ds \ . \qquad (A.6)$$

For the first integral we again assume that $\sec\chi$ can be taken outside the integral:

$$\int_{-\infty}^{s_L} \sigma n ds = \sigma n(h) H(h) \sec\chi_L \qquad (A.7)$$

For the second integral we assume that n varies exponentially with height for any point between P and L:

$$n = n_G \exp(-{}^{\xi}/_{H}) \ , \qquad (A.8)$$

using this approximation (A.5) gives

$$\int_{s_L}^{s_p} \sigma n ds \simeq \sigma \int_{s_L}^{s_p} n_G \exp\left[\frac{-s^2}{2r_G H}\right] ds$$

$$= \sigma n_G \left[\int_{s_L}^{0} \exp\left[\frac{-s^2}{2r_G H}\right] ds - \int_{0}^{s_p} \exp\left[\frac{-s^2}{2r_G H}\right] ds\right] . \qquad (A.9)$$

To proceed we recall that the error function is defined by

$$\mathrm{erf}(y) = \frac{2}{\sqrt{\pi}} \int_0^y \exp(-t^2)dt \qquad (A.10)$$

To make use of the error function in (A.9) we substitute

$$t = \frac{-s}{(2r_G H)^{\frac{1}{2}}} \qquad (A.11)$$

and (A.9) becomes

$$\int_{s_L}^{s_p} \sigma n ds = \sigma n_G (2r_G G)^{\frac{1}{2}} \left[\int_0^{t_L} \exp(-t^2)dt - \int_0^{t_p} \exp(-t^2)dt \right]$$

$$= \sigma n_G \left[\frac{\pi r_G H}{2} \right]^{\frac{1}{2}} \left\{ \mathrm{erf}(t_L) - \mathrm{erf}(t_p) \right\}. \qquad (A.12)$$

From equations (A.5) and (A.11) we have

$$t^2 = \frac{\xi}{H} \qquad (A.13)$$

and defining ζ, the reduced height, by

$$\zeta = \frac{\xi}{H} \qquad (A.14)$$

equation (A.12) can be written

$$\int_{s_L}^{s_p} \sigma n ds \simeq \sigma n_G \left[\frac{\pi r_G H}{2} \right]^{\frac{1}{2}} \left[\mathrm{erf}(\zeta_L^{\frac{1}{2}}) - \mathrm{erf}(\zeta_p^{\frac{1}{2}}) \right]. \qquad (A.15)$$

It is desirable to remove the dependence of this expression on G. First, we note from (A.8) and (A.14) that

$$n_p = n_G \exp(-\zeta_p)$$

so that (A.16) can be written

$$\int_{s_L}^{s_p} \sigma n ds = \sigma\left[\frac{2r_G H}{2}\right]^{\frac{1}{2}} n_p \exp(\zeta_p)\left[\mathrm{erf}(\zeta_p^{\frac{1}{2}}) - \mathrm{erf}(\zeta_L^{\frac{1}{2}})\right]. \qquad (A.16)$$

Also we note that

$$r_G = r_p \sin\chi_p \qquad (A.17)$$

so that

$$\zeta_p = \frac{\xi_p}{H} = \frac{r_p - r_G}{H} = \frac{r_p}{H}(1 - \sin\chi_p) \quad , \qquad (A.18)$$

noting that $\xi_p = r_p - r_G$ from Fig. 1. A similar expression holds for ζ_L.

Finally, substituting from equations (A.7) and (A.16) into (A.6) yields

$$\tau = \sigma n_L H_L \sec\chi_L +$$

$$+ \sigma n_p \exp(\zeta_p)\left[\frac{\pi r_p \sin\chi_p H}{2}\right]^{\frac{1}{2}}\left[\mathrm{erf}(\zeta_L^{\frac{1}{2}}) - \mathrm{erf}(\zeta_p^{\frac{1}{2}})\right]$$

for the point P close to sunset, or, dropping the p suffices

$$\tau = \sigma H\left[n_L \sec\chi_L + n \exp(\zeta)\left[\frac{\pi r \sin\chi}{2H}\right]\left[\mathrm{erf}(\zeta_L^{\frac{1}{2}}) - \mathrm{erf}(\zeta^{\frac{1}{2}})\right]\right] \qquad (A.19)$$

$$\text{where} \quad \zeta = \frac{r}{H}(1 - \sin\chi) \qquad (A.20)$$

Equation (A.19) holds for $|\chi| \leq \frac{\pi}{2}$. When $|\chi| \gtrsim \frac{\pi}{2}$ so that P is in the anti-sunwards side of G, equation (A.9) is replaced by

$$\int_{s_L}^{s_p} \sigma n ds \simeq \sigma n_G \left[\int_{s_L}^{0} \exp\left[\frac{-s^2}{2r_G H} \right] ds + \int_{0}^{s_p} \exp\left[\frac{-s^2}{2r_G H} \right] ds \right] \qquad (A.21)$$

putting $x = s/(2r_G H)^{\frac{1}{2}}$ in the first integral and $y = s/(2r_G H)^{\frac{1}{2}}$ in the second integral leads to

$$\int_{s_L}^{s_p} \sigma n ds = \sigma n_G (2r_G H)^{\frac{1}{2}} \left[\int_{0}^{x_L} \exp(-x^2) dx + \int_{0}^{y_p} \exp(-y^2) dy \right] . \qquad (A.22)$$

Using (A.5) and (A.14) we see that

$$x^2 = y^2 = \frac{\xi}{H} = \zeta .$$

Since s is measured from G towards P it is clear that s_p is positive and s_L is negative. In view of the definitions of x and y it follows that y_p is positive and x_L is positive and therefore

$$x_L = \zeta_L^{\frac{1}{2}} , \qquad y_p = \zeta_p^{\frac{1}{2}} .$$

Thus (A.22) can be written

$$\int_{s_L}^{s_p} \sigma n ds = \sigma n_p \left[\frac{\pi r_G H}{2} \right]^{\frac{1}{2}} \left[\mathrm{erf}(\zeta_L^{\frac{1}{2}}) + \mathrm{erf}(\zeta_p^{\frac{1}{2}}) \right] \qquad (A.23)$$

where n_G has been eliminated using (A.8). Substituting

(A.7) and (A.23) into (A.6) gives

$$\tau = \sigma H\left[n_L \sec\chi_L + n\left\{\frac{\pi r \sin\chi}{2H}\right\}^{\frac{1}{2}}\exp(\zeta)\left[\mathrm{erf}(\zeta_L^{\frac{1}{2}}) + \mathrm{erf}(\zeta^{\frac{1}{2}})\right]\right] \qquad (A.24)$$

where the p suffices have been dropped and ζ can be determined from (A.20). The only difference between (A.24), for $|\chi| \gtrsim \frac{\pi}{2}$, and (A.19) for $|\chi| \lesssim \frac{\pi}{2}$ is the sign in front of the last term.

Finally we wish to determine an expression for the optical depth at a point P on the anti-sunward side of G ($|\chi| > 90$) and not close to G (see Fig. 2). This case must be treated separately because the assumption that ξ is small compared to r_G, which led to equation (A.5) and (A.24), is only valid when P is close to G.

With reference to Fig. 2 the integral for τ can be split as follows

$$\tau = \int_{-\infty}^{s_p} \sigma n ds = \int_{-\infty}^{s_{L+}} \sigma n ds + \int_{s_{L+}}^{s_p} \sigma n ds \qquad (A.25)$$

and the first integral can be determined from equation (A.24)

$$\int_{-\infty}^{s_{L+}} \sigma n ds = \sigma H\left[n_{L-} \sec\chi_{L-} + n_{L+}\left[\frac{\pi r_{L+} \sin\chi_{L+}}{2H}\right]^{\frac{1}{2}}\exp(\zeta_{L+}) \left\{\mathrm{erf}(\zeta_{L-}^{\frac{1}{2}}) + \mathrm{erf}(\zeta_{L+}^{\frac{1}{2}})\right\}\right].$$

However, $\zeta_{L-} = \zeta_{L+}$ and $n_{L-} = n_{L+}$ so that this equation can be simplified to

$$\int_{-\infty}^{s_{L+}} \sigma n ds = \sigma H n_L \left[\sec\chi_L + 2\exp(\zeta_L) \left\{ \frac{\pi r_L \sin\chi_L}{2H} \right\}^{\frac{1}{2}} \mathrm{erf}(\zeta_L^{\frac{1}{2}}) \right] \quad (A.26)$$

where L can be L+ or L-. The remaining integral in (A.25) is

$$\int_{s_{L+}}^{s_p} \sigma n ds = \int_{s_{L+}}^{\infty} \sigma n ds - \int_{s_p}^{\infty} \sigma n ds$$

$$= - \int_{h_{L+}}^{\infty} \sigma n \sec\chi dh + \int_{h_p}^{\infty} \sigma n \sec\chi dh$$

$$= \sigma n_p \sec\chi_p H - \sigma n_{L+} \sec\chi_{L+} H$$

using the plane Earth approximation. Noting that $\sec\chi_{L+} = - \sec\chi_{L-}$ it follows that

$$\tau = \sigma n H \sec\chi$$

$$+ 2\sigma n_L H \left[\sec\chi_{L-} + \exp(\zeta_L) \left\{ \frac{\pi r_L \sin\chi_L}{2H} \right\}^{\frac{1}{2}} \mathrm{erf}(\zeta_L^{\frac{1}{2}}) \right] \quad (A.27)$$

where $\zeta_L = \frac{r_L}{H} (1 - \sin\chi_L)$.

The quantities evaluated at L in the formulae for τ depend on the location of the point P. The exception is χ_L

which is specified initially as 75° say. Referring to Figure 1 we make use of the result $r\sin\chi = r_G$ for any point P on the radiation path. In particular

$$r_L \sin\chi_L = r \sin \chi \tag{A.28}$$

and therefore

$$\zeta_L = \frac{r_L}{H}(1 - \sin\chi_L)$$

$$= \left(\frac{1 - \sin\chi_L}{\sin\chi_L}\right) \frac{r \sin \chi}{H} \quad . \tag{A.29}$$

Also, using equation (A.9)

$$n = n_G \exp(-\zeta), \; n_L = n_G \exp(-\zeta_L)$$

leading to

$$n_L = n \exp(\zeta - \zeta_L) \quad . \tag{A.30}$$

Summary:

In this summary we choose $\chi_{L-} = 75°$ and $\chi_{L+} = 105°$. The optical depth, τ, is calculated from the following formulae, which are obtained from (A.4), (A.19) and (A.24), substituting for n_L from (A.30) where necessary:

$|\chi| < 75°$

$$\tau = \sigma n H \sec \chi$$

$75^\circ \le |\chi| \le 105^\circ$

$$\tau = \sigma H n \exp(\zeta)\left[\exp(-\zeta_L)\sec\chi_L + \left\{\frac{\pi r \sin\chi}{2H}\right\}^{\frac{1}{2}}\left\{\operatorname{erf}(\zeta_L^{\frac{1}{2}}) \pm \operatorname{erf}(\zeta^{\frac{1}{2}})\right\}\right]$$

$|\chi| > 105^\circ$

$$\tau = \sigma n H\left[\sec\chi + 2\exp(\zeta)\left\{\exp(-\zeta_L)\sec\chi_L + \left[\frac{\pi r \sin\chi}{2H}\right]^{\frac{1}{2}}\operatorname{erf}(\zeta_L^{\frac{1}{2}})\right\}\right]$$

where

$$\zeta = \frac{r}{H}(1 - \sin\chi) \quad , \quad \zeta_L = \left\{\frac{1 - \sin\chi_L}{\sin\chi_L}\right\}\frac{r\sin\chi}{H} \quad .$$

Finally it is noted that the different forms of the Chapman function, $Ch(x,\chi)$, can be obtained from the above formulae by dividing throughout by $\sigma n H$.

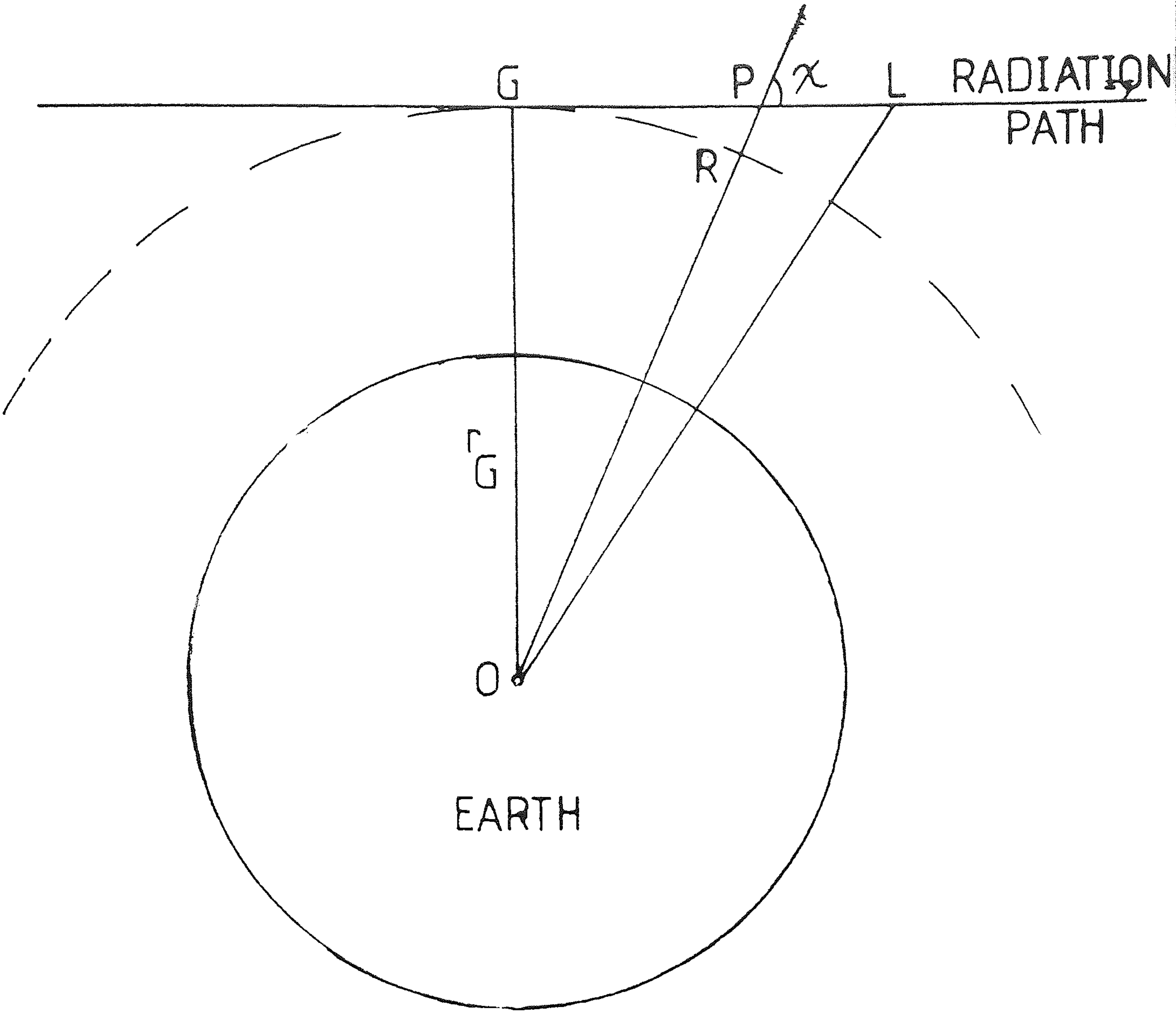

Figure 1. The radiation path (extended) from the sun to a point P is shown. The solar zenith angle at P is χ and is distance r from O, the centre of the Earth. It is assumed that P is sufficiently close to G to ensure that $\xi << r_G$ where ξ = RP, r_G = OG and L is the furthest point from G for which this assumption is valid.

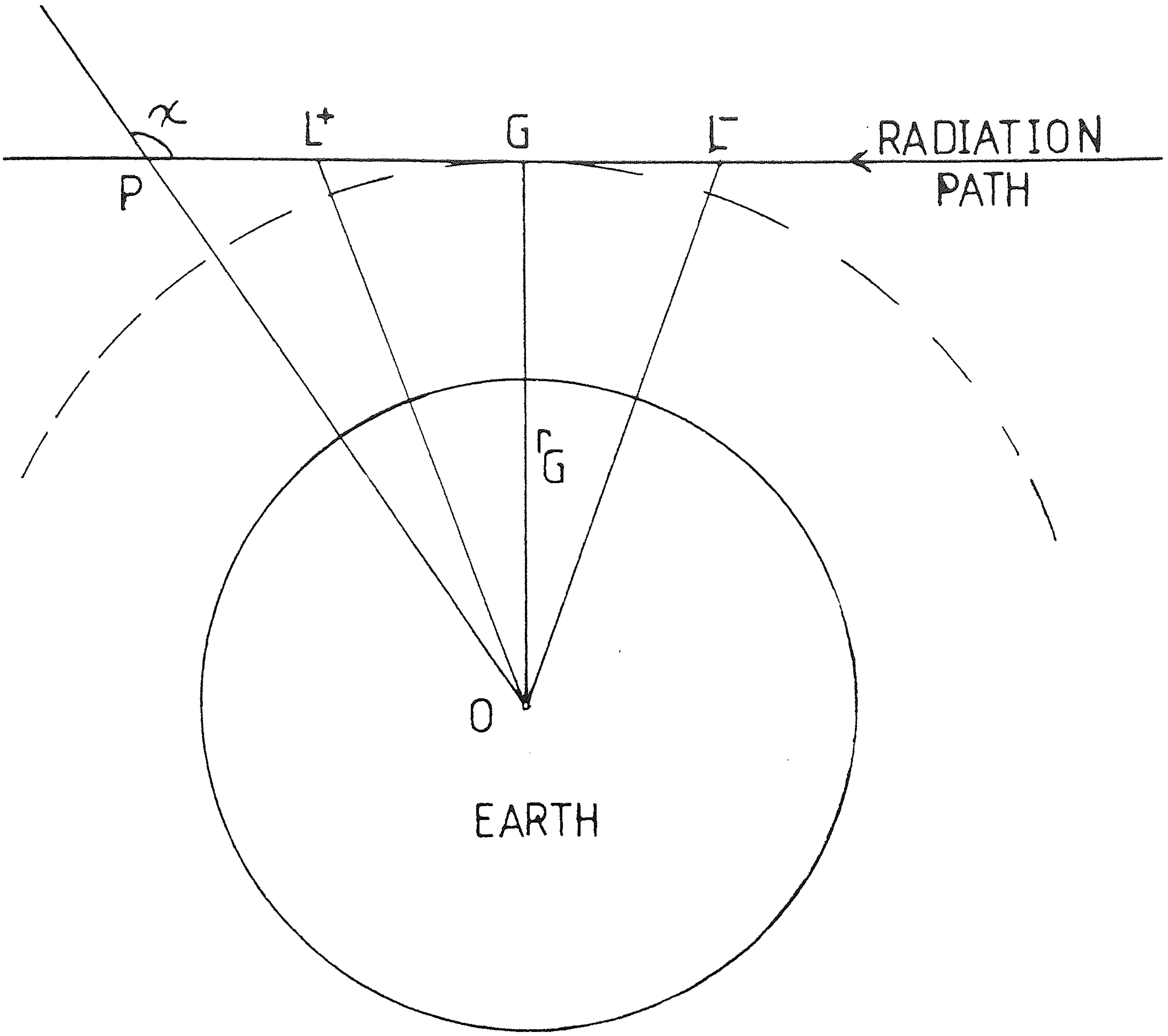

Figure 2. The radiation path (extended) from the sun to a point P on the anti-sunward side of the Earth is shown. L+ and L- define the region in which it is assumed that $\xi \ll r_G$ (see Figure 1). P lies outside this range.

APPENDIX B

THE DIPOLE APPROXIMATION TO THE EARTH'S MAGNETIC FIELD AND ASSOCIATED VARIABLES

A dipole approximation is used for the Earth's magnetic field. With this approximation the equation of a field line is

$$r = r_e \sin^2\theta \tag{B.1}$$

and the magnetic flux density, B, is given by

$$B = B_0 \frac{(1 + 3\cos^2\theta)^{\frac{1}{2}}}{r^3} , \tag{B.2}$$

where r is the radial distance from the centre of the Earth, θ is colatitude, r_e is the radial distance of the equatorial crossing point of the field line and B_0 is a constant.

If s is the arc length along a magnetic field line and I is the angle of dip (the inclination of a field line to the unit vector $\underline{e}_\theta$) then

$$ds \sin I = dr \quad , \qquad ds \cos I = r\, d\theta \tag{B.3}$$

and therefore

$$\tan I = \frac{1}{r}\frac{dr}{d\theta} = 2\cot\theta . \tag{B.4}$$

From equation (B.4) it can easily be shown that

$$\sin I = \frac{2\cos\theta}{(1 + 3\cos^2\theta)^{\frac{1}{2}}} \tag{B.5}$$

$$\cos I = \frac{\sin\theta}{(1 + 3\cos^2\theta)^{\frac{1}{2}}} \quad . \tag{B.6}$$

Arc length along a field line.

The equation of a space curve can be expressed in the parametric form

$$\underline{r} = \underline{r}(t) = (x(t), y(t), z(t)) \quad , \tag{B.7}$$

where $\underline{r}$ is the position vector of a point on the curve, t is a parameter and x, y, z are rectangular Cartesian coordinates. The arc length, s, measured from $t = t_0$ to some general point on the curve can then be expressed in the form

$$s(t) = \int_{t_0}^{t} \left\{ \left(\frac{dx}{dt} \right)^2 + \left(\frac{dy}{dt} \right)^2 + \left(\frac{dz}{dt} \right)^2 \right\}^{\frac{1}{2}} dt \quad . \tag{B.8}$$

For a magnetic field line defined by equation (B.1), using the colatitude θ as the parameter, we have

$$x = - r_e \sin^2\theta \cos\theta \quad , \quad y = r_e \sin^3\theta \tag{B.9}$$

and the equation for the arc length, measured from some general point θ to the equator ($\theta = \pi/2$), takes the form

$$s(\theta) = r_e \int_{\theta}^{\pi/2} \sin\theta \, (1 + 3\cos^2\theta)^{\frac{1}{2}} \, d\theta \quad . \tag{B.10}$$

The evaluation of this integral is simplified by the substitution

$$\sinh x = \sqrt{3} \cos\theta . \tag{B.11}$$

Equation (B.10) can then be written

$$s(x) = \frac{r_e}{\sqrt{3}} \int_0^x \cosh^2 x \; dx$$

$$= \frac{r_e}{2\sqrt{3}} \int_0^x \left\{ 1 + \cosh 2x \right\} dx$$

$$\doteqdot \frac{r_e}{2\sqrt{3}} \left(x + \sinh x \; \cosh x \right) . \qquad (B.12)$$

In summary equation (B.12) gives the arc length from a general point on the field line to the equator in terms of x, where x is defined in equation (B.11).

<u>Expression for $B \frac{\partial}{\partial s}\left(\frac{1}{B}\right)$ as a function of r and θ.</u>

If $\underline{e}_r$ and $\underline{e}_\theta$ are unit vectors in polar coordinates and $\underline{e}_s$ is the unit tangent vector pointing towards the equator then

$$\underline{e}_s = \underline{e}_r \sin I + \underline{e}_\theta \cos I \qquad (B.13)$$

and therefore

$$\frac{\partial}{\partial s} = \underline{e}_s \cdot \underline{\nabla} = \sin I \frac{\partial}{\partial r} + \frac{\cos I}{r} \frac{\partial}{\partial \theta} . \qquad (B.14)$$

Thus, using (B.2) we may write

$$\frac{\partial}{\partial s}\left(\frac{1}{B}\right) = \left[\sin I \frac{\partial}{\partial r} + \frac{\cos I}{r} \frac{\partial}{\partial \theta} \right] \left[\frac{r^3}{B_0 (1 + 3\cos^2\theta)^{\frac{1}{2}}} \right]$$

$$= \frac{3r^2}{B_0 (1 + 3\cos^2\theta)^{\frac{1}{2}}} \left[\sin I + \frac{\cos I \sin\theta \; \cos\theta}{(1 + 3\cos^2\theta)} \right] .$$

Finally, substituting for $\sin I$ and $\cos I$ from (B.5) and (B.6) leads to

$$B \frac{\partial}{\partial s}\left(\frac{1}{B}\right) = \frac{3\cos\theta\,(3 + 5\cos^2\theta)}{r(1 + 3\cos^2\theta)^{3/2}} \tag{B.15}$$

Expression for $\frac{\partial \phi}{\partial s}$ in terms of r,θ where ϕ is the gravitational potential.

The gravitational potential ϕ is defined by the equation

$$\underline{g} = -g_0 \frac{r_0^2}{r^2}\,\underline{e}_r = -\nabla\phi\ . \tag{B.16}$$

Taking the scalar product with $\underline{e}_s$ (see B.13) and substituting for $\sin I$ from (B.5) leads immediately to

$$\frac{\partial \phi}{\partial s} = g_0 \frac{r_0^2}{r^2} \frac{2\cos\theta}{(1 + 3\cos^2\theta)^{\frac{1}{2}}}\ . \tag{B.17}$$

Note also that taking the scalar product of (B.16) with $\underline{e}_r$ and integrating leads to

$$\phi = -g_0 \frac{r_0^2}{r} \tag{B.18}$$

apart from the constant of integration.

Expression for $\frac{\partial}{\partial s}(g \sin I)$ in terms of r,θ

From equations (B.5), (B.14) and (B.16) we have

$$\frac{\partial}{\partial s}(g \sin I) = \left[\sin I \frac{\partial}{\partial r} + \frac{\cos I}{r}\frac{\partial}{\partial \theta}\right]\left[\frac{2g_0 r_0^2 \cos\theta}{r^2(1+3\cos^2\theta)^{\frac{1}{2}}}\right] .$$

After considerable algebraic manipulation and substitutions from equations (B.5) and (B.6) we have

$$\frac{\partial}{\partial s}(g \sin I) = \frac{-2g_0 r_0^2(12\cos^4\theta + 3\cos^2\theta + 1)}{r^3(1+3\cos^2\theta)^2} .$$

APPENDIX C

COLLISION FREQUENCIES AND EFFECTIVE COLLISION FREQUENCIES

Two formulations have been used in this work. In the first theoretical formulation there are two major ions (O^+, H^+) and one minor ion (He^+ in Chapter IV and O^{++} in Chapter V). In the second formulation all three ions in the theoretical model (O^+, H^+ and He^+) are treated as major ions. In both formulations the corresponding collision frequencies are identical. However, there are some differences in the effective collision frequencies when He^+ is treated as a major ion compared to the formulation when He^+ is treated as a minor ion. All variables are defined in Chapter II. Recall that the suffices 1,2,3 and 4 refer to O^+, H^+, He^+ and O^{++} respectively.

1. Formulation allowing for two major ions and one minor ion

From St. Maurice and Schunk (1977) the collision frequency for species s colliding with species t is given by

$$\nu_{st} = 1.27 \frac{Z_s^2 Z_t^2 A_{st}^{\frac{1}{2}}}{A_s} \cdot \frac{n_t}{T_{st}} \qquad (C.1)$$

and the major ion effective collision frequencies are

$$\nu_i' = \nu_{ii} + \frac{5}{4} \nu_{ij} \left[D_{ij}^{(1)} + \frac{3}{2} \frac{\mu_{ij}}{m_i} \cdot \frac{T_i}{T_{ij}} \right] , \qquad (C.2)$$

$$\nu'_{ij} = \frac{5}{4}\left[D^{(4)}_{ij} + \frac{3}{2}\cdot\frac{\mu_{ij}}{m_i}\cdot\frac{T_i}{T_{ij}}\right] . \qquad (C.3)$$

The effective collision frequencies for the minor ion are

$$\nu'_{x} = \frac{5}{4}\sum_{s=1,2}\nu_{xs}\left[D^{(1)}_{xs} + \frac{3}{2}\cdot\frac{\mu_{xs}}{m_x}\cdot\frac{T_x}{T_{xs}}\right] , \qquad (C.4)$$

and

$$\nu'_{xi} = \frac{5}{4}\,\nu_{xi}\left[D^{(4)}_{xi} + \frac{3}{2}\cdot\frac{\mu_{xi}}{m_x}\cdot\frac{T_x}{T_{xi}}\right] \qquad (C.5)$$

where

s and t take 1,2,3 and 4 ,

i and j take 1 and 2 ,

x takes 3 and 4 ,

A_s is the particle mass in atomic mass units ,

$A_{st} = \dfrac{A_s A_t}{A_s + A_t}$ is the reduced mass in atomic mass units,

z_s is the charge on species $s(z_1 = z_2 = z_3 = 1$ and $z_4 = 2)$,

$$D^{(1)}_{ij} = \frac{(3m_i^2 + \frac{1}{10} m_i m_j - \frac{1}{5} m_j)}{(m_i + m_j)^2} ,$$

$$D^{(4)}_{ij} = \frac{(\frac{6}{5} m_j^2 - \frac{3}{2} m_i m_j)}{(m_i + m_j)^2} ,$$

$$T_{ij} = \frac{m_i T_i + m_j T_j}{m_i + m_j} .$$

and $\mu_{ij} = \dfrac{m_i m_j}{m_i + m_j}$.

Assuming that all ions have a common temperature T_i (i.e. $T_{ij} = T_i$), the collision and effective collision frequencies are given by

$$\nu_{12} = 0.07701\ n_2 T_i^{-3/2} ,$$

$$\nu_{21} = 1.23208\ n_1 T_i^{-3/2} ,$$

$$\nu_{31} = 0.56796\ n_1 T_i^{-3/2} ,$$

$$\nu_{32} = 0.28398\ n_2 T_i^{-3/2} ,$$

$$\nu_{13} = 0.142\ n_3 T_i^{-3/2} ,$$

$$\nu_{23} = 0.07701\ n_3 T_i^{-3/2} ,$$

$$\nu_{11} = 0.22451\ n_1 T_i^{-3/2} ,$$

$$\nu_{22} = 0.898\ n_2 T_i^{-3/2} ,$$

$$\nu_{41} = 0.898\ n_1 T_i^{-3/2} ,$$

$$\nu_{42} = 0.308\ n_2 T_i^{-3/2} ,$$

$$\nu_1' = (0.22451\ n_1 + 0.26475\ n_2) T_i^{-3/2} ,$$

$$\nu'_2 = (1.926\, n_1 + 0.89803\, n_2) T_i^{-3/2} ,$$

$$\nu'_{12} = 0.000899\, n_2 T_i^{-3/2} ,$$

$$\nu'_{21} = 3.68345\, n_1 T_i^{-3/2} ,$$

$$\nu'_3 = (0.8576215\, n_1 + 0.790886\, n_2) T_i^{-3/2} ,$$

$$\nu'_{31} = 1.2268\, n_1 T_i^{-3/2} ,$$

$$\nu'_{32} = 0.038337\, n_2 T_i^{-3/2} ,$$

$$\nu'_4 = (1.599563\, n_1 + 1.36467\, n_2) T_i^{-3/2} ,$$

$$\nu'_{41} = 0.757688\, n_1 T_i^{-3/2} ,$$

$$\nu'_{42} = 0.00333\, n_2 T_i^{-3/2} ,$$

$$\nu_{ee} = 38.5373\, n_e T_e^{-3/2} ,$$

$$\nu_{e1} = 54.5\, n_1 T_e^{-3/2} ,$$

$$\nu_{e2} = 54.5\, n_2 T_e^{-3/2} ,$$

$$\nu_{e3} = 54.5\, n_3 T_e^{-3/2} ,$$

$$\nu_{e4} = 54.5\, n_4 T_e^{-3/2} ,$$

and $$\nu'_e = \nu_{ee} + \frac{13}{8}(\nu_{e1} + \nu_{e2})$$

$$= (38.5373n_e + 88.5625(n_1 + n_2)T_e^{-3/2}$$

$$= 127.0998\, n_e T_e^{-3/2}$$

2. Formulation allowing for three major ions.

Details of the formulation are given by Quegan et al. (1981). The collision frequencies are identical to those listed above. The formulae for the effective collision frequencies are

$$\nu'_s = \nu_{ss} + \frac{5}{4}\sum_{t\neq s} \nu_{st}\left| D^{(1)}_{st} + \frac{3}{2}\frac{\mu_{st}}{m_s} \right| ,$$

$$\nu'_{st} = \frac{5}{4}\nu_{st}\left| D^{(4)}_{st} + \frac{3}{2}\frac{\mu_{st}}{m_s} \right| ,$$

where s and t take the values 1, 2 and 3. Letting s and t take on these values leads to

$$\nu'_1 = \nu_{11} + \frac{5}{4}\left| \nu_{12}\left(D^{(1)}_{12} + \frac{3}{2}\frac{\mu_{12}}{m_1}\right) + \nu_{13}\left(D^{(1)}_{13} + \frac{3}{2}\frac{\mu_{13}}{m_1}\right) \right|$$

$$= (0.224506\, n_1 + 0.26477\, n_2 + 0.3955\, n_3)T_i^{-3/2} ,$$

$$\nu'_2 = (1.925924\, n_1 + 0.898026\, n_2 + 0.11627\, n_3)T_i^{-3/2} ,$$

$$\nu'_3 = (0.85762\, n_1 + 0.79088\, n_2 + 0.4490\, n_3)T_i^{-3/2} ,$$

$$\nu'_{12} = 0.000899\, n_2 T_i^{-3/2} ,$$

2

$$\nu'_{13} = 0.01917\, n_3 T_i^{-3/2} ,$$

$$\nu'_{21} = 3.683451\, n_1 T_i^{-3/2} ,$$

$$\nu'_{23} = 0.16584\, n_3 T_i^{-3/2} ,$$

$$\nu'_{31} = 1.226794\, n_1 T_i^{-3/2} ,$$

and $$\nu'_{32} = 0.03834\, n_2 T_i^{-3/2} .$$

APPENDIX D

THE O^+ NUMERICAL PROCEDURE

Applying the Laasonen finite difference procedure to the O^+ diffusion equation led to the system of linear equations (see equation 2.79)

$$P_i n_{i-1} + Q_i n_i + R_i n_{i+1} = S_i \quad i = N, M-1. \qquad (D.1)$$

where n is the O^+ number density, P_i, Q_i, R_i and S_i are defined in Chapter II and N and M correspond to the upper and lower boundaries respectively. The left-hand side of (D.1) is evaluated at $t + \Delta t$ and the right-hand side is a function of n evaluated at t. The number of unknowns in (D.1) exceeds the number of equations by two, so two more equations are required to complete the system (D.1). The extra two equations are supplied by the boundary conditions. At the lower boundary (about 200 km) we assume photochemical equilibrium during the daytime. This leads to an additional equation of the form (see equation 2.89)

$$n_M = S_M \quad .$$

During the night-time the condition at the lower boundary is given by equation (2.91) and we therefore have an additional equation of the form

$$P_M \, n_{M-1} + Q_M \, n_M = 0 \quad .$$

Thus with P_M, Q_M and S_M suitably defined both daytime and night-time lower boundary conditions lead to the additional equation

$$P_M\, n_{M-1} + Q_M\, n_M = S_M\ . \tag{D.2}$$

The remaining equation is supplied by the assumption of zero O^+-flux at s_N (2000 km) and this condition leads to

$$\alpha_1 \frac{\partial n_N}{\partial s} = \alpha_2 n_N\ , \tag{D.3}$$

where α_1 and α_2 are given by (2.82) and (2.83). Using the approximation

$$\frac{\partial n_N}{\partial s} = \frac{n_{N-1} - n_{N+1}}{2\Delta s_N}$$

equation (D.3) is put in the form

$$\gamma n_{N-1} - \alpha_2 n_N - \gamma n_{N+1} = 0$$

where

$$\gamma = \frac{\alpha_1}{2\Delta s_N}\ .$$

Thus the full system of equations is

$$\left.\begin{aligned} \gamma n_{N-1} - \alpha_2 n_N - \gamma n_{N+1} &= 0 \\ P_i n_{i-1} + Q_i n_i + R_i n_{i+1} &= S_i \quad (i = N, M-1) \\ P_M\, n_{M-1} + Q_M\, n_M &= S_M \end{aligned}\right\} \tag{D.4}$$

This system of equations is now manipulated into the standard tridiagonal form. The first two equations of this system are

$$\left.\begin{array}{l} \gamma n_{N-1} - \alpha_2 n_N - \gamma n_{N+1} = 0 \\ P_N\, n_{N-1} + Q_N\, n_N + R_N\, n_{N+1} = S_N \end{array}\right\} \qquad (D.5)$$

Elimination of n_{N-1} from the second of these equations gives

$$Q_N'\, n_N + R_N'\, n_{N+1} = S_N \qquad (D.6)$$

where

$$\left.\begin{array}{l} Q_N' = Q_N + \dfrac{P_N \alpha_2}{\gamma} \\ R_N' = R_N + P_N \end{array}\right\} \qquad (D.7)$$

The system of equations (D.4) can now be written in the standard tridiagonal form

$$\left.\begin{array}{l} Q_N\, n_N + R_N\, n_{N+1} = S_N \\ P_i\, n_{i-1} + Q_i n_i + R_i n_{i+1} = S_i \\ P_M\, n_{M-1} + Q_M\, n_M = S_M \end{array}\right\} \qquad (D.8)$$

In this system we have dropped the primes from the coefficients $Q_N^{'}$ and $R_N^{'}$ noting that they have been redefined by (D.7).

An algorithm is now derived to solve the system (D.8). Suppose that Gaussian elimination has been applied to the system of equation (D.8) and the following stage has been reached

$$\left.\begin{aligned} P_i\, n_{i-1} + Q_i n_i + R_i\, n_{i+1} &= S_i \\ - G_{i+1} n_i + n_{i+1} &= H_{i+1} \end{aligned}\right\} \qquad (D.9)$$

At each stage the variable with the largest suffix is eliminated so that the remaining equation has only two unknowns. Then the coefficient of the remaining variable with the largest suffix is made to be unity. Eliminating n_{i+1} between the two equations of (D.9) we get

$$P_i n_i + (G_i + R_i G_{i+1}) n_i = S_i - R_i H_{i+1}$$

or $$n_i = - \frac{P_i}{Q_i + R_i G_{i+1}}\, n_{i-1} + \frac{S_i - R_i H_{i+1}}{Q_i + R_i G_{i+1}} \qquad (D.10)$$

and comparing with

$$n_i = G_i n_{i-1} + H_i \quad (i = N+1, M) \qquad (D.11)$$

gives

$$G_i = \frac{-P_i}{Q_i + R_i G_{i+1}} , \qquad H_i = \frac{S_i - R_i H_{i+1}}{Q_i + R_i G_{i+1}} \qquad (D.12)$$

for $i = M-=, M-2, M-3, \ldots, N+1$.

The remaining two equations from the Gaussian elimination are

$$G_N n_N + R_N n_{N+1} = S_N$$

$$- G_{N+1} n_N + n_{N+1} = H_{N+1}$$

Eliminating n_{N+1} between these two equations we get

$$n_N = \frac{S_N - R_N H_{N+1}}{Q_N + R_N G_{N+1}} \qquad (D.13)$$

To start the recurrence relations (D.12), G_M and H_M are required. These are defined by the last equation of (D.8) and they are

$$G_M = - \frac{P_M}{Q_M} , \quad H_M = \frac{S_M}{Q_M} \qquad (D.14)$$

SUMMARY OF 0^+ NUMERICAL PROCEDURE

(1) Calculate P_i, Q_i, R_i and S_i for $i = N, M-1$.

(2) Recalculate Q_N and R_N from equation (D.7) (this applies

the upper boundary condition).

(3) Calculate P_M, Q_M, S_M using either the daytime boundary condition (equation 4.27) or the night-time boundary condition (equation 4.28).

(4) Calculate G_M and H_M from equation (D.14).

(5) Calculate G_i and H_i for $i = M-1, M-2, \ldots, N+1$ from equation (D.12).

(6) Calculate n_N from equation (D.13).

(7) Calculate n_i for $i = N+1, \ldots, M$ using equation (D.11).

References

Angerami, J. J. and Thomas, J. O.(1964), J. Geophys. Res. 69,4537.

Axford, W. I.(1968), J. Geophys. Res., 73,6855.

Bailey, G. J., Moffett, R. J. and Murphy, J. A.(1977), Planet. Space Sci., 25,967.

Bailey, G. J., Moffett, R. J. and Murphy, J. A.(1978), Planet. Space Sci., 26,753.

Bailey, G. J., Moffett, R. J. and Murphy, J. A.(1979), J. Atmospheric Terr. Phys., 41,417.

Banks, P. M. and Holzer, T. E.(1969), J. Geophys. Res., 74,6317.

Banks, P. M., Nagy, A. F. and Axford, W. I.(1971), Planet. Space Sci., 19,1053.

Banks, P. M. and Kockarts, G.(1973), Aeronomy, Academic Press, New York.

Banks, P. M., Schunk, R. W. and Raitt, W. J.(1974), J. Geophys. Res., 79,4691.

Bates, D. R. and Patterson, T. N. L.(1962), Planet. Space Sci., 9,599.

Bauer, S. J.(1963), Nature, 197,36.

Bauer, S. J.(1966), The Structure of the topside ionosphere. In Electron density profiles in the ionosphere and exosphere (Ed. J. Frihagn), North-Holland, Amsterdam.

Bauer, S. J.(1966), Ann. Geosphy., 22,247.

Behnke, R. A.(1970), Ph.D. Thesis, Rice University, Houston, Texas.

Brace, L. H., Reddy, P. M. and Mayr, H. G.(1967), J. Geophys. Res., 72,265.

Brace, L. H., Maier, E. J. R., Hoffman, J. H., Whittaker, J. and Shepherd, G. G.(1974), J. Geophys. Res., 79,5211.

Breig, E. L., Torr, M. R., Hanson, W. B., Hoffman, J. H., Walker, C. G. and Nier, A. O.(1977), J. Geophys. Res., 82,1008.

Brinton, H. C., Pharo, M. W., Mayr, H. G. and Taylor, H. A. (1969), J.Geophys. Res., 74,2941.

Brinton, H. C. and Mayr, H. G.(1972), Space Research, XII, 751.

Burgers, J. M.(1969), Flow Equations for Composite Gases, Academic Press, New York.

Carpenter, D. L.(1963), J. Geophys. Res., 68,1675.

Carpenter, D. L.(1966), J. Geophys. Res., 71,693.

Chapman, S.(1931a), Proc. Phys. Soc. (London), 43,26.

Chapman, S.(1931b), Proc. Phys. Soc. (London), 43,483.

Chapman, S.(1950), J. Atmospheric Terr. Phys., 1,121.

Chapman, S. and Cowling, T. W.(1970), Mathematical Theory of Non-Uniform Gases, Cambridge University Press, London.

Chapell, C. R., Harris, K. K. and Sharp, G. W.(1970), J. Geophys. Res., 75,50.

Conard, J. R. and Schunk, R. W.(1979), J. Geophys. Res., 84,811.

Evans, J. V.(1967), Planet. Space Sci., 15,1387.

Evans, J. V.(1969), Proc. IEEE, 57,496.

Evans, J. V.(1971a), Radio Sci., 6,609.

Evans, J. V.(1971b), Radio Sci.,6,843.

Fontheim, E. G. and Banks, P. M.(1972), Planet. Space Sci., 20,73.

Frederik, D. and Chang, T. S.(1965), Continuum Mechanics, Allyn and Bacon, Inc., Boston.

Geiss, J., Balsiger, H., Eberhardt, P., Walker, H., Weber, L., Young, D. and Rosenbauer, H.(1978), Space Sci. Rev., 22,537.

Geiss, J. and Young, D.(1981), J. Geophys. Res., 86,4739.

Grad, H.(1949), Commum. Pure Appl. Math., 2,331.

Grad, H.(1958), Principle of the kinetic theory of gases, Handb. Phys., 12,205.

Hangen, J. B.(1972), Nat. Astro. Ionosphere Centre, Arecibo, Puerto Rico, Rep., 18.

Hanson, W. B.(1962), J. Geophys. Res., 67,183.

Hanson, W. B.(1965), Structure of the ionosphere, in Satellite Environment Handbook (Ed. F. S. Johnson), Stanford University Press, California.

Heelis, R. A., Moffett, R. J. and Windle, D. W.(1972), J. Atmospheric Terr. Phys., 35,223.

Hildebrand(1974), Introduction to numerical analysis, Tata. McGraw-Hill.

Hoffman, J. H.(1967), Science, 155,322.

Howorka, F., Viggiane, A. A., Albritton, D. L., Ferguson, E. E. and Fehsenfield, F. C.(1979), J. Geophys. Res., 84,5941.

Jacchia, L. G.(1965), Smithsonian Centr. Astrophys., 8,215.

Jacchia, L. G.(1971), Smithsonian Astrophys. Obs. Special Report 332.

Johnson, F. S.(1960), J. Geophys. Res., 65,577.

Johnson, R. and Biondi, M. A.(1978), Geophys. Res. Lett., 5,847.

Kockarts, G. and Nicolet, M.(1963), Ann. Geophys., 19,370.

Lemaire, J.(1972), J. Atmospheric Terr. Phys., 34,1647.

Maher, L. J. and Tinsley, B. A.(1977), J. Geophys. Res., 82,689.

Mange, P.(1960), J. Geophys. Res., 65,3833.

Massa, J. I., Ciceron, R. J. and Nagy, A. F.(1974), Summary in Atmosphere, 3,338.

Mayr, H. G., Fontheim, E. G., Brace, L. H., Brinton, H. C. and Taylor, H. A.(1972), J. Atmospheric Terr. Phys., 34,1659.

McElroy, M. B.(1965), Planet. Space Sci., 13,403.

Nironov, A. V., Prohudina, V. S., and Shefav, N. N.(1959), Spectral Electropho. Radar Res. Aurora Airglow, 1,20.

Moffett, R. J. and Murphy, J. A.(1973), Planet. Space Sci., 21,43.

Moulton, F. R.(1926), New Methods in Exterior Ballistics, University of Chicago Press; reprinted in 1962: Methods in Exterior Ballistics, Dover Publications, Inc., New York.

Murphy, J. A., Bailey, G. J. and Moffett, R. J.(1976), J. Atmospheric Terr. Phys., 38,351.

Murphy, J. A. and Moffett, R. J.(1978), Planet. Space Sci., 26,281.

Murphy, J. A., Bailey, G. J. and Moffett, R. J.(1979), Planet. Space Sci., 27,1441.

Murphy, J. A., Bailey, G. J., Moffett, R. J., Quegan, S. and Heelis, R. A.(1981), submitted to Planet. Space Sci.,

Nakada, M. P. and Singer, S. F.(1968), Geophys. J. R. Astr. Soc., 15,163.

Nagy, A. F., Bauer, P. and Fontheim, E. G.(1968), J. Geophys. Res., 73,6259.

Nagy, A. F. and Banks, P. M.(1972), J. Geophys. Res., 77,4277.

Nicolet, M.(1961), J. Geophys. Res., 66,2263.

Paresce, F., Bowyer, C. S. and Kumar, K.(1974), J. Geophys. Res., 79,174.

Park, C. G.(1974), J.Geophys. Res., 79,169.

Quegan, S., Bailey, G. J. and Moffett, R. J.(1981), Planet. Space Sci., 29,851.

Raitt, W. J., Schunk, R. W. and Banks, P. M.(1975), Planet. Space Sci., 23,1103.

Raitt, W. J., Schunk, R. W. and Banks, P. M.(1977), Planet. Space Sci., 25,291.

Raitt, W. J., Schunk, R. W. and Banks, P. M.(1978), Planet. Space Sci., 26,255.

Rishbeth, H. and Garriot, O. K.(1969), Introduction to ionospheric physics, International Geophysics series, Academic Press, New York.

Sanatani, S. and Hanson, W. B.(1970), J. Geophys. Res., 75,769.

Schunk, R. W. and Walker, J. C. G.(1969), Planet. Space Sci., 17,853.

Schunk, R. W. and Walker, J. C. G.(1970a), Planet. Space Sci., 18,535.

Schunk, R. W. and Walker, J. C.G.(1970b), Planet. Space Sci., 18,1319.

Schunk, R. W.(1975), Planet. Space Sci., 23,437.

Serbu, G. P. and Maier, E. J. R.(1970), J. Geophys. Res., 75,6102.

St.-Maurice, J.-P. and Schunk, R. W.(1977), Planet. Space Sci., 25,907.

Strobel, D. F. and Weber, E. J.(1972), J. Geophys. Res., 77,6864.

Taylor, H. A., Brace, L. H., Brinton, H. C. and Smith, C. R. (1963), J. Geophys. Res., 68,5339.

Vasseur, G. and Waldteufel, P.(1968), J. Atmospheric Terr. Phys., 30,779.

Victor, G. A., Constantinides, E. R.(1979), Geophys. Res. Lett., 6,519.

Walker, J. C. G.(1967), Planet. Space Sci., 15,1151.

Walker, J. C. G.(1970), Planet, Space Sci., 18,559.